Advances in electroaerodynamic thrusters for aircraft propulsion

by

Nicolás Gómez Vega
MEng in Aeronautical Engineering, Imperial College London (2019)

Submitted to the Department of Aeronautics and Astronautics
in partial fulfillment of the requirements for the degree of
Doctor of Philosophy
at the
MASSACHUSETTS INSTITUTE OF TECHNOLOGY
June 2023

Authored by: Nicolás Gómez Vega
Department of Aeronautics and Astronautics
May 23, 2023

Certified by: Steven R. H. Barrett
H. N. Slater Professor of Aeronautics and Astronautics
Thesis Supervisor

Certified by: Carmen Guerra García
Assistant Professor of Aeronautics and Astronautics

Certified by: Jaime Peraire
H. N. Slater Professor of Aeronautics and Astronautics

Accepted by: Jonathan P. How
R. C. Maclaurin Professor of Aeronautics and Astronautics
Chair, Graduate Program Committee

This page intentionally left blank.

Advances in electroaerodynamic thrusters for aircraft propulsion

by

Nicolás Gómez Vega

Submitted to the Department of Aeronautics and Astronautics
on May 23, 2023, in partial fulfillment of the
requirements for the degree of
Doctor of Philosophy

Abstract

An electroaerodynamic (EAD) thruster is a propulsion system for small aircraft that is mechanically simple, has no moving parts, and is nearly silent. EAD thrusters produce ions from atmospheric air and accelerate the ions across two electrodes separated by an air gap: collisions of ions with neutral molecules result in momentum transfer to the neutral air, generating an ionic wind and a thrust force. EAD has been demonstrated to be a feasible form of propulsion for airships and, recently, for airplanes. A major challenge that has to be overcome is that EAD thrusters have a low thrust density (thrust per unit volume or frontal area) compared to conventional propulsion systems, such as propellers.

This thesis focuses on thruster physics and explores different techniques to improve the thrust density and/or efficiency of EAD thrusters. Four studies are conducted to achieve these goals. The first one is a study of "decoupled" EAD thrusters with a dielectric barrier discharge ion source, in which the ionization and ion acceleration processes are separated. This is different from alternative EAD architectures using corona discharges, in which these processes cannot be independently controlled. By using benchtop and thrust-measurement tests, it is found that the current and thrust produced by these decoupled devices scales with the DC voltage and gap distance in the same manner as the ideal space-charge limited current in a thin ion slab. Similarly, the results show that current is mostly affected by the power draw of the ion source instead of by the ion source parameters independently.

The second study involves reverse emission, a critical non-ideal effect that increases power consumption and lowers the sparking voltage without contributing to thrust. This work shows that reverse emission is caused by a gas discharge in the ion-collecting electrode, primarily at its two ends. Several techniques to mitigate this discharge are identified; all of these consist of modifying the electrode geometry to weaken the electric field at the tips. If reverse emission is mitigated, it is possible to achieve substantial improvements in power consumption, maximum thrust, and noise signature.

The third study is a theoretical investigation of multistaged ducted (MSD) thrusters

containing several serially-stacked EAD stages enclosed in a duct. The duct also includes an inlet and a nozzle and is hypothesized to provide a thrust component similar to that in ducted fans. Combining momentum theory with relevant models for the EAD stage performance, it is shown that MSD thrusters have the potential to provide order-of-magnitude improvements in thrust density and thrust-to-power ratio with respect to single-stage devices.

The fourth study involves an implementation of multistaged EAD thrusters to both establish their performance and validate the predictions from theory. Single-stage experiments suggest that stages with small gap distances are advantageous as they provide a high force on the fluid per unit volume. By stacking multiple stages in series, it is found that the thrust density can be significantly increased as compared to single-stage thrusters: 10 stages provide a factor of 5.6 increase in thrust at the maximum voltage tested. However, these improvements occur with diminishing returns due to increasing pressure losses as more stages are added. The theoretical models are found to be consistent with the experimental data, being able to capture the effects of all the physical parameters tested.

The work in this thesis provides a pathway for developing EAD thrusters that could deliver a high thrust density at a practical thrust-to-power ratio, potentially enabling EAD-propelled aircraft to perform useful missions.

Thesis Supervisor: Steven R. H. Barrett
Title: H. N. Slater Professor of Aeronautics and Astronautics

Acknowledgments

First and foremost, I would like to thank my advisor Steven Barrett for taking me in not once but twice: first as an exchange student in 2018 and then as a PhD student in 2019. Steven's guidance and advice have been instrumental throughout my academic journey. This thesis would not have been possible without his support.

I would also like to thank the other members of my committee, Carmen Guerra García and Jaime Peraire, and my readers, Dan Hastings and Manuel Martínez Sánchez, for their valuable suggestions and feedback that helped to improve this thesis. Additionally, I would like to acknowledge the financial support provided by the Deshpande Center, MHI, MathWorks, and NASA through the NIAC program.

I wish to thank the other members of the EAD team: Haofeng, Arthur, Suzanne, Jamie, Mihir, and the two Nicks. I am particularly thankful to all the UROPs that I have supervised over these four years for their hard work and meaningful insight: Jaya, Dongjoon, Chris, and Alazar. I also want to extend my gratitude to the other UROPs in the EAD team for all the effort they put into this project: Sienna, Umar, Hiromu, Jose, Faith, Gabi, Chad, and Nicole.

I would like to express my gratitude to my lab's leadership and administrative staff, including Florian, Seb, Ray, Jayant, Esther, Joyce, and Robin, for helping me with the logistics of my work. I am also thankful to Dave and Todd for helping me every time I needed to use the machine shop and for their valuable technical suggestions. I would also like to thank Carmen and Jayant for giving me the invaluable opportunity to be a teaching assistant in an MIT class.

I want to thank my friends and colleagues in LAE for their continued support, mentorship, and lunch companionship over these years, including Cassandre, Grace, Vincent, Prashanth, Carla, Inés, Jad, China, Laurens, Yang, Joonhee, Louis, Diego, TJ, Adrien, Olivier, Christoph, Bang, Prateek, Niamh, and many others. Special thanks to my MIT friends for spending time with me even during the worst moments of the pandemic, including Adriana, Peter, Kevin, Farri, Cynthia, Marek, and Juju. I would also like to thank Sean for all the support he has given me and for putting

up with my sporadic frustration.

I am very grateful to my friends from across the pond for their continuous affection and occasional visits, including Carlos, Álex, Ro, Luis, Irene, Patri, Alberto, Raquel, Óscar, Pablo, Héctor, Brenda, Guille, and Maksym. Finally, I wish to thank my dad, grandparents, uncles, aunts, cousins, and other relatives for their unwavering support and constant calls over these years.

Thank you all for being there for me.

Contents

List of Figures

List of Tables

This page intentionally left blank.

Nomenclature

Acronyms

AC	Alternating current
DBD	Dielectric barrier discharge
DC	Direct current
EAD	Electroaerodynamics
EHD	Electrohydrodynamics
MSD	Multistaged ducted
NRP	Nanosecond repetitively pulsed
RH	Relative humidity
RMS	Root mean square
SDBD	Surface dielectric barrier discharge
VTOL	Vertical take-off and landing

Symbols

α	Townsend ionization coefficient (m^{-1})
	Normalized electric field at the emitter, $\alpha \equiv \frac{E_0 L}{\varphi_0}$ ($\sim$)
$\bar{\rho}$	Electric source number, $\bar{\rho} \equiv \frac{L^2 \rho_{c,0}}{\varepsilon \varphi_0}$ ($\sim$)
$\bar{v}$	Electric slip number, $\bar{v} \equiv \frac{U_0 L}{\mu \varphi_0}$ ($\sim$)
β	Townsend reattachment coefficient (m^{-1})
Δ	Parallel electrode pair distance (m)
δ	Air density ratio ($\sim$)
$\dot{m}$	Mass flow rate ($\mathrm{kg\,s}^{-1}$)
Γ	Surface ($\sim$)
γ	Townsend secondary emission coefficient ($\sim$)
μ	Ion mobility ($\mathrm{m}^2\,\mathrm{V}^{-1}\,\mathrm{s}^{-1}$)
μ_v	Dynamic viscosity ($\mathrm{Pa\,s}$)
ν	Kinematic viscosity ($\mathrm{m}^2\,\mathrm{s}^{-1}$)
ϕ	Nozzle area ratio ($\sim$)
ρ	Fluid density ($\mathrm{kg\,m}^{-3}$)
ρ_c	Charge density ($\mathrm{C\,m}^{-3}$)
Θ	Pressure rise-to-power ratio ($\mathrm{Pa\,m}^2\,\mathrm{W}^{-1}$)
θ	Interstage separation (m)
ε	Permittivity of medium ($\mathrm{F\,m}^{-1}$)
ε_0	Vacuum permittivity, $\varepsilon_0 \approx 8.854 \times 10^{-12}\,\mathrm{F\,m}^{-1}$

φ Electric potential (V)

$\vec{f}$ Body force vector ($\mathrm{N\,m^{-3}}$)

A Area ($\mathrm{m^2}$)

b Span (m)

C Corona constant ($\mathrm{A\,V^{-2}}$)
Capacitance (F)

c Chord length (m)

C_0 Dimensionless corona constant ($\sim$)

C_D Drag coefficient ($\sim$)

D Diameter (m)
Diffusion coefficient ($\mathrm{m^2\,s^{-1}}$)

d Gap length or gap spacing (m)

E Electric field ($\mathrm{V\,m^{-1}}$)

F Thrust force (N)

f Frequency (Hz)

I DC current (A)

j Current density ($\mathrm{A\,m^{-2}}$)

k_B Boltzmann constant,
$k_B \approx 1.381 \times 10^{-23}\,\mathrm{m^2\,kg\,s^{-2}\,K^{-1}}$

K_L Loss coefficient ($\sim$)

L Length (m)

L_s Loss of species s ($\mathrm{m^{-3}\,s^{-1}}$)

M Mobility ratio, $M \equiv \sqrt{\frac{\varepsilon}{\rho}}\frac{1}{\mu}$ ($\sim$)

m Mass (kg)

n Number density ($\mathrm{m^{-3}}$)
Number of stages ($\sim$)

P Power (W)

p Pressure (Pa)

q Electric charge (C)

r Wire radius (m)
Correlation coefficient ($\sim$)

S_s Source of species s ($\mathrm{m^{-3}\,s^{-1}}$)

T Absolute temperature (K)

t Time (s)

u Neutral fluid speed ($\mathrm{m\,s^{-1}}$)

U_0 Reference velocity ($\mathrm{m\,s^{-1}}$)

V Voltage (V)

V_0 DC corona inception voltage (V)
DBD voltage threshold (V)

V_a Applied DC voltage (V)

v_d Ion drift velocity ($\mathrm{m\,s^{-1}}$)

Re Reynolds number, $\mathrm{Re} \equiv \frac{\rho U_0 L}{\mu_v}$ ($\sim$)

Subscripts

0 Reference

a Applied

B	Bulk flow
c	Collector
	Corona
E	Electrostatic
e	Electron, electric or emitter
i	Ion
N	Net
n	Neutral
AC	Alternating current
crit	Critical
DBD	Dielectric barrier discharge
DC	Direct current
MG	Mott-Gurney

This page intentionally left blank.

Chapter 1

Introduction

Electrohydrodynamics (EHD) is the study of the interactions between charged particles subjected to an electric field and neutral molecules in a fluid medium. The alternative term *electroaerodynamics* (EAD) is sometimes used when the working fluid is a gas. A basic EAD device consists of an emitting electrode (emitter), which acts as an ion source where ions are produced from neutral gas particles; and a collecting electrode (collector), where ions are neutralized. Ions drift from the emitter to the collector under the action of an external electric field and collide with neutral molecules along the way. Momentum transfer from ions to neutral molecules increases the static pressure or velocity of the background fluid. The flow induced by this process is often referred to as *ionic wind*. Through this transfer of momentum from ions to neutral molecules, EAD can be used to generate a body force in a gas and, as a reaction, to produce a thrust force on the EAD device itself.

1.1 Literature review

Robinson [1] and Fylladitakis et al. [2] provide accounts of the history of electroaerodynamics. They attribute the first observation of an EAD phenomenon to Hauksbee [3] in 1709, who reported a light blowing sensation when holding a charged tube close to his face. Newton [4] provided a similar account in the second edition of *Opticks* in 1718; he referred to the phenomenon as "electrick vapour", which Fylladitakis et al. [2]

interpret as the precursor to the term *electric wind*. This latter term has remained in use for centuries, although "ionic wind" is more common in the present [2]. In 1750, Wilson [5] achieved what could be considered the first practical use of EAD when he demonstrated an ionic-wind-driven rotating pinwheel. Even though the first qualitative explanation of the phenomenon was provided by Cavallo [6] in 1777, Faraday [7] was the first to recognize that momentum-transferring collisions between charged and neutral gas particles caused the ionic wind. The ionic wind was also examined by Maxwell [8], who commented that studying EAD phenomena would shed light on the nature of electricity and gases. In 1899, Chattock [9] derived an experimentally-validated relation between pressure and current in a set of parallel planar electrodes, representing the first quantitative model of EAD. This came in the wake of the discovery of gaseous ions by Thomson and Rutherford [10] in 1896.

Thomas Townsend Brown is often credited with developing the first EAD device for force generation [2]. In the 1920s, he studied what is now known as the *Biefeld-Brown effect*: a net force experienced when a high voltage is applied across asymmetric electrodes. His patent [11] for a lifter device using this effect was accepted in 1928. Brown misinterpreted the net force as a form of anti-gravity; however, it has since been shown that the Biefeld-Brown effect is simply an EAD phenomenon [12].

1.1.1 Fluid pumping

Several studies on EAD fluid pumping applications were published in the 1950s. In 1954, Lob [13] revisited the theory of Chattock [9] and generalized it to other geometries. Stuetzer [14, 15] extended this analysis in the late 1950s with a one-dimensional model of "ion drag" pumps, an early name for EAD fluid pumps. Stuetzer's one-dimensional model, which included the effects of multi-staging, bulk fluid velocity, and viscous pressure losses, is to this day one of the most complete theoretical descriptions of EAD devices and served as the basis for the models of Robinson [16] and Pickard [17, 18].

Johnson and Go [19] and Lai [20] reviewed recent work on EAD pumping. EAD pumps are solid-state, silent, and mechanically simple; however, they have low electrical–

mechanical efficiency (of the order of 1 %) [2, 16]. Some attempts have been made to improve efficiency through optimization of the geometry and the discharge [21]. Bondar and Bastien [22] tested the effect of changing the fluid velocity on the efficiency of an EAD pump. They showed that efficiency improved with increasing fluid speed: at a speed of 17 m/s, the efficiency was 2.6 %; but at 50 m/s, they recorded an efficiency of 7.5 %.

Recent work on EAD pumps has identified two possible ways to improve efficiency: serial stacking of stages and the use of an exit nozzle. Qiu et al. [23] tested gas pumps with up to 30 EAD stages. They measured higher fluid velocities as they increased the number of stages until they reached saturation at around 25 stages. After this point, the pressure produced by additional stages was balanced by pressure losses. At their optimal number of stages, they measured an exit fluid velocity of 16 m/s and a corresponding electrical–mechanical efficiency of 2.5 %. Rickard et al. [24, 25] explored multistaged pumps fitted with an exhaust nozzle. In their first study [24], they observed higher exit velocities as the nozzle area ratio was decreased, although this came with a reduction in the mass flow rate. In their second study [25], they found that a 7-stage pump could as much as triple the pump exit velocity compared to a single-stage device. Other studies [26, 27] on EAD pumps fitted with nozzles also found that changing the nozzle area can control the pump exit properties.

1.1.2 Propulsion

Cheng [28] published the first peer-reviewed paper on EAD thrust generation in 1962, presenting a one-dimensional theoretical model. This was followed by the first experimental study on EAD thrusters by Christenson and Moller [29] in 1967. They developed a theoretical model for their pin-to-mesh geometry and verified it experimentally with a thruster using a negative-corona-discharge ion source. They reported an energy conversion efficiency of the order of 1 % and identified ion mobility as a critical factor affecting the performance of their thruster.

There was a resurgence of interest in EAD propulsion at the turn of the 21st century. Wilson et al. [30] conducted a parametric study on EAD thrusters, exploring

the effects of voltage and geometry, and found a trade-off between thrust and thrust-to-power ratio (which, when multiplied by velocity, is equal to the overall efficiency). They set the arbitrary goal of simultaneously reaching an areal thrust density (thrust per unit frontal area) of $20\,\mathrm{N\,m^{-2}}$ and a thrust-to-power ratio of $20\,\mathrm{N\,kW^{-1}}$, which they claimed was needed to enable practical applications of EAD propulsion. Their study did not meet this goal and concluded that order-of-magnitude improvements in thrust density were necessary for practical applications. Pekker and Young [31] developed a simple one-dimensional model of a single-stage EAD thruster similar to that of Stuetzer [15] and used it to show that such a thruster cannot exceed a thrust density of 20–$30\,\mathrm{N\,m^{-2}}$.

Masuyama and Barrett [32] studied single-stage and dual-stage thrusters consisting of a single emitter and two collectors in series. They noted that, while the thrust forces produced by the thruster were low, the thrust-to-power ratio was comparable to that of conventional propulsion systems such as jet engines. Moreau et al. [33] characterized the performance of an EAD thruster with a wire-to-cylinder geometry and predicted that increasing the gap distance between the emitter and collector would provide a higher thrust-to-power ratio at a fixed thrust level. This was supported by the experiments of Xu et al. [34], who tested a wire-to-cylinder EAD thruster and found improvements in performance at large gap spacings, namely, a higher thrust-to-power ratio for a constant thrust per unit electrode span. They also identified non-ideal effects, such as current leakage to the surroundings and reverse ion emission from the collector, and developed strategies to mitigate them. Monrolin et al. [35] also reported non-ideal effects in their study with wire-to-cylinder corona-discharge EAD thrusters: they observed that a reverse emission (which they called "backdischarge") of charged species would be ignited at the tip of the cylinders at high voltages. They also noted that this discharge resulted in noise emission and a higher, unstable current but did not affect the thrust density. Masuyama and Barrett [32] also observed this reverse emission and commented that it resulted in a "bilinear degradation" in their thruster's performance.

Gilmore and Barrett [36] tested the effects of stacking sets of emitters and collec-

tors in parallel and in series. They did tests in which they had several sets of parallel emitter/collector pairs in a single stage and varied the distance between these pairs. They observed degradation in the thrust and current produced by any given pair as these pairs were brought closer together and, therefore, estimated that the maximum thrust density of a single-stage thruster was $3.3\,\mathrm{N/m^2}$. They also conducted experiments with up to five serially-stacked stages containing several emitter/collector pairs and measured an approximately linear increase in thrust with the number of stages. Gilmore and Barrett [36] also developed empirical models for the effect of parallel electrode pair distance. These models were validated by Coseru et al. [37], who used numerical simulations to study different parallel electrode arrangements in wire-to-cylinder corona discharges. Belan et al. [38] conducted experiments with several parallel emitter/collector pairs in wire-to-aerofoil corona discharges and found empirical scaling laws of the same form as those first proposed by Gilmore and Barrett [36]. They tested different uncambered airfoil types from the NACA 4-digit family with thickness-to-chord ratios in the range of 6 % to 14 % and reported that the NACA 0010 airfoil provided the best compromise between thrust-to-power ratio and thrust density.

Khomich et al. [39] performed experiments with wire-to-cylinder corona-discharge thrusters in rarefied gases. They measured a maximum thrust per unit collector span of $1.8\,\mathrm{mN\,m^{-1}}$ at a thrust-to-power ratio of $0.052\,\mathrm{N\,kW^{-1}}$ when the pressure was 0.05 atm, corresponding to an altitude of 20 km. They also extrapolated their experimental results to estimate that a hypothetical EAD thruster operating in very low Earth orbit could achieve a thrust-to-power ratio of up to 0.1–$0.3\,\mathrm{mN\,kW^{-1}}$, comparable to that of some space propulsion systems. Casado and Greig [40] performed a feasibility study of a fixed-wing drone in the Martian atmosphere propelled by forces produced by asymmetric surface dielectric barrier discharges. They concluded that an aircraft with a wingspan of 5 m could be capable of flight on Mars: they estimated that this aircraft could reach a thrust-to-weight ratio of 0.14 and a lift-to-drag ratio of 17. However, their models had highly simplified physics, and their proposed concept requires wireless power transfer from a station on the surface.

Most EAD devices studied for aircraft propulsion to date have used a single direct current (DC) field to both produce the ions through a corona discharge and accelerate the resulting ions. Several studies have considered methods to separate the ion generation and acceleration processes. Colas et al. [41] tried to achieve this in corona discharges by using auxiliary electrodes near the emitter to alter the electric field shape. They placed two parallel cylinders a small distance downstream of their wire emitter, such that the emitter lied between them, and two flat plates downstream of these cylinders. By optimizing the distance between the electrodes and their potentials relative to the emitter, they increased the thrust by up to 46 % with respect to their baseline wire-to-plate geometry, while power only increased by 16 %. Recently, Xu et al. [42] showed that an EAD thruster using an ion source decoupled from the ion acceleration stage could provide a higher thrust-to-power ratio than a geometrically-similar corona-discharge thruster for a given thrust. They conducted experiments in a wire-to-cylinder geometry, with a dielectric barrier discharge as the ion source of their "decoupled thruster". Considering only the power spent in accelerating ions, they achieved a thrust-to-power ratio of $20\,\mathrm{N\,kW^{-1}}$ at a thrust level of $50\,\mathrm{mN\,m^{-1}}$ and $10\,\mathrm{N\,kW^{-1}}$ at $150\,\mathrm{mN\,m^{-1}}$, approximately double the thrust-to-power ratio that they achieved with a corona discharge at the same thrust levels. However, the power draw of the ion source was comparable to the ion acceleration power. When this power draw component is accounted for, their decoupled thruster only delivered higher thrust than a corona-discharge thruster for a given power at the highest gap spacing that they tested (150 mm), and when the thruster operated at a high power level (greater than $10\,\mathrm{W\,m^{-1}}$).

Over the past two decades, several groups have built and tested EAD-propelled aircraft. In 2009, Poon et al. [43] demonstrated a lighter-than-air blimp with an EAD propulsive unit and an onboard power supply for indoor surveillance applications. In 2021, He et al. [44] tested a small airship with EAD thrusters that was designed for indoor flight and carried its power supply on board: the airship used the EAD thrusters to perform forward and yaw motions. In 2018, Xu et al. [45] demonstrated the feasibility of EAD propulsion for heavier-than-air, fixed-wing aircraft with the

flight of the first EAD-propelled airplane. The airplane was named Version 2 (or V2), had no moving parts, and was nearly silent. It achieved steady level flight at a velocity of approximately 5 m/s and had an endurance of 90 s. Their airplane used a wire-to-airfoil corona discharge as the ion source and had a two-stage configuration, each stage containing four sets of parallel electrodes, providing a thrust density of $3.6\,\mathrm{N\,m^{-2}}$ and a thrust-to-power ratio of $6.2\,\mathrm{N\,kW^{-1}}$. However, the aircraft only achieved an overall efficiency of around 3 %, an order of magnitude lower than that achievable with conventional propulsion systems. The reasons for this low overall efficiency were explored by Gilmore and Barrett [46], who used the one-dimensional model of Stuetzer [15] to study the effects of atmospheric pressure and flight speed on the performance of an ideal EAD thruster. They showed that the overall efficiency of an EAD-propelled aircraft could be as high as 50 % at flight speeds comparable to the average ion drift velocity. However, they also noted that the thrust-to-power ratio of an EAD thruster decreases monotonically with altitude in the atmosphere.

It has been known for decades that if EAD devices are not required to carry the power source (e.g., battery) and power supply on board, they can be capable of vertical take-off and landing (VTOL). For example, lifter devices consisting of a wire emitter and a thin metallic foil collector tethered to a ground-based power supply are popular science demonstrators: the lifter can fly off the ground if the applied voltage is large enough. In 2017, Drew et al. [47, 48] demonstrated a centimeter-scale tethered micro-drone that was VTOL-capable through EAD forces. In 2018, Khomich and Rebrov [49] built a meter-scale drone that used arrays of wire-to-airfoil corona discharges to take off and land vertically; the aircraft was powered by a wireless external power supply through an onboard receiver.

1.1.3 Heat transfer enhancement

Electroaerodynamic (or, in general, electrohydrodynamic) phenomena have also been studied for heat transfer enhancement due to the coupling between electrostatics and hydrodynamics. Allen and Karayiannis [50] provide a review of experiments on EHD heat transfer enhancement, as well as a summary of the relevant theory. A common

finding in the studies reported by Allen and Karayiannis [50] is that EHD can provide significant increases in the heat transfer coefficient, ranging from a factor of 1.2 to more than 20. For example, Fernández and Poulter [51] tested a discharge from a wire to a concentric pipe with a transformer-oil flow. They reported that the heat transport coefficient was increased up to 20-fold due to the radial EHD forces; pressure losses along the pipe also increased, but only by up to 66 %.

Wang et al. [52] compared EHD heat enhancement devices using corona discharges to other standard cooling technologies, such as heat pipes, fans, or water cooling. Using principal component analysis with parameters such as the cooling rate, power consumption, cost, and noise as inputs, they scored these different technologies and showed that EHD devices ranked first (i.e., provided the best overall performance) among the technologies considered.

1.1.4 Flow control

EAD has been studied as a means to provide active flow control; a review of research in this area is provided by Moreau [53]. EAD devices have generated interest in flow control due to their ability to inject momentum directly into a boundary layer. According to Moreau [53], surface corona-discharge actuators and surface dielectric barrier discharges (SDBDs) are the two most popular configurations for use in flow control.

Surface corona discharges are produced when a high alternating current (AC) or DC voltage is applied across two electrodes very close to or integrated into a surface. In the simplest setup, these electrodes can be a thin wire, where the discharge is ignited; and a flat plate collector flushed on the surface. A discussion of the physics and properties of corona discharges can be found in Section 1.2.2. Surface corona discharges produce an ionic wind near the surface, and the maximum velocity is usually reached at a height of about 1 mm over the surface. However, the maximum velocity that these actuators can produce is limited by electrical sparking: in stagnant air, this maximum velocity is about $5\,\mathrm{m\,s^{-1}}$ [53]. Artana et al. [54] tested a surface corona discharge actuator at the leading edge of a flat plate in a flow with a freestream

velocity of $17.5\,\mathrm{m\,s^{-1}}$ and showed that the actuator could increase the velocity inside the boundary layer by up to $10\,\mathrm{m\,s^{-1}}$.

A surface dielectric barrier discharge occurs when a high AC voltage is applied across two planar asymmetric electrodes separated by a dielectric material. A more detailed description of the properties of dielectric barrier discharges can be found in Section 1.2.3. Despite their AC operation, SDBDs can deliver a unidirectional force tangential to their surface. This can result in a higher maximum momentum injection than surface corona discharges, as SDBDs are not limited by sparking in the same way [53]. In static air, Forte et al. [55] showed that an SDBD actuator can provide a velocity of up to $8\,\mathrm{m\,s^{-1}}$ at a height of about 0.5 mm over the wall. He et al. [56] tested a NACA 0015 wing model with two SDBDs: one near the leading edge and another one near the trailing edge, to mimic the effects of wing slats and flaps. At a Reynolds number of 3.07×10^5, they showed that the actuators could allow the flow to remain attached up to 9° over the normal stall angle.

1.1.5 Electrostatic precipitation

The main commercial application of ionic winds is electrostatic precipitation, in which EAD forces are used to remove pollutants from a flow. In their simplest form, electrostatic precipitators contain parallel arrays of thin bars (which act as the emitters) and metallic flat plate collectors parallel to the incoming flow. A voltage is applied across the bars and flat plates to produce a corona discharge. The corona discharge ionizes pollutant particles, which accumulate on the flat plate collectors and are subsequently removed [57, 58]. Electrostatic precipitators are widely used in industrial and residential settings [58].

As pollutant particles accumulate on the collector, a dust layer is formed which causes a potential drop across it, affecting the electrical properties of the precipitator. If its resistivity is large enough, a back corona discharge can ignite and this severely decreases the efficiency of the device [59]. Therefore, electrostatic precipitators require occasional maintenance or the use of a scrubbing system. Compared to other filtering technologies, such as high-efficiency particulate air (HEPA) filtration,

electrostatic precipitators can result in lower pressure losses as they do not require physical filters [58]. Electrostatic precipitators can also achieve high collection efficiency: the electrostatic precipitator demonstrated by Kim et al. [60] could remove more than 95 % of the ultrafine particles in a flow with very low power consumption and small pressure loss.

1.1.6 Flame control

Ionic winds have also been studied in the context of flame control in combustors. The combustion process can generate ions in high-temperature regions in the flame (through chemi-ionization or thermal ionization) and research has been done on using DC, AC or pulsed electric fields to induce ionic flows and alter the flame properties [61]. Early work in this field was done in the 1960s by Lawton et al. [62], who used theoretical and experimental methods to study the effects of sub-breakdown electric fields on flames. They estimated that a maximum current density of $0.25\,\mu\mathrm{A\,cm^{-2}}$ was possible in a 1-D model of a flame assuming that charge transport was through H_3O^+ ions and electrons, with a corresponding ionic wind velocity of $5.5\,\mathrm{m\,s^{-1}}$. The authors also discussed how this ionic wind could be used to change the flame shape and size or to enhance heat transfer to the walls. In addition to these effects, it has also been shown that ionic winds can be used for soot emissions control [63]: Saito et al. [64] found that high electric fields could suppress up to 90 % of the soot produced in an acetylene flame.

1.2 Overview of non-thermal discharges

Non-thermal discharges are the preferred ion source for EAD devices. Compared to high-temperature plasmas, non-thermal plasmas can be achieved with simpler architectures, are easier to contain, and have lower energy requirements for ionization [65]. The purpose of this section is to describe the main non-thermal discharges in atmospheric-pressure air that are relevant for EAD applications. Fridman et al. [65], Raizer [66], and Roth [67] provide detailed descriptions of the physical processes

in non-thermal discharges.

1.2.1 Townsend breakdown, streamers and sparks

Gas discharges occur when a voltage exceeding some threshold is applied across two electrodes separated by a gas-filled gap. Different types of discharges can occur depending on the electrode geometry, gas composition, and voltage properties (e.g., amplitude and frequency). Most gas discharges have in common the concept of an electron avalanche, which occurs when some primary electron accelerated by the electric field produces an ionization cascade.

Consider the most straightforward discharge geometry: two conductive flat plates at different potentials separated by a gas-filled gap. A primary electron may be produced near the negative electrode (cathode) by, for example, photoionization or cosmic rays. As the primary electron drifts from the cathode to the anode, it collides with neutral gas molecules, producing positive ions and secondary electrons. The number of secondary electrons produced per unit length in an avalanche is defined as the Townsend ionization coefficient or the first Townsend coefficient, α, such that [65]

$$\frac{\mathrm{d}n_e}{\mathrm{d}x} = \alpha n_e, \tag{1.1}$$

where n_e is the electron number density and x is a coordinate going from the cathode to the anode.

If the gas is electronegative, there is also a probability that an electron will attach to a gas particle to form a negative ion. The electron attachment rate per unit length is defined as the second Townsend coefficient, β. The change in electron number density is then given by

$$\frac{\mathrm{d}n_e}{\mathrm{d}x} = (\alpha - \beta)n_e. \tag{1.2}$$

Electron–ion recombination is usually negligible in this process because the ionization degree is low during breakdown [65]. The Townsend coefficients α and β are functions of the reduced electric field, E/n_n, where E is the electric field strength and n_n is the

number density of the neutral gas.

Positive ions produced in the secondary ionization processes drift toward the cathode. When they reach the cathode, they are neutralized, and there is a chance that an electron will be emitted. The probability of electron emission after an ion impact on the cathode is defined as the secondary emission coefficient or third Townsend coefficient, γ, which usually ranges between 0.01–0.1 and is a function of the type of gas, reduced electric field, and the cathode surface's material and state [65]. Mechanisms by which a cathode can emit an electron include the photoelectric effect and the ion–electron emission, in which an electron is released from a surface via quantum tunneling following the neutralization of a positive ion on that surface [66]. These different mechanisms are captured via an "effective" secondary emission coefficient γ [65]. An electron emitted by the cathode through these processes starts an avalanche, producing positive ions and electrons. The discharge is self-sustained when this avalanche produces enough positive ions to release, on average, one new electron at the cathode to start yet another avalanche [65]. This condition is met once the electric field exceeds some threshold, which depends on the gas pressure and the discharge gap length; this type of breakdown is known as *Townsend breakdown*. Since an electron emitted by the cathode produces $\exp\left[\int_0^d(\alpha-\beta)dx\right]-1$ positive ions in the gap, the condition for Townsend breakdown can be expressed in general as

$$1=\gamma\left(\exp\left[\int_0^d(\alpha-\beta)dx\right]-1\right), \tag{1.3}$$

where d is the distance between the electrodes.

In a parallel plate geometry prior to breakdown, the electric field between the plates is constant if the space-charge density is ignored and, therefore, α is also constant. In this case and if the gas is not electronegative, such that $\beta \approx 0$, the condition for Townsend breakdown can be expressed in a simpler form as

$$\alpha d=\ln\left(\frac{1}{\gamma}+1\right). \tag{1.4}$$

A commonly-used semi-empirical formula relating the Townsend ionization coefficient

α to the electric field and gas pressure, p, is [65, 67]

$$\frac{\alpha}{p} = A \exp\left(-\frac{B}{E/p}\right), \tag{1.5}$$

where the parameters A and B are dependent on the gas composition: a table showing the value of these parameters for different gases can be found in Fridman et al. [65]. In a parallel plate geometry, the electric field is given by $E = \frac{V_a}{d}$, where V_a is the voltage applied across the plates. Substituting Equation (1.5) into (1.4), and solving for the minimum voltage that causes breakdown, V_{crit}, yields

$$V_{\text{crit}} = \frac{Bpd}{\ln(pd) + \ln A - \ln[\ln(1/\gamma + 1)]}. \tag{1.6}$$

Equation (1.6) is known as Paschen's law and shows that the breakdown voltage of a gas in a parallel plate geometry is a function of the product of the gas pressure and the gap distance. There exists a product pd that results in minimum breakdown voltage in Equation (1.6): this is known as the Paschen minimum and it has a value of 305 V for air, assuming $\gamma = 0.01$ and using the parameters in Fridman et al. [65]. A voltage below the Paschen minimum will not result in breakdown between two parallel plates regardless of the distance between the plates or gas pressure, as long as the Townsend avalanche is the only discharge mechanism.

The processes that occur after breakdown depend on the electric circuit. The simplest case is when one of the electrodes is connected in series to a resistor, which prevents a runaway current when the electron avalanches are self-sustained. If the resistance is initially very high and then gradually reduced, the non-self-sustaining avalanches will transition to a self-sustaining *dark Townsend discharge* after breakdown. In the dark Townsend discharge, the current is low and the electric field between the electrodes is not disturbed by the space charge, with a voltage drop across the gas tube equal to the breakdown voltage [66]. As the external resistance is reduced, the dark Townsend discharge transitions into a *glow discharge*, in which space charge significantly affects the electric field distribution [66]. The glow discharge is characterized by intense light emission, stratified into bright and dark bands. Glow

discharges have multiple practical applications, such as neon lighting, fluorescent lamps, and plasma display televisions. If the resistance is further reduced, the glow discharge will transition to an abnormal glow discharge followed by an *arc discharge*, which involves large currents and in which thermionic emission from the cathode plays a role [66].

In large gaps at high pressures, breakdown can occur at much lower potential differences between the electrodes than predicted by the Townsend breakdown theory described above. In these cases, breakdown is caused by thin ionized channels known as *streamers*. Streamers develop from an electron avalanche due to the electric field induced by the electrons moving toward the anode and the ions moving toward the cathode [65, 66]. The avalanche-to-streamer transition occurs when the magnitude of the induced electric field becomes comparable to that of the external electric field [65]. Meek's criterion can be used to quantify the external field required for avalanche-to-streamer transition,

$$\int_0^d (\alpha - \beta) \mathrm{d}x \approx K, \tag{1.7}$$

where K usually ranges between 18 and 20, although it depends on the type of gas [65, 68]. If the discharge gap is small, the avalanche-to-streamer transition occurs near the anode: this is known as a positive or cathode-directed streamer [65, 66]. If the gap between the electrodes is large, the transition to streamer may occur at some intermediate point in the gap and develop towards both electrodes: this is known as an anode-directed streamer [65, 66]. Further discussion on the physics of streamers may be found in Raizer [66]. If the voltage is sufficiently large, a streamer may bridge the entire gap. When this occurs, a return wave of intense ionization is triggered and current increases by orders of magnitude: this phenomenon is known as a *spark* [65]. Due to its high power draw and hazardous nature, the onset of sparking marks one of the bounds of operation of EAD devices.

In very large gaps (order of meters to kilometers), breakdown may occur through the formation of a *leader*, which is a thin and highly conductive channel. The leader

process is closely related to the concept of streamers, and a leader includes streamers as its elements [66]. The formation of a leader is the first step in a lightning discharge [66, 69].

1.2.2 Corona discharge

Corona discharges occur when a high DC voltage (of the order of kilovolts) is applied across two asymmetric electrodes. Some geometries in which corona discharges can occur are shown in Figure 1-1: these include needle-to-plate [70, 71], needle-to-mesh [23, 47], needle-to-ring [24, 72], wire-to-cylinder [33, 73, 74], wire-to-airfoil [45], and wire-to-surface [75]. A high electric field develops in the vicinity of the electrode with smaller radius of curvature. An ion-producing self-sustaining discharge develops if the applied voltage is above a given threshold, known as the corona inception voltage. The electrode at which ions are produced is referred to as the emitter or the *coronating electrode*. Positive and negative coronas can occur depending on whether the emitter is the anode or the cathode, respectively. Most studies on EAD thrust generation have used corona discharges as ion sources.

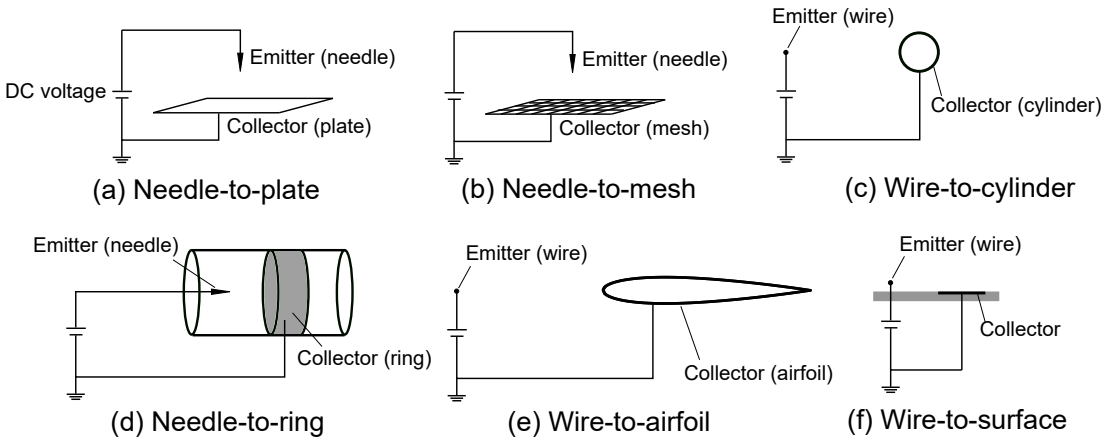

Figure 1-1: Schematic diagrams of some corona discharge geometries. In all cases, the electrical arrangement would result in positive coronas.

Corona discharges contain two main regions of physical importance. The *active corona region or volume* is located near the emitter and is a zone of high electric field where ionization events take place. Ions produced in the active corona volume drift

towards the collector under the action of the electric field through the *drift region*, where the electric field is too low to cause ionization events. The size of the active corona volume depends on the applied voltage and the corona discharge geometry. For example, the active corona radius near a wire emitter in a wire-to-concentric cylinder discharge is typically three times larger than around a sharp point [65], illustrating the advantage of wire emitters in applications where corona discharges are desirable.

Positive and negative coronas occur through different physical mechanisms and have qualitative differences. Similarly to the Townsend breakdown, the ignition of a negative corona occurs through electron avalanches [66]. In fact, an analytical model for the onset of corona discharges in wire-to-cylinder geometries has been developed on the basis of the Townsend criterion [76]. Secondary electrons that sustain the discharge are released when positive ions collide with the emitter surface, by photoemission from the emitter surface, and by photoionization in the gas [66, 77]. In negative coronas, electrons attach to electronegative molecules, such that charge transport in the drift region occurs through negatively-charged ions instead of free electrons [19]; however, a portion of the charge is transported by low-energy electrons for a small length beyond the active corona region [78].

In a positive corona, the electric field near the cathode (the collector) is insufficient to cause an electron avalanche of the same type as the Townsend discharge. The positive corona is initiated with some naturally-occurring seed electron: as this seed electron is accelerated towards the emitter, it collides with neutral molecules to produce positive ions and free electrons, which are in turn accelerated and produce further ionization. While a random electron initiates the avalanches, the positive corona is sustained by secondary electrons released near the positively-charged emitter. These secondary electrons are thought to be produced through photoionization of neutral air molecules; the high-energy photons that drive photoionization are released when molecules are de-excited following collisions [66, 79]. Fridman et al. [65] also discuss how cathode-directed streamers play a role in sustaining the positive corona discharge. As noted by Chang et al. [78] and Chen and Davidson [77], positive coronas tend to be uniformly distributed along the emitter, whereas negative coronas occur

primarily at discrete locations or 'tufts' where irregularities in the surface exist.

Even though positive and negative coronas involve different physical mechanisms, they usually have very similar inception voltages [65]. Different discharge processes occur after inception depending on the polarity. In a needle-to-plate geometry, a positive corona will transition from an initial burst pulse regime (with an unstable current) to a streamer corona (in which streamers form and propagate into the interelectrode gap) as the voltage is increased, followed by a glow corona with visible light emission and, ultimately, spark breakdown [78]. In the same geometry, a negative corona initially occurs through Trichel pulses (short pulses with a peak current orders of magnitude higher than the mean corona current), before transitioning to a pulseless discharge followed by spark breakdown as the voltage is increased [65, 78].

Ignition of both positive and negative coronas depends on the value of the maximum electric field in the vicinity of the emitter. The critical electric field for corona inception was studied by Peek [80], who derived empirical formulas valid for corona discharges in concentric cylinder and parallel wire geometries. For parallel wires, the electric field at corona inception, E_{crit}, takes the form [80]

$$E_{\text{crit}} = 3.0 \times 10^6 \delta \left(1 + \frac{0.0301}{\sqrt{\delta r}}\right), \tag{1.8}$$

where δ is the ratio of air density to standard density, r is the radius of the wires in m, and E_{cr} is in V/m. Despite strictly only being valid for wire-to-wire geometries, Equation (1.8) has been used in numerical studies with different geometries, such as wire-to-plate [81] or wire-to-cylinder [34]. The critical field for corona inception is similar in positive and negative coronas, even though they occur via different mechanisms [65]. For voltages above corona inception, it is commonly assumed that the electric field near the emitter remains fixed at the value at the onset of the corona discharge. This assumption is known as Kaptsov's hypothesis [82], and is supported by more detailed numerical simulations [83].

The relation between the corona discharge current, I_c, and the applied voltage, V_a, is known as the *current–voltage characteristic*. A commonly used semi-empirical

formula valid for a wide range of geometries is [67, 84, 85]

$$I_c = \begin{cases} 0 & \text{if } |V_a| < |V_0| \\ CV_a(V_a - V_0) & \text{if } |V_a| \geq |V_0| \end{cases} \tag{1.9}$$

where V_0 is the corona inception voltage, which is a function of geometry, gap spacing, and polarity; and C is some function of geometry and polarity. In wire-to-cylinder or wire-to-airfoil discharges, the constant C can also be expressed as [33, 35]

$$C = \frac{C_0 \varepsilon \mu b}{d^2}, \tag{1.10}$$

where C_0 is a non-dimensional function of electrode geometry, ε is the permittivity of the medium (if the medium is air, the permittivity is very close to the vacuum permittivity, ε_0 [86]), μ is the ion mobility (a rigorous definition is provided in Section 1.3.1), b is the emitter span, and d is the gap spacing.

The ion species produced in positive and negative coronas in low-pressure (5–30 kPa) air were studied by Skalný et al. [87] and Pavlik and Skalny [88] using mass spectrometry. They found that the species produced depended strongly on air humidity. For positive coronas in dry air, they found that the dominant charged species were positive nitric oxide (NO^+) and oxygen (O_2^+), with other species such as N_2^+, O_2^+, and N^+ also present. In humid air, the water clusters $H_3O^+ \cdot (H_2O)_n$ were the dominant ions even when the air only contained traces of water [87, 88]. As noted by Johnson and Go [19], the dominant ions in negative coronas in dry, low-pressure air are CO_3^-, O_3^- and NO_3^-; however, at higher humidity, negatively-charged water clusters dominate. Compared to negative coronas with similar electrical properties, positive coronas produce much less ozone and are thus preferred in applications such as electrostatic precipitation [58].

Zeng et al. [89] studied the effects of temperature and relative humidity (RH) on the performance of a two-stage pump with a needle-to-ring corona discharge. The authors identified three distinct discharge regimes in which changes in RH had different effects on current, flow velocity, inception voltage, and sparking voltage. At

a high RH (above 70 % at 20 °C), the authors found that water condensation on the electrodes could affect the discharge; in this regime, increasing the RH also increases the current, while the sparking voltage is reduced and the induced velocity remains the same. A different regime occurs at low RH (below 40 % at 20 °C): increasing the RH results in lower current, with no changes in fluid velocity or sparking voltage. At an intermediate RH (in the range of 40–70 % at 20 °C), a higher RH increases the sparking voltage but reduces current and flow velocity. Zeng et al. [89] also found that the ranges of RH at which the different discharge regimes occur depend on temperature: at 60 °C, the condensation regime did not occur at an RH below 98 % and the regime in which sparking voltage and velocity are insensitive to RH only occurred at an RH below approximately 5 %. Since ion mobility was not measured, it is unclear whether the current and velocity effects are caused by changes in mobility, corona inception voltage, or a combination of both.

1.2.3 Dielectric barrier discharge

A dielectric barrier discharge (DBD) occurs when a periodic (AC or pulsed) voltage is applied across two electrodes separated by a dielectric material and, in some cases, an air gap. For a DBD to ignite, the driving voltage usually needs to have an amplitude of the order of kilovolts and a frequency of 0.5–500 kHz [65]. In a DBD, numerous random microdischarges (closely related to streamer discharges) occur in the air gap or the surrounding air, resulting in the generation of a non-equilibrium, low-temperature plasma [53, 65]. The presence of the dielectric barrier prevents streamers from transitioning into a spark. Due to the capacitive nature of the device, a periodic voltage is needed for the discharge to be maintained in time. The main industrial application of DBDs is ozone generation, either directly through the discharge [90] or indirectly via their ultraviolet radiation [91]; DBDs used to be referred to as the "ozonator" discharge [92]. DBDs have also been studied for use in surface treatment [93], excimer lamps [94], aerodynamic flow control [53], and plasma-assisted combustion [95].

Figure 1-2 shows some of the electrode geometries that can be used to produce a DBD. These include parallel plate (Figure 1-2a; also referred to as "volumetric" or

"planar"), which consists of two parallel electrodes separated by an air gap and at least one of the electrodes is covered by a dielectric material [96]; coaxial cylinder (Figure 1-2b), which contains two coaxial electrodes (one insulated and one exposed) separated by an air gap [97]; and coplanar (Figure 1-2e), in which two parallel planar electrodes are inserted in a dielectric medium [98]. Asymmetric surface DBDs also exist (Figure 1-2d): these consist of two adjacent electrodes separated by a dielectric material with no air gap between them [99]. Asymmetric surface DBDs have been studied widely in aerodynamic flow control [53] and EAD propulsion [40, 100, 101] since they can produce a net force tangential to the surface plane.

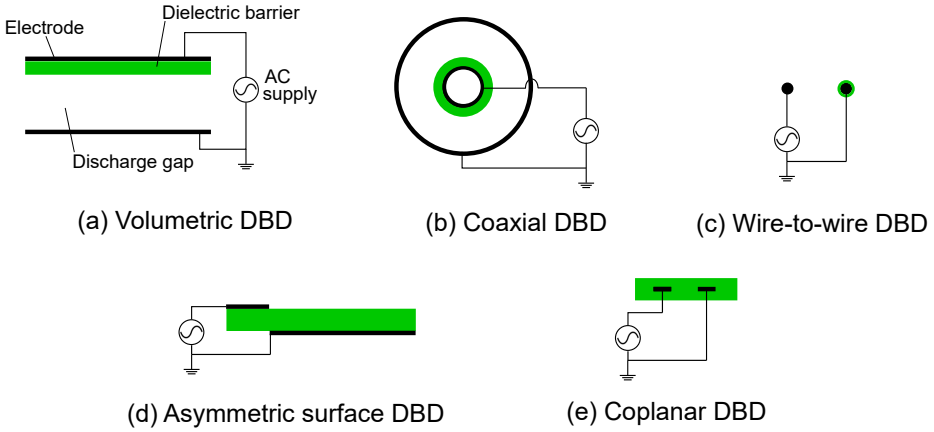

Figure 1-2: Schematic diagrams of some common DBD electrode geometries

Manley [92] observed that sinusoidally-driven volumetric DBDs have two distinct phases: an active phase with plasma generation and a passive phase in which the DBD device behaves as a capacitor. During an AC cycle, the DBD undergoes two active and two passive phases. In the passive phase, the capacitance of the device can be modeled as the serial connection of the gas capacitance (C_g) and the dielectric barrier capacitance (C_d), such that the total capacitance is $\frac{C_d C_g}{C_d + C_g}$. During the active phase, the capacitance of the DBD is just that of the dielectric barrier, C_d, since the plasma is conductive [92, 102]. Therefore, the charge–voltage plot during a discharge cycle takes the form of a parallelogram, providing a simple method to calculate the power draw of the DBD [92, 102]. Surface DBDs also undergo passive and active phases; however, the length of the region covered by the plasma changes during the

active phase, which results in a time-varying capacitance [99].

A wire-to-wire DBD geometry (Figure 1-2c) was recently proposed by Xu et al. [42] as an ion source for EAD thrusters. This consists of two wires in parallel, one encapsulated in a dielectric material and the other one exposed, separated by an air gap. With a DBD, the rate of ion production of an EAD device can be controlled independently of the ion acceleration stage by varying the AC voltage and frequency. This is not possible in devices using corona discharges since the same DC field is used to produce and accelerate ions. As a result, the ion generation and acceleration stages are "decoupled" in a DBD-based EAD device. Chapter 2 in this thesis is dedicated to an experimental characterization of decoupled EAD thrusters with wire-to-wire DBD ion sources.

1.2.4 Nanosecond repetitively pulsed discharge

Nanosecond repetitively pulsed (NRP) discharges have been studied as methods to generate low-temperature plasmas, primarily in the context of plasma-assisted combustion [103–105]. In an NRP discharge, a very high voltage is applied between two electrodes separated by a small air gap. A streamer forms in this gap, and if a constant voltage were maintained, it would bridge the gap in a time in the order of nanoseconds and transition to a spark. To prevent streamer–spark transition, the high voltage is only maintained for an interval shorter than the time it takes the spark to form, of the order of nanoseconds. This pulsed process is repeated periodically to continuously produce electrons, ions, and reactive species without transitioning to a spark [65].

Orrière et al. [106] studied NRP discharges for use in EAD devices: their setup contained two sharp pins separated by a 0.2 mm gap and a flat plate located 40 mm away from the pins. They applied a high repetitively pulsed voltage across the pins and biased the flat plate to a constant DC voltage with respect to the pins' ground. Their objective was to use the NRP discharge to produce ions and then extract them with the flat plate in what is, in effect, a decoupled EAD configuration. The work of Orrière et al. [106] was published only four months after that of Xu et al. [34], in

which decoupled EAD thrusters with DBDs were first proposed. Orrière et al. [106] found that their decoupled architecture could produce either positive or negative ions that survived for enough time to be accelerated by the plate and induce an EAD flow. However, they concluded that the flows generated by their NRP discharges were not substantially faster than what could be achieved with corona discharges or DBDs.

1.3 EAD theory and models

As discussed in the previous section, the properties of gas discharges depend on geometric, material, electrical, and gas parameters. Several simplifying assumptions must be made to enable quantitative analysis of EAD devices. The purpose of this section is to review the relevant analytical and numerical models that have been proposed to describe EAD phenomena.

1.3.1 Electrostatic models

In a gas discharge, conservation of charge can be stated as

$$\frac{\partial \rho_c}{\partial t} + \nabla \cdot \vec{j} = 0, \tag{1.11}$$

where ρ_c is the charge density, t is the time, and $\vec{j}$ is the current density vector.

If there are no externally-applied magnetic fields (as in most EAD devices proposed to date), and under the assumption that induced magnetic fields are negligible, Maxwell's equations reduce to

$$\nabla \cdot \left(\varepsilon \vec{E}\right) = \rho_c \tag{1.12}$$

$$\nabla \times \vec{E} = 0, \tag{1.13}$$

where $\vec{E}$ is the electric field.

A scalar electric potential φ can be defined such that

$$\vec{E} = -\nabla \varphi. \tag{1.14}$$

Under the assumption that the medium has uniform permittivity, combining Equations (1.12) and (1.14) results in Poisson's equation,

$$\nabla^2 \varphi = -\frac{\rho_c}{\varepsilon}. \tag{1.15}$$

Many numerical models of EAD devices assume that current in the drift region is unipolar, i.e., only positive or negative ions are present. More advanced models of EAD devices with currents due to electrons or several species of ions can be found in the literature [107–109]. Ions in the drift region reach a "drift velocity", $\vec{v}_d$, with respect to neutrals due to a balance between electrostatic acceleration and collisional drag. The drift velocity can be modeled as [46]

$$\vec{v}_d = \mu \vec{E}, \tag{1.16}$$

where μ is the ion mobility. In general, ion mobility is a function of the electric field and the type of species involved in the collisions. Analytical approximations for the ion mobility can be reached by making some simplifying assumptions. If there is only one type of ion–neutral collision and the electric field is weak enough such that the energy of ions is mainly thermal (low-field approximation), the ion mobility is independent of the electric field and can be expressed as [110]

$$\mu = \left(\frac{1}{3 k_B T_i}\right)^{1/2} \frac{q}{n_n} \left(\frac{1}{m_i} + \frac{1}{m_n}\right) \frac{1}{\Omega_{in}}, \tag{1.17}$$

where k_B is the Boltzmann constant, q is the charge of the ion, n is the number density, m is the mass of a particle, T is the absolute temperature, and Ω_{in} is the collision cross-section of the ion–neutral interactions. Subscripts i and n refer to ions and neutral molecules, respectively. Equation (1.17) assumes that only one type of ion and neutral are present but can be generalized by incorporating additional particles with different mass and collisional properties. As discussed by Gilmore and Barrett [46], for the low-field approximation to be valid, the electric field strength has to be of the order of $10^5\,\mathrm{V/m}$ or lower for air in normal conditions; this limit is lower at

higher altitudes. At electric fields above this limit, the ion kinetic energy from the drift process is significant and mobility becomes a function of electric field. In the high-field limit (kinetic energy is much greater than thermal energy), the mobility scales as $\mu \propto \frac{1}{\sqrt{E}}$ [46]. Gilmore and Barrett [46] also note that some experiments with EAD devices have been conducted with electric fields large enough that the mobility may be a function of the electric field; however, the approximation of constant mobility remained adequate.

In general, charge transport in an EAD device occurs due to ion drift, ion advection, and random diffusion of ions. Combining these and assuming unipolar transport of a single type of ions, the current density can be expressed as

$$\vec{j} = \rho_c \left(\mu \vec{E} + \vec{u} \right) - D \nabla \rho_c, \tag{1.18}$$

where $\vec{u}$ is the velocity of neutral particles, often referred to as bulk fluid velocity; and D is the ion diffusion coefficient. The three terms in Equation (1.18) represent drift, advective, and diffusive current, respectively. The diffusion component is usually neglected under the assumption that it is small compared to the drift and advective components.

If steady conditions are assumed and diffusion is neglected, Equations (1.15) and (1.18) can be substituted into Equation (1.11) to yield an expression for conservation of charge when the current is unipolar,

$$\nabla \rho_c \cdot (\mu \nabla \varphi - \vec{u}) = \mu \frac{\rho_c^2}{\varepsilon}. \tag{1.19}$$

To reach this expression, conservation of mass in the neutral fluid was used ($\nabla \cdot \vec{u} = 0$).

Continuity equations for charged species

The simplified model in the previous section only considered a unipolar current; however, charge transport in a gas discharge occurs through the motion of electrons and different types of positive and negative ions. Some detailed kinetic models of gas discharges include up to 40 species and 450 individual reactions [111], whereas sim-

pler three-species models only consider electrons and positive and negative ions [108]. The simplest continuity models of gas discharges (such as the one considered in the previous section) only include charge transport due to a single type of ions [112]. In general, the drift of species s is governed by the continuity equation [108, 113]

$$\frac{\partial n_s}{\partial t} + \nabla \cdot \left(n_s \mu_s \vec{E} + n_s \vec{u} - D_s \nabla n_s \right) = S_s - L_s, \tag{1.20}$$

where n_s, q_s, μ_s and D_s are the number density, charge, mobility and diffusion coefficient of species s, respectively. S_s and L_s are the source and loss terms, which are a function of the local electric field. In their simplest form, these source and loss terms can be related to the Townsend coefficients α and β [108]. Expressions for these terms are given in Morrow [114] for a three-species model of corona discharges in air. In some cases, the source and loss terms are also dependent on particle energies: in this case, energy equations for each species also need to be introduced.

Models and boundary conditions

Two main families of numerical models of gas discharges exist. In the simplest one [34, 112, 115–117], the chemical and ionization processes within the ion source are not modeled directly. Instead, the ionization region near the emitter is assumed to be an ion source providing a charge density $\rho_{c,e}$. The unipolar ion drift is then governed by Poisson's equation (Equation (1.15)) and conservation of charge (Equation (1.11)), which have to be solved simultaneously.

Dirichlet conditions can be set at the emitter and collector surfaces in the form of known potentials: φ_e at the emitter surface and φ_c at the collector surface. The applied voltage is defined as $V_a = \varphi_e - \varphi_c$. The conditions on the system's external boundaries depend on the specific problem that is being modeled. For example, Xu et al. [34] considered the case when the external boundaries were at a zero potential and showed that a leakage current from the emitter to the surroundings exists in that case. An additional boundary condition for the current density or the charge density is needed to close the system. For corona discharges, it is usually assumed that the

electric field at the emitter is equal to the one at corona ignition, as per Kaptsov's hypothesis [82]. This critical electric field at corona ignition can be estimated using Equation (1.8), derived by Peek [80], or a similar expression. The charge density at the emitter, $\rho_{c,e}$, can then be iterated until this condition is met. Alternatively, this additional condition may come in the form of a fixed current or current density (e.g., from experimental data) [118], or a fixed $\rho_{c,e}$.

In general, Equations (1.15) and (1.19) are dependent on the bulk fluid velocity. If it is assumed that the bulk fluid velocity is negligible compared to the ion drift velocity, the electrostatic equations are decoupled from the neutral fluid equations. Davis and Hoburg [112] provide an iterative numerical method to solve the electrostatic equations for corona discharges in this case. Once these equations are solved, the electrostatic body force distribution can be calculated and used to solve the fluid equations, in a one-way coupling [119]. The fluid and electrostatic equations can also be solved simultaneously in a two-way coupled system, albeit at higher computational cost [120].

A second family of numerical methods [108, 113, 121] may include chemical reactions and ionization events (such as electron avalanches) and model the evolution of individual species directly by solving a continuity equation of the form of Equation (1.20) for every relevant species coupled with Poisson's equation. These models do not require any assumptions on the charge density or electric field at the emitter; however, they introduce additional sets of partial differential equations that must be solved simultaneously. The boundary conditions used in these models are also more complex [122]. These models are inherently time-dependent, and to avoid a mathematically correct solution in which no discharges take place, they require the introduction of an arbitrary distribution of seeding electrons and ions for the discharge to start [108].

1.3.2 Fluid dynamics model

The Navier-Stokes equations govern the motion of the neutral fluid. If it is assumed that the fluid is incompressible (such as a liquid or a low-speed gas), these reduce to

conservation of mass and momentum, which can be formulated as

$$\nabla \cdot \vec{u} = 0 \tag{1.21}$$

$$\rho \frac{\mathrm{D}\vec{u}}{\mathrm{D}t} = -\nabla p + \mu_v \nabla^2 \vec{u} + \vec{f}, \tag{1.22}$$

where ρ is the mass density of the fluid, p is the static pressure, μ_v is the dynamic viscosity, and $\frac{D}{Dt}$ represents the total or material derivative. The coupling with the electrostatic model is introduced through the electrostatic body force $\vec{f}$. Using the Korteweg-Helmholtz formulation [123], the body force can be expressed as

$$\vec{f} = \rho_c \vec{E} - \frac{1}{2} E^2 \nabla \varepsilon + \frac{1}{2} \nabla \left[E^2 \left(\frac{\partial \varepsilon}{\partial \rho} \right)_T \rho \right]. \tag{1.23}$$

The first term in Equation (1.23) represents the Coulomb force; the second term is the polarization force, which acts on polarized charges; and the third term is the electrostriction force, which is only relevant in compressible fluids [124]. In an incompressible fluid with uniform permittivity, only the Coulomb force term is retained, such that $\vec{f} = \rho_c \vec{E}$.

1.3.3 Dimensional analysis of electrostatic and fluid models

An electrostatic model of a gas discharge with a unipolar ion-drift region can be made by combining Equations (1.15) (Poisson's equation) and (1.19) (conservation of charge). Following the analysis of Seyed-Yagoobi et al. [125], it is possible to define a non-dimensional potential φ', a non-dimensional charge density ρ', and a non-dimensional bulk fluid velocity $\vec{u}'$ such that

$$\varphi' \equiv \frac{\varphi}{\varphi_0} \tag{1.24}$$

$$\rho' \equiv \frac{\rho_c}{\rho_{c,0}} \tag{1.25}$$

$$\vec{u}' \equiv \frac{\vec{u}}{U_0}, \tag{1.26}$$

where φ_0 is some reference potential or potential difference (e.g., the applied DC voltage), $\rho_{c,0}$ is some reference charge density (e.g., the charge density at the emitter), and U_0 is some reference velocity (e.g., the freestream velocity). The spatial coordinates can be non-dimensionalized by a reference length L (e.g., the gap distance). A non-dimensional gradient operator, ∇', can be defined such that it fulfills $\nabla a = \frac{1}{L}\nabla' a$, where a is some scalar field. Using these non-dimensional variables, Equations (1.15) and (1.19) can be expressed in non-dimensional form as

$$\nabla'^2 \varphi' = -\bar{\rho}\rho' \tag{1.27}$$

$$\nabla'\rho' \cdot \left(\nabla'\varphi' - \bar{v}\vec{u}'\right) = \bar{\rho}\rho'^2, \tag{1.28}$$

where the non-dimensional term $\bar{\rho}$ is the electric source number [125] and $\bar{v}$ is known as the electric slip number [125] or the electric Reynolds number No. 3 [126]. They are defined as

$$\bar{\rho} \equiv \frac{L^2 \rho_{c,0}}{\varepsilon \varphi_0} \tag{1.29}$$

$$\bar{v} \equiv \frac{U_0 L}{\mu \varphi_0}. \tag{1.30}$$

A similar procedure can be applied to the incompressible Navier-Stokes equations, given by Equations (1.21) and (1.22). Using the same non-dimensionalization, the continuity equation becomes

$$\nabla' \cdot \vec{u}' = 0. \tag{1.31}$$

All the body force components in the conservation of momentum equation will be neglected except for the Coulomb force, such that $\vec{f} = \rho_c \vec{E}$. A dimensionless pressure, p', can also be defined as

$$p' \equiv \frac{p}{\rho U_0^2}, \tag{1.32}$$

and a dimensionless time, t', can be defined as

$$t' \equiv \frac{t}{L/U_0}. \tag{1.33}$$

The momentum equation can then be expressed in non-dimensional form as

$$\frac{\partial \vec{u}'}{\partial t'} + (\nabla' \cdot \vec{u}')\vec{u}' = -\nabla' p' + \frac{1}{\mathrm{Re}}\nabla'^2 \vec{u}' - M^2 \frac{\bar{\rho}}{\bar{v}^2}\rho' \nabla' \varphi', \tag{1.34}$$

where Re is the Reynolds number and M is the mobility ratio [126]. These are dimensionless quantities defined as

$$\mathrm{Re} \equiv \frac{\rho U_0 L}{\mu_v} \tag{1.35}$$

$$M \equiv \sqrt{\frac{\varepsilon}{\rho}}\frac{1}{\mu}. \tag{1.36}$$

This analysis shows that the coupled electrostatic and fluid dynamics system depends on four non-dimensional parameters: the electric source number $\bar{\rho}$, the electric slip number $\bar{v}$, the Reynolds number Re, and the mobility ratio M. The same conclusion can be reached using the Buckingham π theorem [127], as shown in Appendix A.

1.3.4 Thrust model

Consider the EAD thruster in Figure 1-3 with a single emitter and collector. If the Coulomb term is the only relevant body force, the force exerted by the electric field on the drift volume, $\vec{F}_E$, is

$$\vec{F}_E = \iiint_V \rho_c \vec{E} \mathrm{d}V, \tag{1.37}$$

where V is the volume in which the current is drifting. The reaction to this force acts on the EAD thruster itself: if $\vec{F_E}$ has a component in the positive x-direction, this reaction is experienced as a thrust force.

In general, the charge density and electric field distributions are not known. However, an expression for the thrust can be found using current tubes following the work of Gilmore and Barrett [36], under the assumption that the advective current can be neglected. Consider the current tube in Figure 1-3. Positive thrust is defined as acting in the negative x-direction. A differential thrust element dF_s is given by

$$\mathrm{d}F_s = -\rho_c \vec{E} \cdot (-\hat{x}) A \mathrm{d}s, \tag{1.38}$$

where $\hat{x}$ is the unit vector in the positive x-direction, A is the cross-sectional area of the current tube, and $\mathrm{d}s$ is a differential element along the current tube. The contribution to the thrust force from this tube, F_s, is given by

$$F_s = \int_{s_0}^{s_1} \rho_c \vec{E} \cdot \hat{x} A \mathrm{d}s, \tag{1.39}$$

where s_0 and s_1 are the start and end coordinates of the current tube along the s-direction.

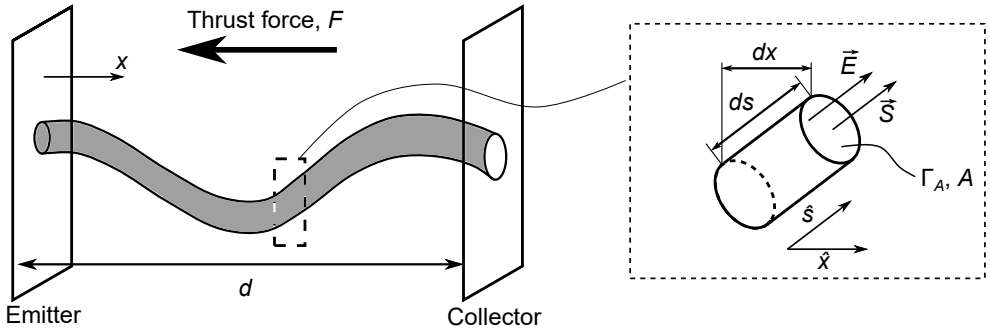

Figure 1-3: Schematic diagram showing a current tube going from an emitter to a collector. A positive electric field corresponding to positive ions in the drift region is shown.

Since the current tubes follow the electric field lines in the absence of a bulk flow, the electric field can be expressed as

$$\vec{E} = E\hat{s}, \tag{1.40}$$

where $\hat{s}$ is the unit vector in the positive s-direction and E can be positive or negative depending on the charge of the ions. From Equation (1.18), the current I_s in a current tube, which is constant by conservation of charge, is given by

$$I_s = \rho_c \mu \iint_{\Gamma_A} \vec{E} \cdot \mathrm{d}\vec{S} = \rho_c \mu E A, \tag{1.41}$$

where Γ_A is the surface that current is crossing and $\mathrm{d}\vec{S} = A\mathrm{d}\vec{s}$ was used.

Substituting this into Equation (1.39),

$$F_s = \int_{s_0}^{s_1} \frac{I_s}{\mu} \frac{\vec{E}}{E} \cdot \hat{x} \mathrm{d}s. \tag{1.42}$$

Since $\frac{\vec{E}}{E} = \hat{s}$ as the current tubes follow electric field lines and $\hat{s} \cdot \hat{x} \mathrm{d}s = \mathrm{d}x$, the integral in Equation (1.42) can be performed in the x-direction instead,

$$\begin{aligned} F_s &= I_s \int_{s_0}^{s_1} \frac{1}{\mu} \hat{s} \cdot \hat{x} \mathrm{d}s \\ &= I_s \int_{x_0}^{x_1} \frac{1}{\mu} \mathrm{d}x \\ &= \frac{I_s d}{\mu}, \end{aligned} \tag{1.43}$$

where x_0 and x_1 are the start and end coordinates of the current tube along the x-direction and $d = x_1 - x_0$ is the gap spacing. To reach the last expression, it was assumed that the mobility was constant. The total thrust F is found by adding the contributions from all the current tubes,

$$F = \frac{Id}{\mu}, \tag{1.44}$$

where I is the total current. Equation (1.44), which predicts a linear relationship between current and thrust, is supported by experiments on static EAD thrusters [34].

1.4 Thesis objectives and contributions

Even though it has been demonstrated that EAD thrusters are viable forms of propulsion for aircraft ranging from small blimps to 5-meter wingspan airplanes, their low thrust density (thrust per unit volume or frontal area) limits the practical applications of EAD devices. A great challenge in this regard is the requirement that both the power source and converter must be carried on board for any practical application of EAD propulsion. When the entire aircraft is designed with an aircraft design tool, these requirements translate to a required thrust level of the order of newtons. With

the thrust densities that have been demonstrated to date, these thrust levels can only be produced with large arrays of thrusters. For example, the aircraft demonstrated by Xu et al. [45] had a frontal area of approximately $1\,\mathrm{m}^2$ and a volume of approximately $0.5\,\mathrm{m}^3$. The main objective of this thesis is to identify strategies to increase the thrust density of EAD thrusters, potentially enabling more compact thrusters that can perform new missions. The two main technologies that have been investigated for this aim are decoupled EAD thrusters with wire-to-wire DBD ion sources and multistaged ducted EAD thrusters. In particular, the long-term goal for EAD propulsion envisioned in this thesis is practical vertical take-off and landing.

The secondary objective of this thesis is to reduce the power draw that is required to produce a given thrust (i.e., to improve the thrust-to-power ratio). In addition to potentially providing larger thrust density, whether multistaged ducted thrusters can deliver greater thrust-to-power ratios than conventional corona-discharge thrusters has also been investigated. This thesis also discusses strategies to mitigate reverse emission, a critical non-ideal effect that can significantly increase the power draw without contributing to thrust.

This thesis includes four contributions to the field of electroaerodynamic propulsion. All of these contributions are focused on improving the thrust density or efficiency of EAD thrusters.

1. Developing a model for the performance characteristics of decoupled thrusters. Decoupled thrusters using a wire-to-wire DBD ion source are an alternative to corona discharges in EAD propulsion. Compared to corona discharges, a decoupled EAD thruster can produce more thrust for a given voltage and geometry. However, the exact effects of electrical and geometric parameters on the performance of decoupled thrusters are not known. This study develops a model for the current–voltage characteristics of decoupled thrusters, accounting for the effects of applied DC voltage, gap spacing, and ion source parameters such as AC voltage and frequency.
2. A study on reverse emission in EAD thrusters. Reverse emission is a non-ideal effect in EAD thrusters that increases the power draw. However, the causes

and effects of reverse emission are not well understood, particularly regarding its impact on thrust. In this study, experiments on reverse emission are performed, exploring its effects on thrust, power and noise, and identifying practical strategies to mitigate it.

3. Theory of multistaged ducted electroaerodynamic thrusters. EAD theory predicts that the maximum static pressure rise that can be produced by a quasi-one-dimensional set of electrodes, such as two parallel meshes or a set of parallel emitters and collectors, is approximately independent of the gap spacing. Hence, serial stages with low gap spacing can provide a high pressure rise (and thrust) while occupying small volume. This study presents multistaged ducted (MSD) thrusters as a way to increase the thrust density or thrust-to-power ratio of EAD thrusters. In an MSD thruster, multiple stages of EAD emitters and collectors are arranged in series. The stages are surrounded by a duct, which also contributes to thrust in a manner similar to ducted fans. This study leverages existing one-dimensional EAD and aerodynamic models to show that MSD thrusters can provide order-of-magnitude improvements in thrust density compared to single-stage or unducted thrusters.
4. Experiments in multistaged ducted electroaerodynamic thrusters. Through EAD theory, it can be shown that MSD thrusters can provide order-of-magnitude improvements in thrust density. This work is an experimental validation of the theoretical predictions on MSD thruster performance. Each stage in these thrusters contains several sets of wire emitters and airfoil or flat-plate collectors, with corona discharges acting as the ion source. Both single-stage and multistage tests with up to 10 stages are conducted. Through these, the effects of geometric parameters (such as parallel electrode separation or gap spacing), number of stages, and duct design on MSD thruster performance are explored.

This page intentionally left blank.

Chapter 2

Performance of decoupled EAD thrusters

2.1 Publication and collaboration statement

The experiments and experimental setup were designed by Haofeng Xu and the author. The experimental setup was constructed by Haofeng Xu and the author. The UROP student James Abel manufactured the airfoil-shaped collector. The author conducted all experiments with the assistance of Haofeng Xu. The relationship between thrust-to-power ratio and gap distance was analyzed by the author along with Haofeng Xu. The author conducted all the remaining data analysis.

This chapter was published previously in N. Gomez-Vega et al. "Performance of decoupled electroaerodynamic thrusters." *Applied Physics Letters* 118.7 (2021): 074101 [128].

2.2 Introduction

In 2018, Xu et al. [45] demonstrated the feasibility of EAD for heavier-than-air flight by flying a solid-state airplane; however, the overall efficiency of the propulsion system was 2.5 %, approximately one order of magnitude lower than that of conventional propulsion. This aircraft used corona-discharge EAD thrusters, which apply a DC

voltage that both ionizes neutral air molecules and accelerates those ions to produce thrust. As noted in Section 1.1, corona discharges are the prevailing ion source for EAD thrusters [29, 30, 35, 46, 129]. In 2019, the author's research group proposed an EAD architecture that uses an independent ion source that is "decoupled" from the DC acceleration stage. It was demonstrated that an implementation of a decoupled thruster that used an AC dielectric barrier discharge ion source could provide a significantly higher thrust for the same power consumption (including the ion source power draw) than the equivalent corona discharge thruster [42]. This results in a higher thrust-to-power ratio, suggesting that decoupled thrusters could increase the endurance and mission capability of solid-state aircraft. Alternative decoupled architectures have also been proposed; for example, Colas et al. [41] separated ion generation and acceleration in a corona discharge via auxiliary electrodes and Orrière et al. [106] recently studied a decoupled EAD device with a nanosecond-repetitively-pulsed-discharge ion source.

A model for the performance (i.e., current, thrust, and power draw) of decoupled EAD thrusters has not been determined before, although previous work found qualitative differences compared to corona-discharge thrusters [42]. The results presented here support a quantitative characterization of decoupled thrusters with a DBD ion source which captures the effect of both DC acceleration parameters such as DC voltage and electrode gap spacing as well as AC ionization parameters such as AC voltage, AC frequency, and DBD electrode separation. In particular, a model for the interaction between the ionization stage and the acceleration stage is developed; this interaction is not relevant in corona-discharge thrusters, in which the ionization cannot be varied independently from the acceleration. This model can enable the design and optimization of decoupled EAD devices for aircraft propulsion. The same model could also be used to design decoupled EAD devices for other EAD applications such as flow control [53, 130, 131], heat transfer enhancement [132–134], and fluid pumping [15, 17, 19, 20], all of which could benefit in efficiency from a decoupled EAD architecture.

The net thrust force, F_N, produced by an EAD thruster in static air is the in-

tegral of the Coulomb force acting on the ions in the drift region between the two electrodes [36] minus the aerodynamic drag, i.e.,

$$F_N = \frac{Id}{\mu} - F_D, \tag{2.1}$$

where I is the DC drift current, μ is the ion mobility, and F_D is the aerodynamic drag force acting on the electrodes. The drift current is a function of the geometry (i.e., electrode design and gap spacing, d) and of the applied DC voltage: the relationship between current and voltage is known as the current–voltage characteristic. Even though Equation (2.1) applies to corona discharge and decoupled thrusters alike, these have different current–voltage characteristics.

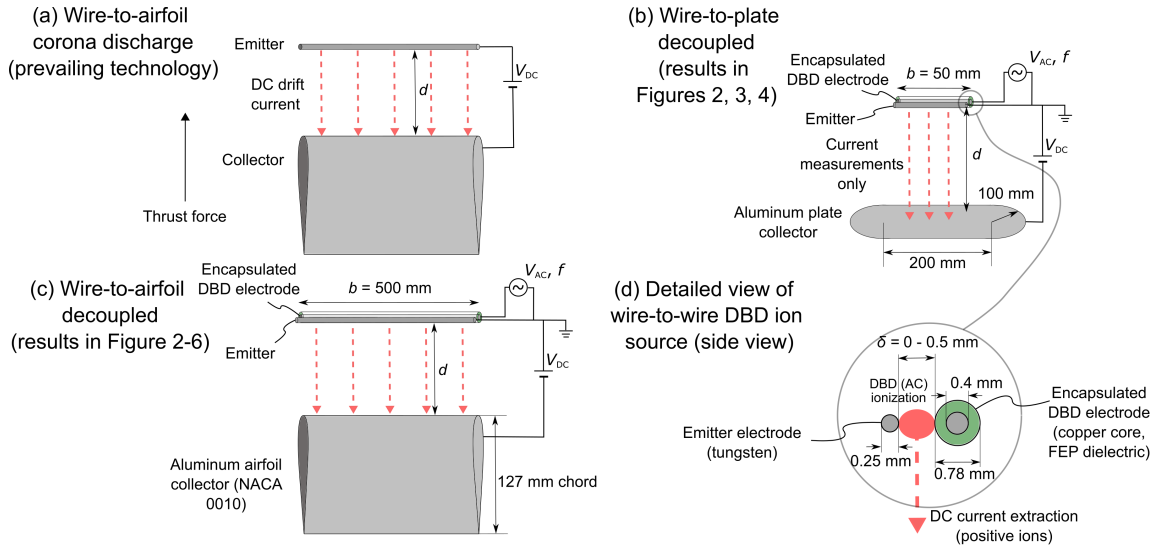

Figure 2-1: (a) Schematic of a corona discharge EAD architecture, which is the prevailing technology that uses a single DC voltage for both ionization and thrust production (not tested here). (b) shows a decoupled EAD device with a wire-to-wire DBD ion source, which uses an AC voltage to ionize and a DC voltage to produce thrust. This setup was used to determine the current–voltage characteristics as a function of both DC parameters: V_{DC} and d; and DBD parameters: V_{AC}, f and δ. This "benchtop" setup allowed the spacing δ between the exposed and the encapsulated electrodes to be varied, but direct thrust measurements were not possible. (c) depicts a "thrust-stand" decoupled EAD device with a wire-to-wire DBD ion source and a low-drag collector shape. In this setup, thrust measurements are possible, but δ was fixed at 0 mm. (d) shows a detailed view of the ion source.

The current–voltage characteristics of a corona discharge for a wire-to-cylinder

electrode geometry, where a thin wire is the emitter and a larger cylinder is the collector, are [33, 84]

$$I_c = C_0 \varepsilon \mu \frac{V_{\mathrm{DC}} \left(V_{\mathrm{DC}} - V_0 \right)}{d^2} b, \tag{2.2}$$

where I_c is the current, V_{DC} is the applied DC voltage, and C_0 is some non-dimensional function of electrode geometry and polarity. The corona inception voltage, V_0, is the threshold for ion (and hence thrust) production.

The electric current produced by a corona discharge is below the space-charge limited current, which represents the maximum DC current for a given geometry and applied DC voltage. Xu et al. [42], who demonstrated that decoupled thrusters could improve the performance of EAD thrusters, suggested that in a decoupled thruster, the current-voltage relationship would not be given by Equation (2.2). It was reported that the current–voltage characteristics were qualitatively consistent with the one-dimensional Mott-Gurney law, which governs the space-charge limited drift current density between two infinite parallel plates [135], i.e.,

$$\frac{I_{\mathrm{MG}}}{A} = \frac{9}{8} \varepsilon \mu \frac{V_{\mathrm{DC}}^2}{d^3}, \tag{2.3}$$

where I_{MG} is the current and A is the cross-sectional area. For a decoupled thruster, the current–voltage characteristics, as well as depending on geometry, also depend on the parameters of the DBD ion source; the explicit form of the relationship of current with voltage and DBD parameters has not been previously determined.

2.3 Methods

In this study, two types of experiments were performed. In the first, a wire-to-plate discharge geometry (shown schematically in Figure 2-1b) was used to identify the detailed current–voltage characteristics of the thruster. This setup allowed the variation of the DC gap distance, d, and the DBD wire separation, δ. A high-voltage AC was applied between the encapsulated electrode and the emitter (or exposed electrode). The encapsulated electrode was a 0.78 mm diameter wire with a copper core of diameter

0.32 mm and a uniform fluorinated ethylene propylene (FEP) coating. The exposed electrode, which was connected to ground, was a 0.254 mm diameter tungsten wire. Tests were performed in a 50 mm section of the DBD mounted on four polyoxymethylene (POM) pillars, similar to the setup in Xu et al. [136]. The encapsulated electrode had an effective length of 100 mm and the exposed electrode had a length of 50 mm. The spacing between the DBD wires (δ) was varied with two Thorlabs PT1/M linear translation stages controlled with depth micrometers, on which two of the supporting pillars were mounted. The AC voltage was a sinusoidal signal produced with an Agilent 33220A waveform generator and amplified 1000 times through a Trek 5/80 HS power amplifier. A flat aluminum collector of discorectangular (oblong) shape, with semicircular radius of 100 mm and straight side length of 200 mm, was placed at a variable gap distance d from the DBD wires. A Matsusada AU-120N2.5 power supply was used to bias the collector to a negative potential with respect to ground. Current readings were obtained directly from the DC power supply. A photograph of the current-measurement setup is shown in Figure 2-2a. Determining the current scaling allows the prediction of the thrust (from Equation (2.1)) and of the power consumed in the acceleration of ions. The power drawn by the DBD was calculated using the method in Manley [92], as described in the author's study of wire-to-wire DBD ion sources [136]. Further details on the power draw calculation can be found in Appendix B.

In the second type of experiment, the wire-to-airfoil geometry shown in Figure 2-1c was used to measure the thrust produced by the thruster and confirm that the measured thrust is consistent with the predicted thrust implied by the current–voltage characteristics. The thrust was measured directly by suspending the device from a Sartorius Entris 4202 balance with 10 mg resolution. The thruster was a rectangular glass fiber reinforced polymer (GFRP) frame which held the DBD electrodes and the collector. The same FEP encapsulated electrode and a 0.32 mm diameter steel exposed electrode were used. The two electrodes were adjacent, at a distance $\delta = 0$ mm. The collector was a NACA 0010 aluminum airfoil with 127 mm chord, and it was biased to a negative potential using a Matsusada AU-120N2.5 power supply, as in the

benchtop experiment. The airfoil collector reduces aerodynamic drag (the second term in Equation (2.1)). Figure 2-2b shows a photograph of the thrust-measurement setup.

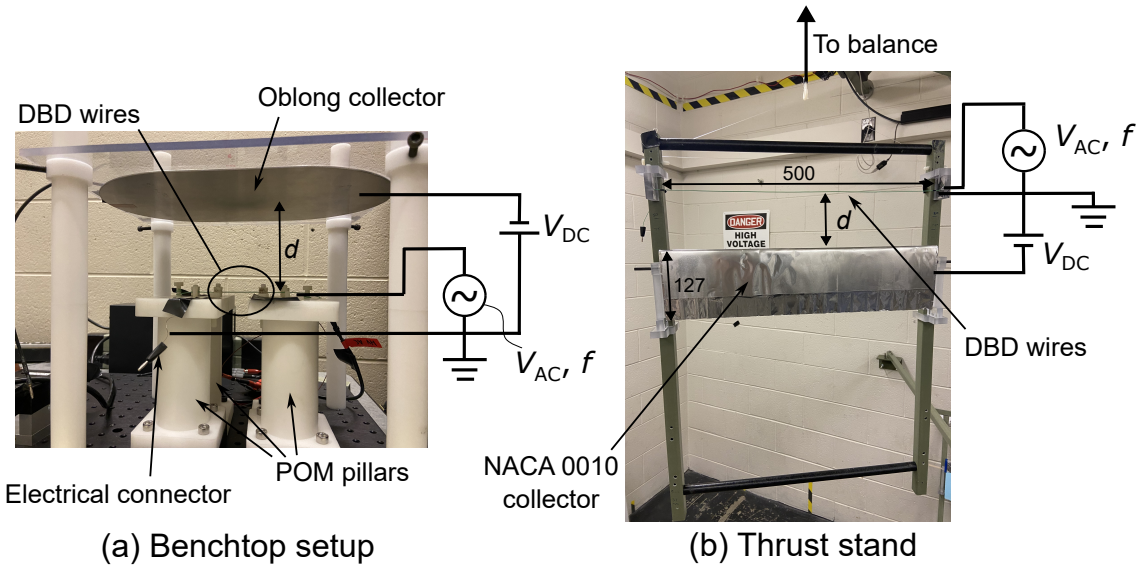

Figure 2-2: Photographs of the experimental setup used in the benchtop and thrust measurement tests. Dimensions in mm.

2.4 Results

Figure 2-3a shows the current–voltage characteristics of the decoupled thruster with fixed DBD ionization parameters (i.e., a fixed DBD power level and DBD wire separation, δ). In this figure, the current has been normalized by the emitter span, b. The current increases quadratically with the applied voltage according to $I/b = f(d)V_{\mathrm{DC}}^2$: this is consistent with the Mott-Gurney law in Equation (2.3). The fit parameter $f(d)$ varies according to $f(d) \propto 1/d^2$. The observed scaling with the gap spacing is the same as that in Equation (2.2) for corona discharges, but different from that in the Mott-Gurney law (Equation (2.3)). The one-dimensional Mott-Gurney law, applicable to the discharge between infinite parallel plates, does not accurately describe the wire-to-plate geometry used here. A two-dimensional model derived by Geurst [137] for the analytical space-charge limited current in a thin (in the transverse direction)

collisional slab of length d is

$$I_{\text{Geurst}} = \frac{2}{\pi}\varepsilon\mu\frac{V_{\text{DC}}^2}{d^2}b, \tag{2.4}$$

where I_{Geurst} is the current and b is the span of the slab. Similar expressions with different coefficients have been derived for other boundary conditions [138]. The current–voltage characteristics of the decoupled thruster take the same functional form as the model in Equation (2.4). Figure 2-3b shows the extracted current plotted against I_{Geurst}, where a mobility $\mu = 2.0 \times 10^{-4}\,\text{m}^2\text{V}^{-1}\text{s}^{-1}$ (inferred from thrust measurements, which are shown later in Figure 2-6) was used. This mobility is within the range of reported ion mobilities for air [139]. The measured DC current is proportional to that predicted by I_{Geurst} with a proportionality constant of 1.54. This proportionality constant is dependent on the DBD characteristics (see Figure 2-5); Figure B-2 in Appendix B shows that the proportionality holds at a lower DBD power level.

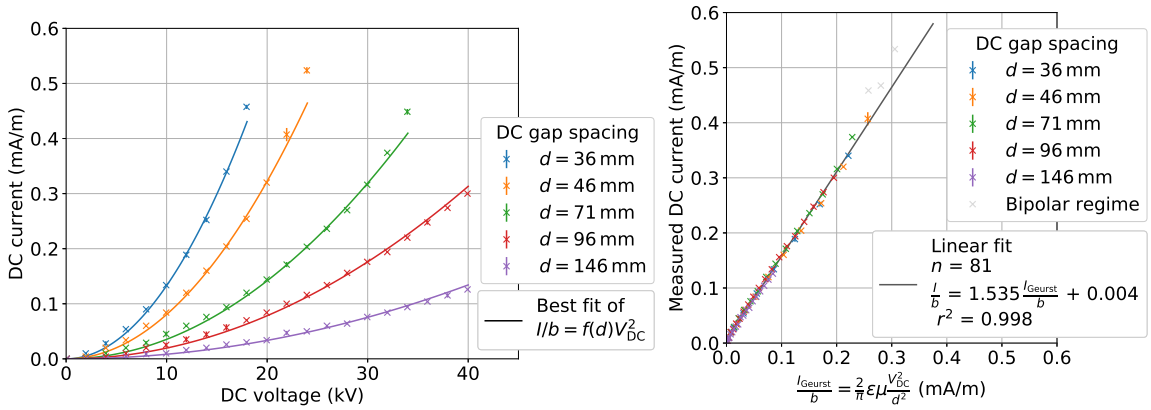

(a) Current–voltage characteristics

(b) Current against I_{Geurst}

Figure 2-3: Effect of the DC voltage and gap spacing on the current extracted at the flat collector. The spacing between the DBD electrodes was $\delta = 0.25\,\text{mm}$. An AC signal with peak-to-peak voltage $V_{\text{AC}} = 7\,\text{kV}$ at frequency $f = 10\,\text{kHz}$ was applied to the encapsulated electrode. The power drawn by the DBD was $P_{\text{DBD}}/b = 14\,\text{W}\,\text{m}^{-1}$. Error bars represent a 95 % confidence interval.

The $d = 36\,\text{mm}$, $d = 46\,\text{mm}$, and $d = 71\,\text{mm}$ results in Figure 2-3 show deviations from the quadratic trend at the highest voltages tested. This is attributed to the onset

of reverse emission, which increases the current but does not contribute to thrust. This reverse emission has been observed in tests with corona discharge thrusters [34, 35] and is the focus of Chapter 3. In Figure 2-3b, this is labeled as the "bipolar regime" due to the presence of both positive and negative species between the emitter and collector.

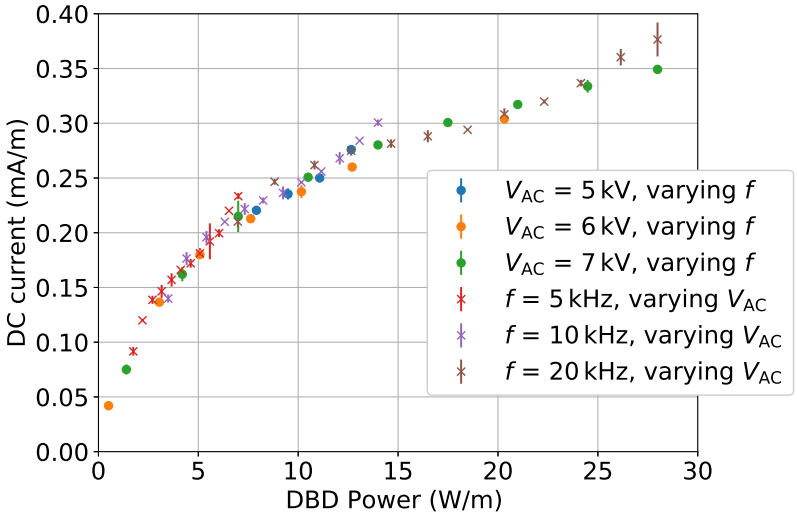

Figure 2-4: DC current versus the power drawn by the DBD ion source with fixed DC gap spacing ($d = 46\,\text{mm}$) and fixed DC voltage ($V_{DC} = 20\,\text{kV}$). The DBD power was varied by changing the AC voltage and AC frequency (see legend). The separation between the DBD wires was $\delta = 0.25\,\text{mm}$. Error bars represent a 95 % confidence interval.

The results in Figure 2-3 were obtained at a constant DBD power level. Figure 2-4 shows the effect of changing the DBD parameters. The AC voltage applied to the DBD was varied over the range $4 \leq V_{AC} \leq 7\,\text{kV}$ peak-to-peak, and the frequency, over the range $0.5 \leq f \leq 20\,\text{kHz}$. The DC drift current for fixed DC parameters (δ and V_{DC}) and geometry is found to be a function of the DBD power only and does not depend separately on the AC voltage or frequency.

In Figure 2-4, the current increases monotonically with the DBD power. However, there are two different regimes: an initial sharp rise in current with DBD power, followed by a saturation at around $P_{DBD}/b = 10\,\text{W m}^{-1}$. In the saturation regime, relatively large increases in DBD power are needed to produce substantial changes in current. Xu et al. [42], who used circular cylinders as collectors, identified this

saturation regime as a "space-charge limited" regime. This more detailed study with a planar collector shows that even at the highest powers tested, the DC current continues increasing with the DBD power, showing that a strict space-charge *limit* has not been reached in the range of DBD powers tested here. With EAD devices usually being power-limited, the results in Figure 2-4 show an opportunity for optimization at low DBD power levels depending on the application: an optimal point may be found that results in sufficient current draw at a low DBD power draw.

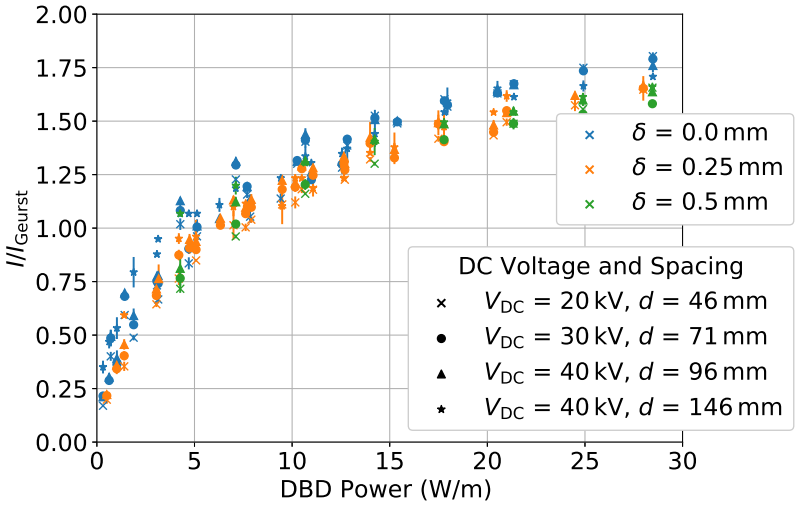

Figure 2-5: Extracted current against the power drawn by the DBD source, at different combinations of DBD wire separation δ, DC voltage V_{DC} and gap spacing d. Error bars represent a 95 % confidence interval.

The complete relationship between the ion production and acceleration stages, where both DBD and DC acceleration parameters are varied, is shown in Figure 2-5. The current has been non-dimensionalized by the I_{Geurst} corresponding to the d and V_{DC} tested. In addition, the DBD wire separation, δ, is also varied. The results show normalization by I_{Geurst} results in a convergence into a single band of normalized current versus DBD power. A dependency on the DBD wire separation is observed, with the current measured at $\delta = 0.0\,\text{mm}$ at any given DBD power being higher than those at larger DBD wire separations, although this difference is less than 10 % at higher DBD powers.

The results in Figures 2-3 to 2-5 show that an appropriate model for the current–

voltage characteristics is

$$I = \zeta\left(\frac{P_{\mathrm{DBD}}}{b}\right) I_{\mathrm{Geurst}} = \zeta\left(\frac{P_{\mathrm{DBD}}}{b}\right)\frac{2}{\pi}\varepsilon\mu\frac{V_{\mathrm{DC}}^2}{d^2}b, \tag{2.5}$$

where ζ is a function of the DBD power per unit span, $\frac{P_{\mathrm{DBD}}}{b}$; and the DBD wire separation, δ. The coefficient ζ is also expected to be a function of electrode geometry, but this dependency was not tested here. Figure 2-5 shows the experimentally-measured dependency of ζ on P_{DBD}/b. A functional fit that ignores the dependency on δ and provides a correlation coefficient of $r^2 = 0.944$ to the data in Figure 2-5 is

$$\zeta \approx \frac{AP_{\mathrm{DBD}}/b}{P_{\mathrm{DBD}}/b + B}, \tag{2.6}$$

where $A = 1.88$ and $B = 4.66\,\mathrm{W\,m^{-1}}$. Equation (2.5) assumes a linear relationship between current and ion mobility that was not explicitly tested here (all experiments were performed in air at room temperature and pressure, where the mobility is approximately constant [46]), although a theoretical argument for this is provided in Appendix B.

Using Equation (2.1) and ignoring the drag force, the thrust force corresponding to the current would be

$$F_N = \frac{Id}{\mu} = \zeta\frac{2}{\pi}\varepsilon\frac{V_{\mathrm{DC}}^2}{d}b. \tag{2.7}$$

The thrust-to-power ratio is

$$\frac{F_N}{P} = \frac{\frac{Id}{\mu}}{P_{\mathrm{DBD}} + V_{\mathrm{DC}}I} = \frac{1}{\mu}\frac{d}{\frac{P_{\mathrm{DBD}}}{I} + V_{\mathrm{DC}}} \approx \sqrt{\frac{2\varepsilon\zeta}{\pi\mu^2}}\sqrt{\frac{d}{F_N/b}}, \tag{2.8}$$

where $V_{\mathrm{DC}}\,I$ is the power consumed in the ion acceleration stage. To reach the right-hand expression, it was assumed that the applied DC voltage is large compared to the ratio P_{DBD}/I, as is the case if operating at high V_{DC} and low P_{DBD}. A trade-off between thrust and thrust-to-power ratio is seen in Equation (2.8). The expression also predicts that larger gap spacings should provide higher thrust-to-power ratio for a given thrust per unit span, in a similar manner to corona-based thrusters [33, 34].

This thrust-to-power scaling is confirmed by the thrust and current results in this study, which are shown in Figure B-4 in Appendix B.

Thrust measurement tests using the setup in Figure 2-2b with an airfoil collector validate the thrust predictions of Equation (2.7). The thrust–voltage characteristics at constant DBD power level are shown in Figure 2-6a. Similarly to the DC current in Figure 2-3, a quadratic scaling with the DC voltage of the form $F_N/b = g(d)V_{\mathrm{DC}}^2$ is observed, where $g(d)$ is some function of the gap spacing. Figure 2-6b shows how this fit parameter $g(d)$ changes with the gap spacing. The fit parameter, and hence the thrust, is approximately inversely proportional to the gap spacing, i.e., $F_N \propto g(d) \propto 1/d$. Figure B-3 in Appendix B shows that the thrust also increases with the DBD power in a manner analogous to the current; and Figure B-5 shows that the scaling in Equation (2.7) is also consistent with the data in Xu et al. [42].

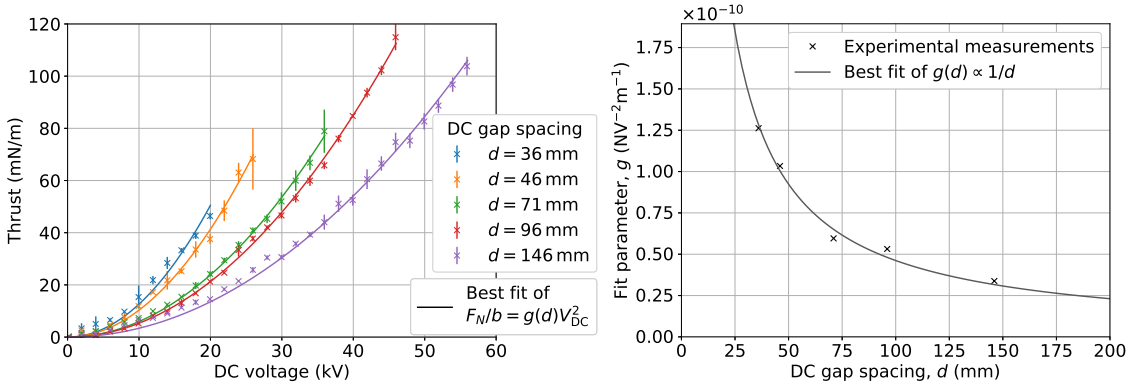

(a) Thrust–voltage characteristics

(b) Fit parameter against DC gap spacing

Figure 2-6: Thrust–voltage characteristics of a decoupled EAD thruster with a NACA 0010 airfoil collector. The DBD wire spacing was $\delta = 0.0\,\mathrm{mm}$ and the AC signal had $V_{\mathrm{AC}} = 7\,\mathrm{kV}$, $f = 3\,\mathrm{kHz}$. The power consumed by the DBD was $P_{\mathrm{DBD}}/b = 3.7\,\mathrm{W\,m^{-1}}$. Error bars represent a 95 % confidence interval.

The magnitude of the thrust results in Figure 2-6a is comparable to that achievable with corona discharges [33–35], although the experimental data in Xu et al. [42] shows that decoupled thrusters can provide a higher thrust-to-power ratio for the same power consumption than corona-discharge thrusters in some operating points. Higher thrust forces than measured here could be achieved by increasing the DC voltage at a fixed

gap spacing, although this would be subject to the limits of electrical sparking at higher voltages; these limits are not evaluated here. The decoupled architecture offers several other potential advantages: the magnitude of the thrust can be controlled independently of the DC parameters by varying the DBD power; decoupled thrusters can produce thrust at lower DC voltages than corona discharge thrusters, since the applied voltage does not need to be above the corona inception voltage, V_0; and the performance of decoupled thrusters may not be as adversely affected by series and parallel staging of multiple sets of electrodes as was observed in corona thrusters [36].

2.5 Conclusions

The performance of a decoupled EAD thruster with a wire-to-wire DBD ion source as a function of the main electrical and geometric parameters has been characterized. The results suggest that the scaling of the current with the DC parameters takes the same form as the classical space-charge limited current in a thin ion slab. Current extraction was found to depend primarily on the power drawn by the DBD, instead of on the AC ionization parameters independently. These results show that increasing the DBD power provides more current and thrust; however, this occurs with diminishing returns, suggesting that there is an application-dependent optimum operating point. From these results, empirical models for the thrust, current, and power draw of the device have been derived and validated. These models, which represent the first complete characterization of the performance of a decoupled EAD thruster, could be generalized to other decoupled architectures with a different ion source.

While this analysis has been performed in the context of thrust production, these decoupled devices could be used in other areas such as pumping or flow control due to their increased thrust-to-power ratio and, hence, efficiency. The models derived here provide the means for the design and optimization of these solid-state aerodynamic applications.

Chapter 3

Mitigating reverse emission in EAD thrusters

3.1 Publication and collaboration statement

The author designed the experiments and the experimental setup, which was constructed along with the UROP student Jayaprakash Kambhampaty. The author conducted all experiments with the assistance of Jayaprakash Kambhampaty. The author conducted all the data analysis.

This chapter was published previously in N. Gomez-Vega et al. "Mitigating reverse emission in electroaerodynamic thrusters". *Journal of Physics D: Applied Physics* 55.50 (2022):505202 [140].

3.2 Introduction

Previous work from the author's group identified two main types of non-ideal effects that can arise when performing experiments on EAD in a laboratory setting: "leakage current" and "reverse emission" [34]. Leakage current occurs when ions travel from the emitter to the grounded surroundings instead of the collector. The experimental and simulated data in Xu et al. [34] shows that the net effect of leakage current is to increase the power draw of EAD devices without contributing to thrust. Xu et al.

[34] showed that leakage current can be mitigated by changing the electric potential of the emitter and collector with respect to the surroundings.

Reverse emission, also referred to as "backdischarge" [35], is a non-ideal effect associated with the collector geometry. Monrolin et al. [35] argued that reverse emission occurs when the electric field at some location in the collector becomes large enough to cause dielectric breakdown of the air: in their particular wire-to-cylinder geometry, they stated (but did not show) that it occurred mostly at the two ends of the collector. They also reported that reverse emission makes the current unsteady and produces audible noise. Monrolin et al. [35] suggested that reverse emission can be mitigated by weakening the electric field at the tips of the cylindrical collector, for example, by using collectors of larger diameter.

Other studies have also noted the presence of reverse emission, attributing it to a corona discharge at the collector [32, 34] or to streamer discharges [141]. In Xu et al. [34], the author's group showed that reverse emission causes deviations from the predictions of EAD theory: in particular, more power is required to produce a given thrust than predicted by theory. It was shown that these deviations from theory could be mitigated by using collectors of larger diameter, improving the thrust-to-power ratio by up to a factor of two for a given voltage.

Whereas it has been reported that reverse emission increases current (and hence power draw) at a given voltage [32, 34–36, 141], the effect on thrust is not as clear: Masuyama and Barrett [32] and Xu et al. [34] argue that reverse emission results in reduced thrust as compared to if it were absent, while Monrolin et al. [35] state that it does not affect thrust. Lemetayer et al. [141] report that they did not observe an increase in thrust corresponding to the increase in current due to reverse emission; they attribute the absence of a thrust increase to the effect of a reverse ionic wind from a reverse corona discharge. To the best of the author's knowledge, no study comparing the thrust–voltage characteristics with and without reverse emission had been conducted prior to this work.

"Back corona discharge" is a similar phenomenon to reverse emission that has been widely reported in electrostatic precipitation [59, 142–144]. Back corona discharge in

electrostatic precipitators is ignited after a high-resistivity dust layer is deposited on the collector: the predominant explanation for back corona discharge is that it is initiated when the electric field across this dust layer is large enough to cause electrical breakdown in the layer [59, 144]. The net effect of back corona discharge is to increase the current (and hence power draw) of electrostatic precipitators [143, 144]. Unlike reverse emission in EAD thrusters, back corona discharge in electrostatic precipitators requires the formation of a dust layer on the collector, and it may only be initiated after minutes or hours of operation [144].

Due to its significant impact on efficiency, understanding and mitigating reverse emission is critical for practical applications of EAD thrusters. In this study, experiments on wire-to-cylinder EAD thrusters with either corona discharge or wire-to-wire DBD ion sources were performed. The results show that reverse emission can occur if the ends of the cylinder are open. Three different strategies to mitigate reverse emission are considered: increasing the collector diameter, increasing the collector span, and using hemispherical end caps. Ultraviolet (UV) photography is also used to identify the locations on the collector where reverse emission is being ignited, and acoustic tests are performed with and without reverse emission mitigation to explore its effect on the thruster's acoustic signature.

3.3 Methods

Experiments with wire-to-cylinder EAD thrusters were performed, in which either a thin wire (corona discharges) or a wire pair (decoupled thrusters) acted as the emitter, and the cylinder was the collector. The electrode pair was supported by a rectangular glass-fiber reinforced plastic (GFRP) frame, as shown in Figure 3-1.

The collectors were hollow aluminum cylinders with a wall thickness of 1.1 mm. Cylinders with either 12.7, 19.1, 25.4, or 38.1 mm diameter and a span (length), b_c, of 510 mm were tested. Collectors with 19.1 mm diameter and a span of 750 mm and 1000 mm were also tested. An additional collector with a 19.1 mm diameter was fitted with two hemispherical end caps at its two tips, and its cylindrical section had a span

of $b_c = 510\,\text{mm}$ (total span of 529 mm); in all other cases, the cylinder's ends were open. Two acrylic plastic holders were used to mount the collectors to the frame; the collectors were secured to these holders with thin strips of mounting tape that were attached to the collector on the side most distant from the emitter (see Figure 3-1).

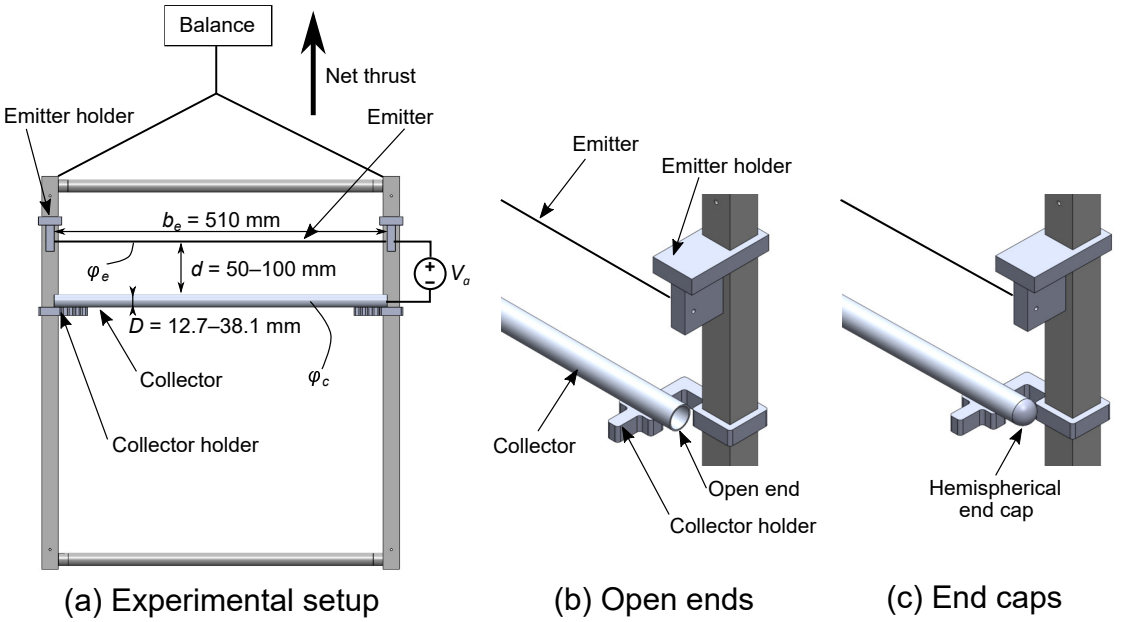

Figure 3-1: Schematic diagrams of the experimental setup. (a) Frontal view of the thruster frame with relevant geometric and electrical parameters; (b) isometric view of the frame's side showing a collector with open ends; and (c) isometric view of the frame's side showing a collector with hemispherical end caps.

In the corona-discharge tests, the emitter was a 0.127 mm diameter tungsten wire with a $b_e = 510\,\text{mm}$ span, selected for its resistance to sputtering and corrosion [145]. Two DC power supplies were used: a Matsusada AU-120P2.5 positive supply and a Matsusada AU-120N2.5 negative power supply. In the positive corona tests, the emitter was connected to the output of the positive power supply and biased to a potential $\varphi_e = +0.5V_a$ with respect to ground, where φ_e is the emitter potential and V_a is the applied voltage; whereas the collector was connected to the output of the negative power supply and was biased to a potential $\varphi_c = -0.5V_a$. In the negative corona tests, the opposite polarities were used; i.e., the emitter was biased to $\varphi_e = -0.5|V_a|$ and the collector was biased to $\varphi_c = +0.5|V_a|$. These "differential" polarity modes were shown by Xu et al. [34] to minimize leakage current to the

surroundings: leakage current accounted for less than 2 % of the total current in the cases shown in this study, with an average of 0.5 %.

In the decoupled thruster tests, the emitter consisted of a set of two adjacent wires with $b_e = 510\,\text{mm}$ span: a 0.32 mm diameter exposed steel wire and an encapsulated wire with a uniform fluorinated ethylene propylene (FEP) coating with 0.78 mm overall diameter and a copper core of diameter 0.32 mm. The exposed steel wire was connected to ground, while a high-voltage AC was applied to the encapsulated wire. The AC sinusoidal signal was produced by an Agilent 33220A waveform generator and amplified 1000 times by a Trek 5/80 HS power amplifier, whose output was connected to the encapsulated wire. A constant AC with peak-to-peak voltage $V_{pp} = 7\,\text{kV}$ and frequency $f = 3\,\text{kHz}$ was used in all tests with DBDs. The collectors were connected to the output of the Matsusada AU-120N2.5 negative power supply and biased to a potential $\varphi_c = -V_a$. In the absence of non-ideal effects, this electrical configuration results in a unipolar drift of positive ions only.

Experiments were conducted indoors in an experimental space 3 m wide by 2.5 m long. The frame supporting the emitter and collector was hanged from a Sartorius Entris 4202 balance with a resolution of 10 mg, which was supported by a cantilevered GFRP structure at a height of 2.5 m above ground. The thrust force was estimated through the change in weight measured by the balance. DC current was measured directly by the DC power supplies. In each test, the DC voltage was increased gradually in increments of 2 kV, and a constant DC voltage was maintained for 15 s before proceeding to the next voltage setting. The thrust and DC current were digitally sampled at a rate of 1.5 Hz. The mean and standard deviation of the data were calculated over the last 10 s of the 15 s data-recording interval. A 95 % confidence interval was calculated for each point, and it was taken to be 1.96 times the standard deviation. Temperature and relative humidity were also recorded in each test with an Omega HH311 probe. Tests with positive coronas were done at a temperature in the range 22–24 °C and with relative humidity in the range of 10 %–12 %. Tests with decoupled thrusters were done at a temperature of 21 °C and with relative humidity in the range of 33 %–54 %.

UV photography was used to identify regions in the collector where gas discharges were occurring. Photographs were taken with a modified Canon T1i camera with an internal UV band-pass filter sensitive in the 350–400 nm range, located approximately 1 m away from the EAD setup. The exposure time was 30 s. For the first 5 s of exposure, light produced by fluorescent lamps (which also emit light in the UV spectrum) was shone on the frame so that the background could be visualized; these were subsequently turned off for the remaining 25 s of exposure. The sharpness and brightness of images were then digitally enhanced to aid visualization. UV photographs were only taken for some voltage and gap spacing set points to reduce the experimental time and ensure that all experiments could be completed with similar ambient conditions.

The noise signature of the EAD devices was found to change after the onset of reverse emission. To study this change in noise, the acoustic waveform was sampled with a Behringer ECM8000 ultra-linear condenser microphone at a rate of 44.1 kHz and with a bit depth of 16 bits. The microphone was placed approximately 2 m away from the EAD setup. Audio samples with a duration of 10 s were recorded. A fast Fourier transform was applied to a 5 s portion of these samples; this was used to compute the power spectral density, which was then smoothed through an energy-preserving moving average filter.

3.4 Results

The results section is organized as follows. In Section 3.4.1, three different strategies to mitigate reverse emission are tested: increasing the collector diameter, increasing the collector span, and using hemispherical end caps. Section 3.4.2 explores whether reverse emission affects thrust. Sections 3.4.1 and 3.4.2 contain results obtained with positive corona discharges; qualitatively similar results were obtained with negative coronas, and these are included in Appendix C. In Section 3.4.3, it is shown that reverse emission is not a phenomenon limited to corona discharges and that it can also occur in a qualitatively similar manner with decoupled thrusters. In Section 3.4.4, UV photography is used to identify the locations in the collector where reverse emission

is occurring. Finally, the effects of reverse emission and the mitigation techniques on the acoustic signature of the thruster are explored in Section 3.4.5.

3.4.1 Mitigating reverse emission: collector diameter, span, and end caps

As discussed in Section 1.2.2, a commonly-used semi-empirical formula for the current draw of wire-to-cylinder corona discharges as a function of voltage (the current–voltage characteristic) is [33, 35]

$$I = \begin{cases} 0 & \text{if } |V_a| < |V_0| \\ C_0 \varepsilon \mu \frac{V_a(V_a - V_0)}{d^2} b_e & \text{if } |V_a| \geq |V_0| \end{cases}. \tag{3.1}$$

As shown in Chapter 2, decoupled thrusters have different current–voltage characteristics; this will be discussed in Section 3.4.3.

The net thrust, F_N, produced by the thruster in stagnant air is equal to the integral of the Coulomb force acting on the ions in the gap minus the aerodynamic drag force [36]

$$F_N = \frac{Id}{\mu} - F_D, \tag{3.2}$$

where F_D is the drag acting on the electrodes. Assuming that emitter drag is negligible compared to collector drag, the drag force can be modeled as

$$F_D = \frac{1}{2} \rho v^2 C_D b_c D, \tag{3.3}$$

where v is the flow velocity, D is the collector diameter, and C_D is the drag coefficient, which is a function of the Reynolds number. As noted by Moreau et al. [33], Equation (3.3) is only valid approximately for EAD devices since it applies to a uniform freestream, whereas an EAD thruster would produce a flow with a spatially-varying velocity profile. Moreau et al. [33] also suggested that a model for the velocity induced

by an EAD thruster is

$$v \approx k\sqrt{\frac{Id}{\mu}}, \tag{3.4}$$

where k is a constant. Substituting Equations (3.3) and (3.4) into Equation (3.2), the thrust can be related to the current through

$$F_N = \frac{Id}{\mu}\left(1 - \frac{1}{2}\rho k^2 C_D b_c D\right). \tag{3.5}$$

From this analysis, it can be seen that in the absence of non-ideal effects and for voltages above corona inception, the ratio $\frac{I}{V_a b_e}$ is related linearly to the applied voltage via

$$\frac{I}{V_a b_e} = C_0 \varepsilon \mu \frac{(V_a - V_0)}{d^2} \propto (V_a - V_0). \tag{3.6}$$

The drag coefficient of a smooth circular cylinder is approximately constant for Reynolds numbers in the range $1 \times 10^3 \leq \mathrm{Re} \leq 3 \times 10^5$ [146], which can be expected for EAD flows past cylinders of the diameters tested here, assuming velocities similar to those measured by Moreau et al. [33]. If the drag coefficient is assumed constant, the ratio $\frac{F_N}{V_a b_e}$ is also related linearly to the applied voltage,

$$\frac{F_N}{V_a b_e} \propto (V_a - V_0). \tag{3.7}$$

As suggested by Lemetayer et al. [141], deviations in either $\frac{I}{V_a b_e}$ or $\frac{F_N}{V_a b_e}$ from the linear relationship with voltage can be interpreted as evidence of reverse emission.

The first strategy to mitigate reverse emission that was considered was changing the collector diameter, as suggested by Monrolin et al. [35] and Xu et al. [34]. Figure 3-2 shows the ratios $\frac{I}{V_a b_e}$ and $\frac{F_N}{V_a b_e}$ against the applied voltage, obtained with collectors of different diameters at two different gap spacings. Examining the current results in Figure 3-2a, all data sets follow the linear trend predicted by Equation (3.6) at low voltages; however, a change in slope can be observed after some critical voltage: this is attributed to the onset of reverse emission. At a gap spacing $d = 50\,\mathrm{mm}$, this change in slope occurs at $V_a \approx 22\,\mathrm{kV}$ when $D = 12.7\,\mathrm{mm}$, whereas it only occurs at

$V_a \approx 30\,\text{kV}$ when $D = 38.1\,\text{mm}$. In general, the voltage at which deviations from the linear trend first occur increases with increasing collector diameter. A similar trend can be observed at a gap spacing $d = 100\,\text{mm}$: while deviations occur for voltages above $V_a \approx 30\,\text{kV}$ when $D = 19.1\,\text{mm}$, these only occur above $V_a \approx 44\,\text{kV}$ when $D = 38.1\,\text{mm}$.

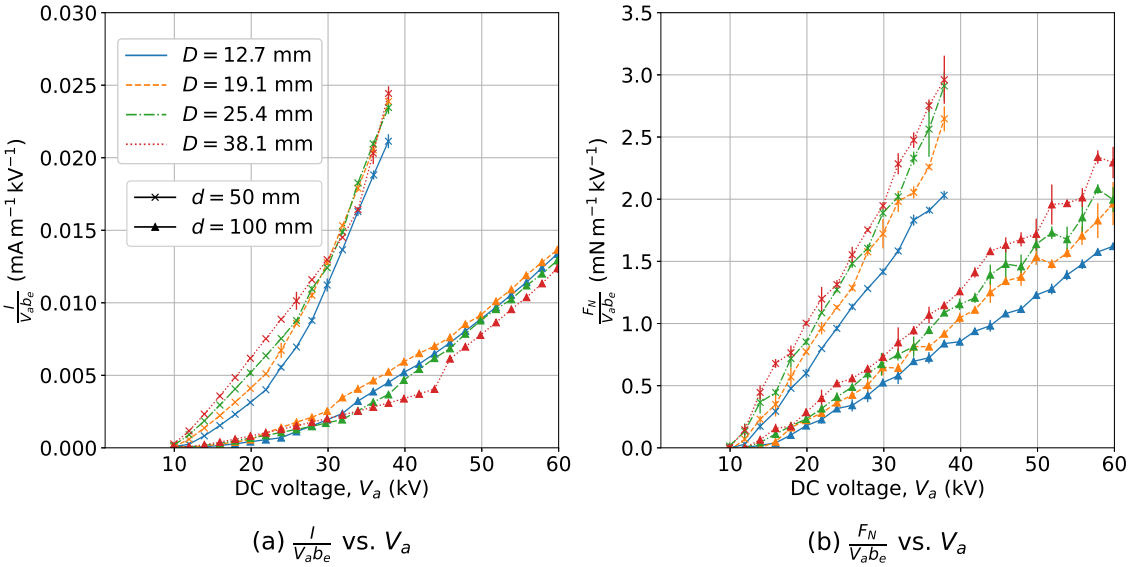

(a) $\frac{I}{V_a b_e}$ vs. V_a (b) $\frac{F_N}{V_a b_e}$ vs. V_a

Figure 3-2: Ratios (a) $\frac{I}{V_a b_e}$, and (b) $\frac{F_N}{V_a b_e}$ against the applied voltage in a positive corona for different collector diameters. All collectors had a span $b_c = b_e = 510\,\text{mm}$ and open ends. All tests done up to the same maximum voltage, even if the arcing limit was higher. Error bars represent a 95 % confidence interval.

In contrast, deviations from the linear trend at low voltages cannot be clearly observed in the plot of $\frac{F_N}{V_a b_e}$ versus applied voltage in Figure 3-2b. In this figure, it can be seen that the thrust produced by an EAD thruster at a given voltage and gap spacing increases with the collector diameter. This was previously reported by Moreau et al. [33] and can be attributed to the stronger electric field at the emitter when a larger collector is used, which enhances the discharge. Even though Equation (3.5) predicts the thrust to be directly proportional to current (in the absence of non-ideal effects), at $V_a = 60\,\text{kV}$ and $d = 100\,\text{mm}$, the collector with $D = 38.1\,\text{mm}$ produces 41 % more thrust than the $D = 12.7\,\text{mm}$ case while drawing 7 % less current. This discrepancy cannot be attributed to aerodynamic drag, as the larger collector would be expected to experience more drag than the smaller one. As a result, the $D = 38.1\,\text{mm}$ case has

a 52 % higher thrust-to-power ratio at that particular point than the $D = 12.7\,\text{mm}$ case. The results in Figure 3-2 suggest that increasing the collector diameter mitigates reverse emission by increasing its onset voltage, as predicted by Monrolin et al. [35] and shown by Xu et al. [34].

The effects of changing the collector span and using hemispherical end caps were also tested. Figure 3-3 shows plots of the ratios $\frac{I}{V_a b_e}$ and $\frac{F_N}{V_a b_e}$ against voltage for tests with three different collector spans and one case in which the collector contained hemispherical end caps. The difference between emitter and collector spans, Δb, is defined as $\Delta b \equiv b_c - b_e$; e.g., a collector with $\Delta b = 490\,\text{mm}$ was 490 mm longer than the emitter.

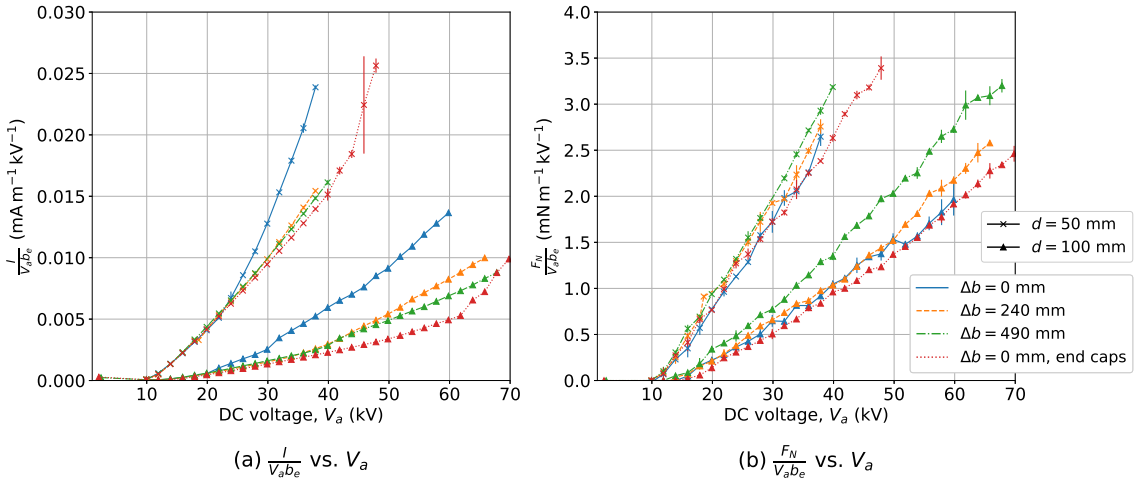

(a) $\frac{I}{V_a b_e}$ vs. V_a (b) $\frac{F_N}{V_a b_e}$ vs. V_a

Figure 3-3: Ratios (a) $\frac{I}{V_a b_e}$, and (b) $\frac{F_N}{V_a b_e}$ versus the applied voltage in a positive corona for different collectors. The collector in the data set labeled "end caps" had two hemispherical end caps, while the other ones had open ends. The collector diameter was $D = 19.1\,\text{mm}$ in all cases. Tests done up to the sparking voltage. Error bars represent a 95 % confidence interval.

Considering Figure 3-3a, the collector with $\Delta b = 0\,\text{mm}$ and open ends shows deviations from the linear trend at $V_a \approx 22\,\text{kV}$ when $d = 50\,\text{mm}$, and at $V_a \approx 20\,\text{kV}$ when $d = 100\,\text{mm}$. In contrast, no clear deviation from the linear trend can be seen in the $\Delta b = 240\,\text{mm}$ and the $\Delta b = 490\,\text{mm}$ collectors at $d = 50\,\text{mm}$ before sparking occurs. In the case with hemispherical end caps, clear deviations can only be observed at $V_a \approx 42\,\text{kV}$ when $d = 50\,\text{mm}$. The results in Figure 3-3a suggest that either increasing the collector span or using hemispherical end caps can mitigate reverse

emission. The tests in Figure 3-3a were conducted up to the maximum voltage (in steps of 2 kV) prior to sparking: the cases with end caps or with $\Delta b > 0$ consistently reach voltages higher than the $\Delta b = 0$ mm case with open ends before sparking. This suggests that reverse emission lowers the sparking voltage and, consequently, that mitigating reverse emission allows the thruster to operate at higher voltages before sparking. At the tested gap spacings, the highest voltages were reached in the tests with end caps: at $d = 100$ mm, the sparking voltage in the test with end caps was approximately 10 kV higher than in the $\Delta b = 0$ mm case with open ends.

No clear deviations from the linear trend can be observed in the $\frac{F_N}{V_a b_e}$ versus voltage plots in Figure 3-3b. It can be generally seen that the cases with $\Delta b = 0$ mm with and without end caps generate similar thrust at a given voltage and gap spacing, whereas the cases with $\Delta b > 0$ produce more thrust. This observation is compatible with the larger collectors enhancing ionization by increasing the electric field at the emitter. At $d = 100$ mm and 60 kV, the $\Delta b = 0$ mm collector with end caps produces approximately the same thrust as the $\Delta b = 0$ mm case with open ends, but it draws 64 % less current and, therefore, power.

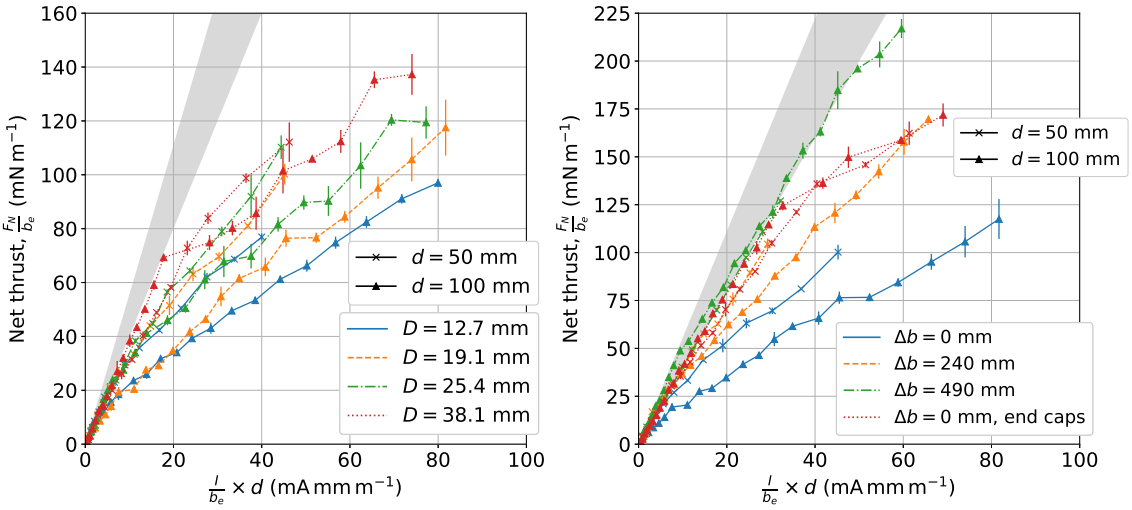

(a) Collector diameter

(b) Collector span & end caps

Figure 3-4: Net thrust per unit emitter span versus $\frac{Id}{b_e}$ for (a) different collector diameters, and (b) different collector spans with and without end caps in a positive corona thruster. The shaded band corresponds to a range of ion mobilities reported in the literature. Error bars, only shown in thrust, represent a 95 % confidence interval.

The results in Figures 3-2 and 3-3 suggest that increasing the collector diameter, increasing the collector span, and using hemispherical end caps mitigate reverse emission. However, a direct comparison between these three different mitigation strategies cannot be made using these figures since changing the collector geometry affects not only the current draw but also the thrust. Equation (3.5) shows that in the absence of non-ideal effects and assuming a constant drag coefficient, net thrust will be proportional to the product of current and gap spacing; the effect of drag is to change the slope of the F_N versus Id line. Figure 3-4 shows the net thrust per unit emitter span, $\frac{F_N}{b_e}$, versus the ratio $\frac{Id}{b_e}$: the data in Figure 3-4a is the same as that in Figure 3-2, while the data in Figure 3-4b is the same as that in Figure 3-3. The shaded band in the figures corresponds to the range of ion mobilities reported in the literature, $1.8 \times 10^{-4} \leq \mu \leq 2.5 \times 10^{-4}\,\mathrm{m^2\,V^{-1}\,s^{-1}}$ [147]: if drag is small and reverse emission is not present, the results should lie within this band.

In Figure 3-4a, lower current is drawn at a given net thrust and gap spacing as the collector diameter is increased. When the thrust per unit span is below approximately $20\,\mathrm{mN\,m^{-1}}$, the net thrust in all data sets is proportional to $\frac{Id}{b_e}$; however, deviations from the linear trend can be seen in all cases at higher thrust levels. These deviations can be attributed to reverse emission, as discussed by Xu et al. [34]. Collectors of larger diameters show deviations at higher thrust levels, showing that larger collectors can mitigate reverse emission.

In Figure 3-4b, the $\Delta b = 0\,\mathrm{mm}$ case with open ends shows deviations from its initial linear trend and from the shaded region. These deviations are smaller and start at higher thrust levels in the tests when $\Delta b > 0$ or when end caps are used: whereas the $\Delta b = 0\,\mathrm{mm}$ collector with open ends at $d = 100\,\mathrm{mm}$ shows evidence of reverse emission for $\frac{F_N}{b_e} > 20\,\mathrm{mN\,m^{-1}}$, the $\Delta b = 490\,\mathrm{mm}$ collector only shows evidence of reverse emission when $\frac{F_N}{b_e} > 180\,\mathrm{mN\,m^{-1}}$. In fact, the results in the $\Delta b = 490\,\mathrm{mm}$ tests lie within the band of previously reported ion mobilities except when $\frac{F_N}{b_e} > 190\,\mathrm{mN\,m^{-1}}$. The results in Figure 3-4b also show that the hemispherical end caps are an effective way to mitigate reverse emission without significantly increasing the collector length or mass.

The results suggest that reverse emission can be mitigated by increasing the collector diameter, increasing the difference between the collector and emitter spans, and using smooth hemispherical end caps. All of these mitigation strategies are expected to decrease the electric field at the collector ends. Hence, these results are consistent with the hypothesis of Monrolin et al. [35] that reverse emission occurs when a critical electric field is reached at some point in the collector. Since the hollow cylindrical collectors used here have sharp ends, reverse emission would be first expected to ignite at the two open ends.

3.4.2 Reverse emission and thrust

There is not a consensus in the literature as to whether reverse emission affects thrust. In the previous section, it has been shown that using hemispherical end caps can mitigate reverse emission with only a minor change in the collector geometry and effective span.

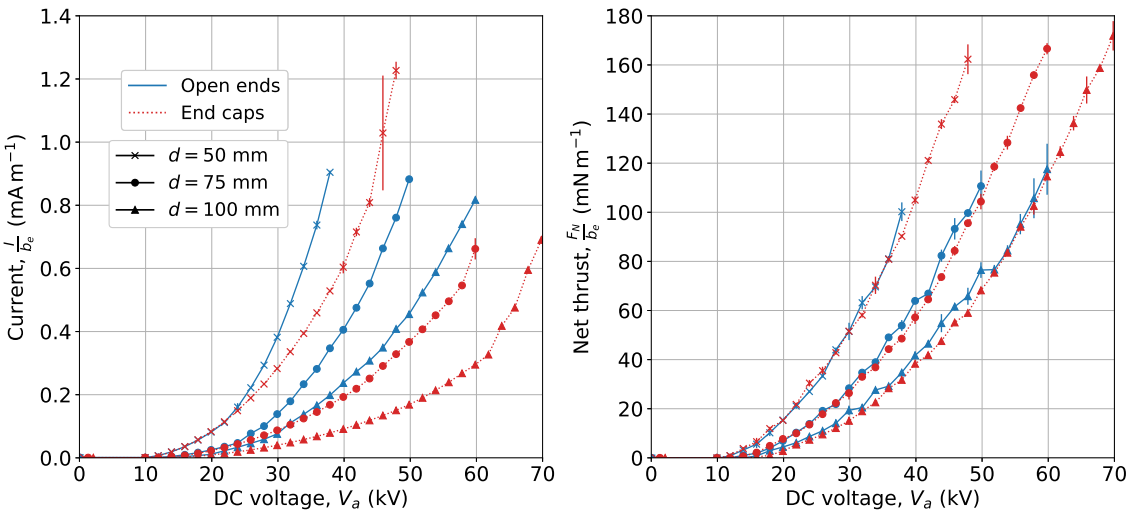

(a) Current (b) Thrust

Figure 3-5: (a) Current per unit span, and (b) thrust per unit span versus the applied voltage in a positive corona. Collectors had a diameter of $D = 19.1\,\text{mm}$ and cylindrical portions of the same span ($\Delta b = 0\,\text{mm}$), with open ends and with hemispherical end caps. Tests done up to the sparking voltage. Error bars represent a 95 % confidence interval.

Figure 3-5 compares the current and net thrust produced by two EAD thrusters

with cylindrical collectors of the same span as the emitter ($\Delta b = 0\,\text{mm}$) with open ends and with hemispherical end caps. Examining the characteristics in Figure 3-5a, the two cases draw similar currents at voltages below approximately 20 kV, but the collector with open ends draws significantly more current than the collector with end caps at voltages above that. This is attributed to the onset of reverse emission as discussed in the previous section. Figure 3-5, in which tests were done up to the sparking voltage, shows that higher voltages can be reached at a given gap spacing when reverse emission is mitigated.

However, the tests with and without end caps show similar thrust–voltage characteristics in Figure 3-5b. The average difference between the thrust produced at a given voltage and gap spacing in these two cases (for voltages below sparking) is $2.0\,\text{mN}\,\text{m}^{-1}$, while the root mean square (RMS) difference is $3.5\,\text{mN}\,\text{m}^{-1}$; these differences are comparable to the experimental uncertainty. In Appendix C, it is shown that the thrust differences between these two collectors are also comparable to the experimental uncertainty when negative coronas are used. These results show that if reverse emission has any effect on thrust, this effect is small compared to its effect on current. The results in Figure 3-5a, obtained with thrusters with very similar geometry, suggest that the net effect of reverse emission is to increase the current (and therefore power draw) at a given voltage and to lower the sparking voltage, while the net thrust at a given voltage is approximately the same as if reverse emission did not occur.

3.4.3 Reverse emission in decoupled thrusters

The current–voltage characteristics of decoupled thrusters are different from those of corona discharges. An empirical model for the current–voltage characteristics of decoupled thrusters was proposed in Chapter 2; this takes the form

$$I = \zeta \frac{2}{\pi} \varepsilon_0 \mu \frac{V_a^2}{d^2} b_e, \tag{3.8}$$

where ζ is a function of the DBD power draw to emitter span ratio, $\frac{P_{\mathrm{DBD}}}{b_e}$. Equation (3.8) suggests that, in the absence of non-ideal effects, the ratio $\frac{I}{V_a b_e}$ is proportional to V_a,

$$\frac{I}{V_a b_e} = \zeta \frac{2}{\pi} \varepsilon_0 \mu \frac{V_a}{d^2} \propto V_a. \tag{3.9}$$

Equations (3.2) and (3.5), which relate the net thrust and current, are derived from an integration of electrostatic forces combined with drag models. These are also valid for decoupled thrusters. Therefore, if non ideal effects are not present, $F_N \propto Id$.

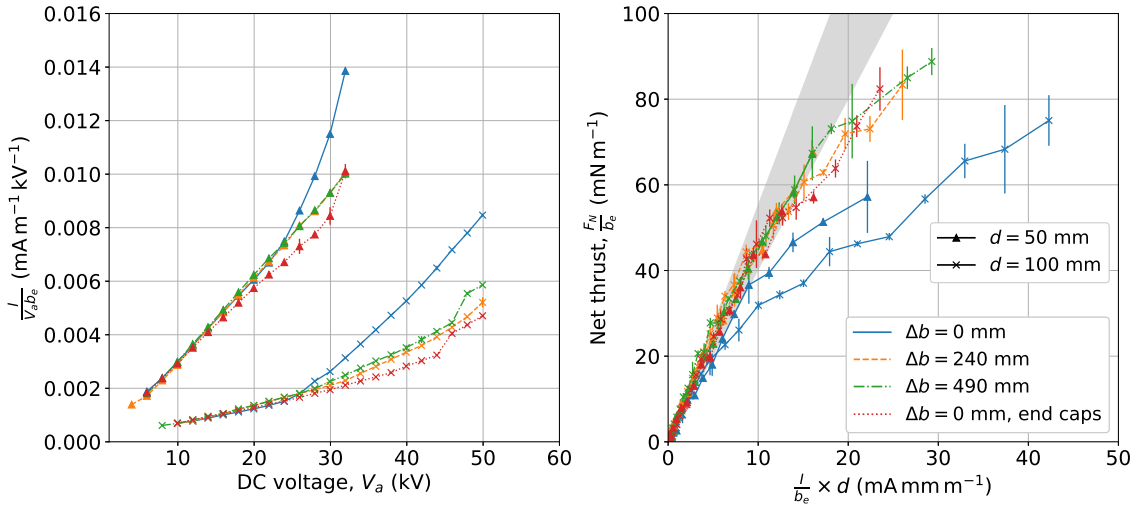

(a) $\frac{I}{V_a b_e}$ vs. V_a (b) $\frac{F_N}{b_e}$ vs. $\frac{Id}{b_e}$

Figure 3-6: (a) Ratio $\frac{I}{V_a b_a}$ against V_a, and (b) thrust per unit span versus ratio $\frac{Id}{b_e}$ in a decoupled thruster. The DBD was produced with an AC signal at a constant frequency of 3 kHz and a peak-to-peak voltage of 7 kV. All collectors had a diameter $D = 19.1$ mm. All collectors had open ends except the one labeled "end caps". At a given gap spacing, tests done up to a constant maximum voltage (even if sparking voltage was higher). Error bars represent a 95 % confidence interval; these are omitted in the x-axis in (b).

Tests were done on decoupled thrusters with collectors of different spans, and one set of tests was done on a collector with end caps. Only these reverse emission mitigation strategies were considered here as they appeared to be more effective than increasing the collector diameter in the corona discharge tests. Figure 3.8a shows the ratio $\frac{I}{V_a b_e}$ against the applied voltage in a decoupled thruster; only points with a corresponding thrust per unit span greater than 2 mN m^{-1} are shown. At voltages

below $V_a \approx 22\,\text{kV}$, all tests show an approximately proportional increase in the ratio $\frac{I}{V_a b_e}$ with voltage; some deviations from the linear trend can be seen at voltages above that. These deviations are attributed to reverse emission. The test with $\Delta b = 0\,\text{mm}$ and open ends shows the largest deviations: at a gap spacing of $d = 100\,\text{mm}$ and a voltage $V_a = 50\,\text{kV}$, the collector with $\Delta b = 0\,\text{mm}$ and end caps draws 44 % less current than the collector with the same span and open ends.

Figure 3-6b shows the net thrust per unit span against the ratio $\frac{Id}{b_e}$; as per Equation (3.5), this plot should be a straight line if reverse emission is not present. A band showing the range of previously reported ion mobilities is also shown. The tests with $\Delta b = 0\,\text{mm}$ and open ends deviate from the linear trend at lower thrust levels than in the other cases. Similarly to the cases with corona discharges, this suggests that increasing the collector span or using end caps helps mitigate reverse emission. These results also show that reverse emission is not a phenomenon limited to thrusters with corona discharges: it can also degrade the performance of thrusters with decoupled ion sources.

3.4.4 UV photography

Gas discharges are often accompanied by light emission. Light is emitted as electrons that have been excited to electronic levels above the ground state return to lower energy levels; this can occur following particle collisions or electron–ion recombination [148]. For gases in the atmosphere, a fraction of the light emitted is in the UV spectrum.

The results in Sections 3.4.1–3.4.3 suggest that reverse emission is caused by a gas discharge primarily located at the two ends of the collector since weakening the electric field at the collector tips mitigates reverse emission. Monrolin et al. [35] also stated (but did not show) that reverse emission originates primarily at the tips of the collector.

A UV-sensitive camera was used to detect sources of UV emission in the EAD thrusters. Tests were performed with positive and negative coronas and different collector types to identify the source of reverse emission. All tests were done at the

same voltage ($V_a = 50\,\mathrm{kV}$) and gap spacing ($d = 100\,\mathrm{mm}$).

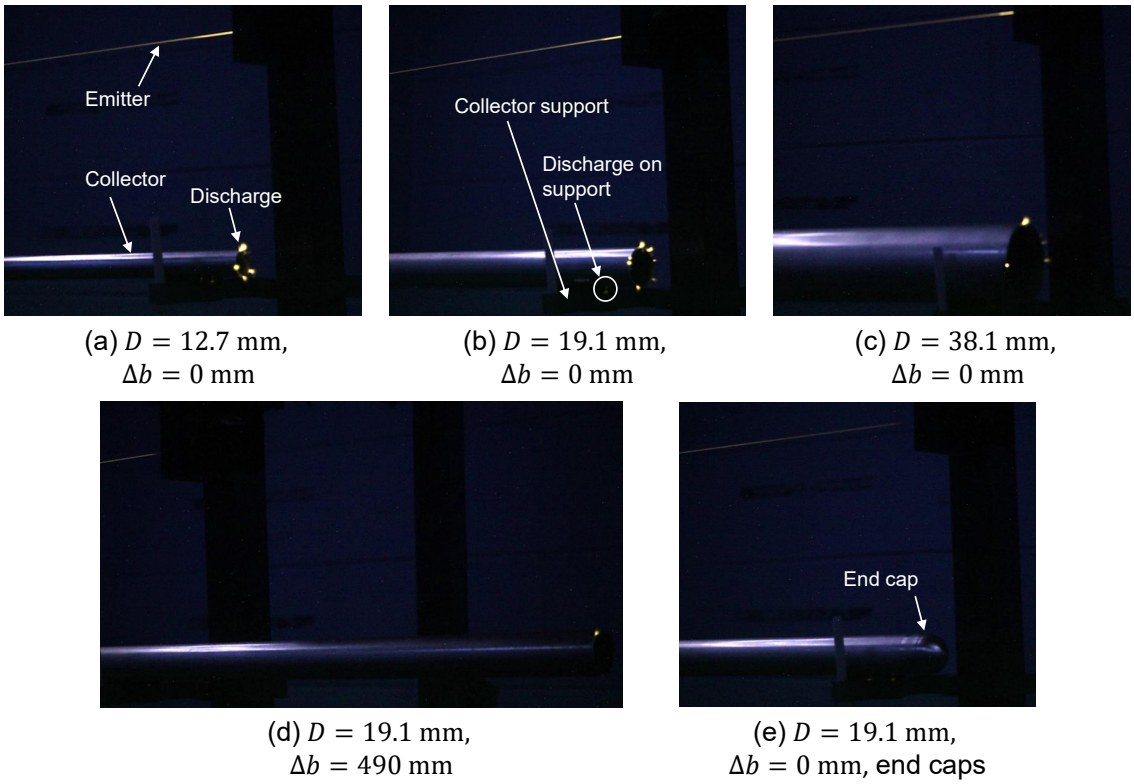

(a) $D = 12.7$ mm, $\Delta b = 0$ mm

(b) $D = 19.1$ mm, $\Delta b = 0$ mm

(c) $D = 38.1$ mm, $\Delta b = 0$ mm

(d) $D = 19.1$ mm, $\Delta b = 490$ mm

(e) $D = 19.1$ mm, $\Delta b = 0$ mm, end caps

Figure 3-7: View near the tips of the collector in positive corona discharges. Photographs obtained with a UV-sensitive camera at a gap spacing $d = 100\,\mathrm{mm}$ and a voltage $V_a = 50\,\mathrm{kV}$. Images are in false color.

Figure 3-7 shows UV images of EAD thrusters with different collectors and a positive-corona ion source, focusing on the region near the collector's tips. In Figure 3-7a, corresponding to a collector with open ends and $D = 12.7\,\mathrm{mm}$, several glowing spots can be seen at the tip of the collector. This suggests that gas discharges were occurring there; a corresponding stronger glow near the end of the emitter can also be observed. As the collector diameter is increased (Figures 3-7a to 3-7c), the intensity of the glowing spots is generally diminished.

Figure 3-7d shows a collector with $\Delta b = 490\,\mathrm{mm}$; this was found to be one of the most effective reverse emission mitigation strategies in Section 3.4.1. A single weak glowing spot can be seen at the tip of the collector, suggesting that the collector tip discharge has been weakened as compared to Figure 3-7b, with the same diameter but a different span. Figure 3-7e shows a collector with hemispherical end caps: no

glow can be observed at the tip of the collector, showing that the discharge has been weakened with respect to Figure 3-7b or completely eliminated.

Reverse emission is attributed to the gas discharges seen in Figure 3-7: the figure shows that these discharges occur primarily at the tips of the collectors and can be mitigated by weakening the electric field there. Figure 3-7 also supports the hypothesis by Monrolin et al. [35] that reverse emission is ignited in regions in the collector with a high electric field but not necessarily at the tips: some weak glowing spots can be observed on the lower parts of the collector in Figures 3-7a, 3-7b and 3-7e, where it attaches to the supporting frame. An example of these discharges on the collector's supports has been labeled in Figure 3-7b.

The UV images taken with negative corona discharges are shown in Appendix C. They also show glowing regions at the tip of the collectors. In contrast to the positive corona images in Figures 3-7, in which discharges occur at discrete spots on the tips, the negative corona images show a uniform glow on the collector's tips.

In Appendix C, a qualitative model for the observed effects of reverse emission on current and thrust is hypothesized, in which reverse emission is attributed to the onset of a corona discharge at the collector as suggested by previous work [34, 35]. The correctness of this hypothesis should be the focus of future work.

3.4.5 Reverse emission and noise

It has been suggested that reverse emission causes audible noise emission from the thruster [35]. Since one of the main advantages of EAD propulsion is that it can be nearly silent, understanding the impact of reverse emission on noise is of importance for practical applications of EAD. Acoustic tests were performed at three different voltages with collectors of $D = 19.1\,\text{mm}$ diameter and $\Delta b = 0\,\text{mm}$, both with open ends (which results in significant reverse emission as shown in Section 3.4.1) and with end caps (which mitigate reverse emission).

The spectra of the noise produced by the thrusters are shown in Figure 3-8. The y-axes show the power spectral density, which is proportional to the magnitude of the signal's Fourier transform squared and is a measure of the power distribution at

different frequencies [149]. The spectral density is shown in decibels relative to full scale (dBFS); this is a relative scale since the microphone used to record the audio samples was not calibrated for sound pressure level measurement. The x-axes show frequency; frequencies up to 20 kHz are shown as this is the upper end of the human hearing range.

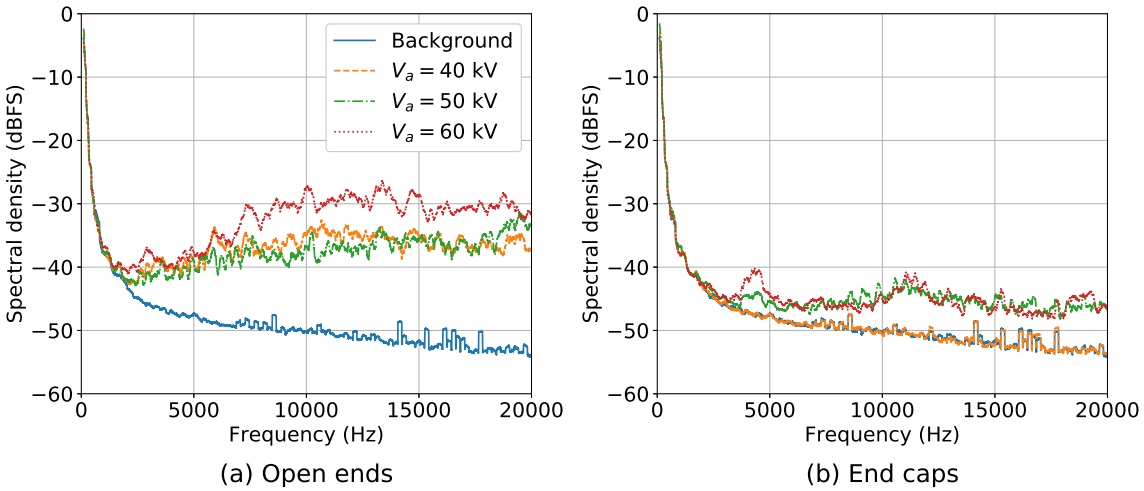

Figure 3-8: Power spectral densities in decibels relative to full scale against frequency for EAD thrusters with positive corona ion sources. Tests done at a gap spacing $d = 100$ mm with collectors with $D = 19.1$ mm, $\Delta b = 0$ mm and (a) open ends, and (b) hemispherical end caps.

The results in Figure 3-8a show that the collector with open ends produced noise above the background level at the three voltages tested (in the range of 40–60 kV). The thruster produced similar noise levels at 40 kV and 50 kV, given that the spectral density plots are similar in these two cases; at these voltages, the spectral density is approximately 10–15 dB larger than the background noise for frequencies above 5 kHz. At 60 kV, the spectral density for frequencies in the range 8–20 kHz is approximately 5 dB higher than at the other two voltages shown.

In Figure 3-8b, it can be seen that the power spectral density in the $V_a = 40$ kV test is approximately the same as the background spectral density when end caps are used, implying that the thruster was silent. The tests at 50 kV and 60 kV do show a noise level higher than the background: in general, the spectral density is approximately 5 dB higher than the background one for frequencies above 5 kHz. For

frequencies above 5 kHz, the tests with end caps in Figure 3-8b show a power spectral density approximately 10–15 dB lower than the tests with open ends in Figure 3-8a. Therefore, the results in Figure 3-8 show that mitigating reverse emission can reduce the noise produced by an EAD thruster. Conversely, these results also show that reverse emission can cause audible noise emission. Despite the reverse emission mitigation, Figure 3-8b shows that the collector with end caps produced noise levels above the background when V_a was 50 kV or 60 kV. Future work should study if this noise is caused by some level of reverse emission or by other effects such as mechanical vibration of the emitter.

3.5 Conclusions

Reverse emission is a non-ideal effect in EAD systems that reduces efficiency by increasing the power draw. The results suggest that reverse emission is caused by a spurious gas discharge that ignites in regions in the collector with a high electric field. In a wire-to-cylinder geometry, these discharges occur primarily at the collector's tips: this has been shown directly through UV images and indirectly by testing collectors with different tip geometries.

It has been shown that reverse emission can occur in EAD thrusters with either corona discharge or decoupled ion sources. Reverse emission can greatly increase current and, therefore, the power draw of the device at a given voltage; however, the results do not show clear evidence of a corresponding increase or decrease in thrust for a given voltage. The results show that reverse emission lowers the sparking voltage, therefore reducing the maximum thrust that the thruster can produce. Moreover, it has been shown that reverse emission is associated with an increase in the noise produced by the thruster, which can potentially negate one of the major advantages of EAD: near-silent operation.

Three different strategies to mitigate reverse emission have been identified: to increase the collector diameter, to increase the collector span, and to use hemispherical end caps. Through these mitigation strategies, the onset voltage of reverse emission

has been increased by as much as 40 kV at a gap spacing of 100 mm, thereby reducing the power draw by as much as 64 % before sparking. The results also show that mitigating reverse emission can reduce the power spectral density of the thruster's noise by as much as 10–15 dB in a wide range of frequencies. While the strategies studied here can improve the thruster's electrostatic performance, they can also result in increased aerodynamic drag. An optimization framework could be used to find a trade-off between these two competing effects.

This study has focused on quantifying the effects of reverse emission on performance metrics such as current, thrust, power, and noise. In Appendix C, a hypothetical qualitative model for reverse emission that is compatible with the findings has also been proposed, attributing reverse emission to a corona discharge at the collector. Plasma diagnostic tools, such as probes and spectroscopy, could be used in the future to identify the types of ions through which current is transported and to assess whether the proposed model is valid. Moreover, this work has focused on the effects of dimensional quantities such as collector diameter and span or gap spacing. Future work should try to identify if reverse emission is governed by non-dimensional parameters.

In this work, a wire-to-cylinder geometry has been used; however, reverse emission also occurs in other geometries, such as wire-to-airfoil [128], and future studies should verify that the reverse emission mitigation strategies that have been identified here also apply to other emitter/collector geometries. Hysteresis effects due to reverse emission and their impact on thruster performance should also be explored in future work. Since the results suggest that reverse emission is primarily affected by the geometry of the collector's tips, alternative emitter/collector geometries with no tips should also be considered in future work, such as a toroidal topology.

This page intentionally left blank.

Chapter 4

Theory of multistaged ducted EAD thrusters

4.1 Publication and collaboration statement

The idea of using multiple EAD stages enclosed in a duct was originally conceived by Steven Barrett, Haofeng Xu, and the author. The author identified suitable models for these thrusters with some input from Steven Barrett, Arthur Brown, and Haofeng Xu. The author performed all the theoretical calculations, which were reviewed by Arthur Brown and Steven Barrett. The author produced all the numerical results.

This chapter was published previously in N. Gomez-Vega et al. "Model of Multistaged Ducted Thrusters for High-Thrust-Density Electroaerodynamic Propulsion". *AIAA Journal* 61.2 (2023): 767-779 [150].

4.2 Introduction

In this chapter, a model of multistaged ducted (MSD) EAD thrusters for EAD thrust force generation in air is proposed, showing that MSD thrusters have the potential to provide higher thrust density than previously possible. These thrusters contain several ion-acceleration stages that are enclosed in a duct and fitted with an inlet and a nozzle. In addition to providing performance benefits analogous to those in

ducted fans, the duct acts as a physical barrier between the high-voltage electrodes and the surroundings, improving the safety of the system. Furthermore, the duct can contain acoustic lining to further reduce the thruster's acoustic signature, similarly to jet engines [151].

EAD devices containing a set of serially-stacked ion-acceleration stages have been investigated experimentally in the past, both in fluid pumping [15, 23, 25, 60, 152] and in propulsion applications [32, 36, 38, 153]. Some simplified numerical studies on multistaged devices have also been conducted [154, 155]. A common finding of the studies on fluid pumping is that multistaged EAD pumps can provide higher mass flow rate, flow exit velocity, and efficiency than single-stage devices [25, 152]; Kim et al. [60] report that both the exit velocity and the energy conversion efficiency scale with the square root of the number of stages. Rickard et al. [25] and Qiu et al. [23] found that the performance improvement due to multi-staging is limited by pressure losses, which become more significant as more stages are added.

Gilmore and Barrett [36] conducted experiments on unducted corona-discharge thrusters with a varying number of parallel and serial stages with cylindrical collectors. They reported a maximum thrust per unit cross-sectional area of $3.3\,\mathrm{N\,m^{-2}}$ when a single stage was used, as well as an approximately linear increase in thrust as more stages were added. Belan et al. [38] conducted tests with a single-stage thruster containing parallel electrode pairs with airfoil collectors. They measured an optimum distance between parallel electrode pairs that provided maximum thrust per unit frontal area and observed a trade-off between thrust density and thrust-to-power ratio when the distance between the electrode pairs was varied. Drew and Follmer [153] recently performed static tests on a thruster containing up to three pin-to-mesh corona-discharge stages surrounded by a duct and measured an almost linear scaling of thrust with the number of stages. By using stages with a millimeter-scale gap distance, they showed that a thrust density of $15\,\mathrm{N\,m^{-2}}$ and a thrust per unit volume of $2\,\mathrm{kN/m^3}$ could be achieved.

The use of a converging nozzle downstream of a ducted EAD gas pump was explored by Rickard et al. for single-stage [24] and multistaged [25] devices. They

found that the mass flow rate and the nozzle exit velocity could be controlled by changing the nozzle area ratio. Similar results were reported by Brindle and Lai [26] and Lin et al. [27], who tested corona discharges with a needle emitter and the nozzle surface acting as the collector.

Most theoretical work on EAD thrusters for propulsion has focused on open or unducted devices. Some theoretical models [15, 16, 25, 60] of multistaged EAD devices enclosed in a duct have been proposed within the context of fluid pumping focusing only on the internal flows or with simplistic models for the flow velocity. These models are not appropriate for propulsion applications due to the complex interaction between the internal and external flows and the duct. Proper duct design can lead to performance improvements similar to those seen in ducted fans or propellers [156]; in particular, there can be a contribution to thrust from the pressure forces acting on the duct.

In Section 4.3, a model of MSD thrusters is developed. The interaction between the internal and external flows is modeled using momentum theory. Two particular stage architectures are considered: ideal one-dimensional (1-D) stages with a uniform current density across their cross-section, based on the theory of Stuetzer [15] and Pickard [17]; and stages using wire-to-airfoil corona discharges. In Section 4.4, the performance of these two types of MSD thrusters is calculated: through this, it is shown that MSD devices have the potential to provide order-of-magnitude improvements in thrust density or thrust-to-power ratio as compared to single-stage devices.

4.3 Theory and models

A schematic diagram of an MSD thruster is shown in Figure 4-1a. The thruster's inlet lies between stations 1 and 2, and the region between stations 3 and e represents the nozzle. The EAD ion-acceleration stages are located between stations 2 and 3: this section is assumed to be of constant cross-sectional area. The flow pressure returns to atmospheric pressure at station 4. This thruster will be analyzed under the assumption that the flow is incompressible. In Figure 4-1b, an unducted thruster

is presented as an actuator disk.

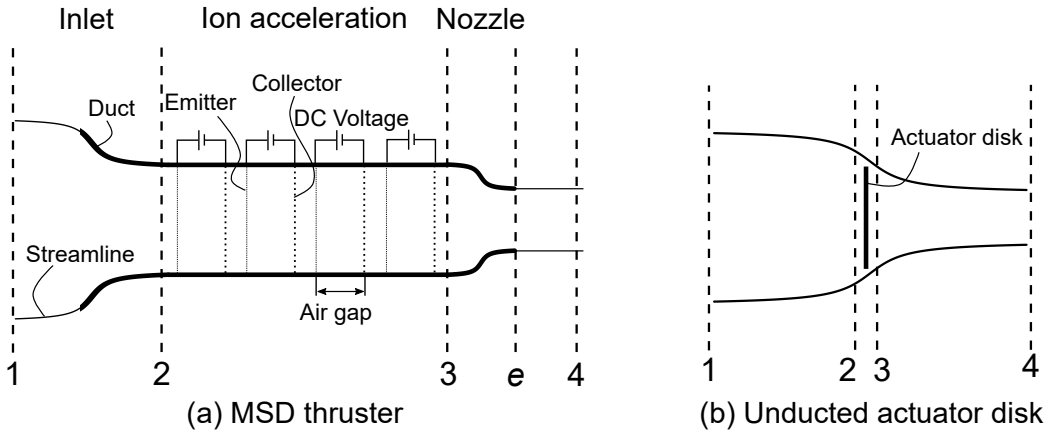

Figure 4-1: Schematic diagrams of (a) an MSD thruster and (b) an unducted thruster.

A 1-D momentum theory model of the flow in Figure 4-1a is described in Section 4.3.1. This model takes as an input the pressure rise produced by the EAD stages and is potentially applicable to a wide range of stage architectures, with either corona discharges or decoupled ion sources. In subsequent sections, two different particular stage architectures are considered. In Section 4.3.2, stages that produce and accelerate ions uniformly across a cross-section are considered; these are referred to as "ideal 1-D" stages. In Section 4.3.3, an alternative model of EAD stages using wire-to-airfoil corona discharges is discussed. Other stage designs are possible, such as stages with pin-to-mesh or pin-to-ring corona discharges: the momentum theory model may still be applicable to them, but these are not modeled here.

4.3.1 Momentum theory

The performance of the ducted thruster in Figure 4-1a depends on the duct geometry. The nature of this problem is analogous to the analysis of ducted or shrouded propellers: a two-dimensional or three-dimensional analysis of the effect of the duct on the flow requires the use of computational methods, such as the method of singularities [157, 158] or computational fluid dynamics [159, 160]. When coupled to an electrostatic model of EAD, these methods are computationally-expensive and not well-suited for parametric analysis. For this reason, a 1-D momentum theory

method, similar to those developed for ducted propellers [157, 161–163], is used here.

Consider the ducted thruster in Figure 4-1a. If the flow between stations 1 and 2 and between 3 and 4 is assumed to be quasi-1-D, steady, incompressible (constant density), inviscid, and isentropic, Bernoulli's principle requires that

$$\begin{cases} p_1 + \frac{1}{2}\rho v_1^2 = p_2 + \frac{1}{2}\rho v_2^2 \\ p_2 + \Delta p + \frac{1}{2}\rho v_3^2 = p_4 + \frac{1}{2}\rho v_4^2 \end{cases} \tag{4.1}$$

where p_x is the static pressure at station x, ρ is the air mass density, v_x is the axial velocity at station x, and Δp represents the static pressure rise across the EAD stages between stations 2 and 3. From conservation of mass and under the constant-density assumption, the flow velocity through the constant-area portion of the thruster is

$$v_2 = v_3 = v_4 \frac{A_4}{A_2}, \tag{4.2}$$

where A_x is the cross-sectional area at station x. Solving Equation (4.1) for the far wake velocity v_4,

$$v_4 = \sqrt{v_1^2 + \frac{2\left(\Delta p + p_1 - p_4\right)}{\rho}} = \sqrt{v_1^2 + \frac{2\Delta p}{\rho}}, \tag{4.3}$$

since station 4 is defined as the point where $p_4 = p_1$. To close these equations, it is assumed that the properties at station 4 are the same as the properties at station e (nozzle exit): this implies that $A_4 = A_e$ and, as a result, that the nozzle exit pressure is atmospheric, $p_e = p_4 = p_1$. This assumption leads to what Sacks and Burnell [157] refer to as "simple momentum theory". In general, the far wake area A_4 depends on the duct design [157], but the ducted propellers tested by Pereira [163] showed an almost constant wake diameter downstream of the nozzle exit when the freestream conditions were static ($v_1 = 0$). Under this assumption, the nozzle exit velocity is given by Equation (4.3).

Assuming that $A_4 = A_e$, the areal thrust density, $\frac{F}{A_2}$, is

$$\frac{F}{A_2} = \frac{\dot{m}(v_e - v_1) + A_e(p_e - p_1)}{A_2} = \rho v_4(v_4 - v_1)\phi, \tag{4.4}$$

where $\dot{m} = \rho A_4 v_4$ is the mass flow rate through the thruster and $\phi = \frac{A_e}{A_2}$ is the nozzle area ratio.

In an unducted thruster such as the one in Figure 4-1b, the far wake area A_4 is unknown. In this case, the system can be closed with the condition that

$$\frac{F}{A_2} = \frac{\dot{m}(v_4 - v_1)}{A_2} = \Delta p, \tag{4.5}$$

Equation (4.5) does not hold in general when the thruster is ducted due to the contribution to thrust from the pressure forces acting on the duct [156]. If there is a zero freestream velocity and the nozzle area ratio is unity, Equations (4.4) and (4.5) show that the thrust with a duct is double the unducted one for a given Δp, illustrating the benefits of ducting. In the following analysis, it will be assumed that the thruster has a duct with an inlet and a nozzle and that $A_4 = A_e$. This analysis can be extended to unducted thrusters through Equation (4.5).

The models presented in this section enable the calculation of flow velocities or the thrust produced by an MSD device if the pressure rise delivered by the EAD stages, Δp, is known. The next two sections consider two particular EAD stage architectures and present models to calculate Δp as a function of electrical and geometric parameters.

4.3.2 Model of ideal 1-D EAD stages

Consider an idealized 1-D model of a constant-area EAD device similar to those of Stuetzer [14, 15], Pickard [17], or Gilmore and Barrett [46]. In general, the device may consist of several ion-acceleration stages, each containing an emitter electrode (where ions are injected) and a collector (where ions are neutralized) separated by an ion drift region across which a voltage is applied, as shown in Figure 4-1a. It is assumed that ions produced in one stage are neutralized within the stage and not

drifting over to the next one. In order for conditions to be one-dimensional, the ion sources must deliver a uniform charge density across the cross-section at the emitter. Since corona discharges require an asymmetry in geometry for ions to be produced, they cannot be used as the ion sources in an ideal 1-D EAD device; a different model for corona-discharge stages is considered in the next section. Instead, it is assumed that these ideal stages contain a decoupled ion source capable of uniform ionization.

Assuming that only one polarity of ions is present at any given stage, the current density, j, in a stage's ion drift region is uniform across the cross-section and can be modeled as [15, 46]

$$j = \rho_c \left(v_B + \mu E \right), \tag{4.6}$$

where v_B is the bulk velocity of the neutral fluid and E is the electric field, such that $\vec{E} = E\hat{x}$, where $\hat{x}$ is the unit vector in the direction from the emitter to the collector. Note that the ion mobility is defined such that $\mu = \text{sign}(q)|\mu|$, where $\text{sign}(q)$ is the sign function applied to the charge of the ions in the drift region, i.e., the mobility is positive when ions have a positive charge and negative when ions have a negative charge. As shown by Gilmore and Barrett [46], the mobility can be assumed to be constant for the range of electric fields used in EAD devices. The terms on the right-hand side of Equation (4.6) represent convective and ion drift currents, respectively.

If the flow is assumed to be steady and incompressible (constant density), the system is governed by conservation of mass, momentum, and charge, and Gauss's law. In the drift region between an emitter and a collector, these can be respectively expressed in 1-D as

$$\frac{\mathrm{d}}{\mathrm{d}x} \begin{bmatrix} v_B \\ p \\ \rho_c \left(v_B + \mu E \right) \\ E \end{bmatrix} = \begin{bmatrix} 0 \\ \rho_c E \\ 0 \\ \frac{\rho_c}{\varepsilon} \end{bmatrix}, \tag{4.7}$$

where x is a stage coordinate starting at the emitter. A derivation of Equation (4.7) is shown in Appendix D, along with a non-dimensional treatment of its solution.

The system is closed with the condition that

$$V = \int_0^d E(x)dx, \tag{4.8}$$

where V is the DC voltage applied across the stage and d, the gap spacing, is the distance between the emitting and collecting electrodes.

The thruster inlet conditions are that $v_B = v_2$, $p|_{x=0} = p_2$ (at the first stage only) and that $E|_{x=0} = E_0$, where E_0 is the electric field at the emitter. If the thruster is multistaged, each stage has a set of emitting and collecting electrodes, across which a voltage is applied. The outlet pressure of one stage is assumed to be the inlet pressure of the next one. Since the thruster is assumed to have a constant cross-sectional area, the bulk velocity is constant due to mass conservation.

Pressure losses across a stage, Δp_L, are modeled with [16]

$$\Delta p_L = -\frac{1}{2}\rho v_B^2 K_L, \tag{4.9}$$

where K_L is a loss coefficient that depends on the stage geometry and Reynolds number. In general, pressure losses are caused by emitter and collector drag, as well as by skin-friction forces on the duct.

Combining Equations (4.6) and (4.7), it can be shown that the electric field distribution between the emitting and collecting electrodes is given by [15]

$$E(x) = \text{sign}(q)\left[\frac{2jx}{\varepsilon\mu} + \left(E_0 + \frac{v_B}{\mu}\right)^2\right]^{\frac{1}{2}} - \frac{v_B}{\mu}. \tag{4.10}$$

The derivation of Equation (4.10) is shown in Appendix D. Substituting Equation (4.10) into Equation (4.8) results in an implicit equation for the current density,

$$V = \int_0^d \left(\text{sign}(q)\left[\frac{2jx}{\varepsilon\mu} + \left(E_0 + \frac{v_B}{\mu}\right)^2\right]^{\frac{1}{2}} - \frac{v_B}{\mu}\right) \mathrm{d}x. \tag{4.11}$$

This equation defines the current–voltage characteristic of this 1-D EAD device: it is

the relation between the voltage and current density. Equation (4.11) has a simple analytical solution for the case when $v_B = 0$ and $E_0 = 0$. This is known as the Mott-Gurney law [135] and the current density in this case, j_{MG}, is given by

$$j_{\mathrm{MG}} = \frac{9}{8}\varepsilon\mu\frac{V^2}{d^3}. \tag{4.12}$$

As shown in Appendix D, a general analytical solution for the current–voltage characteristic can also be found for any electric field at the emitter and any bulk velocity. This takes the form

$$\bar{j} \equiv \frac{j}{j_{\mathrm{MG}}} = \bar{j}(\alpha, \bar{v}), \tag{4.13}$$

where $\bar{j}$ is the non-dimensional current density; $\alpha = \frac{E_0 d}{V}$ is the non-dimensional electric field at the emitter; $\bar{v} = \frac{v_B d}{\mu V}$ is the non-dimensional bulk fluid velocity, also referred to by Seyed-Yagoobi et al. [125] as the electric slip number; and $\bar{j}(\alpha, \bar{v})$ is a function of α and $\bar{v}$. The non-dimensional electric field at the emitter α has been used to model devices with corona discharges; for example, Xu et al. [42] state that $0.3 \leq \alpha \leq 0.7$ according to empirical data from corona discharges. A more detailed model of corona discharges is presented in Section 4.3.3.

This analysis assumes that the electric field at the emitter is known. Given that the electric field and charge density at the emitter are related through Equation (4.6) as

$$E_0 = \frac{1}{\mu}\left(\frac{j}{\rho_{c,0}} - v_B\right), \tag{4.14}$$

Equation (4.13) can also be extended for the case when the charge density at the emitter, $\rho_{c,0}$, is set. This boundary condition is more appropriate for devices with an ion source decoupled from the acceleration stage, in which $\rho_{c,0}$ can be controlled independently. In this case, the current–voltage characteristic takes the form

$$\bar{j} = \frac{j}{j_{\mathrm{MG}}} = \bar{j}(\bar{\rho}, \bar{v}), \tag{4.15}$$

where $\bar{\rho} = \frac{\rho_{c,0} d^2}{\varepsilon V}$ represents a non-dimensional charge density at the emitter, and is

referred to as the electric source number by Seyed-Yagoobi et al. [125]; and $\bar{j}(\bar{\rho}, \bar{v})$ is a function of $\bar{\rho}$ and $\bar{v}$. Analytical expressions for $\bar{j}(\alpha, \bar{v})$ and $\bar{j}(\bar{\rho}, \bar{v})$ are provided in Appendix D. Note that the functional form of $\bar{j}$ is different depending on whether α or $\bar{\rho}$ is used to evaluate it, but the value of $\bar{j}$ is the same.

In the case when $\bar{\rho} \to \infty$, the current density tends to

$$j|_{\bar{\rho}\to\infty} = \frac{9}{8}\varepsilon\mu\frac{\left(V + \frac{v_B d}{\mu}\right)^2}{d^3} = (1+\bar{v})^2 j_{\mathrm{MG}}. \tag{4.16}$$

The current density in Equation (4.16) represents the space-charge limited current for non-zero bulk velocities.

Integrating the momentum conservation equation in Equation (4.7) across one stage and adding the pressure loss term results in an expression for the static pressure rise across the stage, $\Delta p_{\mathrm{stage}}$,

$$\Delta p_{\mathrm{stage}} = \int_0^d \frac{\mathrm{d}p}{\mathrm{d}x}\mathrm{d}x + \Delta p_L = \int_0^d \rho_c E \mathrm{d}x - \frac{1}{2}\rho v_B^2 K_L = \Delta p_E - \frac{1}{2}\rho v_B^2 K_L. \tag{4.17}$$

As shown by Stuetzer [15] and derived in Appendix D, the pressure rise due to electrostatic forces across a stage, Δp_E, is given by

$$\Delta p_E = \int_0^d \rho_c E \mathrm{d}x = \frac{jd}{\mu} - \frac{\varepsilon v_B}{|\mu|}\left[\left(\frac{2jd}{\varepsilon\mu} + \left(E_0 + \frac{v_B}{\mu}\right)^2\right)^{\frac{1}{2}} - \left|E_0 + \frac{v_B}{\mu}\right|\right]. \tag{4.18}$$

Some of the limits of Equation (4.18) can now be considered. If $v_B = 0$, the electrostatic pressure rise reduces to

$$\Delta p_E|_{v_B=0} = \frac{jd}{\mu}. \tag{4.19}$$

If $v_B = 0$ and the charge density at the emitter is such that $\bar{\rho} \to \infty$, Equation (4.12) can be substituted into Equation (4.19) to obtain an explicit expression for the elec-

trostatic pressure rise as a function of the electrical parameters,

$$\Delta p_E|_{v_B=0,\bar{\rho}\to\infty} = \frac{j_{\mathrm{MG}} d}{\mu} = \frac{9}{8}\varepsilon\frac{V^2}{d^2}. \tag{4.20}$$

In general, it is possible to define a non-dimensional pressure rise, $\bar{p}$,

$$\bar{p} \equiv \frac{\Delta p_E}{\Delta p_E|_{v_B=0,\bar{\rho}\to\infty}} = \frac{\Delta p_E}{\frac{j_{\mathrm{MG}} d}{\mu}}. \tag{4.21}$$

Similarly to $\bar{j}$, the non-dimensional parameter $\bar{p}$ can be formulated in terms of either α and $\bar{v}$, or $\bar{\rho}$ and $\bar{v}$; these two formulations are equivalent. Expressions for $\bar{p}$ as a function of these non-dimensional parameters are given in Appendix D. In the case when $\bar{\rho} \to \infty$,

$$\bar{p}|_{\bar{\rho}\to\infty} = (1+\bar{v})\left(1 - \frac{\bar{v}}{3}\right), \tag{4.22}$$

which represents the pressure rise under space-charge limited conditions for non-zero bulk velocities. A derivation of Equation (4.22) is provided in Appendix D.

The power (P) per unit cross-sectional area (A) drawn by a stage is $\frac{P}{A} = \frac{P_a}{A} + \frac{P_i}{A}$, where $P_a = jVA$ is the power required to accelerate the ions across the gap and P_i is the power draw of the ion source. The pressure rise-to-power ratio Θ of a stage is then defined as

$$\Theta \equiv \frac{\Delta p_E}{P_a/A} = \frac{\Delta p_E}{jV}, \tag{4.23}$$

and is a measure of the static efficiency of the stage analogous to the thrust-to-power ratio of an unducted EAD thruster. If $v_B = 0$, the ratio Θ is

$$\Theta|_{v_B=0} = \frac{\Delta p_E|_{v_B=0}}{jV} = \frac{d}{\mu V}, \tag{4.24}$$

and, in general, the EAD pressure rise of a stage can be related to Θ through

$$\Theta = \frac{\bar{p}}{\bar{j}}\frac{d}{\mu V} = \frac{1}{|\mu|}\sqrt{\frac{9\varepsilon}{8}}\frac{\bar{p}^{3/2}}{\bar{j}}\frac{1}{\sqrt{\Delta p_E}}. \tag{4.25}$$

If the non-dimensional velocity $\bar{v}$ and the electric source number $\bar{\rho}$ are assumed approximately constant ($\bar{j}$ and $\bar{p}$ are constant), Equation (4.25) shows that there is a fundamental trade-off between Δp_E and Θ: a greater pressure rise (which results in higher thrust) implies a lower pressure rise-to-power ratio (lower efficiency). Equivalently, Equation (4.25) shows that the power per unit area scales as $\frac{P_a}{A} \propto \Delta p_E^{3/2}$. This motivates the use of multistaged devices: using multiple ion-acceleration stages decouples the overall pressure rise and the pressure rise-to-power ratio, potentially allowing a device to produce the same overall pressure rise Δp more efficiently. For example, an EAD device with n stages can produce the same electrostatic pressure rise as a single-stage one while drawing $\frac{1}{\sqrt{n}}$ times the power. The latter expression in Equation (4.25) also shows no direct dependency on the electrode gap spacing d. This means that small gap spacings are preferable as they lead to more compact devices and lower DC voltage requirements. Since current density scales as $j \propto \frac{1}{d^3}$, the minimum gap distance would in practice be limited by the current that can be delivered by the ion source or by other engineering limits.

4.3.3 Model of corona-discharge EAD stages

Most of the EAD devices demonstrated to date, both in the context of propulsion and fluid pumping, have used corona-discharge ion sources. An asymmetry in geometry between the emitter and collector is necessary for a corona discharge to occur. Geometries often used include pin-to-mesh [23, 48], wire-to-cylinder [33, 34, 36], or wire-to-airfoil [45]. In this section, a stage geometry consisting of an array of wire emitters and airfoil collectors is considered, in which parallel electrode pairs are separated by a distance Δ as shown in Figure 4-2a. This array is similar to the one tested experimentally by Gilmore and Barrett [36], with the difference that it contains airfoil collectors instead of cylinders to reduce aerodynamic drag.

Stages of corona-discharge electrodes can be stacked in series in different ways. The simplest arrangement is shown in Figure 4-2b: this is the serial stage geometry tested by Gilmore and Barrett [36]. This electrical arrangement only requires one power supply and results in the production of ions of the same polarity in every

stage; however, stages need to be separated by a distance θ to avoid counter-ionic wind, i.e., the drift of ions produced at an emitter to the collector of the previous stage. An alternative electrical arrangement is shown in Figure 4-2c: since an emitter and the previous-stage collector are at the same potential, this electrical arrangement does not result in the production of a counter-ionic wind; therefore, stages could be placed closer together than in the case in Figure 4-2b. A separation θ would still be needed; otherwise, the electric field at the emitter would be weakened by the nearby collector at the same potential [153]. The arrangement in Figure 4-2c results in the production of ions of the same polarity at each stage and requires one separate power supply per stage or one single power supply combined with a potential divider. A third possible electrical configuration that only requires one power supply is shown in Figure 4-2(d): this arrangement alternates stages producing positive and negative corona discharges. Since an emitter and the previous-stage collector are at the same potential, the alternating polarity arrangement in Figure 4-2(d) can also potentially allow stages to be placed close together in series, although a distance θ would still be needed to avoid weakening of the discharge. However, counter-ionic wind (in the direction opposite to the thrust-generating ions) from a stage's emitter to the previous-stage emitter is possible. These three electrical arrangements could also be applied to the ideal stages in the previous section.

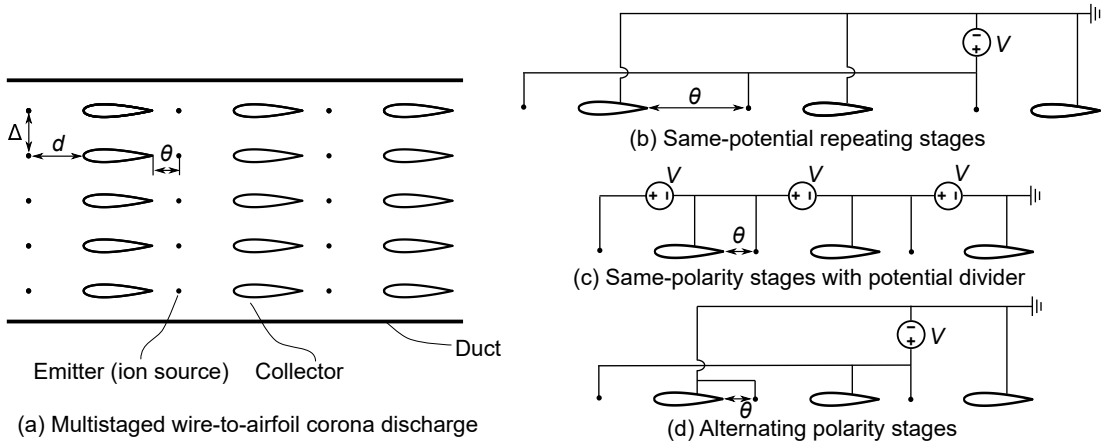

Figure 4-2: Schematic diagram showing a cross-sectional view of an MSD thruster with a wire-to-airfoil corona-discharge ion source. In all figures, three serial stages are shown. The general array geometry is shown in (a): these stages would sit between stations 2 and 3 in the MSD thruster in Figure 4-1a.

The ideal 1-D model considered in the previous section assumes a uniform current density across the cross-section of any given stage. Due to the asymmetry in geometry between the emitter and collector, this model cannot be applied to wire-to-airfoil corona discharges. For this reason, an alternative model for the pressure rise across wire-to-airfoil corona-discharge stages as a function of the electrical and geometric parameters is developed in this section.

When there are no interactions between parallel electrode pairs ($\frac{\Delta}{d} \to \infty$), the current, I_c, produced by an emitter/collector pair in a wire-to-airfoil geometry in stationary air is given by [33, 35]

$$I_c|_{v_B=0,\frac{\Delta}{d}\to\infty} = \begin{cases} 0 & \text{if } |V| < |V_0| \\ C_0 \varepsilon \mu \frac{V(V-V_0)}{d^2} b & \text{if } |V| \geq |V_0| \end{cases}, \tag{4.26}$$

where b is the electrode span and C_0 is some non-dimensional function of electrode geometry and discharge polarity which can be determined experimentally or through simulation. The term V_0 denotes the corona inception voltage, which is a function of the gap spacing and the electrode geometry.

Experimental data shows that the corona-discharge current is a function of both the bulk fluid velocity [164] and the distance between parallel electrode pairs, Δ. Gilmore and Barrett [36] and Belan et al. [38] showed experimentally that as electrode pairs are brought closer together (Δ is decreased), the electric field at the emitters is reduced. As a result of this, the current delivered by any given electrode pair is lower than if they were not in close vicinity of one another. The exact form of these interactions is not known. Here, a model is proposed for the current between an emitter/collector pair of the form

$$I_c = I_c|_{v_B=0,\frac{\Delta}{d}\to\infty} f\left(\frac{\Delta}{d}\right) \bar{j}_c(\bar{v}), \tag{4.27}$$

where f and $\bar{j}_c$ are non-dimensional functions of, respectively, the ratio of inter-electrode distance-to-gap spacing, $\frac{\Delta}{d}$, and the non-dimensional velocity, $\bar{v}$. In Equation (4.27), the function $f\left(\frac{\Delta}{d}\right) \leq 1$ accounts for the weakening in current as electrodes

are brought closer together; the proposed relationship takes the same functional form as those suggested by Gilmore and Barrett [36] and Belan et al. [38]. The term $\bar{j}_c(\bar{v})$ can be interpreted as a correction for the effect of bulk velocity. The corresponding average current density for $|V| \geq |V_0|$ is

$$j = \frac{I_c}{\Delta b} = C_0 \varepsilon \mu \frac{V(V - V_0)}{d^3} \frac{d}{\Delta} f\left(\frac{\Delta}{d}\right) \bar{j}_c(\bar{v}). \tag{4.28}$$

Guerra-Garcia et al. [164] conducted wind tunnel tests on corona discharges with a wire emitter and a wing (airfoil-shaped) collector. They used a "floating" electrical configuration, which eliminates current leakage to the surroundings. They showed that the dependency of current on bulk velocity depends on the electrode orientation: when the emitter is positioned directly upstream of the wing's leading-edge, current increases with velocity. For the purposes of this study, it is assumed that the current scales with bulk velocity according to

$$\bar{j}_c(\bar{v}) = (1 + \bar{v})^2 . \tag{4.29}$$

Equation (4.29) therefore assumes that the current in a corona discharge scales with velocity in the same manner as the 1-D space-charge limited current. This approach is analogous to the one used by Gilmore and Barrett [46] to study the effect of flight velocity on the performance of an unducted EAD thruster. Assuming $|\mu| = 2 \times 10^{-4}\,\mathrm{m^2\,V^{-1}\,s^{-1}}$ [36, 37, 139], Equation (4.29) agrees within 5 % for non-dimensional velocities $\bar{v} < 0.77$ with the experimental data in Guerra-Garcia et al. [164]; however, the actual ion mobility in these experiments is not known and the experimental data corresponds to a single voltage and gap spacing.

Gilmore and Barrett [36] studied the interaction between parallel sets of electrodes in an unducted corona-discharge thruster, and their results were recently validated numerically by Coseru et al. [37]. Gilmore and Barrett [36] tested a single-stage device in static conditions with two sets of parallel emitter wires and cylindrical collectors spaced at a distance Δ and proposed a fit for the thrust density of the form

$$\frac{F_c}{A} = \frac{I_c|_{v_B=0,\frac{\Delta}{d}\to\infty}}{\mu b}\frac{d}{\Delta}\left(1 - 2e^{-4.0\Delta/d}\right), \tag{4.30}$$

where A is the thruster cross-sectional area and F_c is the thrust force produced by the unducted corona discharges.

The thrust force produced by an unducted wire-to-airfoil corona-discharge thruster in static air, $F_c|_{v_B=0}$, is given by [36]

$$F_c|_{v_B=0} = \frac{I_c|_{v_B=0} d}{\mu}. \tag{4.31}$$

From Equations (4.27), (4.30), and (4.31), it can be inferred that the function f, which accounts for the interaction between parallel electrodes, can be modeled as

$$f\left(\frac{\Delta}{d}\right) = 1 - 2e^{-4.0\Delta/d}, \tag{4.32}$$

which takes the same functional form as the fits used by Belan et al. [38] to model the effect of parallel electrode separation.

Equation (4.30) was developed for an unducted, single-stage EAD thruster. In the subsequent analysis, it will be assumed that Equation (4.30) is also applicable to multistaged ducted EAD devices, with a pressure rise across a thruster stage of $\Delta p_E = \frac{F_c}{A}$ as per Equation (4.5). The interaction between serial stages will be ignored, assuming that one of the electrical configurations in Figure 4-2b–d that prevent backward ion flow is used.

The exact effect of bulk velocity on the pressure generation of corona-discharge devices is not known. Here, it will be assumed that the pressure rise scales with bulk velocity in the same way as in the space-charge limited case in an ideal 1-D device, similarly to what was assumed for the current density,

$$\Delta p_E = \Delta p_E|_{v_B=0}\bar{p}_c(\bar{v}), \tag{4.33}$$

where

$$\bar{p}_c(\bar{v}) = (1+\bar{v})\left(1-\frac{\bar{v}}{3}\right). \tag{4.34}$$

Under these assumptions, a model for the EAD pressure rise can be found by combining Equations (4.26), (4.30), and (4.33),

$$\Delta p_E = \begin{cases} 0 & \text{if } |V| < |V_0| \\ C_0\varepsilon\frac{V(V-V_0)}{d^2}\frac{d}{\Delta}f\left(\frac{\Delta}{d}\right)\bar{p}_c(\bar{v}) & \text{if } |V| \geq |V_0| \end{cases}. \tag{4.35}$$

As shown in Appendix D, if $|V| \gg |V_0|$, the pressure rise-to-power ratio, Θ, can be related to the electrostatic pressure rise across a stage provided by an array of corona-discharge electrodes through

$$\Theta = \frac{\bar{p}_c}{\bar{j}_c}\frac{d}{\mu V} \approx \frac{1}{|\mu|}\sqrt{C_0\varepsilon\frac{d}{\Delta}f\left(\frac{\Delta}{d}\right)}\frac{\bar{p}_c(\bar{v})^{\frac{3}{2}}}{\bar{j}_c(\bar{v})}\frac{1}{\sqrt{\Delta p_E}}. \tag{4.36}$$

Equation (4.36) is analogous to Equation (4.25) and shows that there is a trade-off between the EAD pressure rise provided by an array of corona-discharge thrusters and the pressure rise-to-power ratio. This trade-off motivates the use of multiple stages. Equation (4.36) is also independent of the gap spacing, which only appears within the ratio Δ/d. This suggests that stages with small gap spacings and correspondingly small Δ can provide a higher pressure rise per unit volume than those with larger gap spacings. The advantages of small gap spacings were recently confirmed experimentally by Drew et al. [153], who demonstrated an EAD device with a sub-millimeter scale gap spacing, a maximum voltage of 2.3 kV, and a volumetric thrust density of up to $2\,\mathrm{kN\,m^{-3}}$.

In these models, the effect of the separation between the collector of one stage and the emitter in the next one, θ, has been ignored, under the assumption that it is large enough that the stages are independent of each other except through flow velocity (a change in the electrical parameters of one stage alters the constant velocity through the stages and affects other stages' performance). In a real system, the parameter θ would affect pressure losses, due to both wall skin friction and losses at the electrodes;

and the length of the device, which affects its mass and volume. These models also ignore the electrostatic interactions between the EAD electrodes and the duct walls. Previous work on corona discharges with electrodes at very close proximity to surfaces has suggested that charge build-up on the walls can reduce the current delivered by the electrodes at a given voltage [75]. Even though charge build-up on the duct walls might have a negative effect on the thruster, previous studies on ducted EAD systems have not reported any significant reduction in performance due to charge build-up [23, 25, 153].

Similarly to the ideal 1-D model in Section 4.3.2, the thruster inlet condition is that $v_B = v_2$. The static pressure at the inlet of the first stage is p_2, and the outlet pressure of one stage is also assumed to be the inlet pressure of the next one.

To find an expression for the loss coefficient, it is assumed that pressure losses are due to drag forces acting on the collectors, although the analysis could be extended to account for emitter drag or pressure losses due to skin-friction forces on the duct. Assuming quasi-1-D conditions, the loss coefficient, K_L, can be related to the stage drag through

$$K_L = \frac{D_{\text{stage}}}{\frac{1}{2}\rho v_2^2 A_2} = \frac{\frac{w}{\Delta} c_d \frac{1}{2}\rho v_2^2 bc}{\frac{1}{2}\rho v_2^2 b\Delta\frac{w}{\Delta}} = \frac{c}{d}\frac{d}{\Delta}c_d, \tag{4.37}$$

where D_{stage} is the total drag force on the collectors in a stage; w is the width of a stage, such that there are w/Δ emitter/collector pairs in a stage; c is the airfoil chord; and c_d is the drag coefficient. The drag coefficient is expected to increase as $\Delta \to 0$ due to aerodynamic blockage, and this effect can be accounted for by using a "wind tunnel correction" such as Equation (10.35) in Drela [165],

$$c_d = \frac{c_d|_{\Delta\to\infty}}{1 - \frac{1}{2}\frac{c}{d}\frac{d}{\Delta}c_d|_{\Delta\to\infty} - \frac{\pi}{2}\frac{A_a}{\Delta^2}}, \tag{4.38}$$

where $c_d|_{\Delta\to\infty}$ is the uncorrected drag coefficient when there is no blockage and A_a is the airfoil cross-sectional area. The drag coefficient of an airfoil at zero angle of attack in an incompressible flow is a function of the Reynolds number, such that $c_d|_{\Delta\to\infty} = c_d|_{\Delta\to\infty}(\text{Re})$, where $\text{Re} = \frac{v_2 c}{\nu}$ and ν is the kinematic viscosity of the fluid.

The ratio $\frac{A_a}{\Delta^2}$ can be related to other geometric parameters through

$$\frac{A_a}{\Delta^2} = \frac{A_a}{c^2}\left(\frac{c}{d}\right)^2\left(\frac{d}{\Delta}\right)^2, \tag{4.39}$$

where the parameter $\frac{A_a}{c^2}$ is a constant for a given airfoil type.

4.3.4 Thruster performance

In this section, some basic thruster performance results that can be found by combining the momentum theory in Section 4.3.1 with either the ideal 1-D thruster model in Section 4.3.2 or the corona discharge model in Section 4.3.3 are considered. The static pressure rise across a thruster with n stages is given by

$$\Delta p = \sum_{i=1}^{n} \Delta p^i_{\text{stage}} = \sum_{i=1}^{n}\left(\Delta p^i_E - \frac{1}{2}\rho v_2^2 K^i_L\right), \tag{4.40}$$

where the superscript i refers to the properties of stage i. The bulk velocity in the thruster is related to the pressure rise Δp through Equation (4.2). In general, Δp^i_E is a function of the bulk velocity, as expressed by Equation (4.18) for an ideal 1-D device, and by Equation (4.35) for a corona-discharge device. In order to reach an analytical solution, it will be assumed that the stages are repeating, i.e.,

$$\sum_{i=1}^{n}\left(\Delta p^i_E - \frac{1}{2}\rho v_2^2 K^i_L\right) = n\left(\Delta p_E - \frac{1}{2}\rho v_2^2 K_L\right), \tag{4.41}$$

and that Δp_E and K_L are independent of the number of stages and the nozzle area ratio. These assumptions are made in this section only so that simple, explicit expressions for thrust can be derived. In reality, both Δp_E and K_L will vary as the number of stages changes due to the change in flow velocity through the thruster: Δp_E depends on $\bar{v}$, and K_L is a function of the Reynolds number. Substituting Equations (4.2) and (4.41) into Equation (4.40) and rearranging, the pressure rise across

the thruster can be approximated as

$$\Delta p = n \left[\Delta p_E - \frac{1}{2}\rho \left(\phi \sqrt{v_1^2 + \frac{2\Delta p}{\rho}} \right)^2 K_L \right]$$

$$\Delta p \approx n \frac{\Delta p_E - \frac{1}{2}\rho v_1^2 K_L \phi^2}{1 + n K_L \phi^2}. \tag{4.42}$$

Equation (4.42) shows that as more stages are added, the pressure across the thruster increases with diminishing returns. This is compatible with the experimental findings of Qiu et al. [23], who tested the effect of changing the number of stages on the bulk velocity of a multistaged EAD pump with a pin-to-mesh stage geometry and a corona-discharge ion source. They found a saturation point after 25 stages in their particular architecture, after which any additional EAD pressure rise due to the addition of more stages was balanced by pressure losses.

As $n \to \infty$, the pressure rise across the thruster in Equation (4.42) tends to

$$\Delta p \to \frac{\Delta p_E}{K_L \phi^2} - \frac{1}{2}\rho v_1^2. \tag{4.43}$$

The thrust density corresponding to the pressure rise in Equation (4.42) can be computed from Equation (4.4). In non-dimensional form, this is given by

$$\frac{F}{A_2 \Delta p_E} = \phi \left(\frac{2n + \frac{\rho v_1^2}{\Delta p_E}}{1 + n K_L \phi^2} \right) \left(1 - \sqrt{\frac{1 + n K_L \phi^2}{1 + 2n \frac{\Delta p_E}{\rho v_1^2}}} \right). \tag{4.44}$$

A simplified result can be obtained in the case when $v_1 \to 0$, corresponding to static thruster conditions. In this case, the normalized thrust density becomes

$$\frac{F}{A_2 \Delta p_E} = \frac{2n\phi}{1 + n K_L \phi^2}. \tag{4.45}$$

The optimum nozzle area ratio $\phi|_{\text{opt}}$ that maximizes the thrust density in this case is

$$\phi|_{\text{opt}} = \sqrt{\frac{1}{nK_L}}. \tag{4.46}$$

A general expression for the nozzle area ratio that maximizes Equation (4.44) for non-zero v_1 is shown in Appendix D. Depending on the loss coefficient, number of stages, and freestream velocity, the optimum area ratio $\phi|_{\text{opt}}$ can be greater than 1. These divergent nozzles experience an adverse pressure gradient as the nozzle exit pressure is greater than its inlet pressure; as a result of this, separation in the nozzle can occur [163]. In practice, the nozzle area ratio that provides maximum thrust is limited by this flow separation.

The derivation of Equations (4.42)–(4.46) assumes that Δp_E and K_L do not depend on the number of stages and the nozzle area ratio. In general, Equations (4.2), (4.18) or (4.35), and (4.40) should be solved simultaneously to determine the pressure rise across the thruster, Δp, and from this, the thrust density.

Rickard et al. [25] and Qiu et al. [23] conducted tests on multistaged EAD pumps with a geometry similar to that of the MSD thrusters considered here but with pin-to-ring and pin-to-mesh corona-discharge ion sources, respectively. In Appendix D, it is shown that the models derived in this section are able to capture the main trends observed in these experimental studies.

4.3.5 Discussion

The models for ideal ion sources or corona discharges show that the pressure generation and power draw of one stage depend on voltage and gap spacing: for constant gap spacing, pressure increases quadratically with voltage, while ion-acceleration power increases with the voltage cubed. As a result, power scales with pressure as $P_a \propto \Delta p_E^{3/2}$. In addition, the pressure generation of a single stage is limited by electrical breakdown that occurs above some maximum voltage. Because of this, the two strategies to increase the maximum net thrust that can be produced by an EAD thruster, regardless of whether the thruster is ducted or unducted, are (i) increasing the cross-sectional area (or the number of parallel emitter/collector pairs with corona discharges) and (ii)

using serial stages. Since both thrust and power are proportional to the cross-section area, increasing the area results in more thrust but the same thrust-to-power ratio for constant voltage and gap spacing. Alternatively, a thruster with a large cross-section could produce the same thrust as a smaller one but with a higher thrust-to-power ratio by using a lower voltage, due to the $P_a \propto \Delta p_E^{3/2}$ scaling. The main disadvantage of only increasing the thruster cross-sectional area is that practical applications may require very large devices due to the low thrust density of a single-stage thruster, resulting in high structural mass and interference with other aircraft components.

Serial staging, which increases the thrust density, can provide similar thrust or thrust-to-power improvements when the thruster's frontal area is limited. Similarly to the discussion above, multiple serial stages can provide more thrust for the same voltage and gap spacing (as the pressure rise is cumulative) or the same thrust as a single stage but with a higher thrust-to-power ratio. However, serial stages are more adversely affected by pressure losses than geometrically-similar parallel ones, since the higher pressure rise induces a higher flow velocity across the thruster.

Enclosing the EAD electrodes in a duct with an inlet and a nozzle results in two additional effects. First, assuming that the inlet is smooth and avoids pressure losses, changes in static pressure as the flow enters the thruster can result in an additional thrust component if the interior of the inlet experiences an under-pressure compared to the duct's exterior. Since power consumption is due to work on the ions in the EAD stages, adding a duct can increase both the thrust and the thrust-to-power ratio for set electrical parameters. Second, changing the nozzle area ratio alters the flow properties within the thruster. If the loss coefficient is assumed small, the nozzle exit pressure is atmospheric, and changes in EAD pressure with flow velocity are ignored, the thruster exit velocity is independent of nozzle area ratio; the effect of the nozzle is to change the flow velocity through the thruster by conservation of mass. Under these assumptions, a smaller nozzle area ratio would result in less thrust. However, if pressure losses are significant, decreasing the nozzle area ratio can result in higher net thrust since this reduces pressure losses.

The benefits of multistaging in an MSD thruster are limited by pressure losses.

When these pressure losses are accounted for, there is an optimal number of stages that results in a maximum thrust-to-power ratio for a given thrust density. If the product $\phi^2 K_L$ is low, this optimal number of stages is large; however, the optimal stage count decreases to unity as $\phi^2 K_L$ increases.

4.4 Results

The equations governing the performance of MSD thrusters with ideal stages (Equations (4.2), (4.18) and (4.40)) and with corona-discharge stages (Equations (4.2), (4.35), (4.37) and (4.40)) were solved simultaneously using a Newton's method solver in which the Jacobian matrix was evaluated with a finite-difference method. EAD stages were assumed to be repeating. In Section 4.4.1, it was assumed that stages are space-charge limited ($\bar{\rho} \to \infty$) and that the power draw of the ion source was negligible. The nozzle area ratio was selected such that $\phi = \min(1, \phi|_{\text{opt}})$, where $\phi|_{\text{opt}}$ is the nozzle area ratio that maximizes the thrust density for given loss coefficient, freestream velocity v_1, number of stages, and EAD pressure rise Δp_E. The nozzle area ratio was limited to $\phi = 1$ as flow separation in the nozzle is possible for area ratios above that [163]. In some cases, divergent nozzles with $\phi > 1$ could provide better performance than predicted by the results in this section, but these are not considered here due to the inability of the models to predict flow separation. A constant mobility $|\mu| = 2 \times 10^{-4}\,\mathrm{m^2\,V^{-1}\,s^{-1}}$ was assumed [36, 37, 139]. Air density was kept constant and equal to $\rho = 1.23\,\mathrm{kg\,m^{-3}}$. Freestream velocities up to $v_1 = 10\,\mathrm{m\,s^{-1}}$ were considered to represent the flight velocity of an uncrewed aircraft: this is twice the flight speed of the airplane in Xu et al. [45]. More details on the methods can be found in Appendix D.

4.4.1 MSD thruster with ideal 1-D EAD stages

Figure 4-3 shows how the thrust-to-power ratio of an ideal MSD thruster, with a uniform current density across any given cross-section in the ion-acceleration region, changes with the thrust density at static conditions ($v_1 = 0\,\mathrm{m\,s^{-1}}$). The voltage per

unit gap spacing was varied in the range $0 \leq \frac{|V|}{d} \leq 1\,\mathrm{kV\,mm^{-1}}$. Higher voltage-to-gap spacing ratios might be possible, but this upper limit was chosen as electrical breakdown can occur above it [46, 166]. The results show that thrust densities of the order of $100\,\mathrm{N\,m^{-2}}$ (or higher, depending on the loss coefficient) are achievable: this is two orders of magnitude higher than both the estimated maximum thrust density of single-stage corona-discharge thrusters [36] and the thrust density of the EAD thrusters used to propel the airplane of Xu et al. [45]. Figure 4-3 also shows that decreasing the loss coefficient improves the thrust-to-power ratio for given thrust density and number of stages. In Figures 4-3b and 4-3c, it can be seen that there is an optimal number of stages within the range of n shown that provides maximum thrust-to-power ratio for a given thrust density. For example, in Figure 4-3b with $K_L = 0.01$, the optimal number of stages among the cases shown is $n = 50$; however, in Figure 4-3c with $K_L = 0.1$, the optimal number of stages among those shown is $n = 5$. This shows that the higher the loss coefficient is, the lower the optimal number of stages.

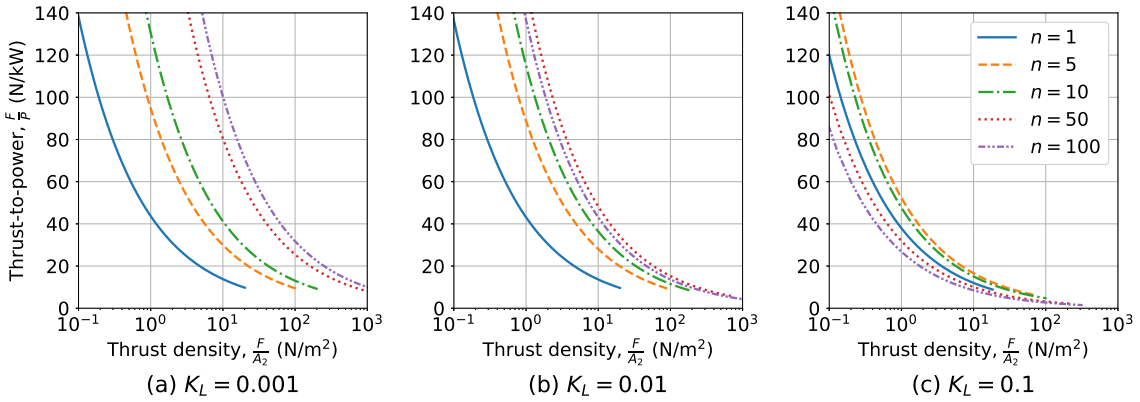

Figure 4-3: Thrust-to-power ratio versus thrust density of an ideal 1-D MSD thruster for different number of stages and stage loss coefficients at static conditions ($v_1 = 0\,\mathrm{m\,s^{-1}}$). Results are parametrized by the voltage-to-gap spacing ratio, $\frac{|V|}{d}$.

The effect of changing the freestream velocity on the performance of an MSD thruster with $n = 10$ stages is shown in Figure 4-4. The thrust-to-power ratio provided by the thruster at a given thrust density is reduced as the freestream speed increases, due to higher pressure losses in the thruster. Figure 4-4 also shows that re-

ducing the loss coefficient improves the performance of MSD thrusters: at a freestream velocity of $v_1 = 10\,\mathrm{m\,s^{-1}}$, a thruster with $K_L = 0.001$ can deliver a thrust density of $\frac{F}{A_2} = 10\,\mathrm{N\,m^{-2}}$ at a thrust-to-power ratio of $\frac{F}{P} = 12.5\,\mathrm{N\,kW^{-1}}$; however, if $K_L = 0.1$, the thrust-to-power ratio at the same thrust density and freestream velocity is reduced to $\frac{F}{P} = 2.2\,\mathrm{N\,kW^{-1}}$.

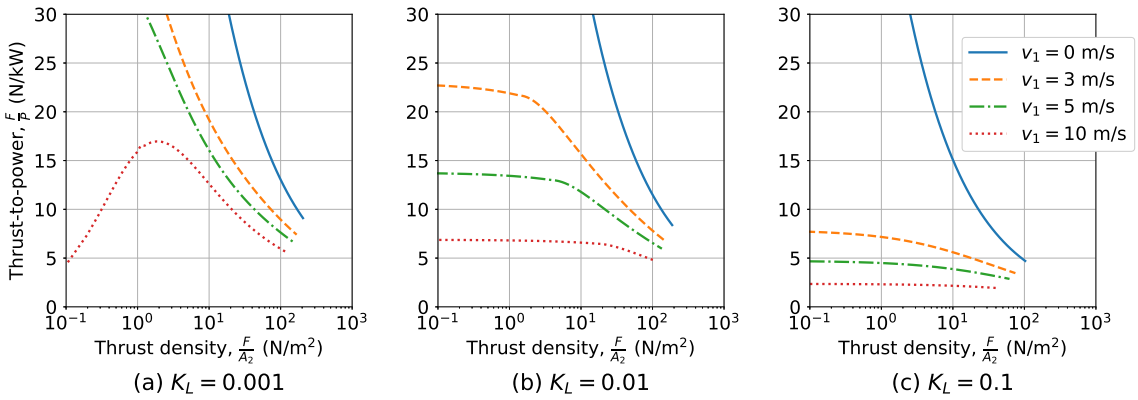

Figure 4-4: Thrust-to-power ratio versus thrust density of an ideal 1-D MSD thruster for different loss coefficients and freestream speeds. The thruster contains $n = 10$ EAD stages.

Figure 4-5 shows the thrust density, power density (total power draw per unit frontal area), and thrust-to-power ratio of an MSD thruster with a freestream velocity $v_1 = 10\,\mathrm{m\,s^{-1}}$ and a voltage per unit electrode gap spacing $|V|/d = 1\,\mathrm{kV\,mm^{-1}}$ against the number of EAD stages. Figure 4-5a shows that the thrust density of an MSD thruster is dependent on the loss coefficient: for a loss coefficient of $K_L = 0.001$, the thrust density scales approximately linearly with the number of stages for $n \leq 100$; however, for $K_L = 0.01$ and $K_L = 0.1$, the thrust density increases with number of stages with diminishing returns. Figure 4-5c shows that for $0.001 \leq K_L \leq 0.01$, there is a number of stages $n > 1$ that provides maximum thrust-to-power ratio. If $K_L = 0.1$, the maximum thrust-to-power ratio is obtained at $n = 1$. Figure 4-5b shows the power demand per unit area of an ideal EAD thruster. For a given number of stages, the power draw is a function of the loss coefficient due to the dependency of current density on the velocity v_2.

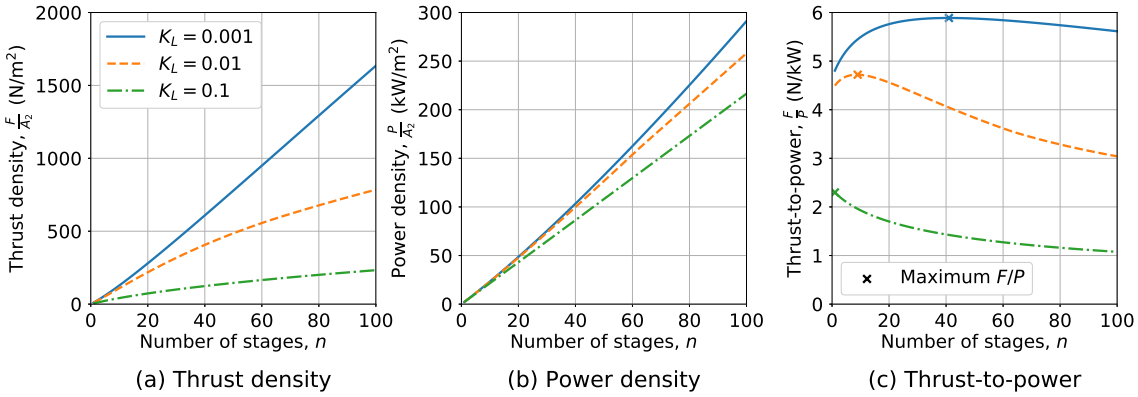

Figure 4-5: Effect of changing the number of EAD stages on the thrust density, power density, and thrust-to-power ratio of an ideal 1-D MSD thruster with a freestream velocity of $v_1 = 10\,\mathrm{m\,s^{-1}}$. The EAD stages are operating at $|V|/d = 1\,\mathrm{kV\,mm^{-1}}$.

The panels in Figures 4-3 and 4-4 and the contours in Figure 4-5 correspond to constant loss coefficients. In a real system, the loss coefficient is a function of the Reynolds number and would, therefore, vary as the thrust density changes. The methods presented in Section 4.3 can be used to analyze a real system with a known variation of loss coefficient with Reynolds number; however, the performance of this system would not follow the plots in Figures 4-3 to 4-5 exactly.

4.4.2 MSD thruster with corona-discharge stages

The results in this section were obtained using the models in Section 4.3.3, corresponding to an MSD thruster with wire-to-airfoil corona-discharge stages. The collectors were assumed to be NACA 0012 airfoils with a ratio of chord-to-gap spacing $\frac{c}{d} = 1$, and a gap spacing of $d = 20\,\mathrm{mm}$ was used for all stages. The drag characteristics of a NACA 0012 airfoil at zero angle of attack were found using the software *XFOIL* [167] as a function of the Reynolds number. The stage loss coefficient was computed using Equation (4.37), which only considers pressure losses due to drag forces acting on the collectors. This analysis can be extended to account for other losses, such as those due to drag forces on the emitters or due to skin-friction forces acting on the duct.

The parameters C_0 and V_0, which define the current–voltage characteristics, depend on the electrode geometry. In the absence of experimental data for corona dis-

charges with a wire emitter and a NACA 0012 airfoil collector, parameters inferred from the experimental data of Moreau et al. [33] were used, which was obtained with a cylindrical collector with a diameter of 12 mm. Due to the difference in geometry, Moreau's data is only valid approximately for the wire-to-airfoil corona discharges considered here. They measured experimentally that $C_0\varepsilon|\mu| = 1.93 \times 10^{-15}\,\mathrm{A\,m\,V^{-2}}$; from this, and using their measured ion mobility, it can be found that $C_0 \approx 0.75$. The inception voltage for a gap spacing of $d = 20\,\mathrm{mm}$ that was used was $|V_0| = 6.1\,\mathrm{kV}$, as reported by Moreau et al. [33].

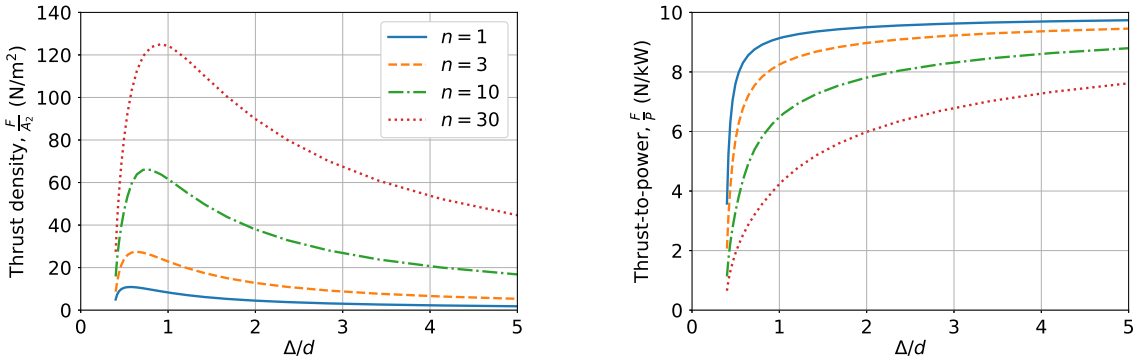

(a) Thrust density (b) Thrust-to-power

Figure 4-6: Thrust density and thrust-to-power ratio versus the ratio of electrode separation-to-gap spacing, $\frac{\Delta}{d}$, of an MSD thruster with corona-discharge stages at static conditions ($v_1 = 0\,\mathrm{m\,s^{-1}}$). Stages are assumed to be repeating, with $d = 20\,\mathrm{mm}$ and $|V| = 20\,\mathrm{kV}$.

Figure 4-6 shows the effect of changing the ratio of interelectrode distance-to-gap spacing, $\frac{\Delta}{d}$, on the performance of an MSD thruster at static conditions. As noted by Gilmore and Barrett [36], Equation (4.35) for the EAD stage pressure rise Δp_E has a maximum at $\frac{\Delta}{d} = 0.41$. The thrust density results in Figure 4-6a show that there is a ratio $\frac{\Delta}{d}$ that provides maximum thrust density; however, the $\frac{\Delta}{d}$ at which thrust density is maximized depends on the number of stages due to the coupling between stage EAD pressure rise and pressure losses. Figure 4-6b shows that for a given number of stages, maximum thrust-to-power is obtained as $\frac{\Delta}{d} \to \infty$. The main reason for this is that increasing $\frac{\Delta}{d}$ reduces the velocity through the thruster and, hence, pressure losses. Figure 4-6a shows that increasing the number of stages provides a higher thrust density at any given $\frac{\Delta}{d}$; in contrast, Figure 4-6b shows that

adding more stages reduces the thrust-to-power ratio for a given $\frac{\Delta}{d}$. This occurs because adding more stages results in higher bulk velocities through the thruster and, therefore, higher stage pressure losses. Since the EAD pressure rise-to-power ratio Θ is only a weak function of the bulk velocity, the result is that as more stages are added, each stage provides a lower net pressure rise but draws approximately the same power, hence resulting in a lower overall thrust-to-power ratio.

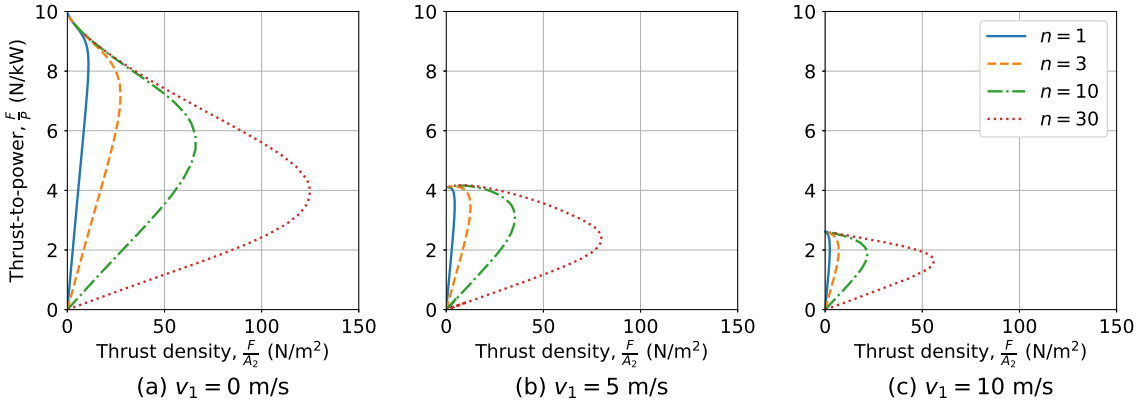

Figure 4-7: Thrust-to-power ratio against thrust density of an MSD thruster with corona-discharge stages for different freestream velocities. The results are parametrized by the ratio $\frac{\Delta}{d}$. Stages are repeating, with $d = 20\,\text{mm}$ and $|V| = 20\,\text{kV}$.

The thrust-to-power ratio is shown against the thrust density in Figure 4-7 for different freestream velocities. The results in Figure 4-7a for $v_1 = 0\,\text{m}\,\text{s}^{-1}$ are the same as those in Figure 4-6, and are parametrized by $\frac{\Delta}{d}$. Figure 4-7 shows that for any freestream velocity, there is a combination of number of stages and $\frac{\Delta}{d}$ that provides maximum thrust-to-power ratio for a given thrust density. Figure 4-7a shows an MSD thruster with 30 stages can deliver a thrust density of $100\,\text{N}\,\text{m}^{-2}$ at a thrust-to-power ratio of $5.6\,\text{N}\,\text{kW}^{-1}$ at static conditions; as a reference, the EAD thruster used to propel the airplane of Xu et al. [45] had two unducted stages and produced a thrust density of $3.6\,\text{N}\,\text{m}^{-2}$ at a thrust-to-power of $6\,\text{N}\,\text{kW}^{-1}$. The results in Figure 4-7 also show the advantages of multi-staging over single-stage thrusters: for all the freestream velocities shown, a thruster with $n = 30$ stages can provide a similar or higher thrust density at a given thrust-to-power ratio than one with $n = 1$.

Since pressure losses scale approximately with the velocity through the thruster

squared, both the thrust density and thrust-to-power ratio decrease as the freestream velocity increases. Figure 4-7 illustrates this effect: an MSD thruster with 30 stages in static conditions (Figure 4-7a) can deliver a maximum thrust density of $125\,\mathrm{N\,m^{-2}}$ at a thrust-to-power ratio of $4.0\,\mathrm{N\,kW^{-1}}$; however, the same thruster at $v_1 = 10\,\mathrm{m\,s^{-1}}$ has a maximum thrust density of $46\,\mathrm{N\,m^{-2}}$ at a thrust-to-power ratio of $1.6\,\mathrm{N\,kW^{-1}}$.

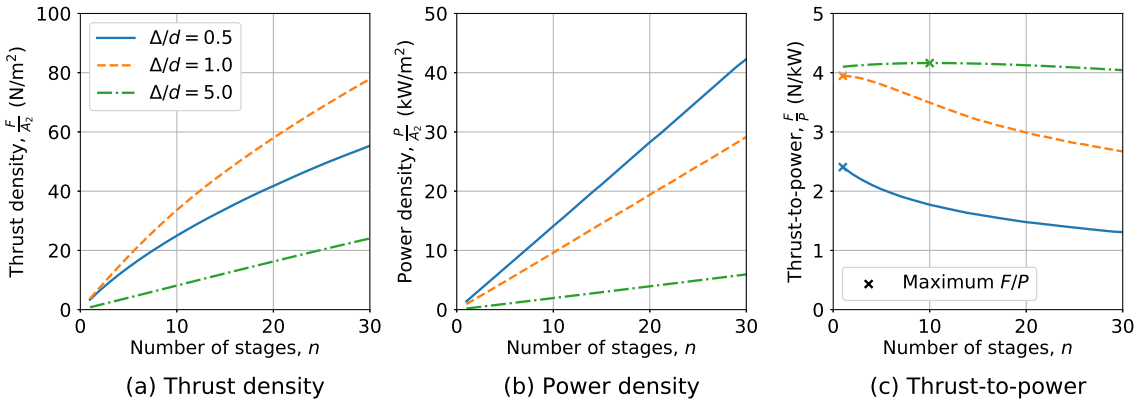

Figure 4-8: Thrust density, power draw per unit area, and thrust-to-power ratio against the number of stages of an MSD thruster with corona-discharge stages. Stages are repeating, with $d = 20\,\mathrm{mm}$ and $|V| = 20\,\mathrm{kV}$. The freestream velocity is $v_1 = 5\,\mathrm{m\,s^{-1}}$.

Figure 4-8 shows how the thrust density, power draw per unit thruster cross-sectional area, and thrust-to-power ratio change with the number of stages in an MSD thruster at a freestream velocity of $v_1 = 5\,\mathrm{m\,s^{-1}}$. In Figure 4-8a, it can be seen that the thrust density is an increasing function of the number of stages; however, the cases when $\frac{\Delta}{d} = 0.5$ and $\frac{\Delta}{d} = 1.0$ show that this increase occurs with diminishing returns. As shown in Figure 4-8b, the power consumption varies approximately linearly with the number of stages. As a result of these two effects, the thrust-to-power ratio in the $\frac{\Delta}{d} = 0.5$ and $\frac{\Delta}{d} = 1.0$ cases, shown in Figure 4-8c, is reduced as more stages are added. In contrast, the thrust-to-power ratio of the $\frac{\Delta}{d} = 5.0$ case is higher than that of the other cases shown and remains approximately constant in the range of n in Figure 4-8c. This finding can be interpreted considering Figure 4-7b: the $\frac{\Delta}{d} = 5.0$ case is near the optimal front that provides maximum thrust-to-power ratio for a given thrust density.

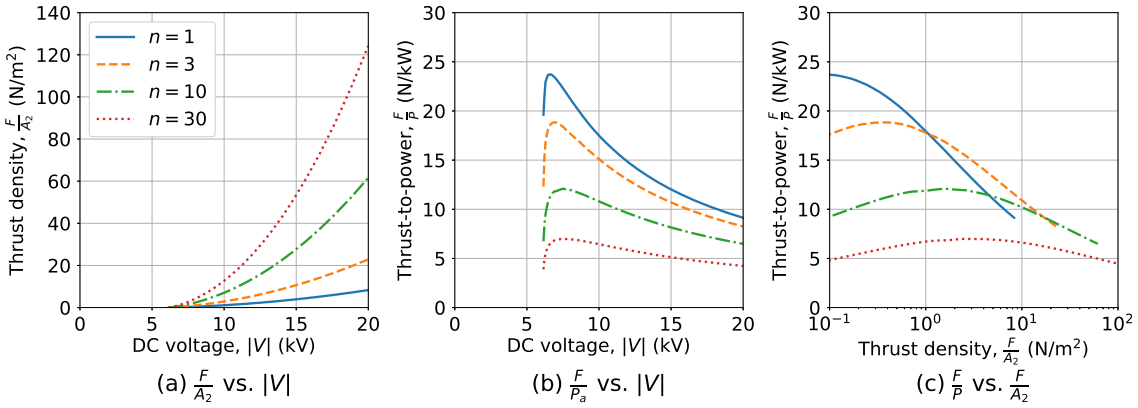

Figure 4-9: Effect of DC voltage on thrust density and thrust-to-power ratio in an MSD thruster with corona-discharge stages. Stages are repeating, with $d = 20\,\text{mm}$ and $\frac{\Delta}{d} = 1$, and freestream conditions are static ($v_1 = 0\,\text{m}\,\text{s}^{-1}$).

The results in Figures 4-6 to 4-8 were obtained at a constant stage DC voltage of $|V| = 20\,\text{kV}$. Figure 4-9 shows the effect of changing the stage DC voltage at static conditions, with a constant $\frac{\Delta}{d} = 1$. Figure 4-9a shows that above the corona inception voltage, the thrust density increases with voltage due to the approximately quadratic dependency of EAD pressure rise on voltage, as expressed by Equation (4.35). However, the thrust-to-power ratio in Figure 4-9b is generally a decreasing function of the DC voltage, except at voltages very close to the inception voltage. This is expected due to the trade-off between the EAD pressure rise and the ratio Θ. Figure 4-9c, in which lines are parametrized by DC voltage, shows that at high thrust density levels, the thrust-to-power ratio decreases with increasing thrust density. Figure 4-9c also shows that there is an optimal front that provides a maximum thrust-to-power ratio for a given thrust density.

4.5 Conclusions

The low thrust density of EAD thrusters has been a barrier to the development of practical applications of this technology. In this chapter, a model has been proposed for the performance of multistaged ducted thrusters with several EAD ion-acceleration stages, which have the potential to provide higher thrust density. Multiple EAD stages are used to decouple the pressure generation and power consumption of individual

stages; it has been shown that there is a trade-off between these if a single stage is used. Enclosing the EAD stages in a duct provides aerodynamic improvements similar to those experienced by ducted fans: most notably, there is a thrust component due to pressure forces acting on the duct. In addition to providing benefits in performance, the duct improves the safety of the system by adding a layer of insulation between the high-voltage electrodes and the surroundings. The duct can also contain an acoustic liner, which would further reduce the noise signature of the thruster in a manner analogous to jet-engine ducts.

The interactions between internal and external flows and the effects of the duct have been modeled using 1-D momentum theory [157], which is agnostic to the particular stage architecture and potentially applicable to a wide range of MSD devices. Two specific EAD stage architectures have been considered: ideal one-dimensional devices, in which each stage has a volumetric ion source (i.e., an ion source that can provide a constant ion density across a cross-section) that is independent of the ion-acceleration stage; and corona-discharge stages, which use wire-to-airfoil corona discharges to both produce ions and accelerate them. The ideal stages have been modeled using analytical results from the one-dimensional EAD theory developed, among others, by Stuetzer [15], Pickard [17], and Gilmore and Barrett [46]. Corona-discharge thrusters have been modeled using empirical models based primarily on the work of Gilmore and Barrett [36].

The results show that MSD thrusters have the potential to provide order-of-magnitude improvements in thrust density at a similar thrust-to-power ratio to single-stage devices or vice-versa. Thanks to this versatility, this type of thruster could enable new missions that are not feasible with single-stage EAD thrusters. For example, a recent computational study by the author's group showed that aircraft propelled by MSD thrusters with ideal 1-D stages could be capable of VTOL if some engineering advances are made [168].

The models predict that MSD thrusters with ideal EAD stages could provide thrust densities of the order of $100\,\mathrm{N\,m^{-2}}$ or thrust-to-power ratios of the order of $100\,\mathrm{N\,kW^{-1}}$. The models can include two different boundary conditions related to

the ion source, in the form of set electric field at the emitter (with an associated non-dimensional parameter α) or set charged density in the emitter (with a non-dimensional parameter $\bar{\rho}$). These two boundary conditions are equivalent as they are related to each other, but the effect of bulk fluid velocity on non-dimensional current or pressure is different depending on whether α or $\bar{\rho}$ are kept constant. The results show that pressure losses due to electrode drag forces or skin-friction forces acting on the duct, captured in the models via a loss coefficient, have a detrimental effect on the performance of MSD thrusters. It has also been found that their performance degrades as the freestream flow velocity increases, resulting in higher pressure losses. The thrust density and efficiency of MSD thrusters with ideal EAD stages are independent of the electrode gap spacing: this implies that the EAD stages could be designed with small gap spacings, resulting in lower DC voltage requirements and higher thrust per unit thruster volume. Practical limits to stage miniaturization may exist. For example, small gap spacings result in larger current density, which may be difficult to produce with an ion source. Similarly, small electrodes may suffer from structural issues due to their low flexural rigidity.

MSD thrusters with wire-to-airfoil corona-discharge stages have also been considered. Each stage in these devices contains a set of emitter/collector electrode pairs; different strategies to prevent ions produced at the emitter of one stage from drifting to the collector of the previous stage have been suggested. Using the models, it has been shown that this type of MSD thruster could provide a thrust density of the order of $100\,\mathrm{N\,m^{-2}}$ in static conditions at a thrust-to-power ratio similar to that of the EAD thruster used to propel the airplane of Xu et al. [45] (approximately $6\,\mathrm{N\,kW^{-1}}$).

Even though the 1-D models can capture the effect of most of the relevant geometric and electrical parameters in a real MSD system, they contain several simplifications. As a result, real systems might perform differently from what is predicted here. The models ignore the boundary layers on the duct, which can increase drag and reduce the mass flow rate. The momentum theory model assumes that the properties in the far wake are the same as those at the nozzle exit; in reality, further expansion or contraction of the flow is possible outside of the nozzle, depending on

the duct geometry. In the corona-discharge stages proposed in this study, the real flowfield will not be one-dimensional; instead, the velocity profile will change across the cross-section due to the Coulomb forces from the EAD stages and skin-friction forces acting on it. Moreover, a correction for the freestream velocity was applied to the corona-discharge stages based on the ideal 1-D models; the real effect of velocity on corona discharges is more complex than predicted by these models and should be studied in more detail.

Future work should focus on validating and improving the models presented in this study through experimentation or detailed computational simulations: Chapter 5 describes an experimental study that verifies some of the main theoretical predictions in this chapter. In addition, some engineering challenges that could limit the performance of MSD thrusters need to be overcome. For example, charge build-up on the duct could reduce the electrostatic pressure rise produced by a stage. While potentially reducing performance, it is not anticipated that charge build-up on the duct walls will affect the feasibility of MSD thrusters, as ducted EAD devices have been demonstrated in the past. This work has shown that reducing the stage loss coefficient can provide large improvements in both thrust density and efficiency; future work should study possible emitter/collector geometries that result in low loss coefficients. Ideal one-dimensional EAD devices require an ion source that can produce volumetric ionization. Some work has been conducted on EAD devices with ion sources separate from the ion-acceleration stage, such as DBDs [42, 128] or NRP discharges [106], but further research into volumetric ion sources is needed to enable this kind of MSD thruster.

This page intentionally left blank.

Chapter 5

Experiments in multistaged ducted thrusters

5.1 Collaboration statement

The author designed all experiments and setup, with the UROP student Christopher Vargas contributing to the multistage collector holder design. The author built the ducts and electrodes for single-stage experiments with assistance from the UROP student Jayaprakash Kambhampaty, and the author built those for multistage experiments with assistance from the UROP students Christopher Vargas and Alazar Lemma. The author carried out all experiments and performed all data analysis.

5.2 Introduction

The theoretical models of MSD thrusters in the previous chapter suggest that EAD devices with multiple stages can provide improvements in thrust density or thrust-to-power ratio over single-stage devices. However, these models make simplifications (such as assuming 1-D conditions or a constant-area wake) and need to be validated experimentally. As noted in the previous chapter, ducted EAD systems had been demonstrated prior to this work for fluid pumping applications [15, 23, 25]. Within the context of propulsion, Drew and Follmer [153] recently tested a 3-stage millimeter-

scale ducted EAD device without an inlet or nozzle and with a needle-to-mesh discharge geometry, demonstrating high areal and volumetric thrust densities but a low net thrust due to the small scale of their device.

In this study, experiments were performed on MSD thrusters with a wire-to-airfoil corona-discharge ion source. Two types of experiments were done: single-stage tests and multistage experiments with up to 10 serial stages. The main aims of this study are to validate the theoretical predictions in Chapter 4 and to establish a baseline for the performance of this type of thruster. This work also represents one of the first implementations of an MSD device for EAD thrust generation and, to the author's knowledge, the first in which the thruster contains an inlet and a nozzle.

5.3 Methods

Two sets of experiments were conducted: single-stage experiments, whose purpose was to explore the effect of stage geometric parameters; and multistage experiments, which studied the impact of changing the stage count. In all experiments, ambient temperature and relative humidity were recorded by an Omega HH311 probe.

5.3.1 Single-stage experiments

The first set of experiments that was conducted involved a duct containing a single stage of EAD electrodes. The experimental setup is shown schematically in Figure 5-1. The emitters were 56 µm diameter tungsten wires. The collectors had an HT14 airfoil profile with a thickness-to-chord-ratio rescaled to 10 % and a 20 mm chord; these were 3D-printed out of polylactic acid and coated in aluminum foil for electrical conductivity. A duct with a square cross-section of 180 mm side was made out of Styrofoam. Two sets of 3D-printed electrode holders, shown schematically in Figure 5-1a, were attached to the duct with epoxy adhesive. These holders contained three rows of holes, which were vertically spaced such that the emitters and collectors would be separated by a gap spacing d. The emitter wire was threaded around the topmost row of holes to achieve a wound pattern of parallel emitters across the duct's cross-section

with an electrically-continuous wire, as shown in Figure 5-1a. To reduce emitter bowing under its own weight or electrostatic forces, the two ends of the emitter were attached to nylon screws inserted into the electrode holders that, when tightened, increased the tension in the wire. Up to two additional intermediate screws were used for the same purpose to ensure wire tension was uniform even if the wire was long. When intermediate screws were used to maintain tension, the emitter wire was cut into several portions to enable tightening; copper tape was used to ensure that these portions were electrically connected to each other.

Each collector contained two 0.8 mm diameter transverse holes located at the quarter-chord and mid-chord points. These holes were used for mounting the collectors to the duct: for each collector, two small metallic pins were run through the second and third rows of holes in each of the electrode holders, such that these went through the duct and into the holes in the collectors, holding them in place. Hence, each collector was held by four pins in total, two on each side. To achieve electrical continuity, the collectors were connected to each other via thin wires with a dielectric coating flushed against the side of the duct. The external portions of the emitter wire and the pins were covered in electrical tape to prevent unwanted external corona discharges.

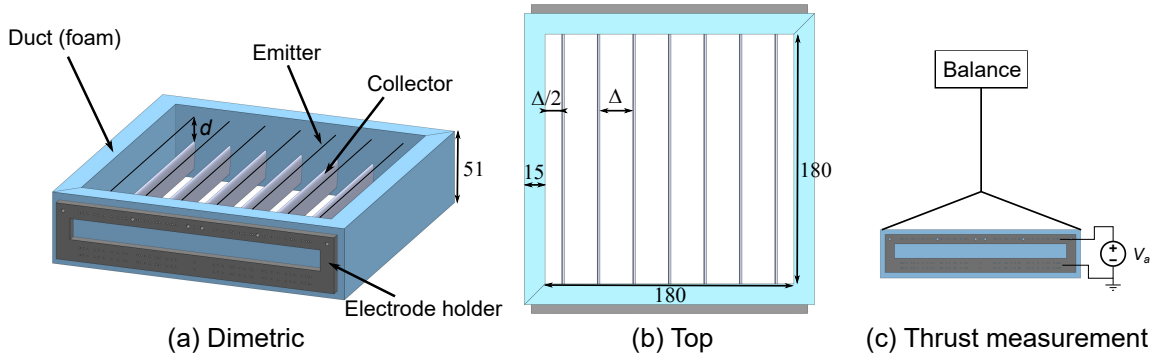

Figure 5-1: Schematic diagrams of the single-stage experimental setup. (a) Dimetric view of the duct showing the emitters, collectors and electrode holders; seven emitter/collector pairs are shown. (b) Top view of the duct. (c) Front view of the duct showing a positive corona electrical arrangement in the thrust stand. Dimensions in millimeters.

The duct and electrode holders were designed to be reused with different numbers

of emitter and collector pairs. In these experiments, between 1 and 13 electrode pairs were tested. These were placed uniformly across the cross-section, resulting in a distance $\Delta = \frac{w}{N_e}$ between pairs, where $w = 180\,\text{mm}$ is the internal width of the square duct and N_e is the number of emitter/collector pairs. This layout is shown schematically in Figure 5-1b; note that the distance between the first and last electrode pairs and the duct is $\frac{\Delta}{2}$. Whereas the presence of the duct imposes an impermeability condition on the flow and the charge transport at the duct surface, the electric field can permeate through the duct material. Therefore, the tested geometry is not equivalent to an infinite array and experiences edge effects. Three different gap spacings were used: 15, 20, and 30 mm. As the setup does not allow changing the gap spacing, ducts with different electrode holders were made for each of these three gap spacings.

Experiments were done with either positive or negative coronas. In the positive-corona configurations, the emitters were connected to a Matsusada AU-120P2.5 positive power supply; in the negative-corona cases, the emitters were connected to a Matsusada AU-120N2.5 negative power supply. In both cases, the collectors were grounded. Current measurements were provided directly by the power supplies' built-in ammeters. The duct was suspended from a Sartorius Entris 4202 balance with a resolution of 10 mg, which was supported by a cantilevered GFRP structure at a height of 2.5 m above ground. The thrust force produced by the duct was estimated using the change in weight measured by the balance. In the single-stage experiments, the relative humidity changed in the range of 57.1–72.7 % in the experiments with $d = 15\,\text{mm}$, in the range of 28.6–41.5 % with $d = 20\,\text{mm}$, and in the range of 52.4–63.7 % when $d = 30\,\text{mm}$. The ambient temperature varied in the range of 19.2–25.0 °C across experiments. Despite these changes in ambient conditions, no apparent effects of temperature or humidity were observed on the discharges.

5.3.2 Multistage experiments

The stage design in the experiments with multiple stages was based on the single-stage ducts. The stages were designed to be modular to facilitate changing the number of

stages in an otherwise identical setup. The ducts containing the EAD stages had a height of 51 mm and a square internal cross-section with a 180 mm side, similar to those in the single-stage tests. The EAD stages, therefore, had a cross-sectional area of $A_2 = 0.0324\,\mathrm{m}^2$ (using the station notation in Figure 4-1a). The duct also contained two external holes that were used for mounting: two nylon M8 threaded rods were inserted into these holes such that the stages could be held together between two sets of nuts. In these tests, the EAD stages were also attached to a parabolic inlet with a length of 80 mm and a width of 35 mm in the direction normal to the thruster's longitudinal axis; the inlet had a thickness of 15 mm in the direction normal to its internal surface and had a rounded tip with a diameter of 15 mm.

Downstream of the EAD stages, the duct was attached to straight nozzles with a longitudinal length of 100 mm and exit area ratios of $\phi = 1.0$, 0.8, 0.6, or 0.4. The modular components were held together by the pressure between the two sets of nuts inserted into the threaded rods. Some small gaps existed between the modular stages due to surface imperfections, implying that a small leakage of air to the surroundings was possible. A 10-stage MSD thruster containing an inlet and a nozzle is shown in Figures 5-2a–b and a modular stage is shown in Figure 5-2c.

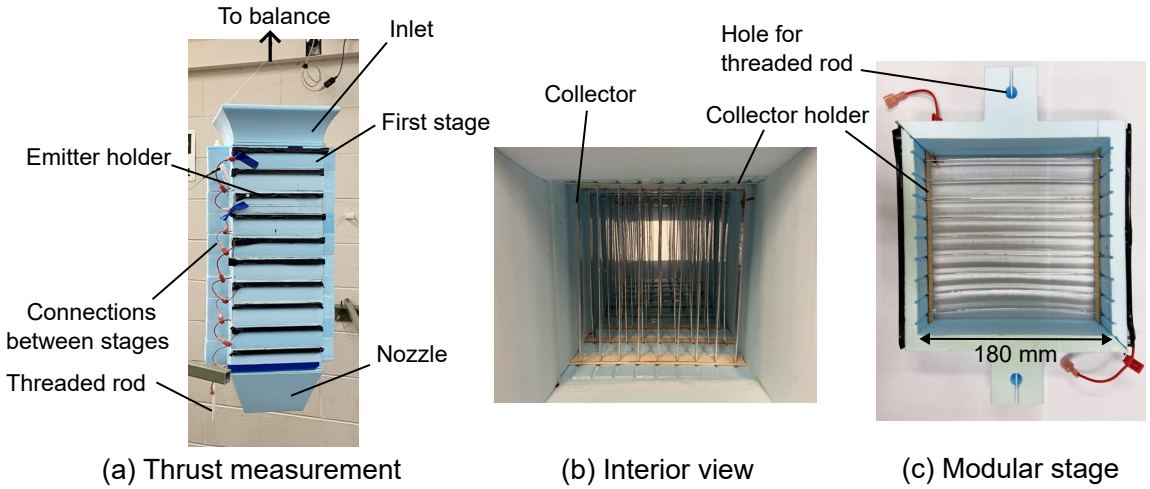

Figure 5-2: Photographs of the experimental setup used in the multistage experiments. (a) shows a 10-stage MSD thruster suspended from a balance, (b) shows the interior of the 10-stage MSD thruster, and (c) shows one of the modular stages. In (a) and (b), the thruster is fitted with a nozzle of area ratio $\phi = 0.4$.

A Matsusada AU-50P12 positive power supply was used to produce the discharges. Stages were arranged using the alternating polarity configuration shown in Figure 4-2d: the emitters of the first stage were connected to the output of the positive power supply and to the collectors of the second stage; the collectors of the first stage were connected to ground and to the emitters of the second one. Subsequent stages had the same electrical arrangement. This electrical setup results in positive coronas in the odd-numbered stages and negative coronas in the even-numbered stages. In the single-stage experiments, it was found that negative coronas had a lower sparking voltage than positive coronas for a given gap spacing. To reach higher thrust levels in the multistage tests, the negative-corona stages had a larger gap spacing than the positive-corona stages: positive stages had a gap spacing $d = 20\,\text{mm}$, and negative stages had $d = 25\,\text{mm}$, ensuring that both stage polarities had similar sparking voltages.

All stages contained nine emitter/collector pairs and had a distance of $\Delta = 20\,\text{mm}$ between electrode pairs. The emitters were 56 µm diameter tungsten wires (same as in the single-stage tests), and the collectors were wooden flat plates covered in aluminum foil with a chord of 10 mm and a thickness of 1.1 mm, selected for ease of manufacturing compared to the 3D-printed airfoils used in the single-stage tests. The emitters were held by externally-mounted acrylic plastic holders, whereas the collectors were held by thin internally-mounted wooden holders containing slots that the collectors were pressure-fitted into. In every stage, one of these collector holders had a side covered in aluminum foil facing the duct wall, which ensured electrical continuity between the collectors. The inside of the duct also contained thin vertical slots approximately 3 mm deep to allow the flat-plate collectors to be inserted into the holders (see Figure 5-2b). The electrodes were placed such that the distances between the top of the stage's duct and the emitters and between the trailing edge of the collectors and the bottom of the duct were the same. Therefore, the distance between an emitter and the previous stage's collector was approximately $\theta = 19\,\text{mm}$. Similarly to the single-stage tests, screws were used to ensure that the emitters were tensioned. Figure 5-2b shows a photograph of the interior of a 10-stage MSD thruster.

The thrust force was measured by suspending the entire device from the same

Sartorius Entris 4202 balance used in the single-stage experiments. Current and voltage readings were obtained directly from the DC power supply. The ambient temperature remained in the range of 21.6–22.3 °C, and relative humidity changed in the range of 13.9–27.3 % during the multistage experiments.

5.3.3 Data processing

The DC voltage was gradually increased in steps of 1 kV, starting from a voltage below corona inception and up to a maximum voltage just below sparking; this maximum voltage depended on the gap spacing and on the discharge polarity. Current, thrust, and voltage readings were sampled at a frequency of 1.5 Hz for 15 s before changing to the next voltage point. Data was averaged over a 10 s interval after a 3 s waiting time for each voltage set point. The 95 % confidence interval for each data point was taken to be 1.96 times the standard deviation over the averaging time.

5.4 Results

The results are divided into two sections. Section 5.4.1 contains the results and discussion of the single-stage experiments, which explore the effect on the current–voltage characteristics of changing the gap spacing d, and the distance between parallel electrode pairs Δ. These results were used to determine the stage geometry used in the multistage experiments, discussed in Section 5.4.2.

5.4.1 Single-stage experiments

The current drawn by the single-stage device with positive coronas is shown in Figure 5-3 against the applied voltage. Three panels are shown, each corresponding to a different gap spacing. The experimental data is shown in the form of markers. In the legend, the parallel electrode pair separation Δ has been normalized by the gap spacing d. Note that similar markers across different panels correspond to the same dimensional separation Δ but to a different $\frac{\Delta}{d}$ ratio as d is different. The data in

Figure 5-3 is only shown for voltages below the onset of reverse emission.

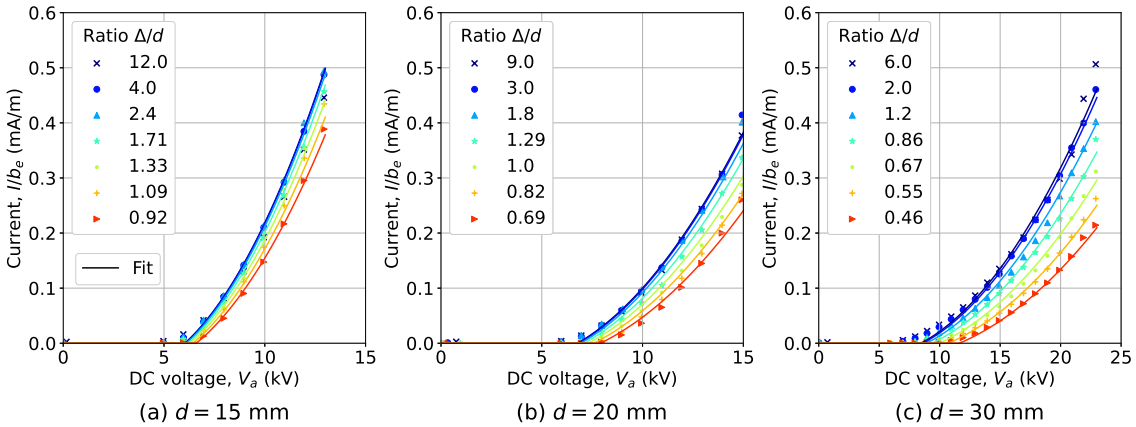

Figure 5-3: Current drawn per unit emitter span against voltage for a single-stage device with a positive corona ion source. Markers show experimental data, whereas solid lines correspond to fits of the form of that in Equation (5.1). Voltages shown up to the onset of reverse emission.

The results in Figure 5-3 show that the current drawn per unit wire span at a given voltage is reduced as the distance between parallel electrode pairs, Δ, decreases. This trend was previously shown experimentally by Gilmore and Barrett [36] using two electrode pairs and by Belan et al. [38] with five electrode pairs, and numerically by Coseru et al. [37]. The reduction in current per unit span at a given voltage can be attributed to the weakening in the electric field at the emitter as the electrode pairs are brought closer together.

The results in Figure 5-3 also show that as Δ is decreased, the corona inception voltage increases. This effect was predicted by Coseru et al. [37] based on computational simulations, but was not accounted by Gilmore and Barrett [36] in their model for the effect of Δ. Based on the results in Figure 5-3, a model is proposed for the effect of parallel electrode pair separation, Δ, in a corona discharge. This model takes the form

$$I = \begin{cases} 0 & \text{if } |V_a| < |V_0| \\ C_0\left(\frac{\Delta}{d}\right)\varepsilon\mu\frac{V_a\left[V_a - V_0\left(d,\frac{\Delta}{d}\right)\right]}{d^2}b_e & \text{if } |V_a| \geq |V_0| \end{cases}, \tag{5.1}$$

with

$$C_0\left(\frac{\Delta}{d}\right) = C_{0,\infty}\left[1 - \exp\left(-\xi_a\frac{\Delta}{d}\right)\right], \tag{5.2}$$

where $C_{0,\infty}$ is the corona constant when there are no interactions between electrode pairs ($\frac{\Delta}{d} \to \infty$) and ξ_a is a dimensionless parameter, and with

$$V_0\left(d, \frac{\Delta}{d}\right) = V_{0,\infty}(d)\left[1 + \left(\frac{\xi_b}{\Delta/d}\right)^2\right], \tag{5.3}$$

where ξ_b is another dimensionless parameter and $V_{0,\infty}(d)$ is the inception voltage when there are no interactions between parallel electrode pairs, e.g., when there is only one electrode pair. This model takes the same functional form as the current–voltage characteristic of a wire-to-cylinder or wire-to-airfoil configuration [33, 35] but allows for both the corona constant C_0 and the inception voltage V_0 to be functions of the ratio Δ/d. The functional forms for $C_0\left(\frac{\Delta}{d}\right)$ and $V_0\left(d, \frac{\Delta}{d}\right)$ are assumed. These have the expected limits: $C_0 \to 0$ and $V_0 \to \infty$ as $\frac{\Delta}{d} \to 0$; and $C_0 \to C_{0,\infty}$ and $V_0 \to V_{0,\infty}(d)$ as $\frac{\Delta}{d} \to \infty$. The expression for C_0 also has the same functional form as those proposed by Belan et al. [38].

Table 5.1: Parameters corresponding to the models in Equations (5.1)–(5.3) for the specific wire-to-airfoil discharge geometry tested here. Parameters determined by a best fit to experimental data.

Polarity	$C_{0,\infty}$	ξ_a	ξ_b	$V_{0,\infty}$ (kV) $d = 15\,\text{mm}$	$V_{0,\infty}$ (kV) $d = 20\,\text{mm}$	$V_{0,\infty}$ (kV) $d = 30\,\text{mm}$	N	r^2
Positive	0.700	1.890	0.285	6.029	6.765	8.425	242	0.994
Negative	0.785	2.074	0.273	−5.902	−6.733	−8.972	244	0.991

The ion mobility in positive coronas was estimated to be $\mu_p = (2.0 \pm 0.1) \times 10^{-4}\,\text{m}^2\,\text{V}^{-1}\,\text{s}^{-1}$ from the thrust and current measurements in the three tests with only one emitter/collector pair, in which the thrust influence of the duct is expected to be smallest; this value is compatible with previous work [37, 128]. The current drawn for a given gap spacing, distance Δ, and thrust per unit span was found to be 1.14 times higher on average with negative coronas than with positive coronas. Therefore, the ion

mobility in negative coronas was assumed to be $|\mu_n| = (2.3 \pm 0.1) \times 10^{-4}\,\mathrm{m^2\,V^{-1}\,s^{-1}}$, which is also the mobility measured in tests with only one electrode pair. Table 5.1 shows the parameters corresponding to the model Equation (5.1) found by applying a fit to the experimental data in Figure 5-3 for positive coronas, and to similar data sets for negative coronas. The average values of ion mobility were used to calculate these parameters. In this table, N represents the number of experimental data points used to produce the fits and r^2 is the coefficient of determination. The parameters in Table 5.1 show that positive and negative coronas have similar inception voltages and that the effect of changing Δ is also similar for both polarities, since the parameters ξ_a and ξ_b differ by less than 10 % across the two polarities. Table 5.1 also shows that C_0 is greater for negative coronas than for positive coronas.

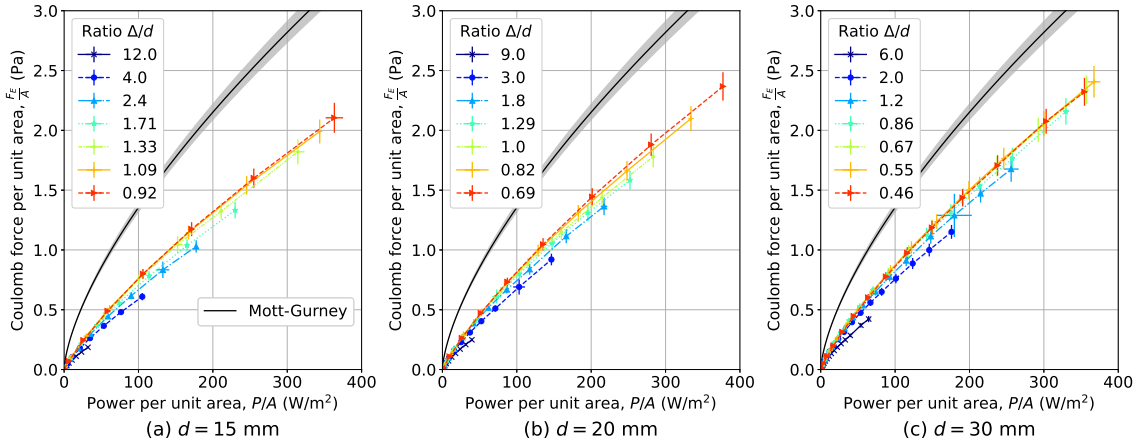

Figure 5-4: Ratio $\frac{F_E}{A} = \frac{Id}{\mu}\frac{1}{b_e\Delta}$ against the power draw per unit cross-sectional area for positive coronas with different ratios Δ/d and gap spacings. Results parametrized by voltage and only shown up to the onset of reverse emission; power levels higher than those shown here are possible. Error bars show a 95 % confidence interval. Theoretical 1-D limit (Mott-Gurney) also shown; the shaded region represents its uncertainty.

As shown by Gilmore and Barrett [36], the electrostatic or Coulomb force, F_E, acting on the fluid in the gap is the integral of the Coulomb body force in the gap and can be expressed as $F_E = \frac{Id}{\mu}$. The electrostatic force acting on the electrodes per unit cross-sectional area, A, is $\frac{F_E}{A} = \frac{Id}{\mu}\frac{1}{b_e\Delta}$. In the absence of fluid acceleration, the pressure rise across a stage is given by $\Delta p_E = \frac{F_E}{A}$: this is the basis of the model for the electrostatic pressure rise Δp_E from corona discharges in Equation (4.35). The

power draw per unit cross-sectional area is $\frac{P}{A} = \frac{IV_a}{b_e \Delta}$. Figure 5-4 shows the ratio $\frac{F_E}{A}$ against the power draw per unit cross-sectional area in a positive corona. The results suggest that there is an optimal front of maximum $\frac{F_E}{A}$ for a given power per unit area; the results tend to that front as $\frac{\Delta}{d}$ is reduced. The 1-D theoretical limit for Coulomb force per unit area is governed by the Mott-Gurney law in Equation (2.3); this limit is shown in Figure 5-4 as a solid black line. The Coulomb force per unit area obtained with positive coronas for a given P/A is below the 1-D limit in all cases; however, the results in Figure 5-4c for $d = 30\,\text{mm}$ reach up to 74 % of the 1-D limit.

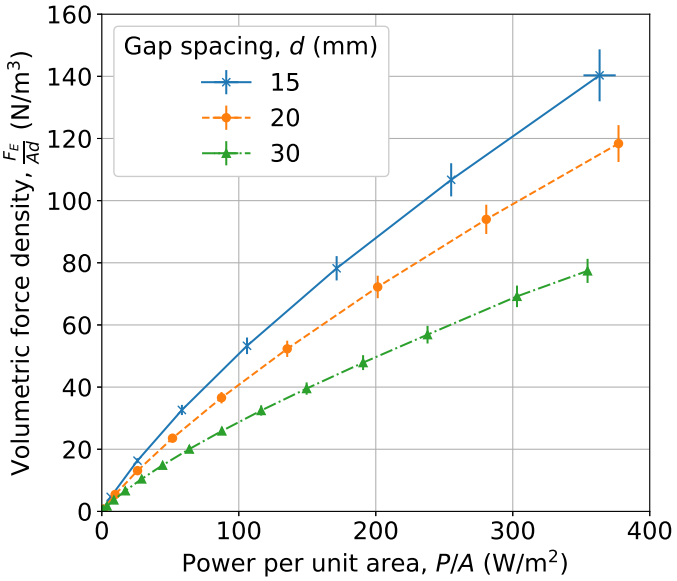

Figure 5-5: Comparison of the Coulomb force per unit gap volume, $\frac{F_E}{Ad}$, produced at three different gap distances. Data for positive coronas with $\Delta = 14\,\text{mm}$, which is close to the optimal front. Error bars show a 95 % confidence interval.

The results in Figure 5-4 show that the optimal front of force per unit area versus power density is only weakly dependent on gap spacing: the maximum ratio $\frac{F_E}{A}$ in Figure 5-4a at a given power with $d = 15\,\text{mm}$ lies within 20 % of that in Figure 5-4c for $d = 30\,\text{mm}$. These results highlight the value of devices with a small gap spacing, as the electrostatic force per unit gap volume for a given $\frac{P}{A}$ is expected to increase as the gap spacing is reduced. Figure 5-5 illustrates this by comparing the electrostatic force per unit gap volume, $\frac{F_E}{Ad}$, produced at the three different gap distances tested. The results show that the ratio $\frac{F_E}{Ad}$ at a given P/A is up to 80 % higher when $d = 15\,\text{mm}$

than when $d = 30\,\text{mm}$.

5.4.2 Multistage experiments

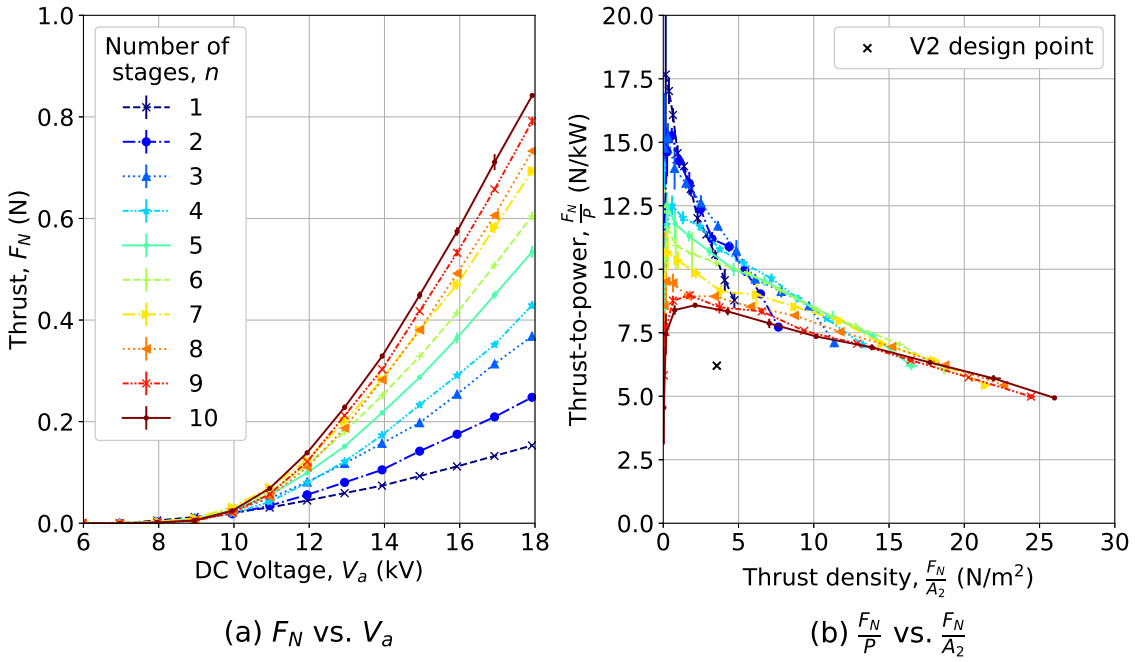

(a) F_N vs. V_a (b) $\frac{F_N}{P}$ vs. $\frac{F_N}{A_2}$

Figure 5-6: Thrust–voltage characteristics of an MSD thruster with $\phi = 1.0$. In (a), the net thrust is shown against the applied voltage for different number of stages. In (b), the thrust-to-power ratio is shown against the thrust density. Error bars show a 95 % confidence interval.

Experiments were performed with MSD thrusters containing up to 10 corona-discharge stages. In these tests, stages used an alternating polarity arrangement, such that odd-numbered stages produced positive coronas and even-numbered stages produced negative coronas. To ensure that all the stages had a similar sparking voltage, the gap spacing of the negative-corona stages was higher than that of the positive-corona stages. Figure 5-6a shows the net thrust produced by these thrusters against the applied voltage for different number of stages. As expected, the results show that increasing the stage count provides a higher thrust at a given voltage. However, these improvements occur with diminishing returns: a one-stage device at 18 kV produces approximately the same thrust as the thrust difference between a 10-stage and a 7-stage thruster at the same voltage. A 10-stage thruster can produce up to 0.84 N

within the range of voltages shown, with an areal thrust density of $26.0\,\mathrm{N\,m^{-2}}$; this thrust density is 7.3 times higher than that of the two-stage thruster used to propel the aircraft in Xu et al. [45]. The volumetric thrust density corresponding to this point is $36.3\,\mathrm{N\,m^{-3}}$, with the volume encompassing the entire thruster internal volume, including the inlet and the nozzle. Figure 5-6 also demonstrates that the alternating polarity arrangement can allow serial EAD stages to be placed in relative proximity to each other without the need for the several-gap-spacing separations discussed in Gilmore and Barrett [36] when only one discharge polarity is used.

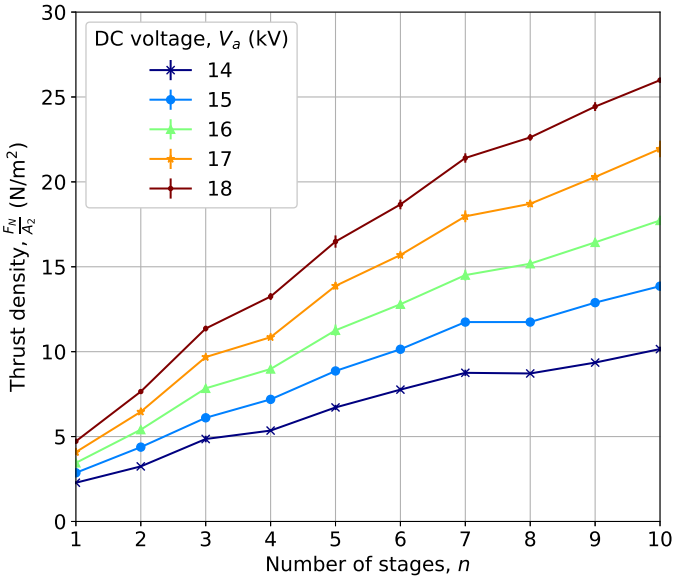

Figure 5-7: Areal thrust density produced by an MSD thruster with $\phi = 1.0$ versus number of stages for different applied voltages. Error bars show a 95 % confidence interval.

Figure 5-6b shows how the thrust-to-power ratio changes with the thrust density for different stage counts. For reference, the design point of the aircraft in Xu et al. [45] is also shown, labeled as "V2 design point" ($3.6\,\mathrm{N\,m^{-2}}$ at $6.2\,\mathrm{N\,kW^{-1}}$). The results show an optimal front of thrust-to-power ratio for a given thrust density and that the optimum number of stages that maximizes the thrust-to-power ratio depends on the thrust density. These findings are compatible with the predictions in Figure 4-9c from the theoretical models. An MSD thruster with three stages can deliver the same thrust density as the V2 thruster at a thrust-to-power ratio of $11.7\,\mathrm{N\,kW^{-1}}$,

88 % higher than the V2 thruster. Conversely, a 10-stage MSD thruster can deliver a thrust density of $19.0\,\mathrm{N\,m^{-2}}$ at the same thrust-to-power ratio as the V2 thruster design point (5.3 times higher thrust density).

The effect of changing the number of stages for a constant DC voltage is shown in Figure 5-7. These results indicate that adding more stages increases the thrust produced by the device with diminishing returns. These results also show that adding a negative-corona (even-numbered) stage generally provides less thrust than adding a positive-corona (odd-numbered) stage; this observation is consistent with the negative-corona stages having a higher gap spacing than the positive-corona stages, which results in lower current and pressure generation for a given voltage.

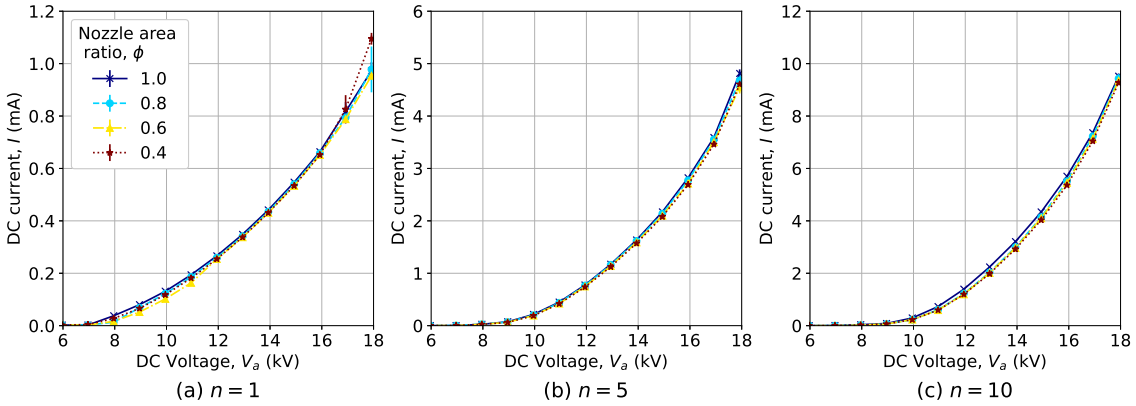

Figure 5-8: Total current draw against applied voltage for different nozzle area ratios. Different panels correspond to different number of stages. The y-axis is scaled according to the number of stages. Error bars show a 95 % confidence interval.

Four nozzles with the same length but different area ratios were used to study the effects of flow constriction downstream of the EAD stages. The models in Chapter 4 suggest that reducing the nozzle area leads to a lower flow speed across the EAD stages, which could be used to reduce pressure losses during flight. Since the nozzle shape primarily affects the flow velocity within the thruster, a change in area ratio is expected to have a negligible effect on the discharge properties of the stage. Figure 5-8 shows the current–voltage characteristics of MSD devices with different number of stages and nozzle area ratios. As expected, the results show that changing the nozzle area ratio does not have a significant impact on the total current. The results in

Figure 5-8a for $n = 1$ at 18 kV do show a change depending on the nozzle area ratio, but this could be attributed to the onset of reverse emission.

In contrast, Figure 5-9 shows that changing the nozzle area ratio does have an impact on the net thrust. The results show that reducing the nozzle area ratio decreases the thrust produced by the device at a given voltage. This is compatible with the predictions of the theoretical models in Chapter 4: according to these models, if pressure losses are small, changing the nozzle area ratio does not affect the flow exit velocity. Therefore, a smaller area ratio would result in a lower mass flow rate and hence lower thrust. In practice, reducing the area ratio decreases the flow velocity across the stages (and hence pressure losses), leading to higher exit velocities. However, the reduction in exit area still results in lower net thrust except if the loss coefficient is high (see Equation (4.46)). The maximum nozzle area ratio used in Figure 5-9 is $\phi = 1$; as noted in Chapter 4, this nozzle area ratio is expected to result in a zero pressure gradient across the nozzle. A nozzle area ratio $\phi > 1$ could provide more thrust than what is produced by the nozzles used here, but separation in the nozzle is possible.

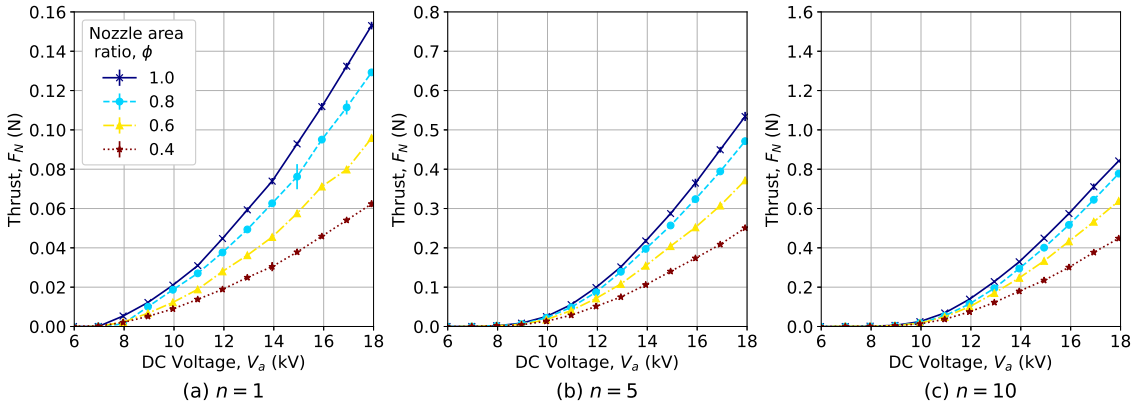

Figure 5-9: Net thrust against applied voltage for different nozzle area ratios. Different panels correspond to different number of stages. The y-axis is scaled according to the number of stages. Error bars show a 95 % confidence interval.

The results in Figure 5-9 also visually illustrate that adding more stages results in diminishing returns: a one-stage thruster with $\phi = 1$ produces a maximum thrust of approximately 0.15 N, whereas a 10-stage thruster with $\phi = 1$ has a maximum

thrust of 0.84 N (5.6 times higher than with a single stage). However, when $\phi = 0.4$, thrusters with $n = 1$ and $n = 10$ have a maximum thrust of 0.062 N and 0.45 N, respectively (a 7.3 times increase). This suggests that the effect of pressure losses is smaller when $\phi = 0.4$ than when $\phi = 1$, which is compatible with the predictions from momentum theory.

Comparison with models

To assess the validity of the models developed in Chapter 4, predicted results for the performance of the MSD thrusters tested here were produced. These results were generated using the models in Sections 4.3.2 and 4.3.3, and the coupled system was solved as described in Section 4.4. However, the current–voltage characteristics in Equations (5.1)–(5.3) and the parameters in Table 5.1 were used instead of the analogous models in Section 4.3.3, which were derived from previous work. The inception voltage for the negative-corona stages, which had a gap spacing of d= 25 mm, was linearly interpolated between the values for $d = 20$ mm and 30 mm. Despite the difference in collector profiles between the single-stage and multistage experiments (20 mm chord HT14 airfoils and 10 mm chord flat plates), the models from the single-stage tests agree with $r^2 = 0.983$ with the multistage experimental power.

The stage loss coefficient was not known prior to the multistage experiments. For this reason, it is assumed that the loss coefficient can be modeled as

$$K_L = k\frac{c}{d}\frac{d}{\Delta}c_{d_{\mathrm{NACA}}}(\mathrm{Re}), \tag{5.4}$$

where $c_{d_{\mathrm{NACA}}}(\mathrm{Re})$ is the drag coefficient of a NACA 0012 airfoil as a function of the Reynolds number, $\mathrm{Re} = \frac{v_2 c}{\nu}$, and models blockage effects through Equation (4.38). The constant k is a scaling factor that accounts for the difference in airfoil profile (NACA 0012 vs. flat plate) and for the pressure losses on the emitters, duct, and collector holders. Equation (5.4) therefore assumes that the relative change in loss coefficient with Reynolds number is the same in the real ducted system as in a NACA 0012 airfoil, but the scale of the loss coefficient is fitted to the data through the

parameter k. This constant scaling was found to be $k = 2.04$ from a least-squares fit to the experimental data: this is the only fitted parameter in the modeled data that was not determined before the multistage experiments. The drag characteristics of the NACA 0012 airfoil as a function of Reynolds number, $c_{d_{\mathrm{NACA}}}(Re)$, were found using the software *XFOIL* [167].

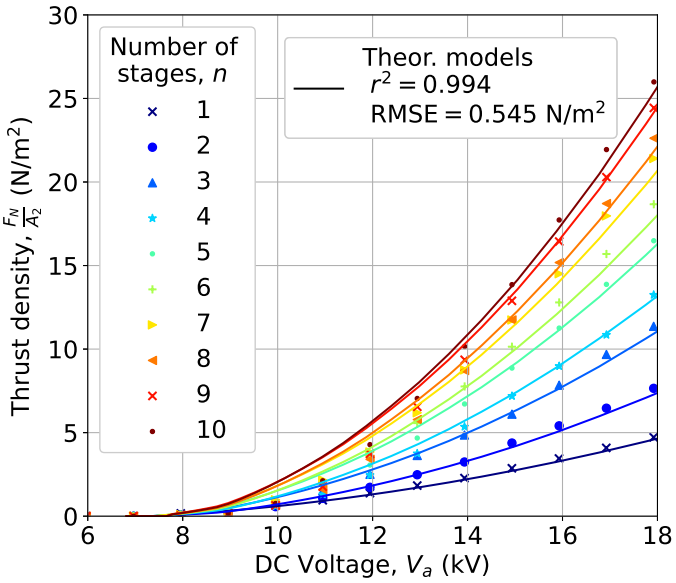

Figure 5-10: Comparison between experimental and modeled thrust density produced by MSD thrusters with $\phi = 1.0$. Markers correspond to experimental data and solid lines show the predictions from models.

The experimental and modeled thrust densities are compared in Figure 5-10. The models agree with the experimental data with a coefficient of determination of $r^2 = 0.994$ and an RMS error of $0.545\,\mathrm{N\,m^{-2}}$. At voltages below approximately 14 kV, the models overpredict the experimental thrust, especially when $n > 3$; this could be a sign of an electric field interaction between the stages that is not currently modeled. The models and experiments have better agreement for voltages above 14 kV, with the models being able to capture the experimental trends.

Figure 5-11 shows that the models can also capture the experimental effect of changing the nozzle area ratio on the thrust density. The modeled data in the three panels in Figure 5-11 agrees with the experimental data with a coefficient of determination of $r^2 = 0.991$ and an RMS error of $0.582\,\mathrm{N\,m^{-2}}$. Similarly to the experimental

data, the models predict that the thrust density at a given voltage decreases as the nozzle area ratio is reduced. However, the models overpredict the thrust density produced by the $\phi = 0.4$ case in Figures 5-11b–c. This is compatible with some flow contraction downstream of this straight converging nozzle, which is not captured by the models that assume a constant-area wake.

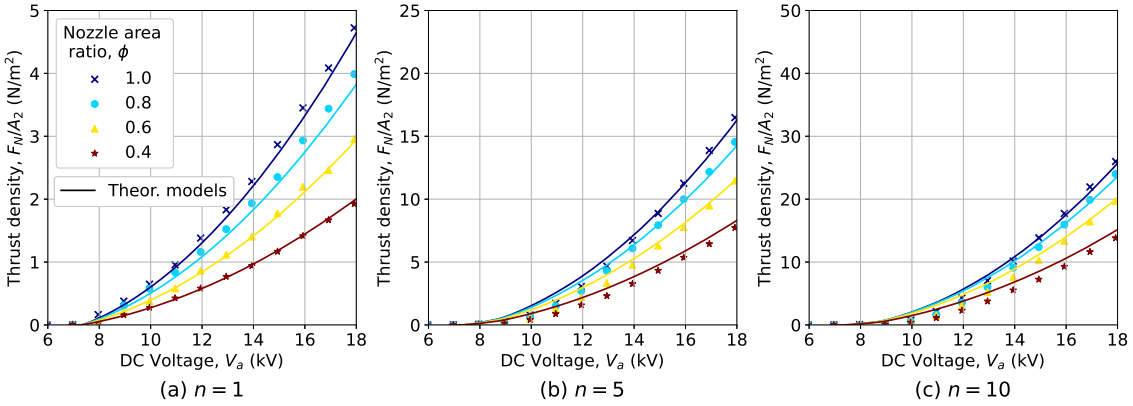

Figure 5-11: Thrust density against applied voltage for different nozzle area ratios and number of stages. Markers correspond to experimental data and solid lines represent the predictions from models.

5.5 Conclusions

This study represents an experimental demonstration of multistaged ducted EAD thrusters. A 10-stage MSD thruster was found to produce a thrust force in static conditions of up to 0.84 N with a cross-sectional area of 0.0324 m^2, corresponding to a thrust density of 26.0 N m^{-2} with a thrust-to-power ratio of 5.0 N kW. This is more than seven times higher than the static thrust density of the 2-stage EAD thruster used to propel the aircraft in Xu et al. [45] at a comparable thrust-to-power ratio. It was found that adding converging nozzles reduces the thrust produced by the MSD devices in the static conditions used in these experiments. However, converging nozzles could be used to reduce the flow velocities within the thruster (and therefore reduce pressure losses) when the freestream velocity is non-zero, potentially resulting in higher net thrust.

The single-stage tests have been used to derive semi-empirical models for the

current–voltage characteristics of parallel sets of corona discharges, modeling the effect of changing the gap spacing d and the distance between parallel electrode pairs Δ. These models take the same form with slightly different parameters for positive and negative coronas and could enable quantitative optimization of stage geometry. These single-stage experiments have also shown that the Coulomb force per unit area experienced by the ions in a stage (analogous to the pressure rise in a 1-D system) is a function of the power draw per unit area and only weakly dependent on the gap spacing: a $d = 15\,\text{mm}$ gap can result in up to 80 % higher Coulomb force per unit volume for a given power draw per unit cross-sectional area than when $d = 30\,\text{mm}$. This was hypothesized in Chapter 4 and shows that stages with a small gap spacing can provide better performance per unit volume while requiring a lower DC voltage. For example, the MSD thrusters demonstrated here have used voltages up to 18 kV, whereas the thruster in Xu et al. [45] with a gap spacing of 50 mm operated at 40 kV. While better performance per unit volume than demonstrated here could be obtained with even smaller gap spacings, manufacturing and assembling small electrode pairs is expected to be a challenge.

The experimental results have also been compared to the predictions from the theoretical models in Chapter 4. The predicted results were obtained using the current–voltage characteristics derived in the single-stage experiments. The only parameter fitted to the multistage data was a scaling for the loss coefficient, which could not be determined a priori. The models were found to provide a coefficient of determination of $r^2 = 0.994$ when compared to the experimental data and were able to capture the effects of changing the number of stages and the nozzle area ratio.

Whereas the results obtained here pave the way for order-of-magnitude improvements in thrust density or thrust-to-power ratio, some engineering challenges still need to be overcome. For example, the loss coefficient could be reduced by using smaller airfoil-shaped electrodes instead of the flat plate electrodes used in the multistage experiments. While reducing the collector chord would reduce pressure losses, it also weakens the corona discharge suggesting that an optimal point may exist. MSD devices with a larger cross-sectional area would also be expected to result in lower loss

coefficients; this is because skin-friction forces act on the surface of the duct, and the ratio of surface area to cross-sectional area is reduced as the thruster size increases. Additional thrust improvement could be obtained by using a decoupled ion source, allowing the ion production and acceleration stages to be separated. As shown in Section 4.4.1, a 10-stage MSD device with a volumetric ion source could produce a thrust density of over $100\,\mathrm{N\,m^{-2}}$.

Future work should consider strategies to reduce the loss coefficient and improve the volumetric performance. The results in this study suggest that small gap spacing could provide higher volumetric thrust density; experiments with even smaller gap spacings than those tested here could be used to validate these predictions. In addition, the effect of the distance θ between adjacent stages, which affects the thruster's length and volume, should also be quantified.

The experimental results in this study support the main theoretical predictions in Chapter 4, showing that ducting can provide aerodynamic benefits and augment the thrust. The models derived in Chapter 4, supported by the data in this study, have already been incorporated in an aircraft design code to show that aircraft with MSD thrusters can be capable of VTOL provided some engineering improvements are made on ion sources, loss coefficient reduction, and power electronics [168].

Chapter 6

Conclusions

The main aims of this thesis were to identify ways to improve the thrust density and thrust-to-power ratio of EAD thrusters, with the long-term goal of enabling more demanding aircraft missions such as vertical take-off and landing. Three main technologies have been identified and studied to achieve these goals:

- Decoupled EAD thrusters: these devices separate the ion generation and acceleration processes. This decoupling has been suggested as a way to increase the thrust produced at a given DC voltage compared to corona discharges [42, 106].
- Reverse emission mitigation: reverse emission is caused by a spurious gas discharge at the collector that increases the power draw of the thruster [32, 34]. Mitigating this effect can provide substantial improvements in thrust-to-power ratio.
- Multistaged ducted thrusters: these thrusters contain several serial EAD stages enclosed in a duct. The duct is also fitted with an inlet and a nozzle to control the flow properties within the EAD stages.

6.1 Main findings

The main findings and conclusions in this thesis are outlined in Figure 6-1. Subsequent sections provide a more detailed summary of the contributions.

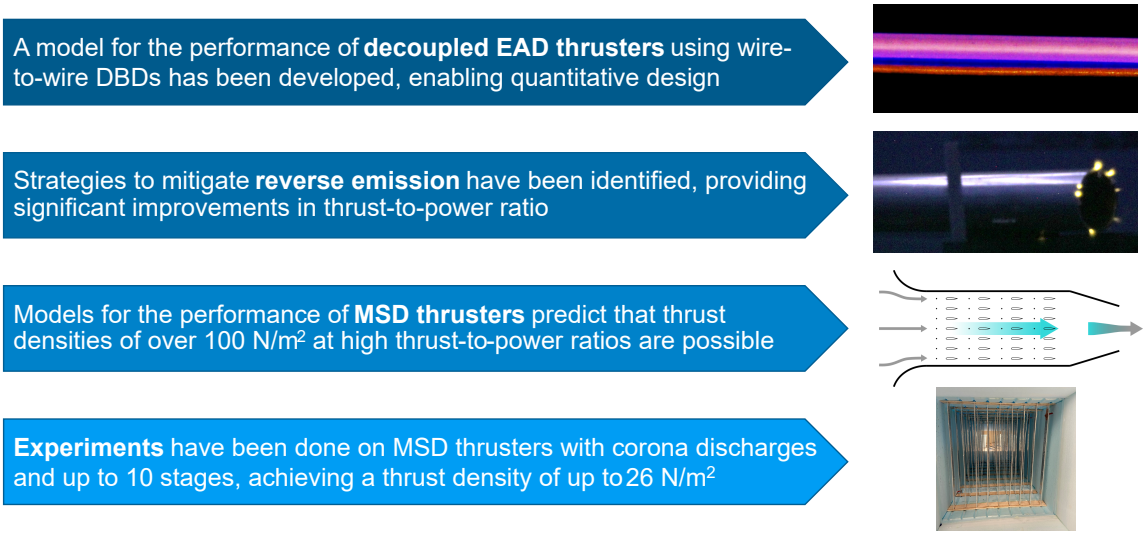

Figure 6-1: Outline of the main thesis contributions.

6.1.1 Decoupled EAD thrusters with wire-to-wire DBD ion sources

This study aimed to characterize the effect of electrical and geometric parameters on the performance of an EAD thruster with a wire-to-wire DBD ion source. Two types of experiments were done: "benchtop" experiments, in which the collector was an oblong flat plate; and thrust measurement tests, with an airfoil collector in a thrust-measurement stand. The benchtop tests showed that the effect on current of the DC voltage and gap spacing for constant DBD power took the same functional form as the space-charge limited current in a thin ion slab. By varying the DBD-driving AC voltage and frequency, it was found that current depended on these parameters through the DBD power draw and not independently. This means that changing the AC voltage or frequency have similar effects on current or thrust as long as the DBD power level is the same. Combining these findings, a model for the performance of decoupled thrusters with a DBD ion source has been proposed. The results from the thrust measurement tests were found to be compatible with the proposed model. This model now enables the design of decoupled EAD thrusters for practical applications.

6.1.2 Reverse emission mitigation

Tests were performed on wire-to-cylinder EAD thrusters using either corona discharges or DBDs as ion sources to study reverse emission. Previous work had found that reverse emission can degrade the performance of EAD thrusters, but the precise causes and effects were not known. The work in this thesis has shown that reverse emission is caused by spurious discharges that ignite in regions of the collector with high electric field: in the geometry used in the experiments, this occurs mostly at the tips of the cylindrical collectors. Reverse emission was found to occur in qualitatively similar ways in both corona-discharge and decoupled thrusters with a DBD ion source. Three ways of mitigating reverse emission were identified, with all of them attempting to weaken the electric field at the collector's tips: increasing the collector span, increasing the collector diameter, and attaching smooth end caps to the collectors' tips. By mitigating reverse emission, it was possible to reduce the power draw by as much as 64 % while still producing approximately the same thrust. Moreover, it was possible to reach higher voltages before spark breakdown when reverse emission was mitigated.

By comparing the thrust produced with and without reverse emission mitigation, it was also found that the effect of reverse emission on thrust (if any) is comparable to the experimental uncertainty. This implies that the main effects of reverse emission are to increase the power draw and to lower the sparking voltage; meanwhile, any effects on thrust appear to be small. Acoustic measurements have also shown that reverse emission has a noticeable impact on the acoustic signature of the thruster, producing more noise than if it were absent. A positive-corona EAD thruster was silent at 40 kV when reverse emission was mitigated; this was not the case when this discharge was present.

The work in this thesis has shown that reverse emission is a crucial non-ideal effect that should be accounted for in the design of EAD device applications. Mitigating this effect can allow the thruster to operate at higher voltages (producing a higher maximum thrust), consume less power, and produce less noise.

6.1.3 Theory of MSD thrusters

In this study, the use of multistaged ducted EAD thrusters has been proposed. An MSD thruster contains multiple sets of electrode pairs in series, enclosed in a duct and fitted with an inlet and a nozzle. Two types of 1-D models were used to simulate the full system. Momentum theory was used to model the interaction between the duct and the internal and external flows. This was combined with models for two limiting cases for the pressure generated by each stage: ideal 1-D EAD stages, based on the theory of Stuetzer [15]; and wire-to-airfoil corona-discharge stages, based on the experiments of Gilmore and Barrett [36]. In addition to housing the electrodes, the models predict that the duct should contribute to thrust, as in ducted propellers.

The modeled results show that MSD thrusters with ideal 1-D stages could produce an areal thrust density of over $100\,\mathrm{N\,m^{-2}}$ or a thrust-to-power ratio of $100\,\mathrm{N\,kW^{-1}}$. The models predict that MSD thrusters using corona discharges produce a lower thrust density or thrust-to-power ratio for a given voltage and geometry but still up to one or two orders of magnitude higher than those of the thrusters used in the aircraft by Xu et al. [45]. In both cases, the predicted data shows a degradation in performance as the freestream velocity increases due to pressure losses in the EAD stages. Similarly, the models predict that increasing the stage count provides more thrust but with diminishing returns, as this increases the flow velocities within the thruster and, hence, pressure losses. The models developed in this chapter have already been used to show that MSD thrusters could enable solid-state VTOL-capable aircraft [168].

6.1.4 Experiments in MSD thrusters

Two types of experiments were performed with ducted devices using corona discharges to validate the predictions from the 1-D EAD theory in Chapter 4: single-stage and multistage experiments. The single-stage tests aimed to quantify the effects of changing stage parameters, such as the gap spacing and the distance between parallel emitter/collector pairs. Through these experiments, a model that captures the effects

of these parameters on the current–voltage characteristics has been developed. The results show that the discharge is weakened as the spacing between electrode pairs is reduced, resulting in less current per unit span. However, the Coulomb force per unit area produced at a given power per unit area converged to an optimal front as the electrode pairs were brought closer together. Similarly, it was found that this optimal front was approximately independent of gap spacing; this implies that EAD devices with a small gap spacing can provide higher force per unit volume than those with larger gaps.

Experiments with multiple stages showed that adding serial stages can significantly increase the areal thrust density of ducted EAD devices. At 18 kV, a 10-stage thruster produced 5.6 times more thrust than its single-stage counterpart. The 10-stage thruster produced a maximum areal thrust density of $26.0\,\mathrm{N\,m^{-2}}$, which is more than seven times higher than that of the 2-stage thruster used to propel the aircraft in Xu et al. [45] at a comparable thrust-to-power ratio. It was found that using a converging nozzle downstream of the EAD stages reduces the thrust produced by the device in static conditions; however, it is hypothesized that converging nozzles could provide thrust advantages in flight. The theoretical models in Chapter 4 were found to agree with a coefficient of determination of $r^2 = 0.994$ with the experimental data.

6.2 Future work: towards a VTOL-capable aircraft

Practical vertical take-off and landing is envisioned in this thesis as the long-term direction of EAD propulsion. Whereas EAD lifters tethered to a ground-based power supply can take off vertically, the scientific literature does not contain any reports of a VTOL-capable airplane propelled by EAD forces only and carrying its power source onboard. The work in this thesis could show a pathway to practical VTOL: MSD thrusters with a decoupled ion source and reverse emission mitigation could simultaneously achieve a high thrust density and thrust-to-power ratio, as shown in Section 4.4.1. Several engineering challenges need to be overcome to make this a reality. This section provides suggestions for future work on EAD propulsion to

improve thruster performance and understand EAD's environmental impact.

6.2.1 Ion sources

The studies in this thesis have focused on two different ion sources: corona discharges and wire-to-wire dielectric barrier discharges. While it has been found that DBDs can provide more thrust at a given voltage than corona discharges, the power draw of the DBD is comparable to the power spent in accelerating the ions. For example, Figure 2-3 shows that a current per unit span of $0.4\,\mathrm{mA\,m^{-1}}$ can be produced when the DBD draws $14\,\mathrm{W\,m^{-1}}$. This corresponds to an energy cost per ion extracted of 35 keV. For reference, the minimum energy cost per ion with electron-impact ionization in an electric field is known as Stoletov's constant and has a value of 66 eV per ion in air [66]. Therefore, the energy cost per ion when DBDs are used is between 2 and 3 orders of magnitude higher than the ideal one. There are several reasons why DBDs may consume more energy per ion than the 66 eV under ideal conditions. First, not all the energy goes into ionization, with significant power being lost in elastic and inelastic collisions of molecules with electrons. As a result, as little as 0.1 % of the power is consumed by ionization [169]. Second, not all of the produced ions are extracted by the DC field, with some of them being trapped in the strong AC field and then being neutralized upon collisions with the DBD electrodes. Increasing either the ionization or the extraction efficiencies would result in lower power consumption by the EAD thruster, improving performance.

There are alternative ion sources for EAD thrusters that could perform better than corona discharges or DBDs. An ion source for an EAD system should ideally produce uniform volumetric ionization across a cross-section, with as little energy spent per ion as possible.

Nanosecond repetitively pulsed discharges

The energy cost to produce an ion–electron pair is a function of the reduced electric field, E/n: this function has a minimum at some critical E/n that corresponds to

electron runaway and increases for a reduced field higher or lower than that optimum [169]. The reduced field that results in minimum energy cost per ion is the Stoletov point, which occurs at $E/n \approx 1.1 \times 10^{-14}\,\mathrm{V\,cm^2}$ with an energy cost of 66 eV for air [66, 169]. This corresponds to an electric field of $27\,\mathrm{MV\,m^{-1}}$ in air at normal temperature and pressure. Short high-voltage pulses with high E/n repeated at high frequency can result in ionization at a much lower energy cost per ion than DC or low-voltage AC discharges [169]. For this reason, nanosecond repetitively pulsed discharges, with pulses with a duration of the order of nanoseconds and repetition frequencies of up to 1 MHz, offer the potential to consume lower power in ionization than DBDs. Macheret et al. [169] estimate that an NRP discharge with a 1 ns high-voltage pulse could result in an energy cost as low as 350 eV per ionization event in air at 1 atm and 2000 K.

Orrière et al. [106] recently tested an EAD device with an NRP discharge ion source and a flat plate collector. They achieved flow velocities of up to $2\,\mathrm{m\,s^{-1}}$ with a power draw of 1 W. As they did not measure the DC current extracted by the flat plate, it is not possible to estimate the effective energy cost per extracted ion. Future work should test NRP discharges with different pulse duration, repetition frequencies, and peak voltages and measure the extracted current to estimate the ionization cost.

Photoelectric effect

When a photon of sufficiently high energy impacts a metallic surface, the surface may emit an electron through the photoelectric effect. The surface's work function is the threshold for photoelectric electron emission and depends on the surface material: for example, the work function of aluminum is 4.2 eV [170], which means that photons with an energy of at least 4.2 eV (wavelength of at most 295 nm, in the UV spectrum) can result in photoelectric emission. In general, the more chemically reactive a metal is, the lower the work function.

The photoelectric effect has been proposed as a way to produce negative ions from air [171], and it could be used in EAD applications. In a potential implementation, electrons produced by the photoelectric effect would be accelerated from the emitter

to a positively-biased collector by a DC electric field. The electric field distribution could be designed such that there is a high electric field region near the emitter, which results in the primary photo-electron causing an ionization cascade that produces secondary electrons and positive ions. These electrons would eventually attach to electronegative gas molecules, producing negative ions that would then drift toward the collector. The surface's work function is the lowest possible energy cost per ion produced by the photoelectric effect; however, the real energy cost is expected to be higher since some of the photons would be lost to heating and reflection.

Challenges to this ion source involve the UV light source design, which should be lightweight and efficient; and the electrode and light source design such that (i) photons strike as much of the emitter's surface as possible, and (ii) most of the intensity is transformed to photoelectric emission.

Photoionization

High-energy photons can be used to ionize gas molecules. For a photon to ionize a molecule, the photon energy must be higher than the molecule's ionization energy (ignoring multiphoton ionization). The ionization energy of the nitrogen molecule is 15.6 eV [172], which corresponds to photons with a wavelength of 79.4 nm in the extreme UV range. A light source that could produce photons of this energy could ionize air very efficiently; however, the UV light generation process would introduce additional energy losses.

The main challenge regarding photoionization is the generation of high-energy photons. It is possible to produce extreme UV light with solid-state sources via high harmonic generation; for example, patterning magnesium oxide crystals can produce photons of up to 20 eV by emitting the high harmonics of an 800 nm laser [173]. Alternative mechanisms for higher photon energies, such as vacuum tubes, may be needed, but these involve additional losses [174]. Another difficulty stems from the high photoionization cross-section of the nitrogen molecule, which is approximately $2.6 \times 10^{-21}\,\mathrm{m}^2$ for photon energies just above the ionization energy and makes air essentially opaque to extreme UV light [66, 175]. With this cross-section, an extreme

UV beam would lose 99 % of its intensity after penetrating a distance of 0.07 mm into air in normal conditions. The photoionization cross-section of nitrogen is a decreasing function of photon energy: at an energy of 250 eV (in the X-ray range), the cross-section is reduced to $2 \times 10^{-23}\,\mathrm{m}^2$ [175], which would allow the light beam to penetrate the air approximately 10 mm before losing 99 % of its intensity.

Radioactive ion sources

The radioactive decay of unstable nuclei could be used as the ion source in EAD devices, potentially in off-planet applications where safety is not a major concern. Out of the different decay mechanisms, alpha and beta (β^-) decays are probably the most promising options: alpha decay releases alpha particles (helium nuclei), and β^- decay releases high-energy electrons. In atmospheric-pressure air, alpha particles can only penetrate a few centimeters, whereas β^- particles can cover distances of the order of meters [176]. As alpha or β^- particles collide with neutral air molecules, ionization events occur, producing secondary pairs of electrons and positive ions. Hence, a radioactive EAD emitter could produce either positive ions through ionization events or negative ions following electron capture. In the case of very high-energy electrons, the energy cost per ionization event can be as low as 34 eV in air, about a factor of 2 higher than the ionization energy of nitrogen, as a result of ionization cascades [169]. Therefore, a single electron with an energy of the order of 100 keV (representative of the β^- particle energy [176]) can produce thousands or tens of thousands of ionization events in air.

Americium-241 (which undergoes alpha decay) is used in household smoke detectors: the alpha particles produce ions and electrons from air in an ionization chamber, such that when a voltage is applied between two electrodes within the chamber, a current is produced. The presence of smoke alters the current, allowing the smoke to be detected [177]. In addition, radioactive materials are also used as an energy source in radioisotope thermoelectric generators in spacecraft. In these devices, heat from the radioactive decay of some material is converted to electricity by the thermoelectric effect [178]. The β^- decay is also a common source of high-energy electrons for

medical radiation therapy [179].

The main advantage of using radioactive ion sources in EAD systems is that they can provide ionization without drawing power from the onboard power supply. The criteria for selecting radioactive ion sources for EAD systems would likely be similar to that used in radioisotope thermoelectric generators [178]. First, the material needs to have a half-life sufficiently long to perform a practical mission but also short enough so that it has sufficient activity to produce the ions required by the EAD system. Second, the material needs to have a low rate of neutron and gamma-ray emissions since these radiation types have high penetrating power and can damage electronics. Third, the decay products would ideally have to be stable, have a very long half-life, or decay further without releasing significant gamma or neutron radiation.

6.2.2 MSD thrusters with low loss coefficient

The results in Chapter 5 showed that the loss coefficient of the EAD stages could be modeled by assuming it was proportional to the drag coefficient of a NACA 0012 airfoil. However, the fitted loss coefficient was 2.04 times higher than expected if the collectors were NACA 0012 airfoils and if drag on the collectors was the only source of pressure losses. In general, there are three sources of pressure losses in a stage: skin-friction forces on the duct and drag forces on the emitters and the collectors. Through proper aerodynamic design, it should be possible to reduce these pressure losses and improve the performance of MSD thrusters, which is particularly important at non-zero flight speeds.

Pressure losses due to the collectors could be reduced in several ways: using airfoil-shaped collectors designed for low Reynolds numbers, reducing the collector chord, and reducing the number of collectors in a stage. Similarly, the pressure losses on the emitters could be decreased by using emitters with smaller diameters and increasing the distance between parallel emitters. There are engineering limits to how much the loss coefficient can be reduced in this way. For example, the electrostatic pressure rise provided by the stage is also degraded as the number of emitter/collector pairs is decreased. If the emitter diameter is reduced, the wire experiences higher stress for

a constant tensile force, making tensile failure more likely due to wire tensioning or aerodynamic or electrostatic loads. An alternative way to reduce emitter drag would be using small airfoil-shaped emitters instead of circular wires, but whether airfoils with micrometer-scale chords can be produced and mounted on a stage at the correct incidence remains to be shown. Pressure losses due to skin friction on the duct can also be reduced by using ducts with smooth inner surfaces.

Using different EAD stage architectures could also lead to lower pressure losses per stage. For example, sets of concentric ducts containing emitters and collectors integrated into the surface could reduce pressure losses: in this case, the only source of pressure losses would be skin friction on the duct.

6.2.3 Inlet and nozzle design for MSD thrusters

The MSD experiments in this thesis have focused on static thrust generation, which is of interest for take-off or hover propulsion conditions. The duct design was arbitrary: the inlet was parabolic, the EAD stages had a constant-area duct, and the nozzle was straight. Since the thruster was tested in static conditions, the external design of the duct was not considered as it cannot result in significant drag forces. However, the exterior duct design is expected to become more important when the thruster is designed for flight at a non-zero velocity. In particular, drag on the outside of the duct should be modeled and minimized. The design of ducted fans and propellers faces a similar challenge, and a simple solution is to integrate the inlet, propeller, and nozzle into a single airfoil-shaped or streamlined duct [163].

Furthermore, the work in this thesis has not considered diverging nozzles with an exit area greater than that of its inlet. This is because flow separation can occur due to adverse pressure gradients, and the 1-D models proposed in this thesis are unable to model separation. As discussed in Chapter 4, divergent nozzles may increase the thrust produced by the MSD thruster, and future work should verify if this prediction holds in practice.

6.2.4 Electrode degradation

Electrode erosion and degradation due to oxidation and sputtering are challenges that could limit the lifetime of EAD devices. Electrode erosion is particularly important at the emitter since ions and electrons have more energy in the high-electric-field region near it. In corona discharges and wire-to-wire DBDs, the emitter consists of thin exposed or insulated wires that are especially susceptible to failure due to their small cross-section. No apparent effects on performance as a result of emitter degradation were observed in the work in this thesis. However, the encapsulated wire's dielectric insulation in the wire-to-wire DBD arrangement was found to be eroded after operation: the wire diameter was smaller after some operational time than it originally was. Eventually, this would cause failure of the DBD wires when a spark formed across the dielectric material. Anecdotal experience suggests that the electrode lifetime was shorter at high DBD power levels; in some cases, the DBD wires failed after less than 5 minutes in use.

While the tungsten wires used in the corona-discharge experiments in this thesis did not fail except in cases of arcing (by melting), it was found that some areas in their surface had a bluish color after some hours of operation. Future work should quantify any changes in performance due to emitter electrode degradation and determine the operational lifetime before failure.

6.2.5 Noise and environmental impact

Quieter operation is one of the main hypothesized advantages of EAD propulsion as compared to alternatives such as propellers. Figures 3-5b and 3-8 in this thesis show that a positive-corona EAD thruster can produce a thrust per unit span of at least $40\,\mathrm{mN\,m^{-1}}$ while being completely silent when reverse emission is mitigated. In addition, previous work by the author has shown that an EAD thruster can be significantly quieter than a thrust-matched propeller. In the indoor experiment, a wire-to-airfoil corona-discharge EAD thruster with a span of 2.9 m and a gap spacing of 120 mm could produce 0.7 N of thrust at a voltage of 70 kV. At this voltage, the

EAD thruster was about 20 dB quieter than a two-blade 8040 propeller producing the same thrust [168]. However, these results correspond to a single operational point and future work should quantify the noise advantages at different conditions, especially outdoors or if reverse emission is present.

As EAD is fully electric, it does not release direct combustion emissions. However, the ionization process can produce ozone (which is harmful to human health) and potentially other hazardous gases, such as nitrogen oxides. Future studies should quantify these emissions, particularly if novel ion sources that could result in different gas chemistry are used. Similarly, the safety of human operators, or bystanders in the case of an accident, should be considered when designing the high-voltage power electronics and electrodes in a practical implementation of EAD.

Appendices

Appendix A

Dimensional analysis of electrostatic and fluid equations

In Section 1.3.1, several electrostatics models of gas discharges were discussed. It was shown that if the medium has a uniform permittivity, the potential distribution was governed by Poisson's equation, (Equation (1.15)),

$$\nabla^2 \varphi = -\frac{\rho_c}{\varepsilon}.$$

Similarly, if charge transport occurs due to the drift of a single type of ions, conservation of charge (Equation (1.19)) can be stated as

$$\nabla \rho_c \cdot (\mu \nabla \varphi - \vec{u}) = \mu \frac{\rho_c^2}{\varepsilon}.$$

These electrostatic equations are coupled to the Navier-Stokes equations that govern the dynamics of the neutral fluid. These include continuity (Equation (1.21)),

$$\nabla \cdot \vec{u} = 0,$$

and conservation of momentum (Equation (1.22)),

$$\rho \frac{\mathrm{D}\vec{u}}{\mathrm{D}t} = -\nabla p + \mu_v \nabla^2 \vec{u} + \rho_c \vec{E},$$

where only the Coulomb force has been retained in the body force term. In addition to boundary conditions, these equations require that at least $n = 8$ parameters be specified, and these are shown in Table A.1. Since these equations involve $k = 4$ physical dimensions (described in Table A.2), the Buckingham π theorem [127] establishes that $p = n - k = 4$ dimensionless parameters can be used to describe this system. These parameters can be determined by defining a dimensional matrix $\mathbf{D}$ [180], which in this case is given by

$$\mathbf{D} = \begin{bmatrix} 1 & 0 & 2 & 1 & -3 & -1 & -3 & -3 \\ 0 & -1 & 1 & 0 & -1 & 1 & 0 & 1 \\ 0 & 1 & -1 & 0 & 2 & 0 & 1 & 0 \\ -1 & 2 & -3 & 0 & 4 & -1 & 1 & 0 \end{bmatrix}.$$

An entry $D_{i,j}$ in this matrix indicates the j^{th} variable in Table A.1 contains the i^{th} physical dimension in Table A.2 raised to the $D_{i,j}^{\text{th}}$ power. For example, consider the entry $D_{4,5} = 4$: this indicates that the permittivity ε ($j = 5$) has units of time ($i = 4$) to the power of 4. As a note, permittivity has dimensions $[\varepsilon] = \frac{[i]^2[t]^4}{[m][l]^3}$. The dimensionless parameters can then be determined from the nullspace of the dimensional matrix $\mathbf{D}$ [180]. It can be easily verified that the nullspace of $\mathbf{D}$ is the column space of matrix $\mathbf{A}$,

$$\mathbf{A} = \begin{bmatrix} 0 & 1 & 1 & 0 \\ 0 & -1 & 0 & -1 \\ -1 & -1 & 0 & 0 \\ 2 & 1 & 1 & 0 \\ -1 & 0 & 0 & \frac{1}{2} \\ 0 & 0 & -1 & 0 \\ 1 & 0 & 0 & 0 \\ 0 & 0 & 1 & -\frac{1}{2} \end{bmatrix}.$$

Matrix $\mathbf{A}$ has a rank of 4, which implies that the coupled electrostatics/fluid

dynamics system is described by 4 dimensionless parameters. A possible choice of parameters can be made by considering the four columns of $\mathbf{A}$ independently. If this is done, an entry $A_{i,j}$ indicates that the j^{th} dimensionless parameter contains the i^{th} dimensional parameter in Table A.1 raised to the power of $A_{i,j}$. From this, four dimensionless parameters can be defined,

$$\bar{\rho} \equiv \frac{L^2 \rho_{c,0}}{\varepsilon \varphi_0},$$

$$\bar{v} \equiv \frac{U_0 L}{\mu \varphi_0},$$

$$\mathrm{Re} \equiv \frac{\rho U_0 L}{\mu_v},$$

$$M \equiv \sqrt{\frac{\varepsilon}{\rho}} \frac{1}{\mu}.$$

These parameters are the same as those derived in Section 1.3.3 from the non-dimensionalization of the governing equations and are referred to, respectively, as the electric source number, electric slip number, Reynolds number, and mobility ratio. Since the dimensionless parameters depend on the column space of matrix $\mathbf{A}$, this choice of dimensionless parameters is not unique.

Table A.1: List of dimensional variables involved in a coupled electrostatic/fluid dynamics model of gas discharges

Number	Symbol	Definition	Dimensions
1	U_0	Reference velocity	$\frac{[l]}{[t]}$
2	μ	Ion mobility	$\frac{[i][t]^2}{[m]}$
3	φ_0	Reference potential	$\frac{[m][l]^2}{[t]^3[i]}$
4	L	Reference length	$[l]$
5	ε	Permittivity	$\frac{[i]^2[t]^4}{[m][l]^3}$
6	μ_v	Dynamic viscosity	$\frac{[m]}{[l][t]}$
7	$\rho_{c,0}$	Reference charge density	$\frac{[i][t]}{[l]^3}$
8	ρ	Fluid density	$\frac{[m]}{[l]^3}$

Table A.2: List of physical dimensions relevant to a coupled electrostatic/fluid dynamics model of gas discharges

Number	Symbol	Definition
1	$[l]$	Length
2	$[m]$	Mass
3	$[i]$	Current
4	$[t]$	Time

Appendix B

Supplementary material of Chapter 2

B.1 DBD power characterization

To characterize the power consumed by the DBDs in Chapter 2, the equivalent circuit method of Manley [92] was used, as described in Xu et al. [136]. According to this, the electrodes behave as a capacitor with a capacitance per unit electrode span C_0 when the DBD is not discharging, and with a capacitance per unit span C_p during the discharge. These capacitances can be measured from a charge–voltage plot during a single AC cycle. For a wire-to-wire DBD discharge, this plot takes the form of a parallelogram. In addition, this plot can also be used to find the threshold voltage V_0, defined as the difference between voltages that give zero charge in the device. The DBD power per unit emitter span is [136]

$$\frac{P_{\mathrm{DBD}}}{b} = C_p V_0 \left(V_{\mathrm{AC}} - \frac{V_0}{1 - C_0/C_p} \right) f. \tag{B.1}$$

A separate set of experiments was used to measure these electrical parameters for the DBD used in the experiments. A 4.4 nF capacitor was connected in series between the exposed electrode and ground in the benchtop setup (shown schematically in Figure 2-1b). The voltage across this capacitor was measured with a Tektronix P2200 probe. The applied AC voltage was measured with a Tektronix P6015A probe. Both probes were sampled by a Tektronix DPO2024B oscilloscope. A $V_{\mathrm{AC}} = 7.0\,\mathrm{kV}$

peak-to-peak, $f = 20\,\mathrm{kHz}$ input was used to characterize the power consumption of the DBD at different DBD electrode separations, δ. The voltage waveform and charge in the device were recorded over 21 AC cycles, and the charge measurements across cycles were averaged using a moving average filter. Straight lines were then fitted to the parallelogram to identify the capacitances C_0 and C_p. A sample charge–voltage plot is shown in Figure B-1. This procedure was repeated for each of the DBD wire spacings that were tested. These measured parameters were used to calculate the power drawn by the DBD in the experiments. The 4.4 nF capacitor was not connected to the exposed electrode during the experiments in which DC current or thrust were measured.

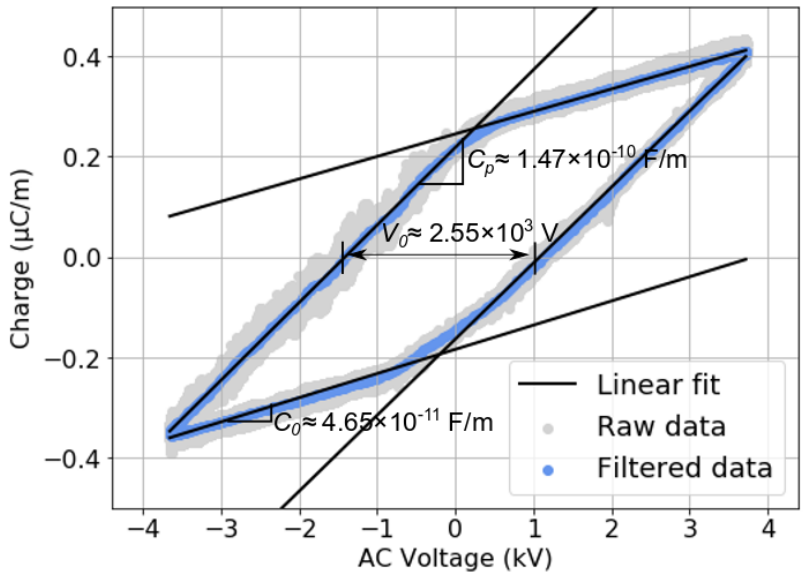

Figure B-1: Charge–Voltage diagram for the discharge in a 50 mm span DBD at $V_{\mathrm{AC}} = 7\,\mathrm{kV}$, $f = 20\,\mathrm{kHz}$ and $\delta = 0.0\,\mathrm{mm}$. The equivalent capacitances C_0 and C_p and the threshold voltage V_0 are shown.

B.2 Additional current–voltage characteristics at lower DBD power

The current–voltage characteristics in Figure 2-3 were obtained at a constant DBD power level of $P_{\mathrm{DBD}}/b = 14\,\mathrm{W\,m^{-1}}$. To test the effect of changing the DBD power,

this experiment was repeated at $P_{\mathrm{DBD}}/b = 4\,\mathrm{W\,m^{-1}}$. The current–voltage characteristics are shown in Figure B-2a, and the measured current is plotted against I_{Geurst} in Figure B-2b. A linear relation between the measured current and I_{Geurst} is still observed. This is compatible with the model in Equation (2.5).

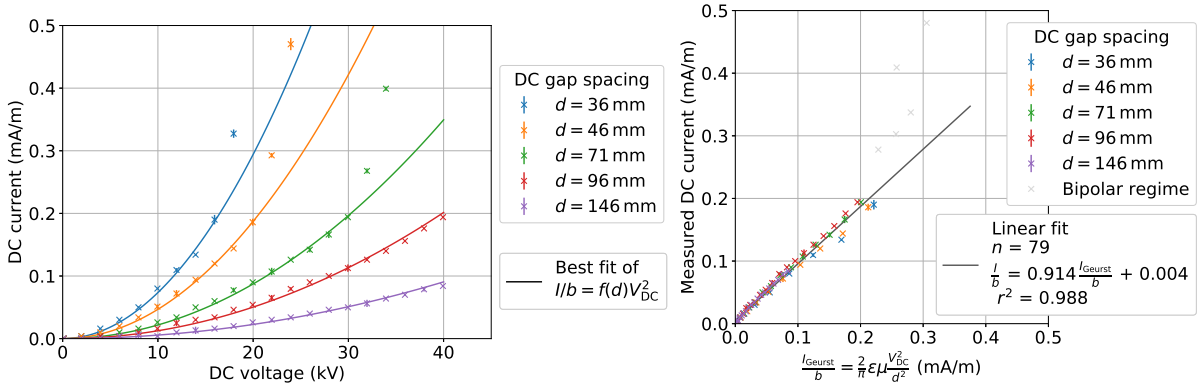

(a) Current–voltage characteristics

(b) Current against I_{Geurst}

Figure B-2: Current–voltage characteristics at a DBD electrode spacing of $\delta = 0.25\,\mathrm{mm}$. An AC signal with peak-to-peak voltage $V_{\mathrm{AC}} = 7\,\mathrm{kV}$ at frequency $f = 3\,\mathrm{kHz}$ was applied to the encapsulated electrode. The power drawn by the DBD was $P_{\mathrm{DBD}}/b = 4\,\mathrm{W\,m^{-1}}$. Error bars represent a 95 % confidence interval.

B.3 Effect of DBD power on thrust

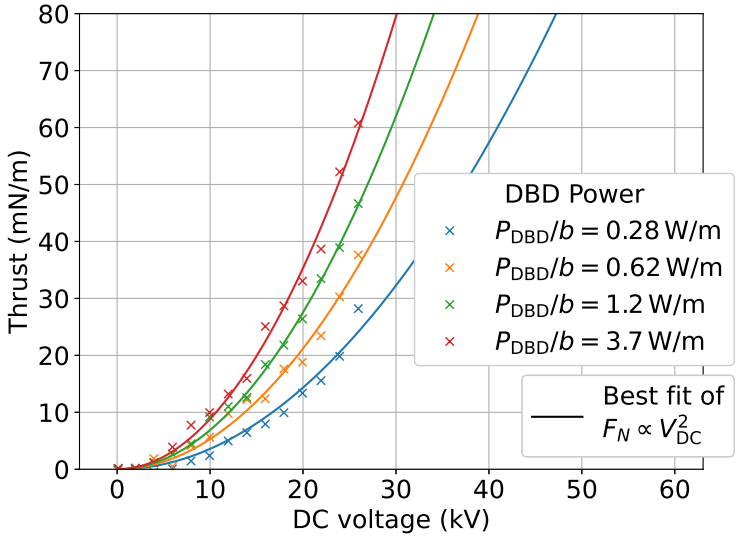

Figure B-3: Thrust–voltage characteristics at different DBD power levels.

In Chapter 2, the extracted current was found to be a function of the power consumed by the DBD. Since Equation (2.1) predicts that current and thrust are directly related, the thrust is also expected to be a function of the DBD power. To verify this, the thruster was tested at a constant AC voltage level $V_{AC} = 7\,\text{kV}$ and at frequencies $f = 0.25$, 0.5, 1, and 3 kHz. The measured thrust is shown in Figure B-3. Similarly to the extracted current, increasing the DBD power results in an increase in the thrust produced by the device.

B.4 Thrust-to-power

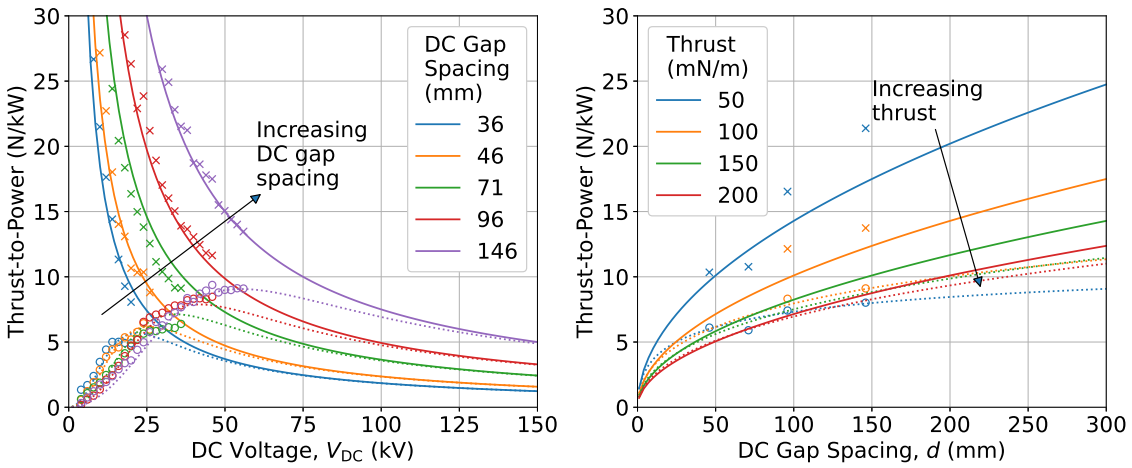

(a) Thrust-to-power vs. DC voltage

(b) Thrust-to-power vs. DC gap spacing

Figure B-4: Thrust-to-power as a function of (a) DC voltage with lines of different DC gap spacings and (b) gap spacing with lines of different thrust levels. Markers show experimental data points (those in (b) are linearly interpolated) while lines show model scalings using the experimentally-measured value of ion mobility, $\mu = 2.0 \times 10^{-4}\,\text{m}^2\text{V}^{-1}\text{s}^{-1}$. Solid lines and crosses show thrust-to-power where power includes only the DC acceleration power, while dashed lines and circles include both DC acceleration power and the DBD power. The DBD wire spacing was $\delta = 0.0\,\text{mm}$ and the AC signal had $V_{AC} = 7\,\text{kV}$, $f = 3\,\text{kHz}$. The power consumed by the DBD was $P_{DBD}/b = 3.7\,\text{Wm}^{-1}$. Thrust measurements are from the data shown in Figure 2-6, while current and DC power are calculated using results from Figure 2-5. The current directly measured in the thrust experiments was subject to reverse emission at the edges of the airfoil collector and is not shown here.

Figure B-4 shows the thrust-to-power ratio as a function of DC voltage and of gap spacing d. The solid lines, which include only the DC acceleration power, represent a long-term limit for thrust-to-power ratio which could be achieved with very efficient ion sources, while the dashed lines, which include both DC acceleration power and DBD power, represent what has been achieved in this study with a wire-to-wire DBD ion source at the specific operating point used.

With reference to Equation (2.8) for the thrust-to-power ratio, the solid lines in Figure B-4a show the $F_N/P \propto 1/V_{\mathrm{DC}}$ scaling at fixed gap spacing d, and the solid lines in Figure B-4b show the $F_N/P \propto d^{1/2}$ scaling at fixed thrust, F_N. The dashed lines, which include DBD power, do not follow these scalings exactly but converge to the solid lines at higher DC acceleration powers (to the right and to the left of panels (a) and (b) respectively).

B.5 Fit to data in Xu et al. (2019)

Figure B-5 shows the variation of thrust with voltage of the decoupled thruster in Fig. 3 in Xu et al. [42], obtained with a wire-to-wire ion source and a cylinder collector at a constant $V_{\mathrm{AC}} = 3\,\mathrm{kV}$ and $f = 10\,\mathrm{kHz}$. A fit to the data of the form $F_N \propto \frac{V_{\mathrm{DC}}^2}{d}$ has also been included. This fit provides a coefficient of determination of $r^2 = 0.974$.

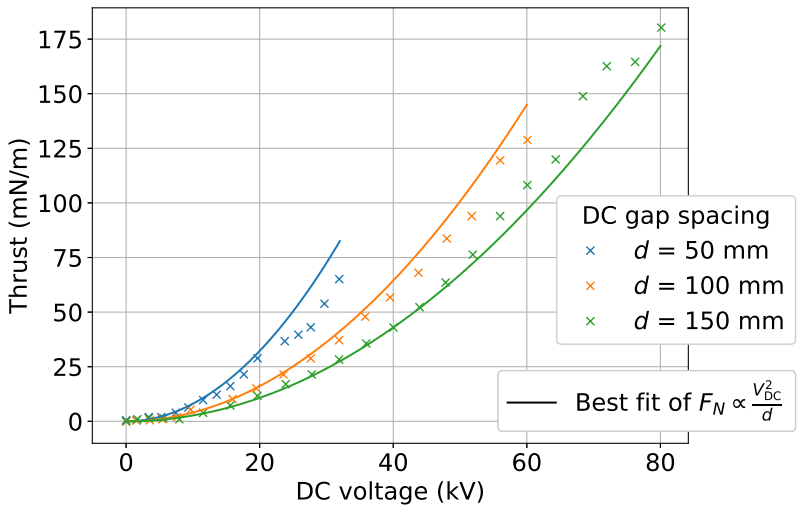

Figure B-5: Thrust-to-voltage characteristics of the decoupled thruster in Fig. 3 in Xu et al (2019). A fit of the form $F_N \propto \frac{V_{\mathrm{DC}}^2}{d}$ is shown.

B.6 Proof that current is proportional to ion mobility

To develop the model in Equation (2.5), it was assumed that current was proportional to ion mobility. This proportionality, which was not tested in the experiments, can be justified using physical arguments.

The electric field between the emitter and the collector is governed by Gauss's law,

$$\nabla \cdot \vec{E} = \frac{\rho}{\varepsilon}. \tag{B.2}$$

As charged species travel between the electrodes, conservation of charge requires that

$$\frac{\partial \rho}{\partial t} + \nabla \cdot \vec{j} = 0.$$

Assuming that charge transport occurs solely due to ion drift (i.e., ignoring diffusion and advective transport due to bulk fluid motion), the current density can be expressed as

$$\vec{j} = \mu \rho \vec{E}.$$

Substituting this result into the charge continuity equation and assuming steady-state,

$$\nabla \cdot \left(\mu \rho \vec{E} \right) = 0$$

$$\mu \nabla \cdot \left(\rho \vec{E} \right) = 0$$

Since $\mu \neq 0$, the last equality requires

$$\nabla \cdot \left(\rho \vec{E} \right) = 0. \tag{B.3}$$

The electric field and charge density distributions in the domain are governed by Equations (B.2) and (B.3); there is no dependency on the ion mobility.

The DC current, I, can be computed at the collector using

$$I = -\oint_{\Gamma} \vec{j} \cdot \hat{n} \mathrm{d}A = -\mu \oint_{\Gamma} \rho \vec{E} \cdot \hat{n} \mathrm{d}A, \tag{B.4}$$

where Γ represents the collector boundary and $\hat{n}$ is the unit vector normal to the collector surface in the outwards direction. The negative sign is added because there is a net influx of charge at the collector. Since both ρ and $\vec{E}$ are independent of μ, this shows that $I \propto \mu$, as assumed in Equation (2.5).

This page intentionally left blank.

Appendix C

Supplementary material of Chapter 3

C.1 Thrusters with negative corona discharges

C.1.1 Mitigating reverse emission

This section contains the results from experiments with negative-corona ion sources. These tests were done at an ambient temperature of 24 °C and with relative humidity in the range of 11–18 %. Qualitatively, the results are similar to those in Sections 3.4.1–3.4.2 with positive coronas. For ease of interpretation, voltages in this section are quoted as positive, i.e., $V_a = |\varphi_e - \varphi_c|$; however, the emitter potential was lower than the collector potential so as to produce a negative corona discharge.

Figure C-1 shows the ratios $\frac{I}{V_a b_e}$ and $\frac{F_N}{V_a b_e}$ against voltage in a negative-corona thruster with different collector diameters. In the absence of non-ideal effects, these plots should be straight lines. In Figure C-1a, the ratio $\frac{I}{V_a b_e}$ evolves linearly with voltage at low voltage levels for a given gap spacing, but there is a change in slope associated with reverse emission after some critical voltage. The reverse emission onset voltage generally increases with the collector diameter.

In Figure C-1b, a change in slope associated with reverse emission cannot be clearly seen in the $\frac{F_N}{V_a b_e}$ versus V_a plots. In general, the results show that the thrust at a given voltage and gap spacing increases with the collector diameter, which can be attributed to the enhancement in the electric field at the emitter. At $d = 100\,\text{mm}$

and $V_a = 60\,\text{kV}$, the $D = 12.7\,\text{mm}$ and $D = 38.1\,\text{mm}$ collectors draw approximately the same current, but the $D = 38.1\,\text{mm}$ collector produces approximately 35 % more thrust than the other one.

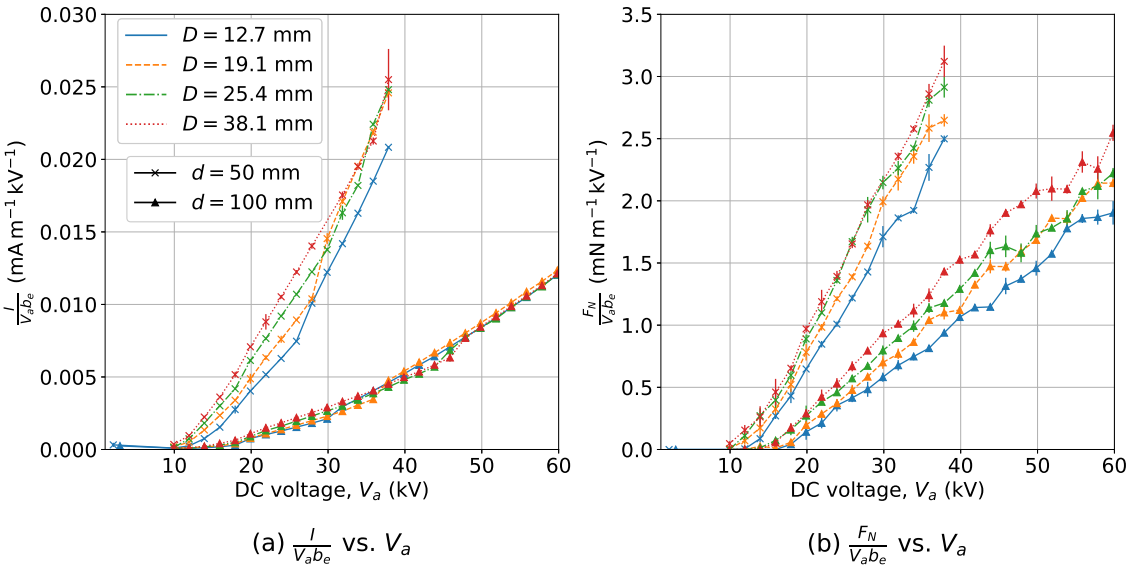

Figure C-1: Ratios (a) $\frac{I}{V_a b_e}$, and (b) $\frac{F_N}{V_a b_e}$ against the applied voltage in a negative corona. All collectors had a span $b_c = b_e = 510\,\text{mm}$ and open ends. All tests done up to the same maximum voltage, even if the arcing limit was higher.

Figure C-2 shows the effects of changing the collector span and of using end caps on the current and thrust produced by the thruster. In Figure C-2a, all the plots approximately overlap when $V_a < 28\,\text{kV}$ at $d = 50\,\text{mm}$; at higher voltages, only the $\Delta b = 0\,\text{mm}$ collector with open ends deviates from the linear trend, showing evidence of reverse emission. At a gap spacing $d = 100\,\text{mm}$, the $\Delta b = 0\,\text{mm}$ collector with open ends shows a clear deviation from the linear trend at voltages $V_a > 38\,\text{kV}$; smaller deviations from the linear trend can also be observed in the other cases shown.

Similarly to the previous cases, no clear deviations from the linear trend can be observed in the $\frac{F_N}{V_a b_e}$ versus V_a plots in Figure C-1b. Generally, the results show that the collectors with $\Delta b > 0$ produce more thrust than the other two tests at a given voltage and gap spacing.

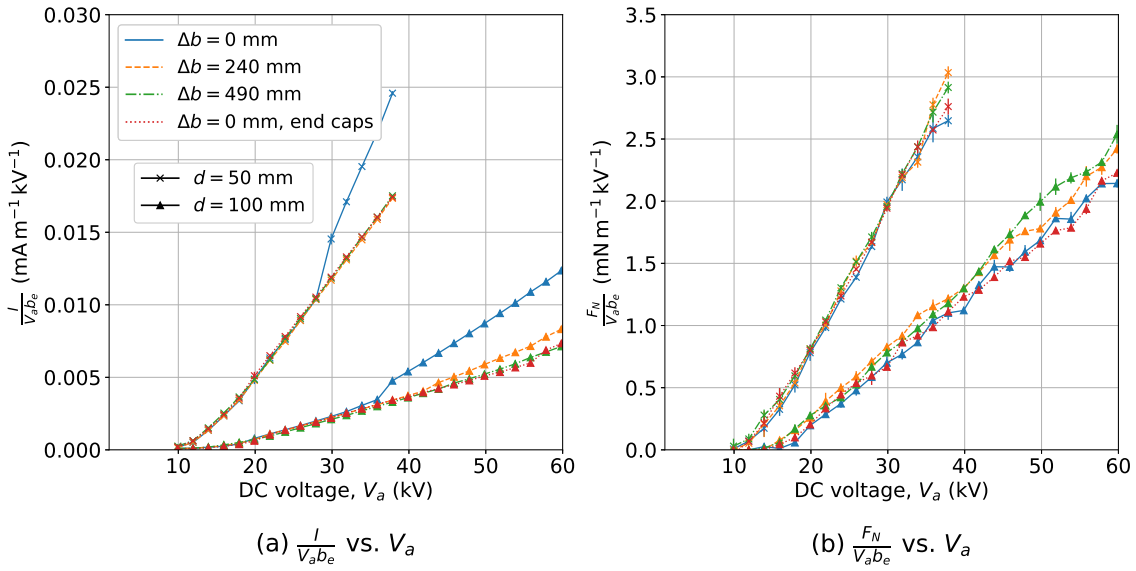

Figure C-2: Ratios (a) $\frac{I}{V_a b_e}$, and (b) $\frac{F_N}{V_a b_e}$ against the applied voltage in a negative corona for varying collector types. All collectors had a diameter $D = 19.7\,\text{mm}$ and open ends, except for the case labeled "end caps", which had hemispherical end caps. All tests done up to the same maximum voltage.

Figure C-3 shows plots of the net thrust per unit span versus the ratio $\frac{Id}{b_e}$: Figure C-3a contains the same results as Figure C-1; and Figure C-3b, those of Figure C-2. If non-ideal effects are not present and the drag coefficient is approximately constant, these two quantities are expected to be proportional to each other as expressed by Equation (3.5).

Figure C-3a shows that for given a given thrust level and gap spacing, the collectors with larger diameters generally draw less current, suggesting that increasing the collector diameter helps mitigate reverse emission. However, deviations from the proportionality trend can still be seen in the $D = 38.1\,\text{mm}$ collector at high thrust levels. In Figure C-3b, the $\Delta b = 0\,\text{mm}$ collector with open ends shows large deviations from the proportionality trend; the other cases show only small deviations, suggesting that reverse emission has been mitigated. At a thrust level of $\frac{F_N}{b_e} = 130\,\text{mN}/,\text{m}^{-1}$ and $d = 100\,\text{mm}$, the collector with $\Delta b = 0\,\text{mm}$ and open ends draws approximately twice more current than the $\Delta b = 490\,\text{mm}$ collector. Even in the cases when reverse emission has been mitigated, the plots in Figure C-3 do not lie within the region of previously reported ion mobilities. This can partly be attributed to the effect of

aerodynamic drag, which changes the slope of the net thrust versus Id curves, as expressed by Equation (3.5). Some of the tests with positive coronas, shown in Figure 3-4, did lie within the shaded regions, suggesting that ions in negative coronas have higher ion mobility than ions in positive coronas.

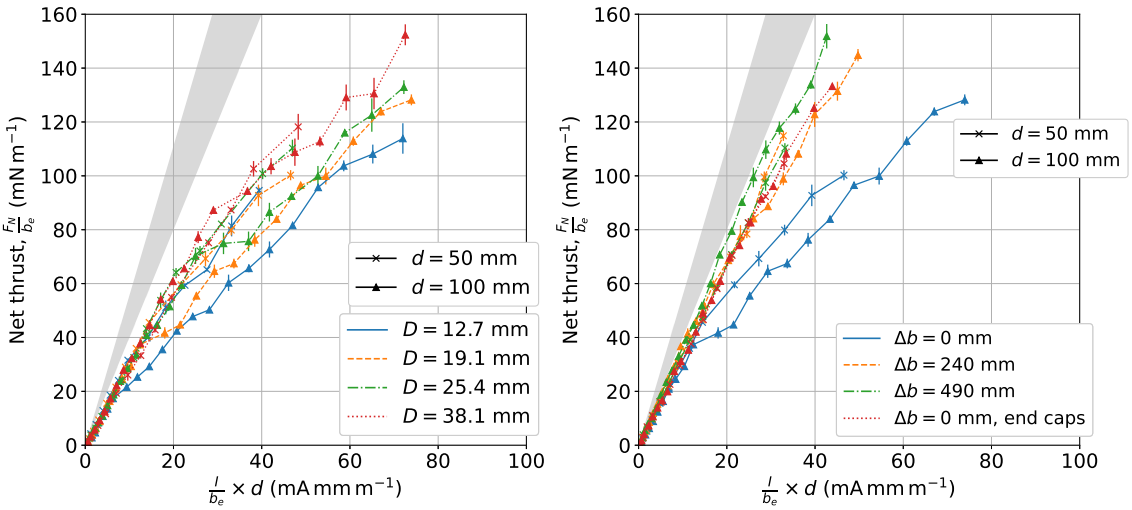

(a) Collector diameter

(b) Collector span & end caps

Figure C-3: Net thrust per unit emitter span versus $\frac{Id}{b_e}$ for (a) different collector diameters, and (b) different collector spans with and without end caps in a negative corona thruster. The shaded band corresponds to a range of ion mobilities reported in the literature: $1.8 \times 10^{-4} \leq \mu \leq 2.5 \times 10^{-4}\,\mathrm{m^2\,V^{-1}\,s^{-1}}$.

C.1.2 Reverse emission and thrust

Figure C-3 compares the current and thrust produced by negative corona thrusters; two collectors were used, with and without end caps. The current against voltage plots in Figure C-4a show that the two collectors draw approximately the same current at low voltages. For all the gap spacings shown, there is a voltage above which the collector with open ends draws significantly more current than the one with end caps.

In contrast, the two collectors show very similar thrust–voltage characteristics in Figure C-4b. The average difference in thrust between the cases with and without end caps is $0.0\,\mathrm{mN\,m^{-1}}$, whereas the root mean square difference is $2.3\,\mathrm{mN\,m^{-1}}$. These differences are small and lie within the experimental uncertainty seen in some cases, suggesting that reverse emission either has a small effect on the thrust produced at a

given voltage or no effect at all.

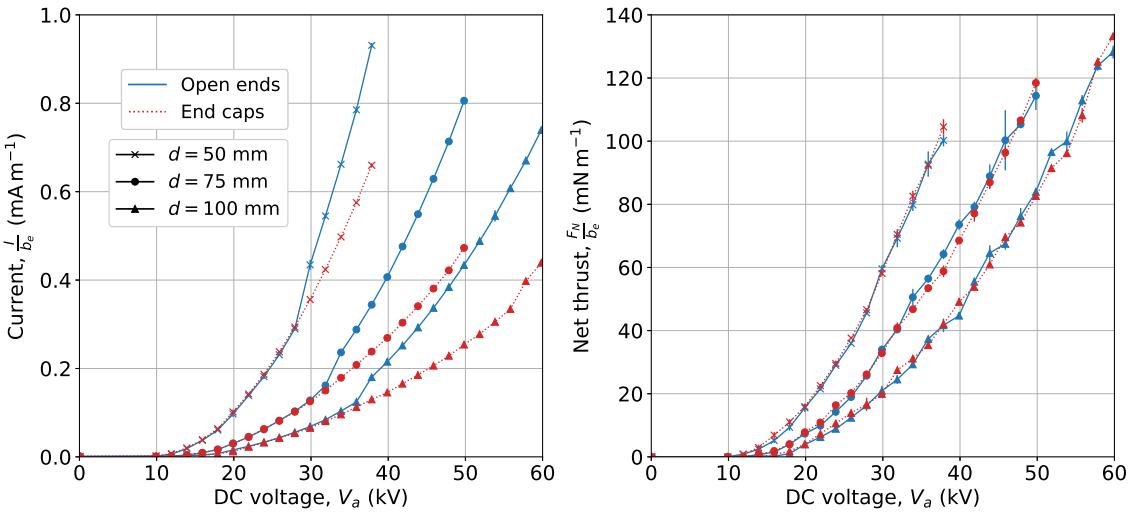

(a) Current (b) Thrust

Figure C-4: (a) Current per unit span, and (b) thrust per unit span versus the applied voltage in a negative corona. Collectors had a diameter $D = 19.1\,\text{mm}$ and cylindrical portions of the same span ($\Delta b = 0\,\text{mm}$), with open ends and with hemispherical end caps. Tests done up to a constant maximum voltage.

C.2 Ultraviolet images with negative corona thrusters

Figure C-5 shows UV images of the region near the collector's tip in tests done with negative corona discharges. The gap spacing was $d = 100\,\text{mm}$ and the applied voltage was $V_a = 50\,\text{kV}$; these were kept constant across all tests.

In Figure C-5a, corresponding to a collector with $D = 12.7\,\text{mm}$, a discharge can be seen on the upper half of the collector's tip. Unlike Figure 3-7a, where the discharge occurs at discrete points on the collector, a more uniform discharge can be seen in Figure C-5a. This discharge at the tip is also visible in Figures C-5b–c, with varying collector diameters. However, the images show no clear sign of a discharge in the cases with $\Delta b = 490\,\text{mm}$ in Figure C-5d or in the test with end caps in Figure C-5e. This suggests that these two cases have mitigated the intensity of the discharge as compared to Figure C-5b or eliminated it.

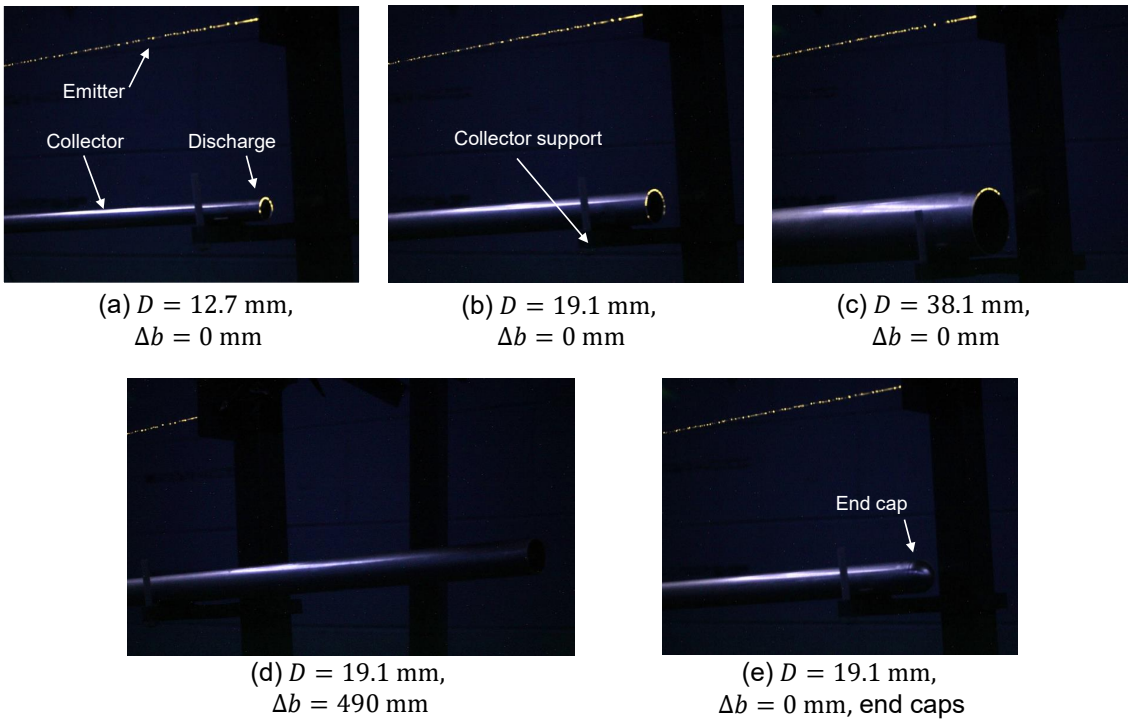

(a) $D = 12.7$ mm, $\Delta b = 0$ mm

(b) $D = 19.1$ mm, $\Delta b = 0$ mm

(c) $D = 38.1$ mm, $\Delta b = 0$ mm

(d) $D = 19.1$ mm, $\Delta b = 490$ mm

(e) $D = 19.1$ mm, $\Delta b = 0$ mm, end caps

Figure C-5: Photographs taken with a UV-sensitive camera of an EAD thruster with a negative corona discharge ion source. The gap spacing was $d = 100\,\text{mm}$ and the applied voltage was $V_a = 50\,\text{kV}$.

C.3 A hypothetical model of reverse emission

In this study, experiments on wire-to-cylinder EAD thrusters have been conducted, observing the effects of reverse emission with acoustic, optical, and electrical diagnostic tools. It has been found that reverse emission results in a significant increase in current (and therefore power draw), but it does not result in noticeable changes in thrust compared to if it were absent. Here, a simplified qualitative physical model for reverse emission and its observed effects on current and thrust is hypothesized.

Reverse emission is attributed to the onset of a corona discharge in regions of high electric field in the collector; in the geometry tested here, this occurs primarily at the tips. This reverse corona discharge has an opposite polarity to that of the ion source at the emitter. The images in Figure 3-7 correspond to a positive-corona ion source at the emitter. The discharges on the collectors in this figure serve as qualitative

evidence that reverse emission in those cases may be caused by a negative corona discharge at the collector: the discharges on the collectors occur at discrete points or "tufts", which is characteristic of negative coronas [77]. In contrast, the discharges on the collectors in Figure C-5 (with a negative corona ion source at the emitter) are more uniform, which is characteristic of positive coronas [77].

These reverse corona discharges would produce a drift of ions of opposite polarity to those of the primary discharge, drifting from the collector to the emitter. This reverse flow of ions would be expected to reduce thrust, as suggested by previous work [32, 34, 141]. However, the results do not show clear evidence of a thrust reduction due to reverse emission. It is hypothesized that this is because the flow of ions of opposite polarity enhances the original discharge at the emitter, increasing the production or extraction of ions of the original polarity. For this model to be compatible with the results, the additional thrust produced through additional original-polarity ions would need to approximately match the thrust reduction due to the reverse drift of opposite-polarity ions.

In corona discharges, ions of the opposite polarity to those in the drift region play a key role in sustaining the discharge. In negative coronas, the discharge is partially maintained by secondary electron emission due to collisions of positive ions with the emitter [79]; whereas in positive coronas, neutralization of negative ions also aids the discharge due to the emission of photons that cause photoionization events and subsequent electron avalanches [77]. The enhancement of the original corona discharge due to oppositely-charged ions from the collector was also suggested by Masuda and Mizuno [142] to play a role in the back corona discharge in electrostatic precipitators. The sides of the emitters in Figures 3-7a–c are significantly brighter than the middle portions of the emitters, which is compatible with having a larger number of ionization and neutralization events. Therefore, current transport in this hypothesized model occurs via three interrelated mechanisms: 1) the original unipolar drift of ions from the emitter to the collector, 2) the drift of ions of opposite polarity from some regions in the collector to the emitter, and 3) a drift of ions of the same polarity as the ion source in the emitter (original polarity) from the emitter to the

collector that results from the interaction of the reverse current with the original ion source.

Other potential explanations for the effects that have been observed in this study are possible: for example, it is possible that the reverse current and the enhanced current at the emitter alternate in a periodic manner, resulting in an apparently unchanged thrust when sampled at a low frequency; or that the discharge at the collector modifies the electric field distribution in such a way that the opposite-polarity ions experience a small Coulomb force in their drift region. Whereas the qualitative model hypothesized here is compatible with the findings in this thesis, further quantitative work is needed to conclude whether this or another different mechanism is responsible for reverse emission and its observed effects. For example, it should be possible to measure the reverse drift of ions through plasma diagnostic tools if this drift exists. Moreover, numerical simulations of corona discharges that model electron avalanches should be capable of capturing the hypothesized processes if this is the real cause of reverse emission.

Appendix D

Supplementary material of Chapter 4

D.1 Analytical model of an ideal 1-D MSD thruster

This section includes the derivation of some of the theoretical results referenced in Section 4.3.2 in Chapter 4.

D.1.1 Governing equations

Gauss's law can be stated as

$$\nabla \cdot \vec{E} = \frac{\rho_c}{\varepsilon}.$$

Under one-dimensional conditions, this can be simplified to

$$\frac{\mathrm{d}E}{\mathrm{d}x} = \frac{\rho_c}{\varepsilon}$$

where x is the spatial coordinate and E is defined such that $\vec{E} = E\hat{x}$, with $\hat{x}$ being the unit vector in the positive x-direction. Conservation of charge can be stated as

$$\frac{\partial \rho_c}{\partial t} + \nabla \cdot \vec{j} = 0.$$

Under steady and 1-D conditions, conservation of charge can be simplified to

$$\frac{\mathrm{d}j}{\mathrm{d}x} = 0,$$

where j is defined such that $\vec{j} = j\hat{x}$. As shown in Equation (4.6), the current density in an EAD device in which a single polarity of ions is present is

$$j = \rho_c(u + \mu E).$$

where u is the 1-D bulk flow velocity. The ion mobility μ can be positive or negative according to $\mu = \text{sign}(q)|\mu|$, where $\text{sign}(q)$ is the sign function applied to the charge of the ions in the drift region.

Assuming that the flow is inviscid and incompressible, the fluid dynamics in the ion acceleration region are governed by the Euler equations. These include conservation of mass,

$$\nabla \cdot \vec{u} = 0,$$

where $\vec{u}$ is the flow velocity vector, and conservation of momentum,

$$\rho \left[\frac{\partial \vec{u}}{\partial t} + (\vec{u} \cdot \nabla)\vec{u} \right] = -\nabla p + \vec{f},$$

where ρ is the mass density of the fluid and p is the pressure. The coupling between the fluid and electrostatic equations is introduced via the body force, $\vec{f}$, which can be modeled as

$$\vec{f} = \rho_c \vec{E},$$

which represents the Coulomb force acting on the ions. Assuming steady and 1-D flow in a constant-area channel, the Euler equations are reduced to

$$\frac{\mathrm{d}u}{\mathrm{d}x} = 0$$

$$0 = -\frac{\mathrm{d}p}{\mathrm{d}x} + \rho_c E.$$

Combining the equations above results in the system in Equation (4.7),

$$\frac{\mathrm{d}}{\mathrm{d}x}\begin{bmatrix} u \\ p \\ \rho_c\,(u+\mu E) \\ E \end{bmatrix} = \begin{bmatrix} 0 \\ \rho_c E \\ 0 \\ \frac{\rho_c}{\varepsilon} \end{bmatrix}.$$

As a note, u in this expression is equivalent to the v_B term used in Chapter 4.

D.1.2 Non-dimensional current–voltage characteristics for set emitter charge density

Consider an ideal 1-D EAD stage that has an emitter at $x = 0$ and a collector at $x = d$. The voltage applied between the emitter and collector is V. From the 1-D current density, the charge density at any point in the gap can be expressed as

$$\rho_c = \frac{j}{v_B + \mu E}.$$

Substituting this into Gauss's law in 1-D,

$$\frac{\mathrm{d}E}{\mathrm{d}x} = \frac{j}{\varepsilon(v_B + \mu E)}.$$

This ordinary differential equation can be solved by separation of variables and has a solution implicitly given by

$$\frac{1}{2}\mu E^2 + v_B E = \frac{jx}{\varepsilon} + C,$$

where C is an integration constant. If $E = E_0$ at $x = 0$ (the emitter), the electric field is given implicitly by

$$\frac{1}{2}\mu E^2 + v_B E = \frac{jx}{\varepsilon} + \frac{1}{2}\mu E_0^2 + v_B E_0,$$

and solving for the electric field,

$$E(x) = \text{sign}(q) \left[\frac{2jx}{\varepsilon\mu} + \left(E_0 + \frac{v_B}{\mu} \right)^2 \right]^{\frac{1}{2}} - \frac{v_B}{\mu}.$$

The sign(q) term is introduced so as to select the physically-correct solution to the quadratic equation depending on the charge of ions. For example, a negative electric field is needed to accelerate negative ions.

Since the electric field must fulfill

$$V = \int_0^d E(x)dx,$$

the current density must meet

$$V = \int_0^d \left(\text{sign}(q) \left[\frac{2jx}{\varepsilon\mu} + \left(E_0 + \frac{v_B}{\mu} \right)^2 \right]^{\frac{1}{2}} - \frac{v_B}{\mu} \right) dx,$$

which is the same as Equation (4.11).

The relation between the electric field and the charge density at the emitter is given by Equation (4.14),

$$E_0 = \frac{1}{\mu} \left(\frac{j}{\rho_{c,0}} - v_B \right).$$

Defining a non-dimensional current density

$$\bar{j} \equiv \frac{j}{j_{\text{MG}}} = \frac{j}{\frac{9}{8}\varepsilon\mu\frac{V^2}{d^3}},$$

making the change of variables $x = d \cdot x'$ and non-dimensionalizing, Equation (4.11) is reduced to the non-dimensional equation

$$1 = \int_0^1 \left[\frac{3}{2} \left(\bar{j}x' + \bar{j}^2 \left(\frac{3}{4\bar{\rho}} \right)^2 \right)^{\frac{1}{2}} - \bar{v} \right] dx',$$

where $\bar{v} = \frac{vd}{\mu V}$ is the electric slip number and $\bar{\rho} = \frac{\rho_{c,0} d^2}{\varepsilon V}$ is the electric source number. Note that $V = \text{sign}(q)\sqrt{V^2}$ was used to eliminate the sign(q) term. To simplify notation, the variable $S = \frac{3}{4}\frac{1}{\bar{\rho}}$, which is analogous to the electric source number, will be used in the subsequent analysis. Integrating,

$$1 = \left[\sqrt{\bar{j}}\left(S^2\bar{j} + x'\right)^{\frac{3}{2}} - \bar{v}x'\right]_0^1.$$

Therefore, the normalized current density $\bar{j}$ can be found from the implicit equation

$$1 = S^3\left[\sqrt{\bar{j}}\left(\bar{j} + S^{-2}\right)^{\frac{3}{2}} - \bar{j}^2\right] - \bar{v} \tag{D.1}$$

An analytical solution to Equation (D.1) was found using the software Wolfram Mathematica for $S > 0$ and $\bar{v} \geq 0$,

$$\bar{j}(S,\bar{v}) = \frac{1}{9}\left(\frac{\sqrt[3]{B_1 + \sqrt{B_1^2 + 4B_2^3}}}{\sqrt[3]{2}} - \frac{\sqrt[3]{2}B_2}{\sqrt[3]{B_1 + \sqrt{B_1^2 + 4B_2^3}}} + \frac{2S\bar{v} + 2S - 3}{S^2}\right)$$

where

$$B_1 = \frac{16\bar{v}^3}{S^3} + \frac{48\bar{v}^2}{S^3} + \frac{171\bar{v}^2}{S^4} + \frac{48\bar{v}}{S^3} + \frac{342\bar{v}}{S^4} + \frac{54\bar{v}}{S^5} + \frac{16}{S^3} + \frac{171}{S^4} + \frac{54}{S^5} + \frac{27}{S^6}$$

$$B_2 = \frac{9}{S^4} - \frac{(-2S\bar{v} - 2S + 3)^2}{S^4}$$

A limiting case can be explored when $\bar{\rho} \to \infty$, or equivalently, $S \to 0$. In this limit, Equation (D.1) reduces to

$$1 = S^3\left[\sqrt{\bar{j}|_{\bar{\rho}\to\infty}}\left(S^{-2}\right)^{\frac{3}{2}}\right] - \bar{v}.$$

Solving for $\bar{j}|_{\bar{\rho}\to\infty}$,

$$\bar{j}|_{\bar{\rho}\to\infty} = (1 + \bar{v})^2,$$

which is the same as Equation (4.16) and represents the space-charge limited current for non-zero bulk fluid velocities.

D.1.3 Non-dimensional current–voltage characteristics for set emitter electric field

An alternative analytical solution can be obtained for the current density in terms of the electric field at the emitter. The charge density at the emitter is related to the electric field at the emitter through

$$\rho_{c,0} = \frac{j}{\mu E_0 + v_B}.$$

Using this, the variable S can be related to the electric field at the emitter through

$$S = \frac{2}{3\bar{j}} \left(\alpha + \bar{v}\right). \tag{D.2}$$

where $\alpha = E_0 \frac{d}{V}$ is the non-dimensional electric field at the emitter. Substituting Equation (D.2) into Equation (D.1),

$$1 = \left(\frac{2\left(\alpha + \bar{v}\right)}{3\bar{j}}\right)^3 \left[\sqrt{\bar{j}} \left(\bar{j} + \left(\frac{2\left(\alpha + \bar{v}\right)}{3\bar{j}}\right)^{-2}\right)^{\frac{3}{2}} - \bar{j}^2\right] - \bar{v}. \tag{D.3}$$

An expression equivalent to Equation (D.3) with different non-dimensional parameters is given by Equation (21) in Pickard [17].

Equation (D.3) has an analytical solution for $\bar{v} \geq 0$ and $-\bar{v} < \alpha < 1$,

$$\bar{j}(\alpha, \bar{v}) = \frac{1}{18}\left(-12\alpha^2 - 24\alpha\bar{v} - 3\bar{v}^2 + 18\bar{v} + 9 + \sqrt{3}\sqrt{(-2\alpha + \bar{v} + 3)^3(2\alpha + 3\bar{v} + 1)}\right).$$

If $\bar{v} = 0$, the normalized current density reduces to

$$\bar{j}|_{\bar{v}=0} = \frac{1}{18}\left(-12\alpha^2 + 9 + \sqrt{3}\sqrt{-16\alpha^4 + 64\alpha^3 - 72\alpha^2 + 27}\right).$$

Similarly, if $\alpha = 0$,

$$\bar{j}|_{\alpha=0} = \frac{1}{6}\left[\left(\frac{64}{3}\bar{v}^3 + \left(\bar{v}^2 - 6\bar{v} - 3\right)^2\right)^{\frac{1}{2}} - \left(\bar{v}^2 - 6\bar{v} - 3\right)\right].$$

This last result was used by Gilmore and Barrett [46] in their analysis of the effects of flight velocity on the performance of EAD thrusters.

D.1.4 Non-dimensional EAD pressure rise

The EAD pressure rise, Δp_E, is the integral of the Coulomb body force acting on the ions in the gap,

$$\begin{aligned}
\Delta p_E &= \int_0^d \rho_c E \mathrm{d}x \\
&= \int_0^d \frac{jE}{\mu E + v_B} \mathrm{d}x \\
&= \int_0^d \left[\frac{j}{\mu} - \mathrm{sign}(q)\frac{jv_B}{\mu^2}\left[\frac{2jx}{\varepsilon\mu} + \left(E_0 + \frac{v_B}{\mu}\right)^2\right]^{-\frac{1}{2}}\right] \mathrm{d}x \\
&= \frac{jd}{\mu} - \frac{\varepsilon v_B}{|\mu|}\left[\left(\frac{2jd}{\varepsilon\mu} + \left(E_0 + \frac{v_B}{\mu}\right)^2\right)^{\frac{1}{2}} - \left|E_0 + \frac{v_B}{\mu}\right|\right]
\end{aligned}$$

which is the same as Equation (4.18). Since the electric field at the emitter E_0 and the charge density $\rho_{c,0}$ are related, this can also be expressed as

$$\begin{aligned}
\Delta p_E &= \frac{jd}{\mu} - \frac{\varepsilon v_B}{|\mu|}\left[\left(\frac{2jd}{\varepsilon\mu} + \left(E_0 + \frac{v_B}{\mu}\right)^2\right)^{\frac{1}{2}} - \left|E_0 + \frac{v_B}{\mu}\right|\right] \\
&= \frac{jd}{\mu} - \frac{\varepsilon v_B}{|\mu|}\left[\left(\frac{2jd}{\varepsilon\mu} + \left(\frac{j}{\mu\rho_{c,0}}\right)^2\right)^{\frac{1}{2}} - \left|\frac{j}{\mu\rho_{c,0}}\right|\right].
\end{aligned}$$

The pressure rise corresponding to the space-charge limited current in static conditions ($v_B = 0$) is

$$\Delta p_E|_{E_0\to 0, v=0} = \frac{j_{\mathrm{MG}} d}{\mu} = \frac{9}{8}\varepsilon\frac{V^2}{d^2}.$$

Defining a normalized pressure rise

$$\bar{p} \equiv \frac{\Delta p_E}{\Delta p_E|_{E_0 \to 0, v=0}}.$$

The normalized pressure rise is related to the normalized current and electric slip and source numbers through

$$\bar{p}(S, \bar{v}) = \bar{j} - \frac{4}{3} S \bar{v} \left[\left(S^{-2} \bar{j} + \bar{j}^2 \right)^{\frac{1}{2}} - \bar{j} \right].$$

As $\bar{\rho} \to \infty$ or, equivalently, as $S \to 0$, the normalized pressure rise tends to

$$\bar{p} \to \bar{j}|_{\bar{\rho} \to \infty} - \frac{4}{3} \bar{v} \sqrt{\bar{j}|_{\bar{\rho} \to \infty}} = (1 + \bar{v})^2 - \frac{4}{3} \bar{v} (1 + \bar{v}) = (1 + \bar{v}) \left(1 - \frac{\bar{v}}{3} \right).$$

Using Equation (D.2), the normalized pressure rise $\bar{p}$ can also be expressed in terms of the normalized emitter electric field α,

$$\bar{p}(\alpha, \bar{v}) = \bar{j} - \frac{8}{9} \bar{v} \left[\left(\frac{9}{4} \bar{j} + (\alpha + \bar{v})^2 \right)^{\frac{1}{2}} - (\alpha + \bar{v}) \right].$$

D.1.5 Non-dimensional EAD pressure rise-to-power ratio

From the definition of the non-dimensional pressure rise,

$$\bar{p} = \frac{\Delta p_E}{\frac{j_{\mathrm{MG}} d}{\mu}} = \frac{\Delta p_E}{\frac{9}{8} \varepsilon \frac{V^2}{d^2}},$$

the DC voltage can be related to the pressure rise across a stage through

$$V = \mathrm{sign}(q) d \sqrt{\frac{8 \Delta p_E}{9 \bar{p} \varepsilon}}. \tag{D.4}$$

From the definitions of $\bar{j}$, $\bar{p}$ and Θ,

$$\Theta = \frac{\bar{p}}{\bar{j}} \frac{d}{\mu V},$$

and substituting Equation (D.4), Equation (4.25) is finally reached,

$$\Theta = \frac{1}{|\mu|}\sqrt{\frac{9\varepsilon}{8}}\frac{\bar{p}^{3/2}}{\bar{j}}\frac{1}{\sqrt{\Delta p_E}}.$$

Analytical expressions for $\bar{p}$ and $\bar{j}$ are given in Sections D.1.2–D.1.4 as functions of the parameters $\bar{v}$ and either $\bar{\rho}$ or α. For constant $\bar{v}$ and α or $\bar{\rho}$, the expression above shows that there is a fundamental trade-off between the pressure rise-to-power ratio and the electrostatic pressure rise.

D.2 Model of a corona-discharge EAD thruster

As shown in Section 4.3.3, the average current density of a corona-discharge stage for voltages above inception can be modeled using Equation (4.28),

$$j = C_0\varepsilon\mu\frac{V(V-V_0)}{d^3}\frac{d}{\Delta}f\left(\frac{\Delta}{d}\right)\bar{j}_c(\bar{v}),$$

and the EAD pressure rise per stage can be modeled using Equation (4.35) as

$$\Delta p_E = C_0\varepsilon\frac{V(V-V_0)}{d^2}\frac{d}{\Delta}f\left(\frac{\Delta}{d}\right)\bar{p}_c(\bar{v}).$$

From these, the stage pressure rise-to-power ratio can be calculated,

$$\Theta = \frac{\Delta p_E}{P/A} = \frac{\Delta p_E}{jV} = \frac{d}{\mu V}\frac{\bar{p}_c(\bar{v})}{\bar{j}_c(\bar{v})}. \tag{D.5}$$

Equation (4.35) can be solved for the voltage as a function of, among other parameters, the pressure rise Δp_E. The exact solution is given by

$$V = \frac{V_0}{2} + \mathrm{sign}(q)\sqrt{\left(\frac{V_0}{2}\right)^2 + \frac{d^2\Delta p_E}{C_0\varepsilon}\frac{\Delta}{d}\frac{1}{f\left(\frac{\Delta}{d}\right)\bar{p}_c(\bar{v})}},$$

and therefore the relation between Θ and Δp_E can be found by substituting this

result into Equation (D.5),

$$\Theta = \frac{1}{\mu}\frac{\bar{p}_c(\bar{v})}{\bar{j}_c(\bar{v})}\frac{1}{\frac{V_0}{2d} + \mathrm{sign}(q)\sqrt{\left(\frac{V_0}{2d}\right)^2 + \frac{\Delta p_E}{C_0\varepsilon}\frac{\Delta}{d}\frac{1}{f\left(\frac{\Delta}{d}\right)\bar{p}_c(\bar{v})}}}. \tag{D.6}$$

Equation (D.6) is analogous to Equation (4.25) for ideal 1-D stages. A significant difference is that Equation (D.6) shows a weak dependency on the gap spacing d through the inception voltage $V_0(d)$. A simplified version of Equation (D.6) can be derived assuming that $|V| \gg |V_0|$. In this case, the voltage simplifies to

$$V \approx \mathrm{sign}(q)\sqrt{\frac{d^2\Delta p_E}{C_0\varepsilon}\frac{\Delta}{d}\frac{1}{f\left(\frac{\Delta}{d}\right)\bar{p}_c(\bar{v})}},$$

and the pressure rise-to-power ratio can be expressed as

$$\Theta \approx \frac{1}{|\mu|}\sqrt{C_0\varepsilon\frac{d}{\Delta}f\left(\frac{\Delta}{d}\right)}\frac{\bar{p}_c(\bar{v})^{\frac{3}{2}}}{\bar{j}_c(\bar{v})}\frac{1}{\sqrt{\Delta p_E}},$$

which is the same as Equation (4.36).

D.3 Model validation

Some studies on multistaged EAD gas pumps have used geometries similar to that of the MSD thrusters considered in this thesis. In particular, Rickard et al. [25] studied a multistaged ducted pump with pin-to-ring corona-discharge stages and fitted with an inlet and a nozzle. They showed that the nozzle pressure and exit flow velocity could be controlled by varying the nozzle area ratio and the number of stages.

The duct used by Rickard et al. [25] had an internal diameter of 25.4 mm. The tip of the pin emitter was placed $d = 5\,\mathrm{mm}$ upstream of the entrance to the ring collector plane. Stages were repeating and operated at $V = -15\,\mathrm{kV}$. Rickard et al. [25] measured the pressure drop across the nozzle and the flow velocity downstream of the nozzle exit. However, they did not estimate the pressure rise provided by electrostatic forces, Δp_E, and the current drawn by each stage is not explicitly stated. Rickard et

al. [25] state that their pump drew 870 µA of current when 7 stages were used, such that, on average, each stage drew $I \approx 120\,\mu\text{A}$. The EAD pressure rise, Δp_E, can be estimated from this as

$$\Delta p_E \approx \frac{Id}{\mu A}.$$

Using their device's cross-sectional area, A, and assuming an ion mobility of $\mu = 2 \times 10^{-4}\,\text{m}^2\,\text{V}^{-1}\,\text{s}^{-1}$, the EAD pressure rise can be estimated to be $\Delta p_E \approx 6\,\text{Pa}$.

To use the models in Section 4.3.4, the loss coefficient needs to be known as well. In general, the loss coefficient is a function of the Reynolds number and, hence, depends on the flow velocity through the device. For the purpose of validating the models in this study, it will be assumed that the loss coefficient is constant. As shown in Sections 4.3.2 and 4.3.4, the nozzle exit velocity can be estimated as

$$v_4 \approx \sqrt{\frac{2n\Delta p_E}{\rho(1 + nK_L\phi^2)}}. \tag{D.7}$$

Figure D-1a shows how the nozzle exit velocity changed with the nozzle area ratio and number of stages in the device tested by Rickard et al. [25]. Markers correspond to the experimental data in Figures 9 and 10 in Rickard et al. [25]. Solid lines represent the model in Equation (D.7), with $\Delta p_E = 6\,\text{Pa}$ and a constant $K_L = 1.55$ found from a best fit to the data. The fits provide a coefficient of correlation of $r^2 = 0.94$. Figure D-1a shows that the models can capture the main trends observed in the device of Rickard et al. [25], although some quantitative differences can be observed. These can be attributed to the assumptions made in modeling and to the fact that the loss coefficient is assumed constant, when in reality it would be expected to decrease as the flow velocity through the device increases.

Figure D-1b shows how the nozzle pressure drop changes with the volumetric flow rate in this device. The models are able to capture the trade-off between nozzle inlet pressure and volumetric flow rate, although there are some quantitative differences due to the reasons mentioned above.

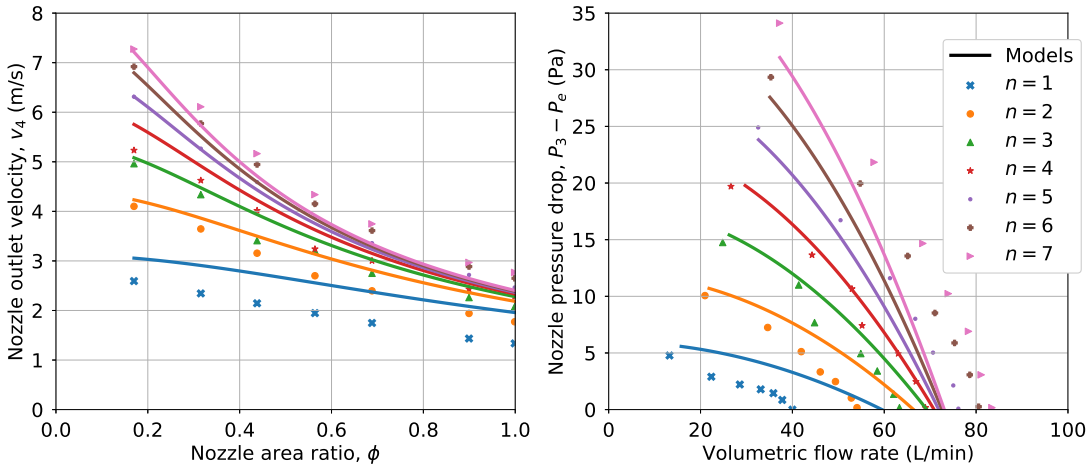

Figure D-1: Average nozzle exit velocity against nozzle area ratio and nozzle pressure drop versus flow rate for different number of stages in a multistaged pump. Markers represent the experimental data in Rickard et al. and solid lines corresponds to the model in Equation (D.7).

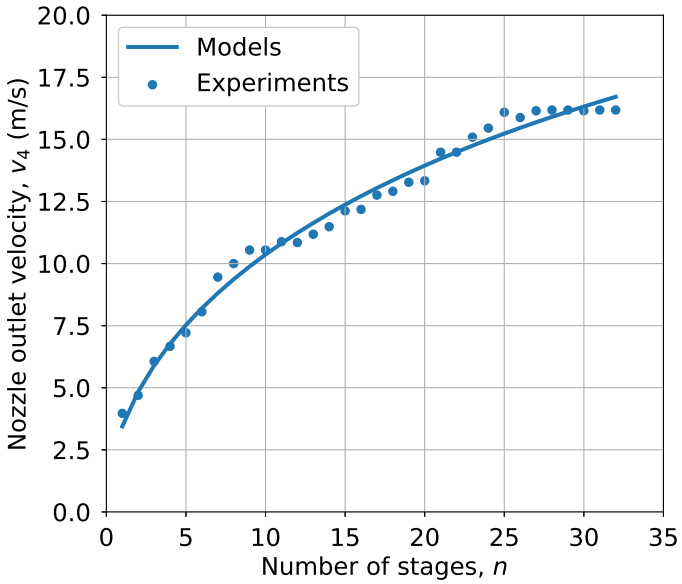

Figure D-2: Average nozzle exit velocity against number of stages in a multistaged pump. Markers correspond to the experimental data in Qiu et al. and the solid line corresponds to the model in Equation (D.7).

Qiu et al [23] tested a multistaged ducted EAD pump with up to 32 pin-to-mesh stages. Their device was cylindrical and did not contain an inlet or a nozzle. The authors did not specify the voltage applied between the electrodes or the current draw of the device; therefore, the pressure produced by the EAD stages cannot be

determined. Instead, a constant $\Delta p_E = 7.38\,\text{Pa}$ and $K_L = 0.012$ was found from a best fit to the data in Figure 8 in Qiu et al [23], which provides a coefficient of determination of $r^2 = 0.99$. Figure D-2 shows a comparison between the experimental data in Qiu et al [23] and the model in Equation (D.7) with these fit parameters. The models capture the rise with diminishing returns in nozzle exit velocity with number of stages; unlike the experimental data, a saturation after 25 stages is not seen and the exit pressure continues increasing with number of stages.

D.4 Results

The model of MSD thrusters combines momentum theory with either ideal 1-D EAD theory or a model of corona-discharge thrusters. This section describes the methods used to solve the governing equations simultaneously.

D.4.1 Ideal 1-D stages

As shown in Equation (4.40), the pressure rise across ideal 1-D stages is given by

$$\Delta p = \sum_{i=1}^{n} \Delta p^i_{\text{stage}} = \sum_{i=1}^{n} \left(\Delta p^i_E - \frac{1}{2}\rho v_2^2 K_L^i \right).$$

The EAD pressure rise at stage i can also be expressed as

$$\Delta p^i_E = \left[\bar{p}(\bar{\rho}, \bar{v}) \Delta p_E |_{E_0 \to 0, v=0} \right]^i,$$

where the superscript i refers to the properties of stage i. If stages are repeating, the pressure rise across the EAD stages can then be expressed as

$$\Delta p = n \left(\bar{p}(\bar{\rho}, \bar{v}) \Delta p_E |_{E_0 \to 0, v=0} - \frac{1}{2}\rho v_2^2 K_L \right),$$

under the assumption that the loss coefficient is independent of the number of stages. From momentum theory, the velocity across the EAD stages is constant and given by

$$v_2 = \phi\sqrt{v_1^2 + \frac{2\Delta p}{\rho}},$$

and, hence, v_2 is a function of the pressure rise Δp.

Therefore, a self-consistent solution is reached when

$$\Delta p - n\left(\bar{p}\left(\bar{\rho}, \frac{\phi\sqrt{v_1^2 + \frac{2\Delta p}{\rho}}d}{\mu V}\right)\Delta p_E|_{E_0\to 0, v=0} - \frac{1}{2}\rho\left(\phi\sqrt{v_1^2 + \frac{2\Delta p}{\rho}}\right)^2 K_L\right) = 0. \tag{D.8}$$

In this equation, the inputs are the freestream velocity, v_1; the loss coefficient, K_L; the number of stages, n; the ratio of voltage-to-gap-spacing, $\frac{V}{d}$; the electric source number, $\bar{\rho}$; and the nozzle are ratio, ϕ. The unknown is the overall pressure rise across the thruster, Δp. This equation has an analytical solution when the stages are space-charge limited ($\bar{\rho} \to \infty$) and if ϕ is set.

However, instead of using a constant nozzle area ratio, it is advantageous to select ϕ so that it maximizes the thrust density. Therefore, Equation (D.8) can be augmented so as to treat the nozzle area ratio as an unknown. The augmented system can then be solved numerically by defining

$$\underline{f}_\phi = \begin{bmatrix} \Delta p - n\left(\bar{p}\left(\bar{\rho}, \frac{\phi\sqrt{v_1^2 + \frac{2\Delta p}{\rho}}d}{\mu V}\right)\Delta p_E|_{E_0\to 0, v=0} - \frac{1}{2}\rho\left(\phi\sqrt{v_1^2 + \frac{2\Delta p}{\rho}}\right)^2 K_L\right) \\ \phi - \phi_{\text{opt}}\left(n, K_L, \frac{\rho v_1^2}{\Delta p_E}\right) \end{bmatrix},$$

where $\phi_{\text{opt}}\left(n, K_L, \frac{\rho v_1^2}{\Delta p_E}\right)$ is the nozzle area ratio that maximizes the thrust density in Equation (4.44), and is given by

$$\phi_{\text{opt}} = \sqrt{\frac{1}{C} + \frac{B}{2C(A+B)} - \sqrt{B}\frac{\sqrt{8A+9B}}{2(A+B)C}},$$

where $A = 2n$, $B = \frac{\rho v_1^2}{\Delta p_E}$ and $C = nK_L$. To reach this expression, it was assumed

that both K_L and Δp_E are independent of ϕ. The solution, $\begin{bmatrix}\Delta p & \phi\end{bmatrix}^T$, is reached when some relevant norm $||\underline{f}_\phi|| \to 0$. This solution was found using a Newton's method solver in which the Jacobian was found using finite-differences. A mobility $|\mu| = 2 \times 10^{-4}\,\mathrm{m^2\,V^{-1}\,s^{-1}}$ was assumed. In general, the nozzle area ratio, ϕ, resulting from this analysis may be greater than 1. Since an area ratio greater than 1 can result in flow separation in the nozzle, the function

$$\underline{f}_{\phi=1} = \Delta p - n\left(\bar{p}\left(\bar{\rho}, \frac{\sqrt{v_1^2 + \frac{2\Delta p}{\rho}}d}{\mu V}\right)\Delta p_E|_{E_0\to 0, v=0} - \frac{1}{2}\rho\left(v_1^2 + \frac{2\Delta p}{\rho}\right)K_L\right),$$

was also defined, where a constant $\phi = 1$ was used. The functions $\underline{f}_{\phi=1}$ and $\underline{f}_\phi$ were zeroed for K_L in the range $0.001 \leq K_L \leq 0.1$, v_1 in the range $0 \leq v_1 \leq 10\,\mathrm{m/s}$, n in the range $1 \leq n \leq 100$, and $|V|/d$ in the range $0 \leq |V|/d \leq 1\,\mathrm{kV/mm}$. The solutions obtained when zeroing $\underline{f}_{\phi=1}$ were selected if $\phi_{\mathrm{opt}} > 1$, and the results obtained from zeroing $\underline{f}_\phi$ were used if $\phi_{\mathrm{opt}} \leq 1$: this implies that the nozzle area ratio used was $\min(1, \phi_{\mathrm{opt}})$.

Once Δp and v_2 have been found, the thrust density $\frac{F}{A_2}$ can be found using

$$\frac{F}{A_2} = \rho v_4(v_4 - v_1)\phi = \rho v_2\left(\frac{v_2}{\phi} - v_1\right),$$

and, assuming negligible ion source power draw, the total power draw can be found using

$$\frac{P}{A_2} = njV = n\bar{j}(\bar{\rho}, \bar{v})j_{\mathrm{MG}}V = n\bar{j}(\bar{\rho}, \bar{v})\frac{9}{8}\varepsilon\mu\left(\frac{V}{d}\right)^3.$$

The thrust-to-power ratio is $\frac{F}{P} = \frac{F/A_2}{P/A_2}$.

D.4.2 Corona-discharge stages

The pressure rise across the EAD stages is given by

$$\Delta p = \sum_{i=1}^{n}\left(\Delta p_E^i - \frac{1}{2}\rho v_2^2 K_L^i\right).$$

If stages are repeating, the pressure rise can be expressed as

$$\Delta p = n\left(\Delta p_E - \frac{1}{2}\rho v_2^2 K_L\right),$$

where the EAD pressure rise provided by a corona-discharge thruster for voltages above inception is given by Equation (4.35),

$$\Delta p_E = C_0 \varepsilon \frac{V(V-V_0)}{d^2}\frac{d}{\Delta} f\left(\frac{\Delta}{d}\right)\bar{p}_c(\bar{v}).$$

Assuming that losses are due to drag forces acting on the collectors only, the loss coefficient can be expressed as

$$K_L = \frac{\frac{c}{d}\frac{d}{\Delta}c_d|_{\Delta\to\infty}}{1-\frac{1}{2}\frac{c}{d}\frac{d}{\Delta}c_d|_{\Delta\to\infty}-\frac{\pi}{2}\frac{A_a}{\Delta^2}},$$

where Equations (4.37) and (4.38) have been combined. The drag coefficient when there are no blockage effects, $c_d|_{\Delta\to\infty}$ is a function of the Reynolds number, $\mathrm{Re} = \frac{v_2 c}{\nu}$; the drag characteristics of the NACA 0012 airfoil at zero angle of attack were found using the software *XFOIL* [167]. A constant $\nu = 1.47\times10^{-5}\,\mathrm{m^2\,s^{-1}}$ was used, corresponding to air at 288 K.

The equations governing the performance of a corona-discharge-based MSD thruster can be combined into a single equation of the form

$$\Delta p - n\left(C_0\varepsilon\frac{V(V-V_0)}{d^2}\frac{d}{\Delta}f\left(\frac{\Delta}{d}\right)\bar{p}_c\left(\frac{v_2 d}{\mu V}\right)-\frac{1}{2}\rho v_2^2 K_L\right)=0, \tag{D.9}$$

where both v_2 and K_L are functions of Δp. The inputs needed to solve this equation are the freestream velocity, v_1; number of stages, n; interelectrode distance-to-gap spacing ratio, $\frac{\Delta}{d}$; and the DC voltage, V. A constant gap spacing $d = 20\,\mathrm{mm}$ was assumed and constant parameters $C_0 = 0.75$ and $|V_0| = 6.1\,\mathrm{kV}$ were used. The collector chord was assumed to be such that $\frac{c}{d} = 1$. The unknown in Equation (D.9) is the overall pressure rise, Δp. The solution to Equation (D.9) was found using a Newton's method solver in which the Jacobian matrix was evaluated with a finite-

difference method. For given inputs, Equation (D.9) was solved for 20 values of ϕ in the range $0.05 \leq \phi \leq 1$ and the value of ϕ resulting in highest thrust density $\frac{F}{A_2}$ was selected.

Once Δp has been determined, the thrust density $\frac{F}{A_2}$ can be found using

$$\frac{F}{A_2} = \rho v_2 \left(\frac{v_2}{\phi} - v_1 \right),$$

and the total power draw can be found using

$$\frac{P}{A_2} = nC_0 \varepsilon \mu \frac{V^2(V - V_0)}{d^3} \frac{d}{\Delta} f\left(\frac{\Delta}{d}\right) \bar{j}_c(\bar{v}).$$

The thrust-to-power ratio is simply $\frac{F}{P} = \frac{F/A_2}{P/A_2}$.

This page intentionally left blank.

Bibliography

[1] M. Robinson, "A History of the Electric Wind," *American Journal of Physics*, vol. 30, no. 5, pp. 366–372, May 1962.

[2] E. D. Fylladitakis, M. P. Theodoridis, and A. X. Moronis, "Review on the History, Research, and Applications of Electrohydrodynamics," *IEEE Transactions on Plasma Science*, vol. 42, no. 2, pp. 358–375, Feb. 2014.

[3] F. Hauksbee, *Physico-Mechanical Experiments on Various Subjects.* J. Senex, 1709.

[4] I. Newton, *Opticks: Or, a Treatise of the Reflections, Refractions, Inflections and Colours of Light. 2nd Edition.* W. and J. Innys, 1718.

[5] B. Wilson, *A Treatise on Electricity.* C. Davis in Holbourn, R. Dodsley in Pallmall, 1750.

[6] T. Cavallo, *A Complete Treatise of Electricity in Theory and Practice: With Original Experiments.* Edward and Charles Dilly, 1777.

[7] M. Faraday, "Experimental Researches in Electricity," *Philosophical Transactions of the Royal Society of London*, vol. 122, pp. 125–162, Dec. 1832.

[8] J. C. Maxwell, *A Treatise on Electricity and Magnetism.* Clarendon Press, 1881, vol. 1.

[9] A. P. Chattock, "On the velocity and mass of the ions in the electric wind in air," *The London, Edinburgh, and Dublin Philosophical Magazine and Journal of Science*, vol. 48, no. 294, pp. 401–420, Nov. 1899.

[10] J. J. Thomson and E. Rutherford, "On the passage of electricity through gases exposed to Röntgen rays," *The London, Edinburgh, and Dublin Philosophical Magazine and Journal of Science*, vol. 42, no. 258, pp. 392–407, Nov. 1896.

[11] T. T. Brown, "A Method of and an Apparatus or Machine for Producing Force or Motion," Nov. 1928, patent 300311, GB.

[12] M. Tajmar, "Biefeld-Brown Effect: Misinterpretation of Corona Wind Phenomena," *AIAA Journal*, vol. 42, no. 2, pp. 315–318, Feb. 2004.

[13] E. Lob, "The pressure effects of ion currents in atmospheric air for different electrode configurations," *Archiv der Elektrischen Ubertragung*, vol. 8, pp. 85–90, 1954.

[14] O. M. Stuetzer, "Ion Drag Pressure Generation," *Journal of Applied Physics*, vol. 30, no. 7, pp. 984–994, Jul. 1959.

[15] O. M. Stuetzer, "Ion Drag Pumps," *Journal of Applied Physics*, vol. 31, no. 1, pp. 136–146, Jan. 1960.

[16] M. Robinson, "Movement of air in the electric wind of the corona discharge," *Transactions of the American Institute of Electrical Engineers, Part I: Communication and Electronics*, vol. 80, no. 2, pp. 143–150, 1961.

[17] W. F. Pickard, "Ion Drag Pumping. I. Theory," *Journal of Applied Physics*, vol. 34, no. 2, pp. 246–250, Feb. 1963.

[18] W. F. Pickard, "Ion Drag Pumping. II. Experiment," *Journal of Applied Physics*, vol. 34, no. 2, pp. 251–258, Feb. 1963.

[19] M. J. Johnson and D. B. Go, "Recent advances in electrohydrodynamic pumps operated by ionic winds: A review," *Plasma Sources Science and Technology*, vol. 26, no. 10, p. 103002, Oct. 2017.

[20] F. C. Lai, "EHD gas pumping – A concise review of recent development," *Journal of Electrostatics*, vol. 106, p. 103469, Jul. 2020.

[21] E. Moreau and G. Touchard, "Enhancing the mechanical efficiency of electric wind in corona discharges," *Journal of Electrostatics*, vol. 66, no. 1-2, pp. 39–44, Jan. 2008.

[22] H. Bondar and F. Bastien, "Effect of neutral fluid velocity on direct conversion from electrical to fluid kinetic energy in an electro-fluid-dynamics (EFD) device," *Journal of Physics D: Applied Physics*, vol. 19, no. 9, pp. 1657–1663, Sep. 1986.

[23] W. Qiu, L. Xia, L. Yang, Q. Zhang, L. Xiao, and L. Chen, "Experimental Study on the Velocity and Efficiency Characteristics of a Serial Staged Needle Array-Mesh Type EHD Gas Pump," *Plasma Science and Technology*, vol. 13, no. 6, pp. 693–697, Dec. 2011.

[24] M. Rickard, D. Dunn-Rankin, F. Weinberg, and F. Carleton, "Characterization of ionic wind velocity," *Journal of Electrostatics*, vol. 63, no. 6-10, pp. 711–716, Jun. 2005.

[25] M. Rickard, D. Dunn-Rankin, F. Weinberg, and F. Carleton, "Maximizing ion-driven gas flows," *Journal of Electrostatics*, vol. 64, no. 6, pp. 368–376, Jun. 2006.

[26] I. W. Brindle and F. C. Lai, "Experimental study of corona jet produced from a circular tube fitted with a nozzle," *Journal of Electrostatics*, vol. 90, pp. 15–22, Dec. 2017.

[27] J. H. Lin, S. C. Lin, and F. C. Lai, "Performance of an electrohydrodynamic gas pump fitted within a nozzle," *Journal of Electrostatics*, vol. 91, pp. 1–8, Feb. 2018.

[28] S.-I. Cheng, "Glow Discharge as an Advanced Propulsion Device," *ARS Journal*, vol. 32, no. 12, pp. 1910–1916, Dec. 1962.

[29] E. A. Christenson and P. S. Moller, "Ion-neutral propulsion in atmospheric media," *AIAA Journal*, vol. 5, no. 10, pp. 1768–1773, Oct. 1967.

[30] J. Wilson, H. D. Perkins, and W. K. Thompson, "An investigation of ionic wind propulsion," NASA, Tech. Rep. TM-2009-215822, 2009.

[31] L. Pekker and M. Young, "Model of Ideal Electrohydrodynamic Thruster," *Journal of Propulsion and Power*, vol. 27, no. 4, pp. 786–792, Jul. 2011.

[32] K. Masuyama and S. R. H. Barrett, "On the performance of electrohydrodynamic propulsion," *Proceedings of the Royal Society A: Mathematical, Physical and Engineering Sciences*, vol. 469, no. 2154, pp. 20 120 623–20 120 623, Apr. 2013.

[33] E. Moreau, N. Benard, J.-D. Lan-Sun-Luk, and J.-P. Chabriat, "Electrohydrodynamic force produced by a wire-to-cylinder dc corona discharge in air at atmospheric pressure," *Journal of Physics D: Applied Physics*, vol. 46, no. 47, p. 475204, Oct. 2013.

[34] H. Xu, N. Gomez-Vega, D. R. Agrawal, and S. R. H. Barrett, "Higher thrust-to-power with large electrode gap spacing electroaerodynamic devices for aircraft propulsion," *Journal of Physics D: Applied Physics*, vol. 53, no. 2, p. 025202, Oct. 2019.

[35] N. Monrolin, F. Plouraboué, and O. Praud, "Electrohydrodynamic Thrust for In-Atmosphere Propulsion," *AIAA Journal*, vol. 55, no. 12, pp. 4296–4305, Dec. 2017.

[36] C. K. Gilmore and S. R. H. Barrett, "Electrohydrodynamic thrust density using positive corona-induced ionic winds for in-atmosphere propulsion," *Proceedings of the Royal Society A: Mathematical, Physical and Engineering Sciences*, vol. 471, no. 2175, pp. 20 140 912–20 140 912, Feb. 2015.

[37] S. Coseru, D. Fabre, and F. Plouraboué, "Numerical study of ElectroAeroDynamic force and current resulting from ionic wind in emitter/collector systems," *Journal of Applied Physics*, vol. 129, no. 10, p. 103304, Mar. 2021.

[38] M. Belan, L. Arosti, R. Polatti, F. Maggi, S. Fiorini, and F. Sottovia, "A parametric study of electrodes geometries for atmospheric electrohydrodynamic propulsion," *Journal of Electrostatics*, vol. 113, p. 103616, Sep. 2021.

[39] V. Y. Khomich, V. E. Malanichev, and I. E. Rebrov, "Electrohydrodynamic thruster for near-space applications," *Acta Astronautica*, vol. 180, pp. 141–148, Mar. 2021.

[40] J. R. Casado and A. D. Greig, "Solid State Atmosphere Breathing Plasma Propulsion for an Autonomous Mars Drone," in *ASCEND 2020*. American Institute of Aeronautics and Astronautics, Nov. 2020.

[41] D. F. Colas, A. Ferret, D. Z. Pai, D. A. Lacoste, and C. O. Laux, "Ionic wind generation by a wire-cylinder-plate corona discharge in air at atmospheric pressure," *Journal of Applied Physics*, vol. 108, no. 10, p. 103306, Nov. 2010.

[42] H. Xu, Y. He, and S. R. H. Barrett, "A dielectric barrier discharge ion source increases thrust and efficiency of electroaerodynamic propulsion," *Applied Physics Letters*, vol. 114, no. 25, p. 254105, Jun. 2019.

[43] H. S. Poon, M. K. K. Lam, M. Chow, and W. J. Li, "Noiseless and vibration-free Ionic Propulsion technology for indoor surveillance blimps," in *2009 IEEE International Conference on Robotics and Automation*. IEEE, May 2009.

[44] Z. He, P. Li, W. Wang, L. Shao, and X. Chen, "Design of indoor unmanned airship propelled by ionic wind," *Journal of Physics: Conference Series*, vol. 1748, p. 062011, Jan. 2021.

[45] H. Xu, Y. He, K. L. Strobel, C. K. Gilmore, S. P. Kelley, C. C. Hennick, T. Sebastian, M. R. Woolston, D. J. Perreault, and S. R. H. Barrett, "Flight of an aeroplane with solid-state propulsion," *Nature*, vol. 563, no. 7732, pp. 532–535, Nov. 2018.

[46] C. K. Gilmore and S. R. H. Barrett, "Electroaerodynamic Thruster Performance as a Function of Altitude and Flight Speed," *AIAA Journal*, vol. 56, no. 3, pp. 1105–1117, Mar. 2018.

[47] D. S. Drew and K. S. J. Pister, "First takeoff of a flying microrobot with no moving parts," in *2017 International Conference on Manipulation, Automation and Robotics at Small Scales (MARSS)*. IEEE, Jul. 2017.

[48] D. S. Drew, N. O. Lambert, C. B. Schindler, and K. S. J. Pister, "Toward Controlled Flight of the Ionocraft: A Flying Microrobot Using Electrohydrodynamic Thrust With Onboard Sensing and No Moving Parts," *IEEE Robotics and Automation Letters*, vol. 3, no. 4, pp. 2807–2813, Oct. 2018.

[49] V. Y. Khomich and I. E. Rebrov, "In-atmosphere electrohydrodynamic propulsion aircraft with wireless supply onboard," *Journal of Electrostatics*, vol. 95, pp. 1–12, Oct. 2018.

[50] P. H. G. Allen and T. G. Karayiannis, "Electrohydrodynamic enhancement of heat transfer and fluid flow," *Heat Recovery Systems and CHP*, vol. 15, no. 5, pp. 389–423, Jul. 1995.

[51] J. Fernández and R. Poulter, "Radial mass flow in electrohydrodynamically-enhanced forced heat transfer in tubes," *International Journal of Heat and Mass Transfer*, vol. 30, no. 10, pp. 2125–2136, Oct. 1987.

[52] J. Wang, T. Zhu, Y.-x. Cai, J.-f. Zhang, and J.-b. Wang, "Review on the recent development of corona wind and its application in heat transfer enhancement," *International Journal of Heat and Mass Transfer*, vol. 152, p. 119545, May 2020.

[53] E. Moreau, "Airflow control by non-thermal plasma actuators," *Journal of Physics D: Applied Physics*, vol. 40, no. 3, pp. 605–636, Jan. 2007.

[54] G. Artana, J. D'Adamo, L. Léger, E. Moreau, and G. Touchard, "Flow Control with Electrohydrodynamic Actuators," *AIAA Journal*, vol. 40, no. 9, pp. 1773–1779, Sep. 2002.

[55] M. Forte, J. Jolibois, J. Pons, E. Moreau, G. Touchard, and M. Cazalens, "Optimization of a dielectric barrier discharge actuator by stationary and non-stationary measurements of the induced flow velocity: Application to airflow control," *Experiments in Fluids*, vol. 43, no. 6, pp. 917–928, Aug. 2007.

[56] C. He, T. C. Corke, and M. P. Patel, "Plasma Flaps and Slats: An Application of Weakly Ionized Plasma Actuators," *Journal of Aircraft*, vol. 46, no. 3, pp. 864–873, May 2009.

[57] A. Sudrajad and A. F. Yusof, "Review of Electrostatic Precipitator Device for Reduce of Diesel Engine Particulate Matter," *Energy Procedia*, vol. 68, pp. 370–380, Apr. 2015.

[58] A. Afshari, L. Ekberg, L. Forejt, J. Mo, S. Rahimi, J. Siegel, W. Chen, P. Wargocki, S. Zurami, and J. Zhang, "Electrostatic Precipitators as an Indoor Air Cleaner—A Literature Review," *Sustainability*, vol. 12, no. 21, p. 8774, Jan. 2020.

[59] S. Masuda and A. Mizuno, "Initiation condition and mode of back discharge," *Journal of Electrostatics*, vol. 4, no. 1, pp. 35–52, Dec. 1977.

[60] H.-J. Kim, B. Han, Y.-J. Kim, and S.-J. Yoa, "Characteristics of an electrostatic precipitator for submicron particles using non-metallic electrodes and collection plates," *Journal of Aerosol Science*, vol. 41, no. 11, pp. 987–997, Nov. 2010.

[61] S. D. Marcum and B. N. Ganguly, "Electric-field-induced flame speed modification," *Combustion and Flame*, vol. 143, no. 1, pp. 27–36, Oct. 2005.

[62] J. Lawton, F. J. Weinberg, and A. G. Gaydon, "Maximum ion currents from flames and the maximum practical effects of applied electric fields," *Proceedings of the Royal Society of London. Series A. Mathematical and Physical Sciences*, vol. 277, no. 1371, pp. 468–497, Feb. 1964.

[63] M. Kono, F. B. Carleton, A. R. Jones, and F. J. Weinberg, "The effect of nonsteady electric fields on sooting flames," *Combustion and Flame*, vol. 78, no. 3, pp. 357–364, Dec. 1989.

[64] M. Saito, T. Arai, and M. Arai, "Control of soot emitted from acetylene diffusion flames by applying an electric field," *Combustion and Flame*, vol. 119, no. 3, pp. 356–366, Nov. 1999.

[65] A. Fridman, A. Chirokov, and A. Gutsol, "Non-thermal atmospheric pressure discharges," *Journal of Physics D: Applied Physics*, vol. 38, no. 2, pp. R1–R24, Jan. 2005.

[66] Y. P. Raizer, *Gas Discharge Physics*. Springer-Verlag, 1991.

[67] J. R. Roth, *Industrial Plasma Engineering*. Institute of Physics Publishing, 1995.

[68] A. Pedersen, I. W. McAllister, G. C. Crichton, and S. Vibholm, "Formulation of the streamer breakdown criterion and its application to strongly electronegative gases and gas mixtures," *Archiv für Elektrotechnik*, vol. 67, no. 6, pp. 395–402, Nov. 1984.

[69] C. Guerra-Garcia, N. C. Nguyen, J. Peraire, and M. Martinez-Sanchez, "Charge Control Strategy for Aircraft-Triggered Lightning Strike Risk Reduction," *AIAA Journal*, vol. 56, no. 5, pp. 1988–2002, May 2018.

[70] E. Moreau, P. Audier, T. Orriere, and N. Benard, "Electrohydrodynamic gas flow in a positive corona discharge," *Journal of Applied Physics*, vol. 125, no. 13, p. 133303, Apr. 2019.

[71] E. Defoort, R. Bellanger, C. Batiot-Dupeyrat, and E. Moreau, "Ionic wind produced by a DC needle-to-plate corona discharge with a gap of 15 mm," *Journal of Physics D: Applied Physics*, vol. 53, no. 17, p. 175202, Feb. 2020.

[72] Y. Zhang, L. Liu, Y. Chen, and J. Ouyang, "Characteristics of ionic wind in needle-to-ring corona discharge," *Journal of Electrostatics*, vol. 74, pp. 15–20, Apr. 2015.

[73] R. D. Morrison and D. M. Hopstock, "The distribution of current in wire-to-cylinder corona," *Journal of Electrostatics*, vol. 6, no. 4, pp. 349–360, Sep. 1979.

[74] K. Yanallah, F. Pontiga, Y. Meslem, and A. Castellanos, "An analytical approach to wire-to-cylinder corona discharge," *Journal of Electrostatics*, vol. 70, no. 4, pp. 374–383, Aug. 2012.

[75] K. L. Strobel, "Experimental characterization of surface integrated electroaerodynamic thrusters," Master's thesis, Massachusetts Institute of Technology, 2020.

[76] S.-Z. Li and H. S. Uhm, "Investigation of electrical breakdown characteristics in the electrodes of cylindrical geometry," *Physics of Plasmas*, vol. 11, no. 6, pp. 3088–3095, Jun. 2004.

[77] J. Chen and J. H. Davidson, "Model of the Negative DC Corona Plasma: Comparison to the Positive DC Corona Plasma," *Plasma Chemistry and Plasma Processing*, vol. 23, no. 1, pp. 83–102, 2003.

[78] J.-S. Chang, P. A. Lawless, and T. Yamamoto, "Corona discharge processes," *IEEE Transactions on Plasma Science*, vol. 19, no. 6, pp. 1152–1166, 1991.

[79] J. Chen and J. H. Davidson, "Electron Density and Energy Distributions in the Positive DC Corona: Interpretation for Corona-Enhanced Chemical Reactions," *Plasma Chemistry and Plasma Processing*, vol. 22, no. 2, pp. 199–224, 2002.

[80] F. W. Peek, *Dielectric Phenomena in High Voltage Engineering*. McGraw-Hill Book Company, 1915, https://openlibrary.org/books/OL6737166M.

[81] L. Zhao and K. Adamiak, "Numerical Simulation of the Electrohydrodynamic Flow in a Single Wire-Plate Electrostatic Precipitator," *IEEE Transactions on Industry Applications*, vol. 44, no. 3, pp. 683–691, 2008.

[82] N. A. Kaptsov, "Elektricheskie yavleniya v gazakh i vakuume," *Mosc OGIZ*, 1947.

[83] R. Morrow and J. J. Lowke, "Streamer propagation in air," *Journal of Physics D: Applied Physics*, vol. 30, no. 4, pp. 614–627, Feb. 1997.

[84] J. S. Townsend, *Electricity in Gases*. Clarendon Press, Oxford, 1915, https://catalog.hathitrust.org/api/volumes/oclc/4294747.html.

[85] J. D. Cobine, *Gaseous Conductors: Theory and Engineering*. Dover Publications, 1958.

[86] L. G. Hector and H. L. Schultz, "The Dielectric Constant of Air at Radiofrequencies," *Physics*, vol. 7, no. 4, pp. 133–136, Apr. 1936.

[87] J. Skalný, G. Hortváth, and N. J. Mason, "Spectra of Ions Produced by Corona Discharges," *AIP Conference Proceedings*, vol. 876, no. 1, pp. 284–293, Dec. 2006.

[88] M. Pavlik and J. D. Skalny, "Generation of [H3O]+.(H2O)n clusters by positive corona discharge in air," *Rapid Communications in Mass Spectrometry*, 1997.

[89] M. J. Zeng, Z. G. Qu, and J. F. Zhang, "Negative corona discharge and flow characteristics of a two-stage needle-to-ring configuration ionic wind pump for temperature and relative humidity," *International Journal of Heat and Mass Transfer*, vol. 201, p. 123561, Feb. 2023.

[90] B. Eliasson, M. Hirth, and U. Kogelschatz, "Ozone synthesis from oxygen in dielectric barrier discharges," *Journal of Physics D: Applied Physics*, vol. 20, no. 11, pp. 1421–1437, Nov. 1987.

[91] H. Claus, "Ozone Generation by Ultraviolet Lamps," *Photochemistry and Photobiology*, vol. 97, no. 3, pp. 471–476, Feb. 2021.

[92] T. C. Manley, "The Electric Characteristics of the Ozonator Discharge," *Transactions of The Electrochemical Society*, vol. 84, no. 1, p. 83, 1943.

[93] K. Pochner, W. Neff, and R. Lebert, "Atmospheric pressure gas discharges for surface treatment," *Surface and Coatings Technology*, vol. 74–75, pp. 394–398, Sep. 1995.

[94] M. I. Lomaev, E. A. Sosnin, V. F. Tarasenko, D. V. Shits, V. S. Skakun, M. V. Erofeev, and A. A. Lisenko, "Capacitive and barrier discharge excilamps and their applications (Review)," *Instruments and Experimental Techniques*, vol. 49, no. 5, pp. 595–616, Oct. 2006.

[95] A. Vincent-Randonnier, S. Larigaldie, P. Magre, and V. Sabel'nikov, "Plasma assisted combustion: Effect of a coaxial DBD on a methane diffusion flame," *Plasma Sources Science and Technology*, vol. 16, no. 1, pp. 149–160, Dec. 2006.

[96] K. G. Kostov, R. Y. Honda, L. M. S. Alves, and M. E. Kayama, "Characteristics of dielectric barrier discharge reactor for material treatment," *Brazilian Journal of Physics*, vol. 39, no. 2, Jun. 2009.

[97] S. Gadkari and S. Gu, "Numerical investigation of co-axial DBD: Influence of relative permittivity of the dielectric barrier, applied voltage amplitude, and frequency," *Physics of Plasmas*, vol. 24, no. 5, p. 053517, May 2017.

[98] V. Procházka, Z. Tučeková, P. Dvorak, D. Kováčik, P. Slavíček, A. Zahoranová, and J. Voráč, "Coplanar surface barrier discharge ignited in water vapor—a selective source of OH radicals proved by (TA)LIF measurement," *Plasma Sources Science and Technology*, vol. 27, no. 1, p. 015001, Dec. 2017.

[99] N. D. Wilde, H. Xu, N. Gomez-Vega, and S. R. H. Barrett, "A model of surface dielectric barrier discharge power," *Applied Physics Letters*, vol. 118, no. 15, p. 154102, Apr. 2021.

[100] S. Sato, H. Furukawa, A. Komuro, M. Takahashi, and N. Ohnishi, "Successively accelerated ionic wind with integrated dielectric-barrier-discharge plasma actuator for low-voltage operation," *Scientific Reports*, vol. 9, no. 1, Apr. 2019.

[101] A. Quinton, A. D. Ngo, and J. D. Jacob, "Exploration of Surface Dielectric Barrier Discharge for Solid State Propulsion," in *AIAA Scitech 2021 Forum*. American Institute of Aeronautics and Astronautics, Jan. 2021.

[102] A. V. Pipa, T. Hoder, J. Koskulics, M. Schmidt, and R. Brandenburg, "Experimental determination of dielectric barrier discharge capacitance," *Review of Scientific Instruments*, vol. 83, no. 7, p. 075111, Jul. 2012.

[103] S. Barbosa, G. Pilla, D. A. Lacoste, P. Scouflaire, S. Ducruix, C. O. Laux, and D. Veynante, "Influence of nanosecond repetitively pulsed discharges on the stability of a swirled propane/air burner representative of an aeronautical combustor," *Philosophical Transactions of the Royal Society A: Mathematical, Physical and Engineering Sciences*, vol. 373, no. 2048, p. 20140335, Aug. 2015.

[104] S. Shcherbanev, B. A. Dharmaputra, and N. Noiray, "Flame stabilization with nanosecond repetitively pulsed discharge in the sequential combustor," in *AIAA SCITECH 2022 Forum*. American Institute of Aeronautics and Astronautics, Jan. 2022.

[105] C. A. Pavan, C. Guerra-Garcia, D. Weibel, M. Nishihara, F. del Campo, S. Shanbhogue, and A. Ghoniem, "Nanosecond Pulsed Discharge Dynamics in a Swirl-Stabilized Combustor with an Unstable Flame," in *AIAA AVIATION 2022 Forum*. American Institute of Aeronautics and Astronautics, Jun. 2022.

[106] T. Orrière, É. Moreau, and D. Z. Pai, "Electric wind generation by nanosecond repetitively pulsed microplasmas," *Journal of Physics D: Applied Physics*, vol. 52, no. 46, p. 464002, Sep. 2019.

[107] J.-C. Matéo-Vélez, P. Degond, F. Rogier, A. Séraudie, and F. Thivet, "Modelling wire-to-wire corona discharge action on aerodynamics and comparison with experiment," *Journal of Physics D: Applied Physics*, vol. 41, no. 3, p. 035205, Jan. 2008.

[108] S. Chen, J. C. P. Y. Nobelen, and S. Nijdam, "A self-consistent model of ionic wind generation by negative corona discharges in air with experimental validation," *Plasma Sources Science and Technology*, vol. 26, no. 9, p. 095005, Aug. 2017.

[109] N. Monrolin, O. Praud, and F. Plouraboué, "Electrohydrodynamic ionic wind, force field, and ionic mobility in a positive dc wire-to-cylinders corona discharge in air," *Physical Review Fluids*, vol. 3, no. 6, Jun. 2018.

[110] H. E. Revercomb and E. A. Mason, "Theory of plasma chromatography/gaseous electrophoresis. Review," *Analytical Chemistry*, vol. 47, no. 7, pp. 970–983, Jun. 1975.

[111] I. A. Kossyi, A. Y. Kostinsky, A. A. Matveyev, and V. P. Silakov, "Kinetic scheme of the non-equilibrium discharge in nitrogen-oxygen mixtures," *Plasma Sources Science and Technology*, vol. 1, no. 3, pp. 207–220, Aug. 1992.

[112] J. L. Davis and J. F. Hoburg, "Wire-duct precipitator field and charge computation using finite element and characteristics methods," *Journal of Electrostatics*, vol. 14, no. 2, pp. 187–199, Aug. 1983.

[113] B. Jayaraman and W. Shyy, "Modeling of dielectric barrier discharge-induced fluid dynamics and heat transfer," *Progress in Aerospace Sciences*, vol. 44, no. 3, pp. 139–191, Apr. 2008.

[114] R. Morrow, "The theory of positive glow corona," *Journal of Physics D: Applied Physics*, vol. 30, no. 22, pp. 3099–3114, Nov. 1997.

[115] M. Rickard and D. Dunn-Rankin, "Numerical simulation of a tubular ion-driven wind generator," *Journal of Electrostatics*, vol. 65, no. 10-11, pp. 646–654, Oct. 2007.

[116] A. A. Martins, "Modelling of an improved positive corona thruster and actuator," *Journal of Electrostatics*, vol. 71, no. 1, pp. 61–67, Feb. 2013.

[117] N. C. Nguyen, C. Guerra-Garcia, J. Peraire, and M. Martinez-Sanchez, "Computational study of glow corona discharge in wind: Biased conductor," *Journal of Electrostatics*, vol. 89, pp. 1–12, Oct. 2017.

[118] C. Kim, S. Lee, and H. G. Lee, "Characterization of electrode charges and forces in an electrohydrodynamic thruster," *AIP Advances*, vol. 12, no. 11, p. 115318, Nov. 2022.

[119] L. Zhao and K. Adamiak, "EHD flow in air produced by electric corona discharge in pin–plate configuration," *Journal of Electrostatics*, vol. 63, no. 3-4, pp. 337–350, Mar. 2005.

[120] N. E. Jewell-Larsen, S. V. Karpov, I. A. Krichtafovitch, V. Jayanty, C.-P. Hsu, and A. V. Mamishev, "Modeling of corona-induced electrohydrodynamic flow with COMSOL multiphysics," in *Proc. ESA Annual Meeting on Electrostatics, Paper E*, vol. 1. Citeseer, 2008, pp. 1–13.

[121] T. N. Tran, I. O. Golosnoy, P. L. Lewin, and G. E. Georghiou, "Numerical modelling of negative discharges in air with experimental validation," *Journal of Physics D: Applied Physics*, vol. 44, no. 1, p. 015203, Dec. 2010.

[122] G. J. M. Hagelaar, F. J. de Hoog, and G. M. W. Kroesen, "Boundary conditions in fluid models of gas discharges," *Physical Review E*, vol. 62, no. 1, pp. 1452–1454, Jul. 2000.

[123] C.-H. Chen, "Electrohydrodynamic stability," in *Electrokinetics and Electrohydrodynamics in Microsystems*. Springer, 2011, pp. 177–220.

[124] Y. Feng and J. Seyed-Yagoobi, "Understanding of electrohydrodynamic conduction pumping phenomenon," *Physics of Fluids*, vol. 16, no. 7, pp. 2432–2441, Jul. 2004.

[125] J. Seyed-Yagoobi, J. E. Bryan, and J. A. Castaneda, "Theoretical analysis of ion-drag pumping," *IEEE Transactions on Industry Applications*, vol. 31, no. 3, pp. 469–476, 1995.

[126] "Recommended international standard for dimensionless parameters used in electrohydrodynamics," *IEEE Transactions on Dielectrics and Electrical Insulation*, vol. 10, no. 1, pp. 3–6, Feb. 2003.

[127] E. Buckingham, "On Physically Similar Systems: Illustrations of the Use of Dimensional Equations," *Physical Review*, vol. 4, no. 4, pp. 345–376, Oct. 1914.

[128] N. Gomez-Vega, H. Xu, J. M. Abel, and S. R. H. Barrett, "Performance of decoupled electroaerodynamic thrusters," *Applied Physics Letters*, vol. 118, no. 7, p. 074101, Feb. 2021.

[129] E. Moreau, N. Benard, F. Alicalapa, and A. Douyère, "Electrohydrodynamic force produced by a corona discharge between a wire active electrode and several cylinder electrodes – Application to electric propulsion," *Journal of Electrostatics*, vol. 76, pp. 194–200, Aug. 2015.

[130] J. R. Roth, "Aerodynamic flow acceleration using paraelectric and peristaltic electrohydrodynamic effects of a One Atmosphere Uniform Glow Discharge Plasma," *Physics of Plasmas*, vol. 10, no. 5, pp. 2117–2126, May 2003.

[131] T. C. Corke, C. L. Enloe, and S. P. Wilkinson, "Dielectric Barrier Discharge Plasma Actuators for Flow Control," *Annual Review of Fluid Mechanics*, vol. 42, no. 1, pp. 505–529, Jan. 2010.

[132] M. E. Franke and L. E. Hogue, "Electrostatic Cooling of a Horizontal Cylinder," *Journal of Heat Transfer*, vol. 113, no. 3, p. 544, 1991.

[133] M. Molki and K. L. Bhamidipati, "Enhancement of convective heat transfer in the developing region of circular tubes using corona wind," *International Journal of Heat and Mass Transfer*, vol. 47, no. 19-20, pp. 4301–4314, Sep. 2004.

[134] A. Rashkovan, E. Sher, and H. Kalman, "Experimental optimization of an electric blower by corona wind," *Applied Thermal Engineering*, vol. 22, no. 14, pp. 1587–1599, Oct. 2002.

[135] N. F. Mott and R. W. Gurney, *Electronic Processes in Ionic Crystals*. Clarendon Press, 1948.

[136] H. Xu, N. Gomez-Vega, N. D. Wilde, J. D. Kambhampaty, and S. R. H. Barrett, "Electrical characteristics of wire-to-wire dielectric barrier discharges," *Plasma Sources Science and Technology*, vol. 30, no. 8, p. 08LT01, Aug. 2021.

[137] J. A. Geurst, "Theory of Space-Charge-Limited Currents in Thin Semiconductor Layers," *Physica Status Solidi (b)*, vol. 15, no. 1, pp. 107–118, 1966.

[138] A. A. Grinberg, S. Luryi, M. R. Pinto, and N. L. Schryer, "Space-charge-limited current in a film," *IEEE Transactions on Electron Devices*, vol. 36, no. 6, pp. 1162–1170, Jun. 1989.

[139] A. M. Tyndall and G. C. Grindley, "The mobility of ions in air.- Part I. Negative ions in moist air," *Proceedings of the Royal Society of London. Series A, Containing Papers of a Mathematical and Physical Character*, vol. 110, no. 754, pp. 341–358, Feb. 1926.

[140] N. Gomez-Vega, J. D. Kambhampaty, and S. R. H. Barrett, "Mitigating reverse emission in electroaerodynamic thrusters," *Journal of Physics D: Applied Physics*, vol. 55, no. 50, p. 505202, Nov. 2022.

[141] J. Lemetayer, C. Marion, D. Fabre, and F. Plouraboué, "Multi-inception patterns of emitter array/collector systems in DC corona discharge," *Journal of Physics D: Applied Physics*, vol. 55, no. 18, p. 185203, Feb. 2022.

[142] S. Masuda and A. Mizuno, "Flashover measurements of back discharge," *Journal of Electrostatics*, vol. 4, no. 3, pp. 215–231, May 1978.

[143] J. A. Cross, "An analysis of the current in a point-to-plane corona discharge and the effect of a back-ionising layer on the plane," *Journal of Physics D: Applied Physics*, vol. 18, no. 12, pp. 2463–2471, Dec. 1985.

[144] M. Ni, X. Wang, G. Xiao, K. Qiu, G. Yang, X. Gao, and K. Cen, "Development of back corona discharge in a wire-cylinder electrostatic precipitator at high temperatures," *Powder Technology*, vol. 286, pp. 789–797, Dec. 2015.

[145] R. S. Islamov and Y. A. Krishtafovich, "Erosion and Lifetime of Tungsten, Gold, and Nichrome Wire Anodes in an Ultracorona in Air," *IEEE Transactions on Plasma Science*, vol. 41, no. 7, pp. 1787–1793, Jul. 2013.

[146] J. D. Anderson, Jr., *Fundamentals of Aerodynamics*, 6th ed. MGraw Hill, 2017.

[147] R. G. Stearns, "Ion mobility measurements in a positive corona discharge," *Journal of Applied Physics*, vol. 67, no. 6, pp. 2789–2799, Mar. 1990.

[148] G. Lister, J. Lawler, W. Lapatovich, and V. Godyak, "The physics of discharge lamps," *Reviews of Modern Physics*, vol. 76, no. 2, pp. 541–598, Jun. 2004.

[149] R. M. Howard, "Principles of Random Signal Analysis and Low Noise Design: The Power Spectral Density and its Applications," in *Principles of Random Signal Analysis and Low Noise Design: The Power Spectral Density and Its Applications*. Wiley-IEEE Press, 2002, ch. The Power Spectral Density, pp. 59–91.

[150] N. Gomez-Vega, A. Brown, H. Xu, and S. R. H. Barrett, "Model of Multi-staged Ducted Thrusters for High-Thrust-Density Electroaerodynamic Propulsion," *AIAA Journal*, vol. 61, no. 2, pp. 767–779, Feb. 2023.

[151] E. Özkaya, N. R. Gauger, J. A. Hay, and F. Thiele, "Efficient Design Optimization of Acoustic Liners for Engine Noise Reduction," *AIAA Journal*, vol. 58, no. 3, pp. 1140–1156, Mar. 2020.

[152] A. Moronis, E. Fylladitakis, and I. Raptis, "Two-stage Cascaded EHD Air Pump Evaluation," in *2018 IEEE International Conference on High Voltage Engineering and Application (ICHVE)*. IEEE, Sep. 2018.

[153] D. S. Drew and S. Follmer, "High Force Density Multi-Stage Electrohydrodynamic Jets using Folded Laser Microfabricated Electrodes," in *21st International Conference on Solid-State Sensors, Actuators and Microsystems (Transducers)*. IEEE, Jun. 2021.

[154] A. K. M. M. H. Mazumder and F. C. Lai, "Enhancement in Gas Pumping in a Square Channel With Two-Stage Corona Wind Generator," *IEEE Transactions on Industry Applications*, vol. 50, no. 4, pp. 2296–2305, Jul. 2014.

[155] I. E. Rebrov and V. Y. Khomich, "Formation of Electrohydrodynamic Flow in Corona Discharge of a Three-Cascade Electrode System with Serial and Alternating Connection," *Plasma Physics Reports*, vol. 47, no. 1, pp. 105–109, Jan. 2021.

[156] B. W. McCormick, Jr., "Aerodynamics of V/STOL flight." Academic Press, 1967, ch. Chapter 9: Ducted propeller and fan-in-wing configurations, pp. 231–260.

[157] A. H. Sacks and J. A. Burnell, "Ducted propellers—a critical review of the state of the art," *Progress in Aerospace Sciences*, vol. 3, pp. 85–135, Jan. 1962.

[158] J. Baltazar, D. Rijpkema, J. F. de Campos, and J. Bosschers, "Prediction of the Open-Water Performance of Ducted Propellers with a Panel Method," *Journal of Marine Science and Engineering*, vol. 6, no. 1, p. 27, Mar. 2018.

[159] I.-C. Chang and R. Rajagopalan, "CFD Analysis for Ducted Fans with Validation," in *21st AIAA Applied Aerodynamics Conference*. American Institute of Aeronautics and Astronautics, Jun. 2003.

[160] S. Gaggero, D. Villa, G. Tani, M. Viviani, and D. Bertetta, "Design of ducted propeller nozzles through a RANSE-based optimization approach," *Ocean Engineering*, vol. 145, pp. 444–463, Nov. 2017.

[161] R. J. Platt, Jr., "Static tests of a shrouded and an unshrouded propeller," National Advisory Committee for Aeronautics, Tech. Rep. NACA RM No. L7H25, 1948.

[162] J. G. Leishman, "Principles of helicopter aerodynamics." Cambridge University Press, 2000, ch. Chapter 6: Conceptual Design of Helicopters, pp. 229–231.

[163] J. L. Pereira, "Hover and wind-tunnel testing of shrouded rotors for improved micro air vehicle design," Ph.D. dissertation, University of Maryland, College Park, 2008.

[164] C. Guerra-Garcia, N. C. Nguyen, T. Mouratidis, and M. Martinez-Sanchez, "Corona Discharge in Wind for Electrically Isolated Electrodes," *Journal of Geophysical Research: Atmospheres*, vol. 125, no. 16, Aug. 2020.

[165] M. Drela, *Flight Vehicle Aerodynamics*. MIT Press, 2014.

[166] S. Chen, Y. Zhu, J. Tu, and F. Wang, "Numerical investigation of an electroaerodynamic driven aeroplane: Electrical properties, ionic wind and flight performance," *Journal of Physics D: Applied Physics*, vol. 52, no. 36, p. 365203, Jul. 2019.

[167] M. Drela, "XFOIL: An Analysis and Design System for Low Reynolds Number Airfoils," in *Lecture Notes in Engineering*. Springer Berlin Heidelberg, 1989, pp. 1–12.

[168] A. Brown, N. Gomez-Vega, and S. R. H. Barrett, "Silent, Solid-State Propulsion for Advanced Air Mobility Vehicles," NASA NIAC Phase I, Tech. Rep., Feb. 2023.

[169] S. Macheret, M. Shneider, and R. Miles, "Modeling of air plasma generation by electron beams and high-voltage pulses," in *31st Plasmadynamics and Lasers Conference*. American Institute of Aeronautics and Astronautics, Jun. 2000.

[170] J. R. Rumble, Ed., *CRC Handbook of Chemistry and Physics*. Taylor & Francis Group, 2022.

[171] C. L. Allen and A. R. Taylor, "Negative ion generator using an ultraviolet source to irradiate electrically conductive material," US Patent US3 128 378A, 1964, classifications H01T23/00: Apparatus for generating ions to be introduced into non-enclosed gases, e.g. into the atmosphere.

[172] K. Kimura, *Handbook of Helium I Photoelectron Spectra of Fundamental Organic Molecules*. John Wiley & Sons Inc, 1981.

[173] A. Korobenko, S. Rashid, C. Heide, A. Y. Naumov, D. A. Reis, P. Berini, P. B. Corkum, and G. Vampa, "In-Situ Nanoscale Focusing of Extreme Ultraviolet Solid-State High Harmonics," *Physical Review X*, vol. 12, no. 4, p. 041036, Dec. 2022.

[174] A. González, "1.5 X-Ray Crystallography: Data Collection Strategies and Resources," in *Comprehensive Biophysics*. Elsevier, 2012, pp. 64–91.

[175] Y. Itikawa, M. Hayashi, A. Ichimura, K. Onda, K. Sakimoto, K. Takayanagi, M. Nakamura, H. Nishimura, and T. Takayanagi, "Cross Sections for Collisions of Electrons and Photons with Nitrogen Molecules," *Journal of Physical and Chemical Reference Data*, vol. 15, no. 3, pp. 985–1010, Jul. 1986.

[176] V. P. Guinn, "Radioactivity," in *Encyclopedia of Physical Science and Technology*. Elsevier, 2003, pp. 661–674.

[177] K. Kostecka, "Americium–from discovery to the smoke detector and beyond," *Bull. Hist. Chem*, vol. 33, no. 2, pp. 89–93, 2008.

[178] R. C. O'Brien, R. M. Ambrosi, N. P. Bannister, S. D. Howe, and H. V. Atkinson, "Safe radioisotope thermoelectric generators and heat sources for space applications," *Journal of Nuclear Materials*, vol. 377, no. 3, pp. 506–521, Jul. 2008.

[179] J. F. Kirwan, P. H. Constable, I. E. Murdoch, and P. T. Khaw, "Beta irradiation: New uses for an old treatment: A review," *Eye*, vol. 17, no. 2, pp. 207–215, Mar. 2003.

[180] H. J. Palanthandalam-Madapusi, D. S. Bernstein, and R. Venugopal, "Dimensional Analysis of Matrices: State-Space Models and Dimensionless Units," *IEEE Control Systems*, vol. 27, no. 6, pp. 100–109, Dec. 2007.